FREQUENCY INDEPENDENT ANTENNAS MULTIMODE COMPARISON

By

Kyle Andrew Zeller

A THESIS

Submitted to
Michigan State University
in partial fulfillment of the requirements
for the degree of

MASTER OF SCIENCE

Electrical Engineering

2011

ABSTRACT

FREQUENCY INDEPENDENT ANTENNAS
MULTIMODE COMPARISON

By

Kyle Andrew Zeller

Antennas with frequency independent properties have previously been developed for applications with various polarization requirements. The most commonly used planar apertures are the Archimedean spiral, the logarithmic spiral, the circular sinuous and the circular log-periodic. Four-arm, self-complementary and related growth-rate versions of each type are simulated using CST Microwave Studio. The objective is to study and describe the ability of each antenna to radiate efficiently in multimodal configurations. Through simulation, magnetic field surface plots illustrate the active regions and modal return loss confirms the bandwidth. Comparisons are made between the radiation pattern magnitude and phase ripple, polarization and active regions.

To my family and my girlfriend who have always encouraged me to pursue my dreams

ACKNOWLEDGEMENTS

The author would like to acknowledge first and foremost his Michigan State University advisor, Dr. Leo Kempel. He would also like to sincerely thank Dr. Stephen Schneider, from the Sensors Directorate, for providing the inspiration for this thesis. The initial motivation for research in frequency-independent antennas came through mentoring by Joshua Radcliffe. Finally, I would never have been able to realize the experimentation of the antennas without the countless hours of help by Raoul Ouedraogo, David Kuhl and Kevin Hamblin.

I would like to thank my thesis committee for providing me with an excellent education: Dr. Edward Rothwell, Dr. Shaker Balasubramaniam and Dr. Prem Chahal. I would also like to thank all of the students in the Electromagnetics Research Group as they have been a pleasure to work and hang out with on a daily basis. I would like to thank all of my coworkers in the Sensors Directorate, as nearly everyone has helped or at the least encouraged my progress in a small way and without them it would not have been possible to put finish. Finally, I would like to personally thank Ben Crowgey and Brandon Brys for supporting my general homelessness throughout my graduate school career by always providing me with a place to stay and something to do with the time in between researching and writing.

TABLE OF CONTENTS

LIST OF TABLES

LIST OF FIGURES

CHAPTER 1: INTRODUCTION

Antennas are the eyes and ears of modern sensor networks (1)(2)(3). To date, many separate publications have described and discussed various types of frequency-independent antennas including a few well-known examples: the Archimedean spiral, the logarithmic or equiangular spiral, the circular log-periodic, and the circular sinuous (4)(5)(6)(7). The designs have been developed to meet specific polarization requirements.

Minimal work has made direct comparisons between the separate antenna types using confined parameters. Three design principles for frequency independent antennas will form the basis of the parameter exploration set: maintain the self-complementary property, describe using "angles" wherever possible, and ensure periodic repetition on a logarithmic basis (5). The chosen antenna designs minimize the use of constants and are capable of adhering to the self-complementary property. For the third principle, logarithmic repetition, similar growth rates are selected for each antenna to ensure the repetitions occur on a similar scale throughout the frequency range of operation, with the exception of the Archimedean spiral. In addition to these principles, the antennas are confined to an inner and outer circumference.

Six antennas are designed to study four antenna type's ability to radiate. Two circular log-periodic designs are created with varying lengths of teeth and two circular sinuous designs are created with varying interleave between elements. Four-element versions are used to study the multi-mode performance. Simulations using the CST Microwave Studio Transient Solver are performed to compare and validate the performance of the designs. The solver was chosen for its ability to solve the large scale,

wide bandwidth problem using low computational resources (time and memory). The simulation models use infinitesimally-thin, copper antenna elements on top of a lossy substrate backed with an aluminum cavity with absorber.

The primary objective is to study the ability of all six antennas to radiate in the first and second mode of operation. The modal return loss and farfield patterns will be the criterion for determining their ability to radiate. The spiral antennas will be used as baseline examples, while the characteristics of the circular log-periodic and sinuous antennas will be compared and contrasted. The farfield radiation pattern symmetry will be examined to determine the amount of magnitude and phase ripple. Also, axial ratio will be used to show the polarization. Finally, to determine where the modal active regions occur, the normal component of the magnetic field (H-field) from the antenna and substrate's open surface are plotted and discussed.

Multi-arm spiral antennas can be used for angle-of-arrival (AoA) estimation to determine the azimuth and elevation of a target (8)(9). The elevation of a target can be estimated by simultaneously comparing the magnitudes of the multiple modes of operation (10). The azimuth of a target can be estimated by simultaneously comparing the phase of the modes that change linearly with respect to azimuth (11). The simplest estimation can be performed using the first two modes of operation for a four-arm spiral (12). This method can achieve accurate results across the bandwidth of the antenna platform (13). The results rely on using antennas with minimal magnitude and phase ripple as well as low axial ratios. The effort to characterize the first and second mode of operation for each antenna corresponds with the ability to estimate the angle-of arrival while inability to maintain low axial ratios leads to ambiguous results.

CHAPTER 2: FREQUENCY INDEPENDENCE

In 1954, the concept of the spiral antenna was born when a dipole antenna was wound into an Archimedean spiral (14)(15). In the late 1950s, research related to frequency independent antennas began with work by V. H. Rumsey (16). The definition as stated from *Frequency Independent Antennas*, "[T]he impedance, polarization, pattern, etc., are invariant to a change of scale that is in proportion to the change in wavelength, provided the antenna is made of practically perfect conductors and dielectrics. This shows that if the shape of the antenna were entirely determined by angles, the performance would have to be independent of frequency, for such a shape would be invariant to a change of scale" (17). This property is known as *Rumsey's Principle* and is true only for infinite logarithmic spiral and biconical antennas (18).

Even though the logarithmic spiral is the only true planar, frequency independent antenna, the Archimedean spiral can be viewed as a logarithmic spiral with an infinitesimally small growth rate (4). Self-complementary versions exhibit properties that are very similar to the logarithmic spiral and virtually frequency independent. The final two antenna types, the circular log-periodic and the circular sinuous, are only quasi-frequency-independent. They are piecewise designs that are logarithmically scaled and repeated to form the structure. The circular log-periodic design is made of teeth that overlap in the center of the elements. The circular sinuous design has cells that wrap back-and-forth to meet at the center, interleaving with the other elements at the outer edges. They show frequency independent characteristics in sections throughout the frequency band of operation, related to the interactions between the piecewise sections (5)(19).

2.1 THE SELF-COMPLIMENTARY PROPERTY

In order to maintain constant impedance across the band of operation a multi-terminal object must be self-complementary (20). Self-complementary elements are identical elements with identical spacing between. Thus, if the elements are rotated about the origin then the metal would entirely fill the open space and vice-versa. Using self-complementary elements eliminates the need to characterize each type for separate impedances. This ideal impedance derived from the self-complementary property relies on the elements being infinitesimally thin. A practical antenna will have elements of finite thickness which will lower the impedance. Also, practical elements cannot be infinity large or infinitesimally small. Once limited to specific inner and outer radii, the self-complementary property will again be violated. If the elements are driven at a frequency lower than it is capable, an effect called truncation will occur as current is reflected from the end of the element. While, if driven at a frequency higher than it is capable, improper radiation from the feed region will occur. As a result, they will only exhibit frequency independent characteristics within the frequency band they are designed to operate. The impedance and farfield patterns will also exhibit non-ideal characteristics at the bounds of the frequency band of operation.

2.2 MULTIPLE ELEMENTS AND MODES

In modeling, multiple self-complementary elements may be fed from their center point using one of two methods (21). The first method is to connect the terminals in a ring formation where each element is connected to its nearest neighbor using a magnetic current source. The second method is to connect the terminals in a star formation where

the electric current sources connect in the center. As the number of terminals increases, modes may be formed by applying precise phase offsets. An infinite number of modes can be input into the multi-terminal system by successively increasing the phase offset between the ports but in practice the number of useful modes is equal to one less than the total number of elements (10). Each useful mode of operation will have a characteristic impedance (20).

As an example, a two-arm spiral has one useful, balanced mode and a second, unbalanced mode that requires a ground plane to operate (12). The method to create the first mode is to excite the arms 180° out-of-phase with each other, for a total phase progression of 360°. This mode has a frequency independent impedance of 60πΩ. The radiation pattern of the first mode is at a peak toward boresight, reduces toward the horizon, and is symmetric about azimuth. The unbalanced mode occurs when both terminals are fed the same, in-phase signal. Only phase progressions that are 360° (2π) multiples will excite a mode of operation. For the two-arm case, if the total accumulated phase progression is increased to 720° the unbalanced mode will dominate and if the accumulated phase progression is increased to 1080° the first mode of radiation will dominate.

Four-terminal structures will have three useful modes of operation. The first mode can be achieved by exciting each arm 90° out-of-phase with the adjacent arms, for a total phase progression of 360°. The second mode is accomplished by exciting each arm 180° out-of-phase with the adjacent arms for a total progression of 720°. The third mode is excited with 270° (or -90°) phase-shifts between adjacent arms, for a total phase progression of 1080°. Table 2-1 shows the required phase-offsets for each mode of

operation with the theoretical phase input on the left and the relative phase input on the right. For the circular log-periodic and circular sinuous antennas, the third mode of operation is also called the negative or reverse of the first mode of operation for reasons that will be explained. The impedance for the first and third modes is $30\sqrt{2}\pi\Omega$, while the impedance for the second mode is $30\pi\Omega$.

TABLE 2-1: FOUR-ELEMENT MODAL PHASE OFFSETS

Element	Mode 1		Mode 2		Mode 3 / -1	
1	0°	(0°)	0°	(0°)	0°	(0°)
2	90°	(90°)	180°	(180°)	270°	(270°)
3	180°	(180°)	360°	(0°)	540°	(180°)
4	270°	(270°)	540°	(180°)	710°	(90°)

2.2.1 RADIATION AND POLAIZATION

All planar frequency independent antennas exhibit bidirectional radiation patterns, with opposite-handed circular polarization in separate directions from the antenna (10). For a spiral, each mode of operation has a distinct radiation pattern. The radiation pattern of the first mode for a four-arm spiral is the same as the first mode, or balanced mode, of the two-arm spiral with a peak at boresight. The radiation pattern for the second mode has a null at boresight, a peak near 40° in elevation approximately 3dB weaker than the peak of the first mode. Finally, the radiation pattern of the third mode is similar to the second except with a peak occurring around 50° in elevation. Figure 2-1 shows an example of the radiation patterns for a four-arm spiral in a single direction. The patterns are theoretically symmetric with rotation about azimuth. In practice, there is some variation, or ripple, in the patterns. The ripple will decrease as the number of elements increases (10)(22).

The radiation pattern for the third mode of operation, from Figure 2-1, is only achievable using the spiral due to its inherent polarization filtering (12). The circular log-

periodic and circular sinuous antennas will instead radiate the pattern of the first mode of operation with opposite-handed circular polarization. The third mode is also titled the negative first mode because the phase inputs are the reverse (10). If a spiral is driven with the third mode, but is not large enough in circumference to support its operation, the negative first mode will instead radiate when energy, reflected from the ends, travels in the opposite direction.

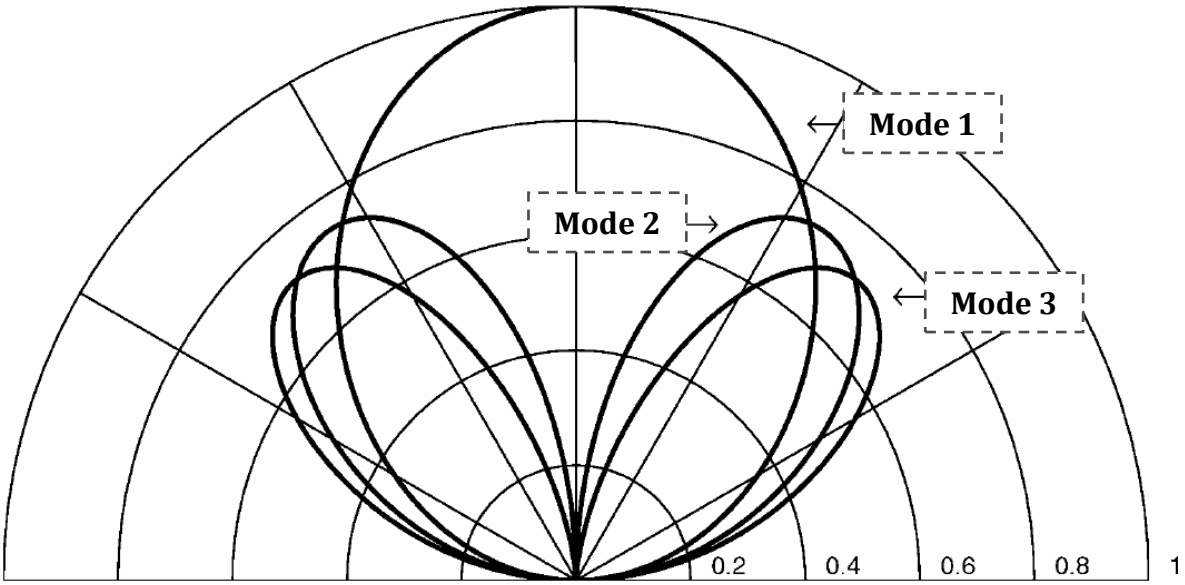

FIGURE 2-1: FOUR-ARM SPIRAL MODAL RADIATION PATTERNS

For each mode of operation of the multi-arm spiral, the radiation pattern also has a characteristic phase progression that occurs (10). The phase changes linearly with respect to azimuth for each mode. The phase undergoes one -360° (-2π) phase progression for the first mode, two for the second mode and three for the third mode. Figure 2-2 shows how the phase progression increases with the mode of operation, where 'phi' is 'azimuth'. The circular log-periodic and circular sinuous will have a phase that is the same for mode one but has a slope in the opposite direction for the first negative mode. Similar to the

magnitude, in practice the slope of the phase is not perfectly linear but will have some variation, or ripple. Again, the ripple will decrease as the number of elements increases.

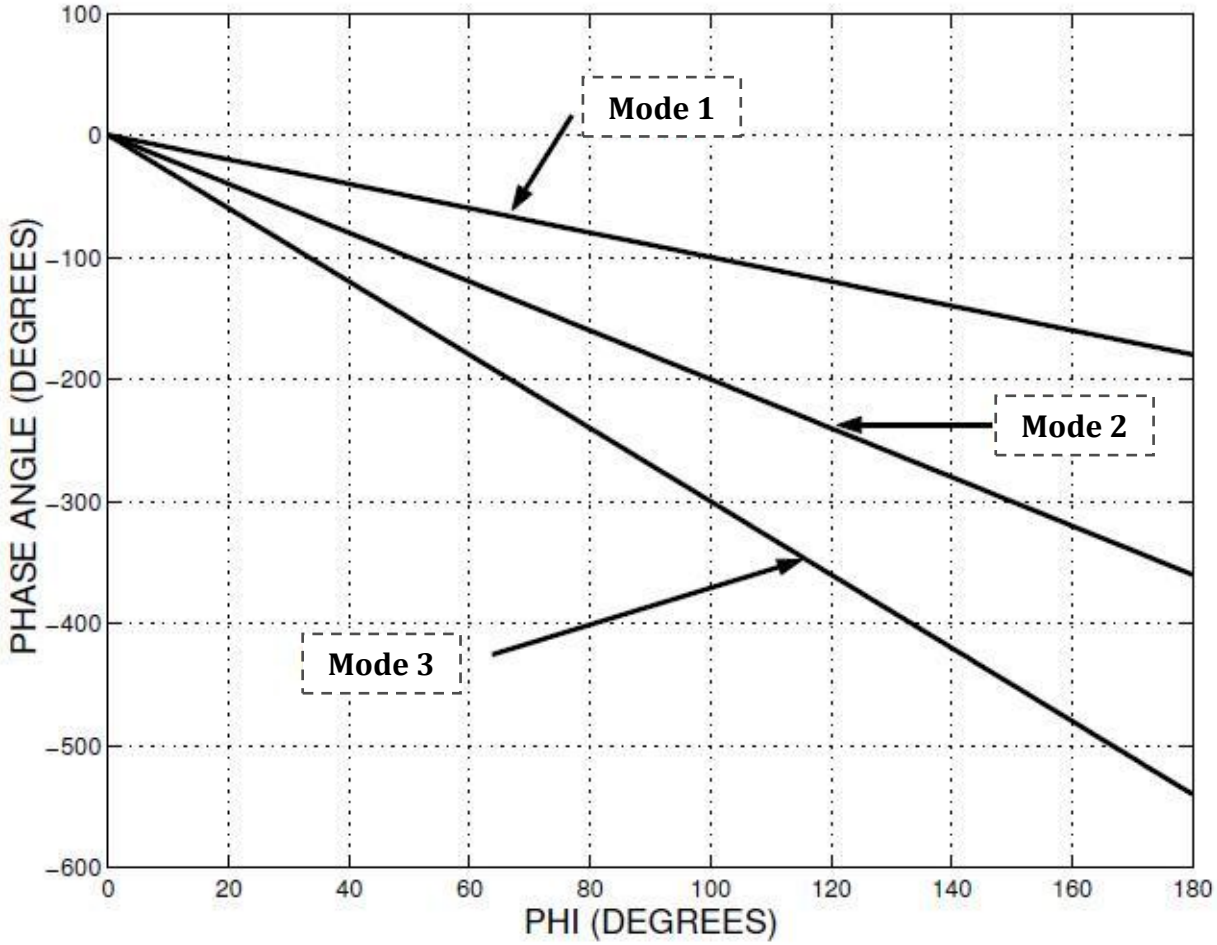

FIGURE 2-2: FOUR-ARM SPIRAL MODAL PHASE PATTERNS [WITH COMPENSATION]

2.2.2 ACTIVE REGION

The active region of a frequency independent antenna is where the currents align to induce radiation at a specific frequency (11). The active region of the logarithmic and Archimedean spirals occurs at an increasing circumference for each mode of operation. Within the active region, the currents can be shown to align across the gaps, or across the arms, to form a circle (4). For the first mode, the active region occurs at a circumference equal to one wavelength (15)(10). For the second, the active region occurs at a

circumference of two wavelengths and three wavelengths for the third. The minimum diameter of a spiral is directly linked to the highest frequency of operation and correspondingly the maximum diameter of the spiral is linked to the lowest frequency of operation combined with the highest mode of operation. The active region of the two-element, circular log-periodic has been shown to be linked to the length of the tooth while the active region of the multi-element circular sinuous is suggested through suggested design equations (5)(23).

For the case of using four-element versions of the antennas introduced, there are drawbacks to using any version. Drawbacks to using the logarithmic or Archimedean spiral are that, in order to radiate at increasing mode numbers, the circumference must also increase by one wavelength and that they are only capable of a single circular polarization. While drawbacks to using the circular log-periodic or sinuous is that they are incapable of radiating in the third mode of operation.

2.3 DESIGN

The basic relation between frequency (f), wavelength (λ) and the speed of light (c) is represented by Equation 2-1. Equation 2-2 is the circumference required to operate a spiral, based on a given mode of operation (m), related to the radius (r). Combining the two, Equation 2-3 relates the radius of a spiral antenna with the frequency and mode of operation.

$$\boldsymbol{f * \lambda = c} \qquad \textbf{(2-1)}$$

$$\boldsymbol{cir = m * \lambda = 2\pi r} \qquad \textbf{(2-2)}$$

$$\boldsymbol{r = m * c/(2\pi f)} \qquad \textbf{(2-3)}$$

Given a target frequency band of 2-18GHz and a requirement to radiate in the second mode of operation, the inner and outer radius for both the logarithmic and Archimedean spiral antennas can be calculated using these equations. The maximum inner radius is 2.65mm, while the outer radius is 47.7mm. For the final designs, values of 2.5mm for the inner radius and 53.5mm for the outer radius are chosen. The remaining antenna designs are confined to these dimensions.

The logarithmic spiral is the basic logarithmic design that the circular log-periodic and circular sinuous designs are compared. All three antenna types grow based on a logarithmic growth rate that can be chosen as a basic parameter in their design equations. The logarithmic spiral has been shown to have uniform properties when using one-and-a-half or more turns(6). A growth rate of 0.325 is selected and it allows for the logarithmic spiral to undergo three turns, where each turn is one half of a full revolution.

An individual log-periodic element is confined to a quadrant, or 90° (π/2), of the circle. To design an equivalent circular log-periodic antenna, two teeth are added for each quadrant the logarithmic spiral passes through with the final tooth always ending in the same direction as the spiral wrap. The logarithmic spiral chosen undergoes three turns (six quadrants), therefore an equivalent log-periodic will have twelve teeth. For the two-element case, increasing tooth size and decreasing the growth rate are shown to increase the directivity of the antenna (5).

In the circular sinuous design equation, the growth rate is contained within a logarithm function, itself within a denominator. Increasing the value does the opposite of a traditional growth rate and as a result it is controlled in an inverse exponential manner. The growth rate for the final designs is the inverse exponential of the growth rate chosen

for the other logarithmic antennas. This value, 0.7225, creates a circular sinuous design with nine cells.

The Archimedean spiral arms do not grow logarithmically but instead maintain the same width as they travel away from the center. As previously stated, they can be viewed as a logarithmic spiral with an infinitesimally small growth rate. They are common in practice and are used to achieve the highest number of turns within a given circumference. Increasing the number of turns, and subsequently decreasing the growth rate, reduces axial ratio yet also reduces gain (4). The final design of the Archimedean spiral undergoes ten turns. The circular log-periodic can be designed similarly to the Archimedean spiral by removing the logarithmic growth rate parameter and instead maintaining the same width for each tooth. The circular sinuous can be chosen to grow in a similar manner if the growth rate is chosen to vary as a function of distance from the origin (24).

2.3.1 LOGARITHMIC SPIRAL

The logarithmic spiral is the only planar structure that can be defined by only angles. Equation 2-4 defines the logarithmic spiral curve (6). The spiral begins at an inner radius (r) and grows exponentially with respect to an angle (φ) multiplied by a growth rate (a). An offset (δ) can be added to φ to draw separate curves, shown in Equation 2-5. These equations are all that are required to define the spiral structure shown in Figure 2-3. The two curves, offset by a 45° ($\pi/4$) in order to be self-complementary, can be connected at their ends with straight lines, or for this case with arcs.

$$\boldsymbol{\varphi_{\phi} = re^{a\phi}} \qquad \textbf{(2-4)}$$

$$\boldsymbol{\varphi_{\phi} = re^{a(\phi \pm \delta)}} \qquad \textbf{(2-5)}$$

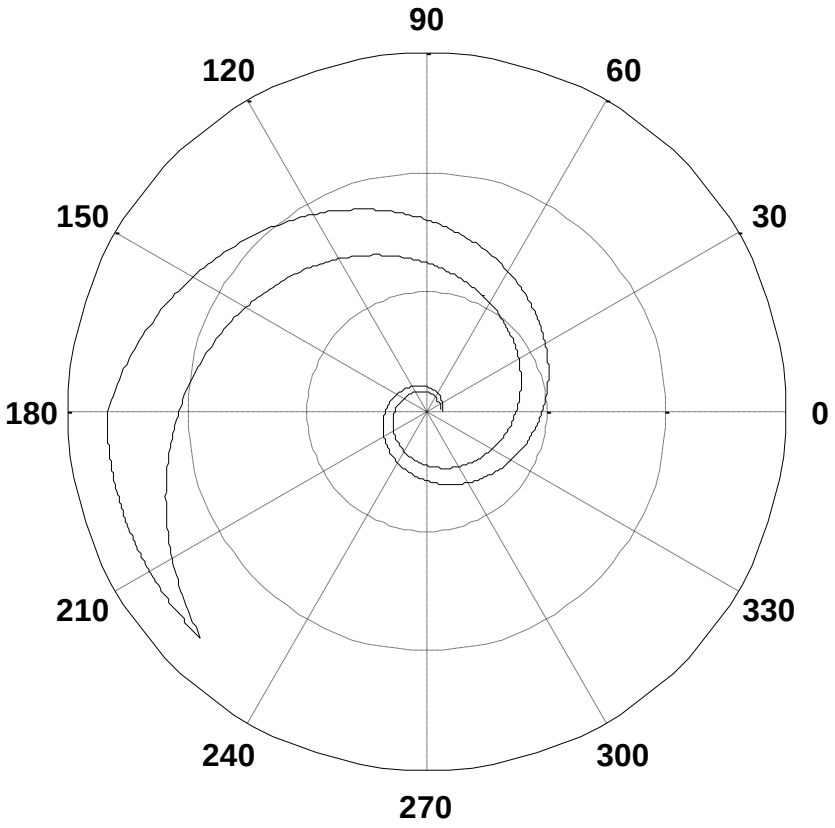

FIGURE 2-3: LOGARITHMIC SPIRAL – INDIVIDUAL ARM

Connecting the arms with arcs allows for the design to conform to specific inner and outer radii. Figure 2-4 shows eight spiral curves plotted using MATLAB with the original element plotted in red. The curves extend three turns or rotations through phi by 180° (π). To summarize the final design, a growth rate of 0.325 is used in combination with a starting radius of 2.5mm and three turns to extend out to an outer radius of 54mm. Individual arms are created with to be self-complementary, with 45° (π/4) offsets, neighboring arms are 90° (π/2) offset between each other for symmetry.

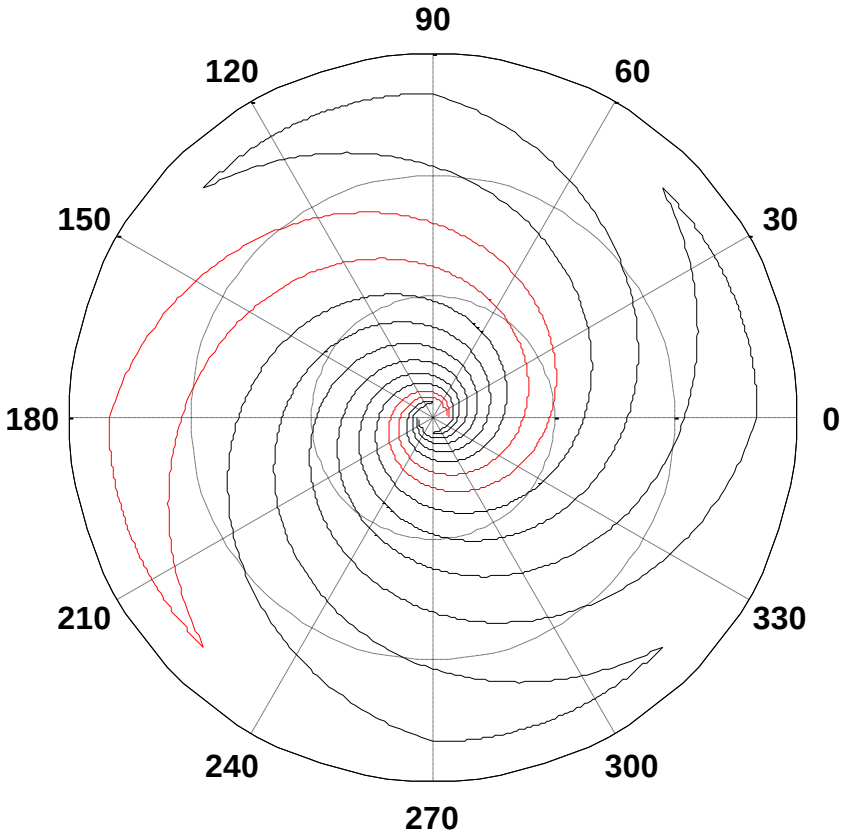

FIGURE 2-4: FOUR-ARM LOGARITHMIC SPIRAL
"FOR INTERPRETATION OF THE REFERENCES TO COLOR IN THIS AND ALL OTHER FIGURES, THE READER IS REFERRED TO THE ELECTRONIC VERSION OF THIS THESIS."

2.3.2 ARCHIMEDIAN SPIRAL

The Archimedean spiral is similar to the logarithmic spiral, with the exception that the angular component (φ) and growth rate (a) are not located inside an exponential(15). Equation 2-6 defines the curve and Equation 2-7 shows how *phi* is given an offset (δ).

$$\boldsymbol{\varphi_{\phi} = r + a\phi} \qquad \textbf{(2-6)}$$

$$\boldsymbol{\varphi_{\phi} = r + a(\phi \pm \delta)} \qquad \textbf{(2-7)}$$

Figure 2-5 shows the pair of offset curves plotted in MATLAB and connected with arcs at the inner and outer radii. Again, the offset is 45° (π/4) for elements that are self-complementary.

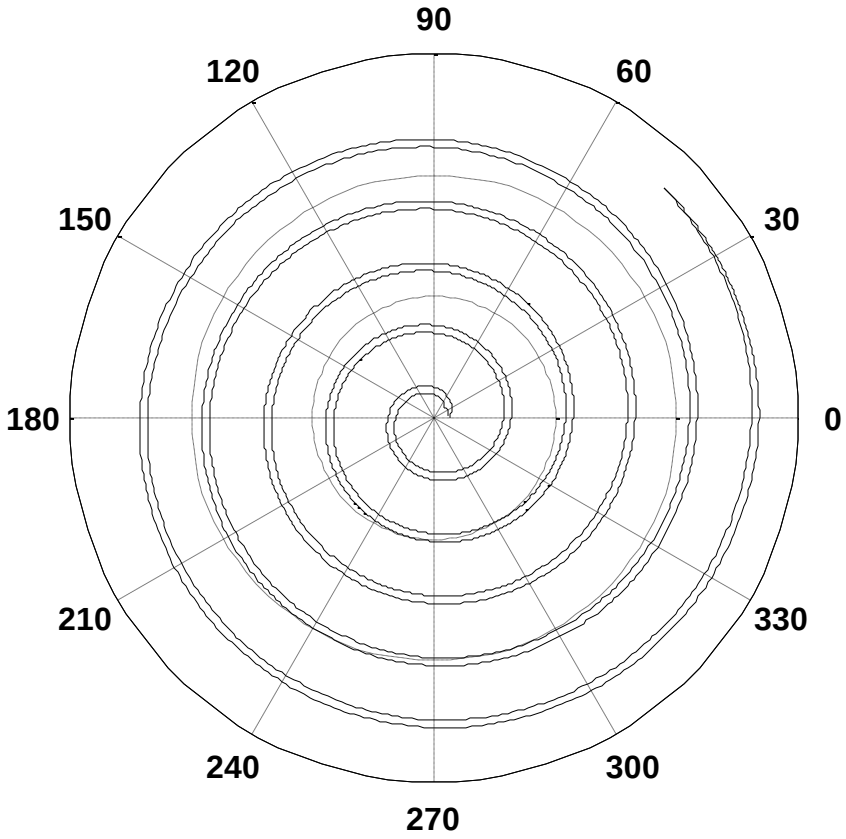

FIGURE 2-5: ARCHIMEDEAN SPIRAL – INDIVIDUAL ARM

Figure 2-6 shows eight spiral curves plotted using MATLAB with the original element shown in red. To summarize the final design, a growth rate (a) of 1.625 is used in combination with a starting radius of 2.5mm and ten turns to extend out to an outer radius of 54mm. As with the logarithmic spiral, individual arms are created to be self-complementary, with 45° (π/4) offsets and neighboring arms that are 90° (π/2) offset between each other. The final arm width of the elements is a constant 1.276mm.

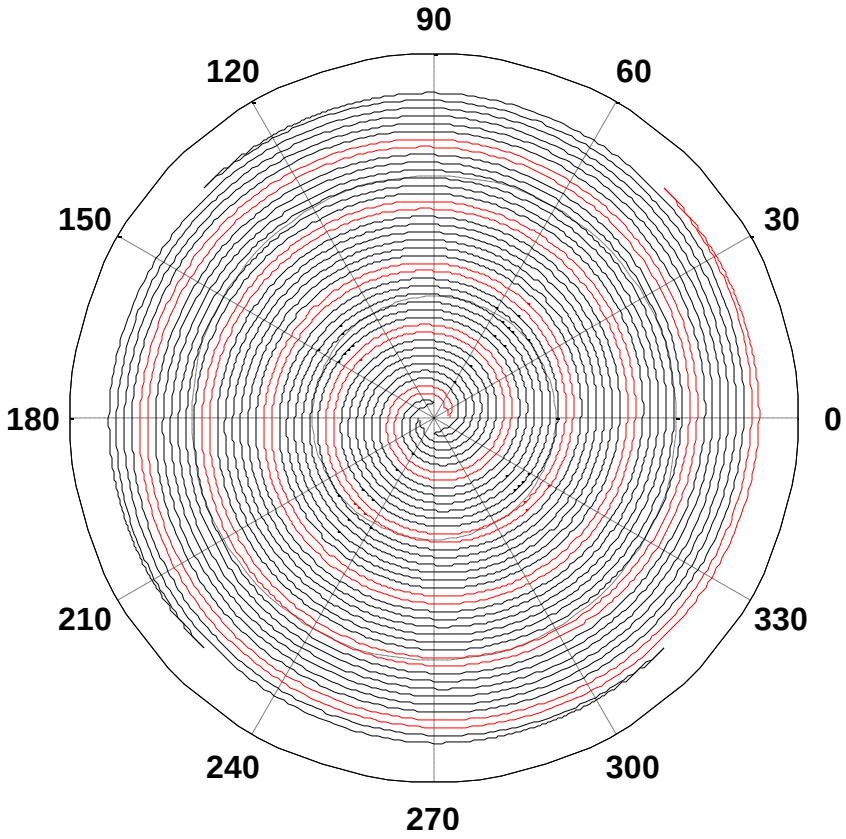

FIGURE 2-6: FOUR-ARM ARCHIMEDEAN SPIRAL

2.3.3 CIRCULAR LOG-PERIODIC

The circular log-periodic element is defined by a group of teeth that are overlapping at the center. For the four-element case, individual elements are confined to a quadrant of the circle. To specify the inner radii, or inside arcs of each tooth Equation 2-4 is solved using the starting radius of 2.5mm and stepping *phi* by π/4 from 0 to 3π. This allows the growth rate (a) to define the same logarithmic ratio between teeth. Elements have an overlap angle (β) and tooth length angle (α) which define the start and stop the element span (*phi*), shown in Equations 2-8 and 2-9.

$$\boldsymbol{\phi_{start} = \mp\beta/2} \quad \textbf{(2-8)}$$

$$\boldsymbol{\phi_{end} = \pm\beta/2 \pm \alpha} \quad \textbf{(2-9)}$$

In order to retain a self-complementary, four-element structure alpha and beta must sum to 45° (π/4). Figure 2-7 shows two circular log-periodic elements plotted with MATLAB, both having twelve teeth and using a growth rate of 0.325. As stated previously, longer teeth are associated with lower frequency of operation. The left element in Figure 2-7 has an overlap of 22.5° (π/8) and a tooth length of 22.5° (π/8), while the right element has an overlap of 15° (π/12) and a tooth length of 30° (π/6). In both designs, the innermost tooth begins at a radius of 2.5mm and the outermost tooth has a final radius of 53.5mm.

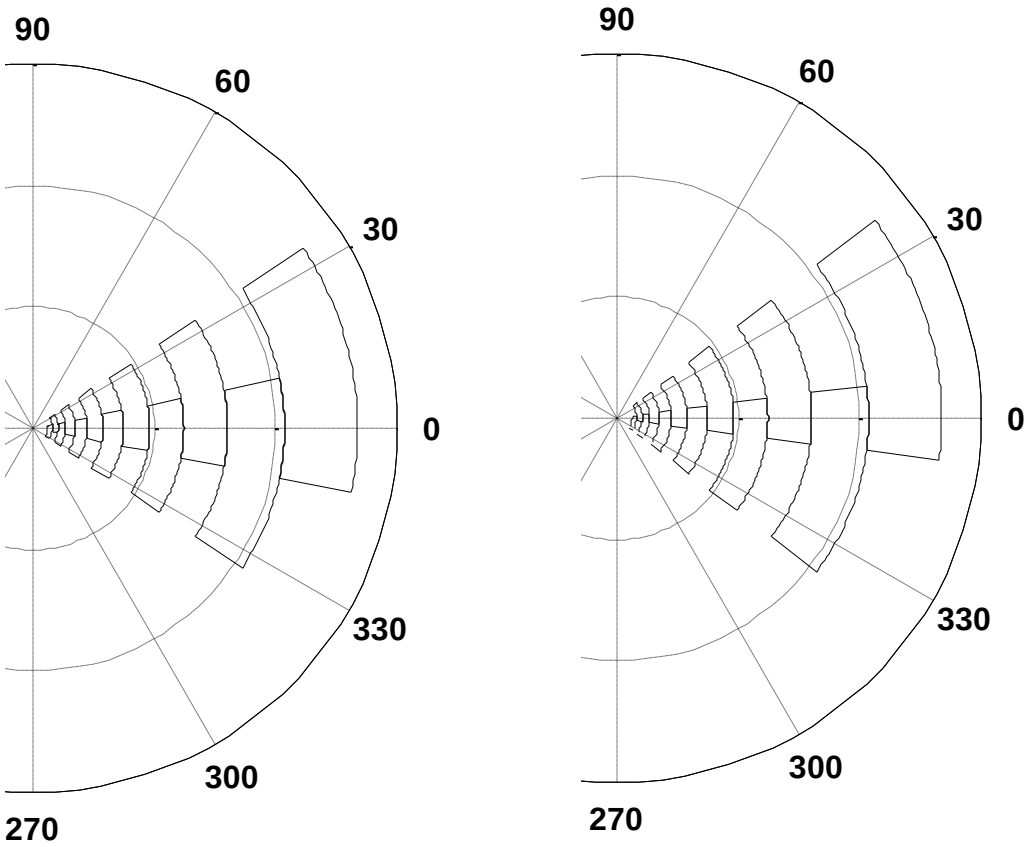

FIGURE 2-7: CIRCULAR LOG-PERIODIC – INDIVIDUAL ELEMENTS

Figure 2-8 shows four circular log-periodic elements, with the original element from Figure 2-7 (*left*) shown in red, with an overlap of 22.5° (π/8) and a tooth length of 22.5° (π/8).

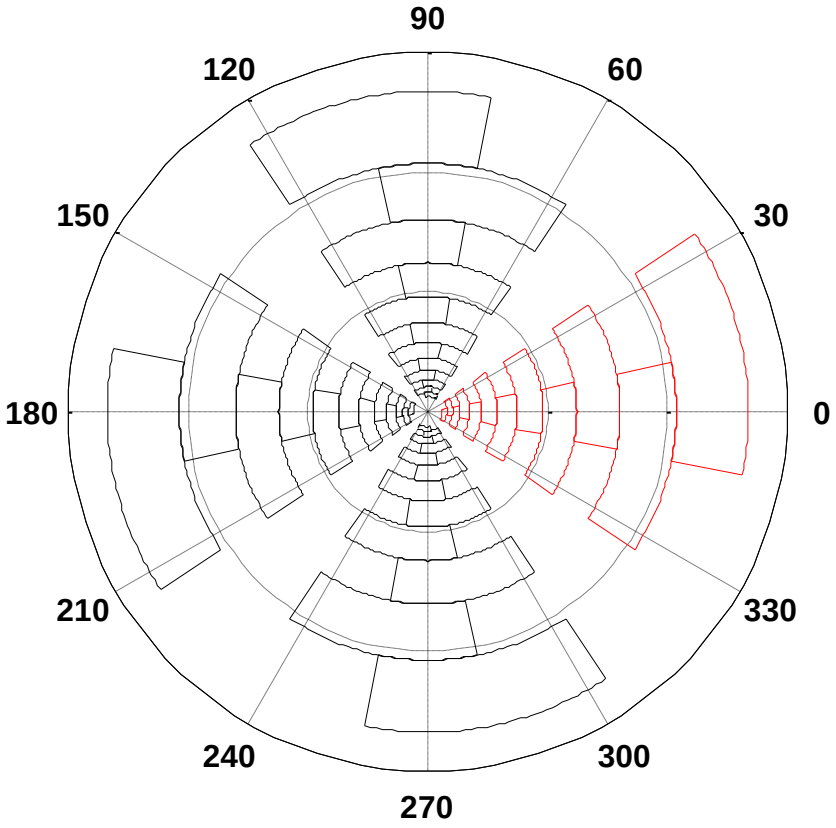

FIGURE 2-8: FOUR-ELEMENT CIRCULAR LOG-PERIODIC [Π/8]

Figure 2-9 shows four circular log-periodic elements with the original element from Figure 2-7 (*right*) shown in red, again with an overlap of 15° (π/12) and a tooth length of 30° (π/6). In the remainder of the report for the sake of condensing titles, the individual designs are identified by their overlap angle (π/8) vs. (π/12).

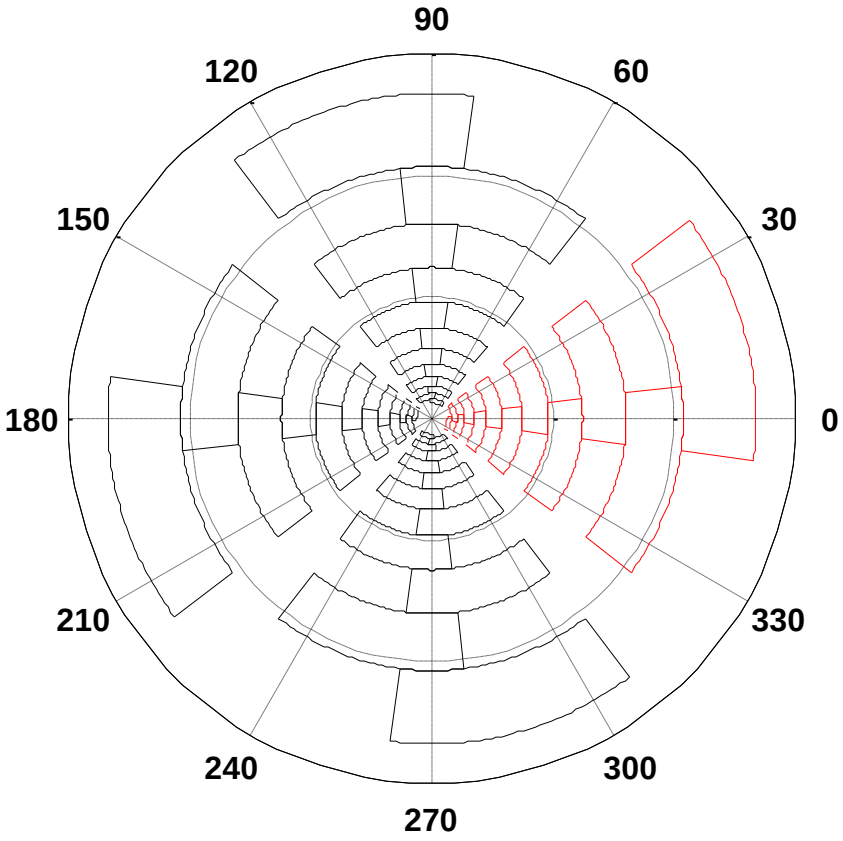

FIGURE 2-9: FOUR-ELEMENT CIRCULAR LOG-PERIODIC [Π/12]

2.3.4 CIRCULAR SINUOUS

The equations to describe the circular sinuous curves begin from a given outer radius (R_p) as opposed to an inner radius as with the previous curves. Equation 2-10 describes a sinuous curve, while in Equation 2-11 an offset (δ) creates a second curve (23).

$$\boldsymbol{\varphi_r = (-1)^p(\alpha_p)\sin\left[\left(\pi\ln\left(r/R_p\right)\right)/\ln\left(\tau_p\right)\right]} \qquad \textbf{(2-10)}$$

$$\boldsymbol{\varphi_\delta = (-1)^p(\alpha_p \pm \delta)\sin\left[\left(\pi\ln\left(r/R_p\right)\right)/\ln\left(\tau_p\right)\right]} \qquad \textbf{(2-11)}$$

From the starting outer radius, the structure wraps back-and-forth about a center angle creating cells, also called wraps. The growth rate (τ_p) in this case works as the exponential inverse of the growth rate (a) from the spiral equation, shown in Equation 2-12. As this growth rate nears one, the structure grows slowly with many cells. An interleave

angle (α) determines the amount the elements interleave at the maxima of each cell. The growth rate and interleave for the two-element version has been studied (24).

$$\tau_p = e^{-a} \qquad \textbf{(2-12)}$$

Similar to the spiral, Equations 2-10 and 2-11 are all that are required to define the sinuous structures in Figure 2-10. The curves are connected at their ends with arcs confining the elements to inner and outer radii. The left element in Figure 2-10 has an interleave of 45° (π/4), while the right element has an interleave of 60° (π/3). As with the spiral antennas, the self-complementary arm width is defined by an offset of 45° (π/4). In both designs, the outer radius begins at 53.5mm and extends to an inner radius of 2.5mm.

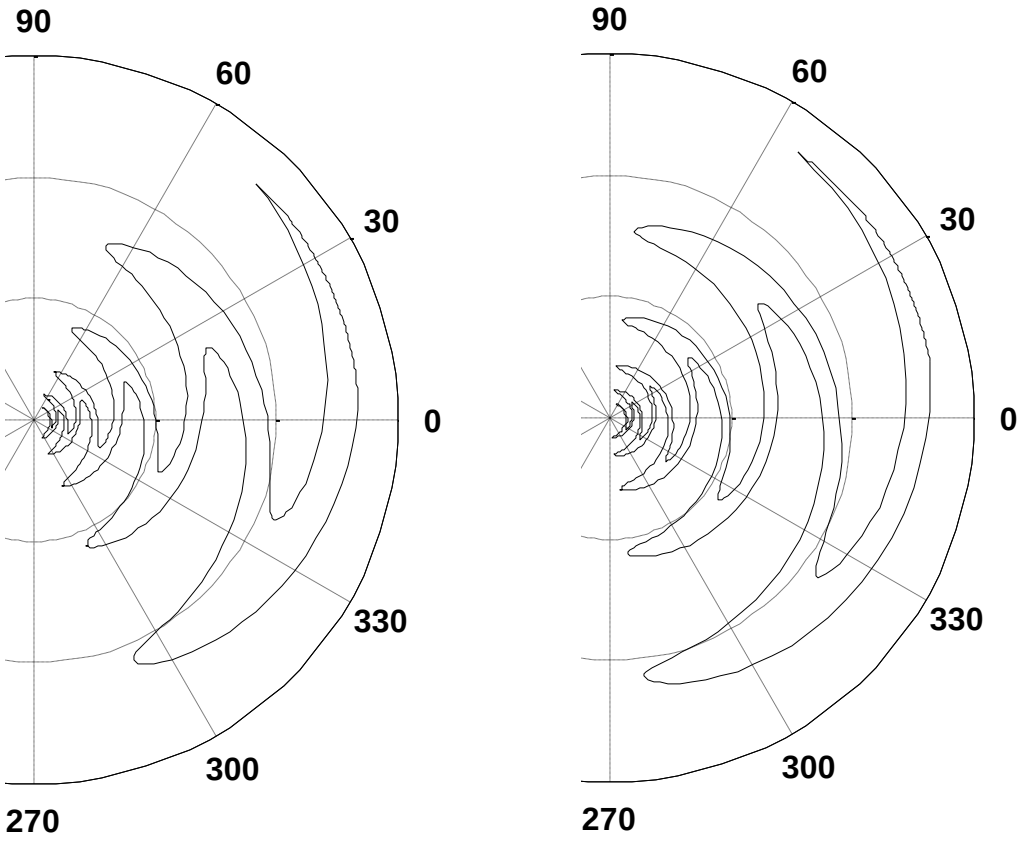

FIGURE 2-10: CIRCULAR SINUOUS – INDIVIDUAL ELEMENTS

The active regions for the multi-arm circular sinuous antenna have been outlined for the two-element case and shown to exist within specified circumferences (23). Equations 2-13 and 2-14 are given as guidelines, by the inventor, for inner and outer circumferences for desired high and low frequency limits.

$$\lambda_H = 4 * r_i \quad \textbf{(2-13)}$$

$$\lambda_L = 4 * r_o(\alpha + \delta) \quad \textbf{(2-14)}$$

The suggested inner radius is 4.15mm and the outer radius, 24.0mm (π/4) and 20.5mm (π/3). The final designs extend to both twice the suggested outer radius and half the inner radius. Including the original element from Figure 2-10 in red, Figure 2-11 has a four-element design with an interleave of 45° (π/4).

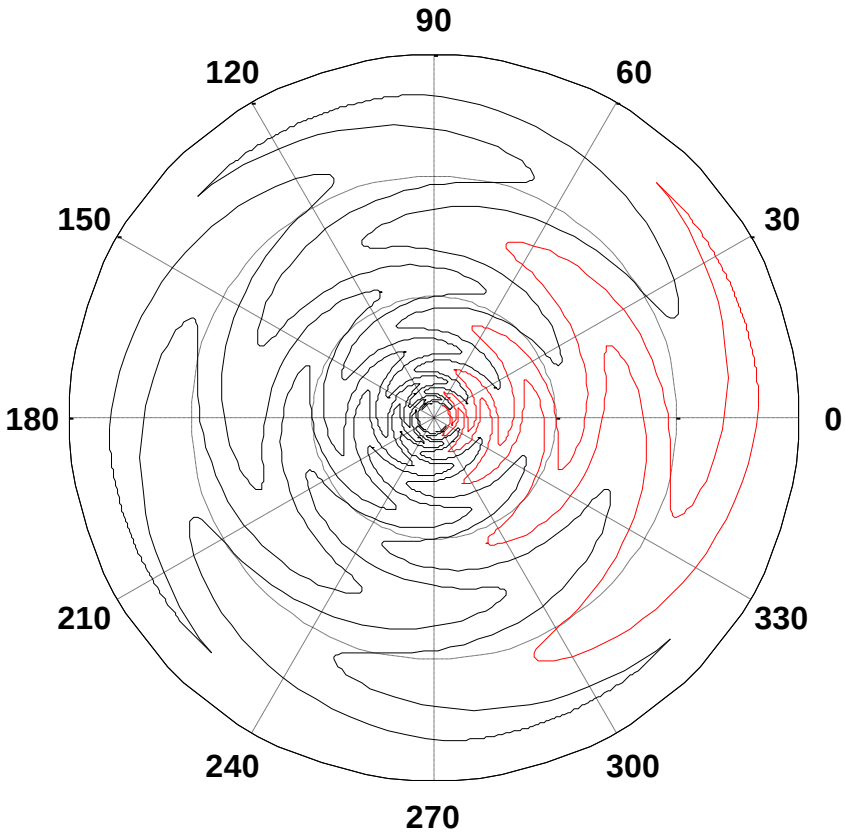

FIGURE 2-11: FOUR-ELEMENT CIRCULAR SINUOUS [Π/4]

Figure 2-12 has a four-element design with an interleave of 60° (π/3). Again as with the circular log-periodic antennas, in the remainder of the report for the sake of condensing titles the individual designs are identified by their interleave angle (π/4) vs. (π/3).

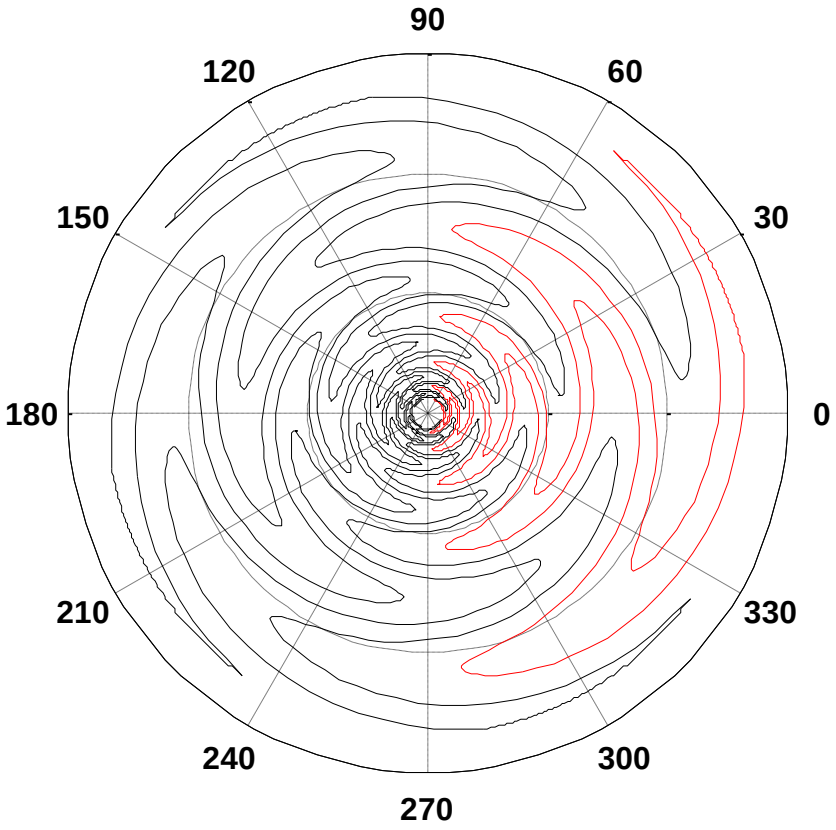

FIGURE 2-12: FOUR-ELEMENT CIRCULAR SINUOUS [Π/3]

2.3.5 SUBSTRATE, ABSORBER AND CAVITY

In order to realize the designs for experimentation and application, the antennas must be fabricated on a substrate and reduced to unidirectional radiation by placing them above an absorber-filled cavity.

Placing the elements on top of a substrate with a relative permittivity above that of free-space will lower the impedance and shift the frequency of operation (25). An ideal substrate for usage in this application would be thin, durable and low-loss. The substrate

chosen is Rogers Corp. RT/duroid® 5880, with a relative permittivity of 2.2 and a loss tangent of 0.0009 measured at 10GHz, at a thickness of 0.015in (381μm). Building an antenna using a metal of finite thickness also reduces the effective impedance (20). Copper may be added either by rolling and adhering or by electrodepositing it onto the surface of the substrate. The latter is chosen because it can be applied at ¼ ounce (9μm) thickness.

Due to bidirectional radiation, an absorber-filled cavity is added to one side. An antenna over an empty cavity is equivalent to a circular waveguide with an arbitrary feed and a short at either end. An arbitrary feed will excite an infinite number of modes in a waveguide structure (26). The excitable modes will be those with cutoff frequencies below the operation frequency. The TM_{0X} modes in circular waveguides consist of circular magnetic fields with radial-directed electric fields, similar to the currents induced by a spiral, and the first three can be seen in Figure 2-13(27). For a 4.5" (114mm) diameter waveguide, the cutoff frequency of the TM_{01} mode is 2.008GHz, TM_{02} is 4.608GHz, TM_{03} is 7.225GHz and TM_{04} is 9.825GHz.

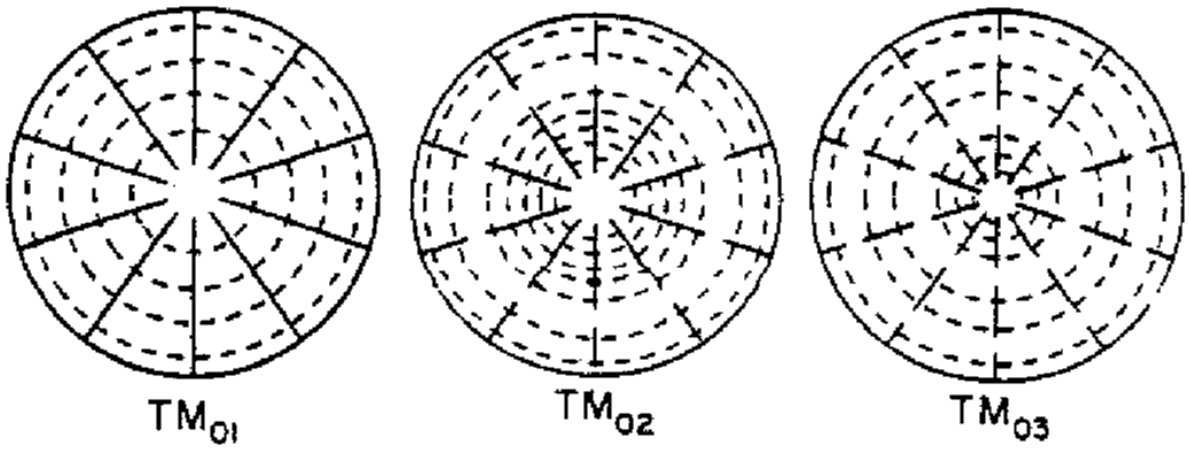

FIGURE 2-13: CIRCULAR WAVEGUIDE MODES [TM_{0X}]

An empty cavity has 32 modes with cutoff frequencies between 1.5-12GHz. An absorber is designed to attenuate energy, yet it will also have an increasing relative permittivity that lead to reflections at transitions. Layering absorber allows for more loss to occur at increasing distances away from the antenna, while minimizing abrupt changes and therefore reflections (11). The cavity has 0.125" (3.175mm) of Divinycell® H45 foam core material, with a relative permittivity of 1.1 or electrically nearly equivalent to air, that minimally disturbs energy in the near-zone of the elements. Following the foam layer are three layers of Emerson & Cuming ECCOSORB® LS cavity-fill absorber, each layer having increasing relative permittivity and providing increasing loss. The three layers are: 1.0" (25.4mm) of LS-22, 0.375" (9.525mm) of LS-24, and 1.0" (25.4mm) of LS-26. Finally, directly above the aluminum back-plate is a 0.040" (1.0mm) ECCOSORB® MCS layer with an elevated relative permeability to impede surface current propagation.

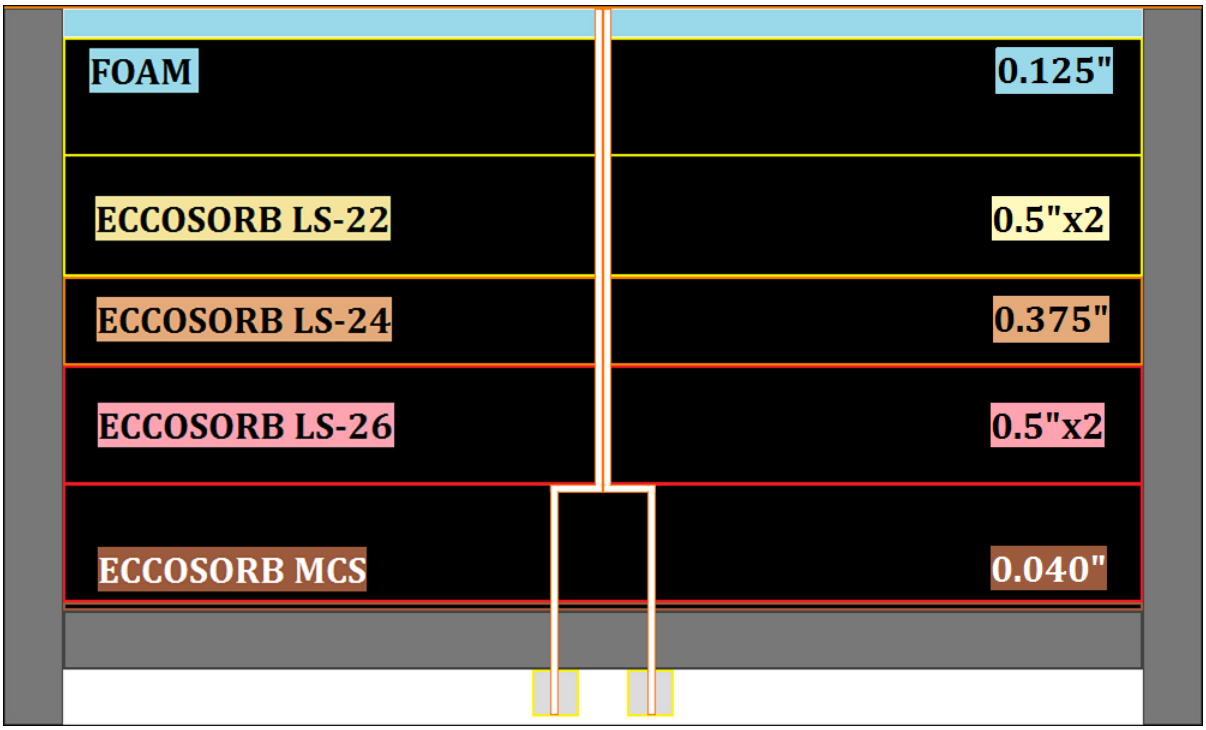

FIGURE 2-14: ECCOSORB® CAVITY ABSORBER LAYERS

CHAPTER 3: SIMULATION

The CST Studio Suite™ is an extensive simulation platform that contains a number of computational electromagnetic simulation modules. CST Microwave Studio® performs full three-dimensional electromagnetic simulations at high frequencies. Models are constructed using the ACIS 3D modeling kernel and/or Visual Basic scripts, or macros, to automate the process. Models are automatically meshed using hexahedral or tetrahedral grids. A number of different solvers in both the time and frequency domains are included. The two primary solvers for single antenna problems are the transient, or time domain, solver and the frequency domain solver.

The transient solver is originally based on the MAFIA 4 electromagnetic simulation software package (28). It is an implementation of Finite Integration Theory (FIT) and it only supports the hexahedral mesh. This solver has the ability to solve multiple ports simultaneously. The frequency domain solver is a simple implementation of Finite Element Method (FEM) and it supports both hexahedral and tetrahedral meshes. This solver has no ability to solve multiple ports simultaneously; therefore it could not be used to acquire radiation patterns for multi-element modal cases.

3.1 TRANSIENT FULL-WAVE SIMULATION USING FINITE INTEGRATION THEORY (FIT)

The transient solver simulates the antenna structure exciting the port(s) with a Gaussian pulse, tailored to the frequency range of interest, and calculating the propagation of the energy through the system. In the case of discrete ports, the power of the input signal fixed to 1W and the impedance set to a user defined value. Throughout the simulation, the

current and voltage at the port are allowed to change. The simulation will progress until the energy from the input signal(s) dissipates away from the structure and the model is considered to be in steady-state. An accuracy setting, with levels from -20dB to -80dB, defines the amount of energy that must be dissipated before completion. As the remaining energy level is decreased, the accuracy of the simulation will tend to increase. The solver accuracy setting of -40dB is selected, which is described by CST as accurate enough to generate reliable farfield results. The energy within the circular sinuous antenna remains bound to the structure for a longer period of time and as a result is solved to an accuracy setting of -35dB is instead selected.

Total simulation time is a function of the required number of time-steps. The Courant condition must be satisfied. As a result the smallest mesh step reduces the individual time step but increases the total solver run time. The hexahedral mesh requires a significant number of mesh cells to accurately solve a wide bandwidth problem. Mesh cells are limited to a minimum mesh step of one tenth of a wavelength ($\lambda/10$) at the highest frequency (18.0GHz). For the antenna structures of interest, even smaller steps, up to one two-hundredth of a wavelength ($\lambda/200$), are used to accurately model the feed region.

The solver implements an 'open' boundary using the perfectly matched layer (PML) boundary condition. Using this boundary condition simulates the structure as if it were in free-space. In the case of modeling antenna radiation problems, the boundary condition is changed to 'open (add space)' to prevent the radiation fields from being disrupted in the near-zone, allowing for accurate farfield results. By default, four (4) layers of PML with reflection coefficients of 0.0001 are implemented, offset from the structure by an eighth of a wavelength at the lowest frequency of operation.

When the simulation is complete, the output signal from the discrete port is transformed from the time domain into the frequency domain, using the Fourier Transform, to determine the S-parameter results. To obtain results beyond the S-parameters at the ports, monitors must be created. Field monitors, selectable for individual frequencies, allow the user to view the electromagnetic field distribution within and around the structure. They store farfield radiation patterns and create electric and magnetic field (E-field and H-field) surface plots on the structure. The electric and magnetic field surface plots are instantaneous at a specific input signal phase. In the case of the surface magnetic field, varying the input signal phase illustrates how currents rotate circularly about the surface of the antenna structures.

3.1.1 MULTIPLE ELEMENTS

Individual elements are created using Visual Basic Macros that draw curves based on the equations in the previous chapter. The curves are connected with arcs at the outer and inner radii and then a command forms them into a surface. As an infinitesimally-thin surface, the material is set to copper with a conductivity of 5.8×10^7 S/m. The network implemented to excite the four-element structure is based on the star method (electric sources), described by Mushiake (21). In the method, ports are connected from the center, or origin, where they join to the elements. In simulation, if discrete ports are connected at the origin, the inductance increases and diminishes the S-parameter results. Therefore, they are connected to a metal circle centered on the origin. Minimizing the space between the central ground circle and the elements to around three mesh steps ($\lambda/66$), shown in Figure 3-1, reduces the inductance without increasing the capacitance.

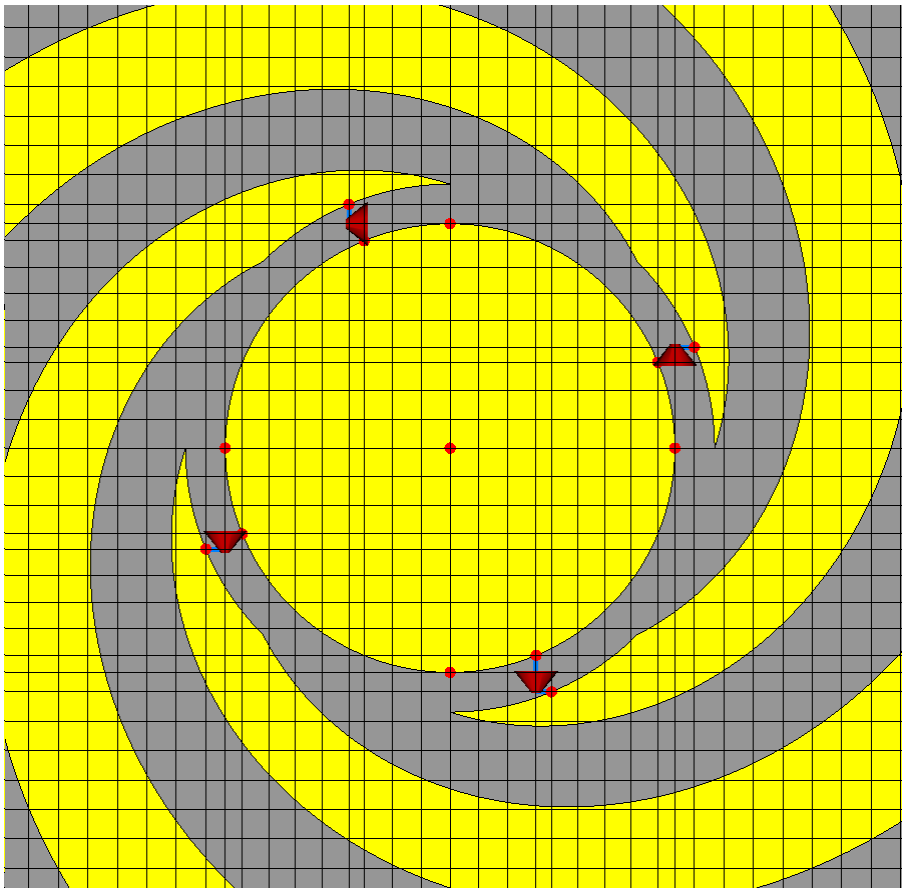

FIGURE 3-1: PORT STRUCTURE AND MESH [CST MWS]

When solving a four-port structure, the transient solver can solve each arm separately for individual S-parameters or it can solve all simultaneously to induce a mode of operation. The simultaneous excitation solves the system with user defined amplitude and/or phase-shifts at each port. To generate a phase-shift in the time domain, input signals are offset based on a selected frequency and phase offset. For example, in order to implement a ±90° phase-shift at 2GHz, the input signal would be advanced or delayed by 0.125ns. Therefore to solve for each mode, individual models must be created and run at every frequency. Since the second mode of operation can be created with only 180° phase-shifts, it may be implemented by an inversion of the input signal amplitude from positive to negative allowing for a broadband simulation.

The discrete port impedance is set to $30\sqrt{2}\pi\Omega$ when driven in mode 1 and $30\pi\Omega$ when driven in mode 2. The ports are connected to their respective structures at the midway point of their inner arc. For the spiral this occurs at a rotation of 22.5° and for the log-periodic it occurs at 45°, where it also aligns with the center of the overlap in the teeth. The location of the sinuous element inner arc, since the curve is defined from outside to inside, varies and must be calculated for each case.

3.1.2 CAVITY AND ABSORBER

As previously stated, an antenna at the opening of a circular waveguide will act as an arbitrary excitation and induce an infinite number of modes. A cavity model, without the antenna and substrate, can be simulated as an open waveguide with a number of modes excited. A waveguide port placed at the face of the cavity will be in contact with a foam spacer, which is electrically equivalent to air, and appears as an open waveguide. When excited by a waveguide mode, the S-parameter results show the amount of energy reflected, or the return loss, as well as the amount of energy cross-coupled into other modes. Absorber is introduced into the cavity after the foam spacer and will lead to the waveguide modes having diminished return losses above their cutoff frequencies. The ECCOSORB® absorber's (LS) relative permittivity, as well as the magnetic absorber's (MCS) relative permeability, are variable with respect to frequency and therefore must be approximated across the spectrum. The curves are second to sixth-order approximations and are based on measurement data from the manufacturer.

Using CST to simulate a select number of waveguide modes leads to a calculation of their cutoff frequencies. The solver has no ability to distinguish degenerate modes, or those which share the same cutoff frequency as another mode with only a different orientation.

When the first 19 modes are selected for simulation, 8 modes are found to be degenerate, so the first 11 modes were simulated including: TE_{11}, TM_{01}, TE_{21}, TE_{01}, TM_{11}, TE_{31}, TM_{21}, TE_{12}, TM_{02}, TM_{31}, and TE_{22}. The return loss for each mode reaches nearly 0dB below the cutoff frequency and is considered invalid in this region. At the cutoff frequency the return loss is -3dB, while reaching as low as -21dB within the band-of-operation, and above the band-of-operation is around -10dB at 6GHz and nearly -15dB at 18GHz. The return loss of the modes is shown in Figure 3-2 with TM_{01} and TM_{02} highlighted. The modal cross-coupling is at most -60dB and is not shown. From this we can suggest that when the cavity is arbitrarily excited, the return response will likely be below -60dB unless a fundamental mode is excited. If this were to occur, for instance in the case of the TM_{01} mode, the return loss at the antenna should be -10dB across nearly the entire frequency band. The final models of the spiral, log-periodic and sinuous can be viewed in Figures 3-3, 3-4 and 3-5.

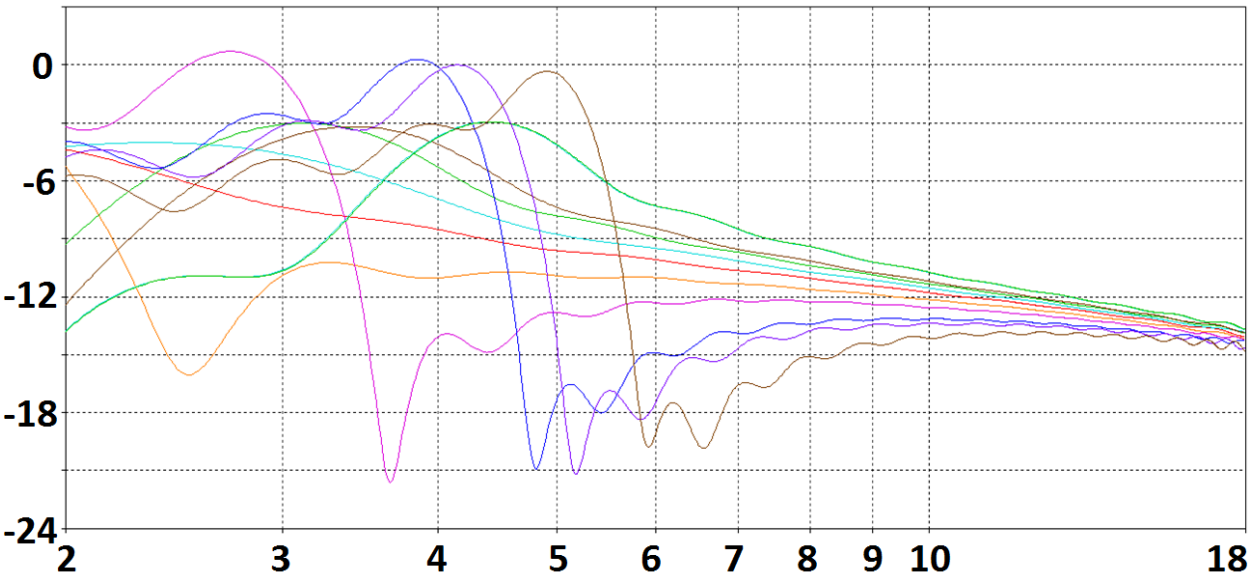

FIGURE 3-2: CAVITY MODE RETURN LOSS (DB / GHZ)

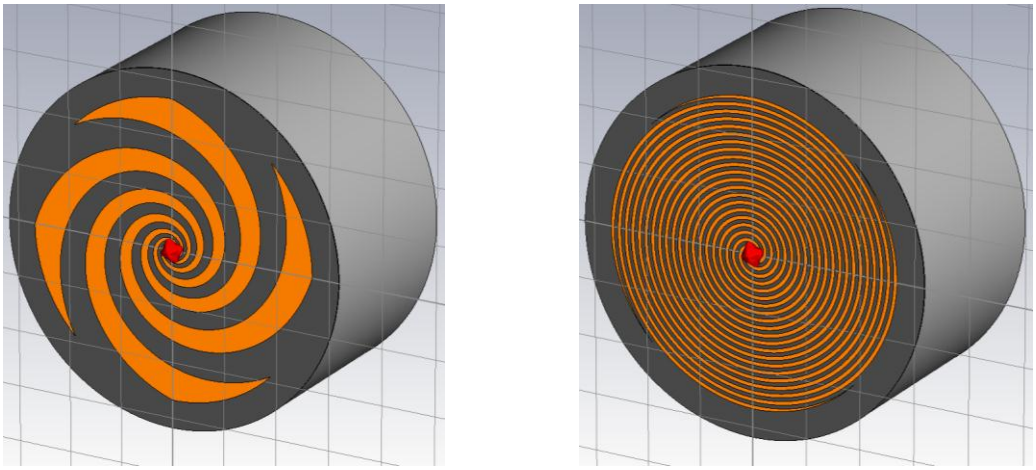

(a) (b)

FIGURE 3-3: SPIRAL MODELS [CST MWS] – [LOGARITHMIC (A) & ARCHIMEDEAN (B)]

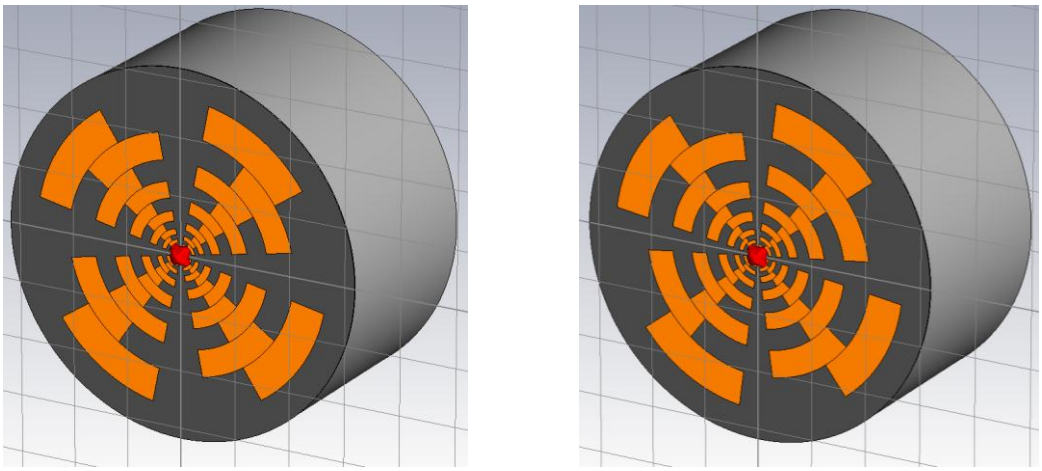

(a) (b)

FIGURE 3-4: CIRCULAR LOG-PERIODIC MODELS [CST MWS] – [П/8 (A) & П/12 (B)]

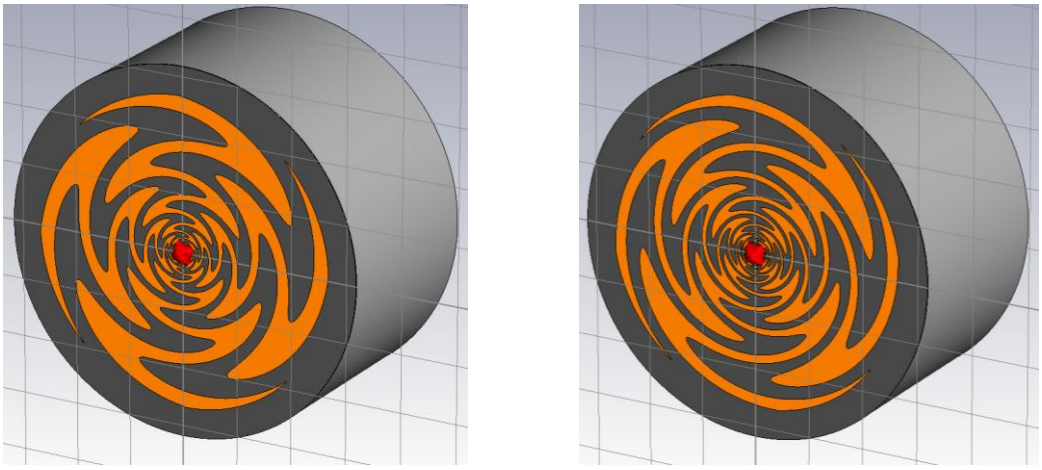

(a) (b)

FIGURE 3-5: CIRCULAR SINUOUS MODELS [CST MWS] – [П/4 (A) & П/3 (B)]

3.1.3 GROUND PLANE

Experimental measurements of the fabricated antennas will be taken with the cavities placed inside a large test-body designed to mimic an infinite ground plane. In order to correlate the results of the simulation models with that of the experimental structures, a model with an infinite ground plane around the original logarithmic spiral model is simulated. An infinite ground plane is implemented by creating a perfect electric conductor (PEC) layer that extends from the edge of the cavity wall past the bounding box, shown in Figure 3-6. The PEC layer begins at the same level as the substrate and extends deep enough to make contact with the cavity wall.

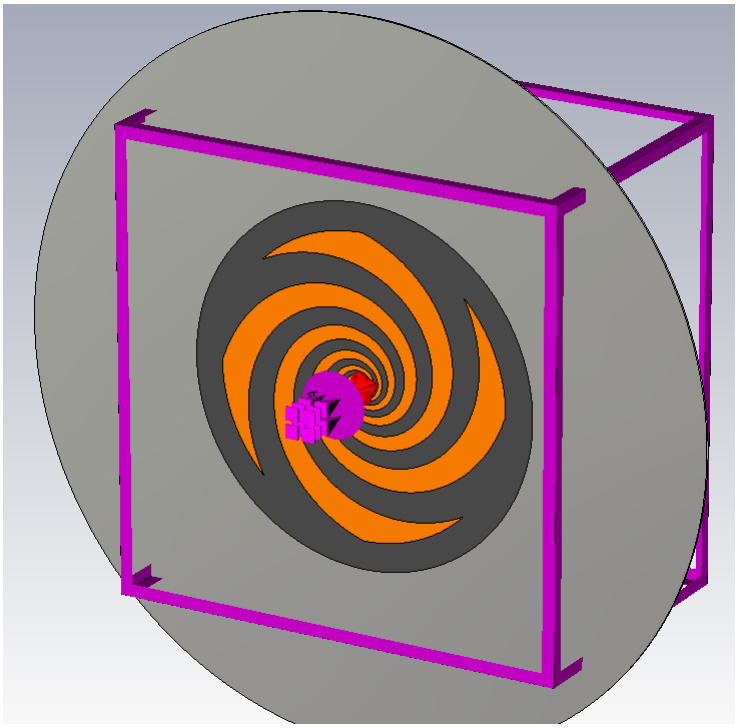

FIGURE 3-6: GROUND PLANE WITH BOUNDING BOX [CST MWS]

The tradeoff associated with including the ground plane is increasing simulation time versus a result more closely related to the experimentation. The model with a ground plane requires an increased number of mesh cells, which directly affects the simulation

time. In order to obtain the maximum amount of information in one simulation, the second mode of operation is simulated using the broadband method. This allows for comparisons between both the modal return loss and farfield plots. Due to the length of the simulation, results were only obtained for the logarithmic spiral. These results should sufficiently show the difference between simulation results and experimental results.

3.2 SIMULATION RESULTS

The six antenna designs are simulated in both modes of excitation at frequencies of 2.0, 4.0, 6.0, 8.0, 9.0, 12.0 and 18.0GHz. Results are obtained in the form of modal return loss, farfield radiation patterns and magnetic field surface plots.

Solving a multiport structure using simultaneous excitation creates F-parameter, or 'modal', return loss data for each port that converge to the same value at the phase-offset frequency. The data point from each model is combined to form the modal return loss plots. Each antenna has a plot comparing the first and second modes as well as a plot comparing the broadband response with the individual simulations in the second mode. A comparison between the first and third modes is included in Appendix A.

The ideal modal radiation patterns for a four-arm spiral antenna have been shown in Figure 2-1 and their ideal phases in Figure 2-2. The patterns are of a single circular polarization component, which is related to the wrap of the spiral. The wrap of the designed spirals will cause right-hand circular polarization (RHCP) to dominate. Therefore, this component of the modal farfield radiation patterns is shown through plots of the magnitude and phase. The circular log-periodic and circular sinuous antennas radiate in RHCP for the first mode of operation and the second mode will be characterized. The axial ratio, or a comparison between two linear cross-polarizations, is plotted to characterize the

circularity of the polarization. The linear polarization components are generally referred to as either horizontal and vertical or parallel and perpendicular. If the axial ratio is zero, the polarization components are equal and the polarization is circular and if the axial ratio reaches infinity, one polarization component is dominant and the polarization is linear.

A comparison to the four-arm Archimedean spiral modal current distributions from *Four-Arm Spiral Antennas* is made by plotting the normal component of the magnetic field captured at the surface of the substrate. At the surface of the conducting elements, the tangential electric field is zero and a normal component of the magnetic field will not exist. In the gaps between the conductors, the magnetic field on the surface is free to travel in both the positive direction, away from the substrate, and the negative direction, into the substrate. Plots of the positive normal component of the magnetic field at the surface of the substrate illustrate the active regions showing the extent of the currents.

3.2.1 MODAL RETURN LOSS

The ideal impedance values are used for the discrete ports in the simulation, but the use of lossy copper elements and a substrate will lower the effective impedance. With that in mind, the modal return loss of the logarithmic spiral for both modes of operation is steady, shown in Figure 3-7 where the diamonds indicate the simulated frequencies. The first mode is around -18dB, equivalent to an impedance of around 70Ω, with a sharp decrease to -30dB at 2.0GHz where the impedance increases. The second mode is nearly constant at around -15dB for the entire frequency band.

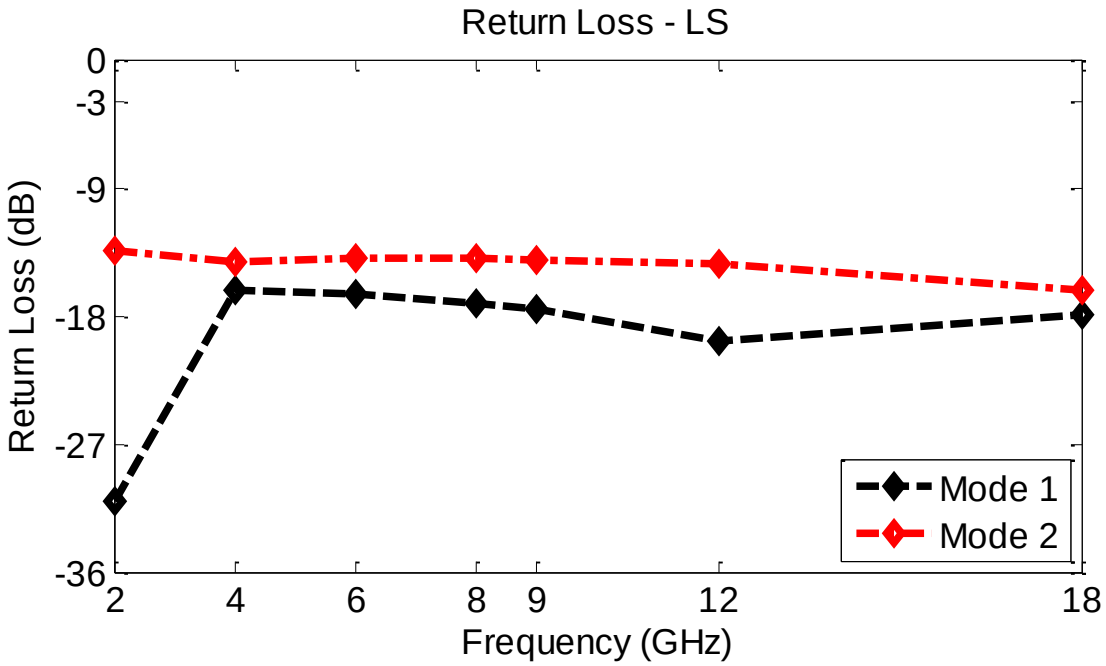

FIGURE 3-7: LOGARITHMIC SPIRAL MODAL RETURN LOSS

The modal return loss of the Archimedean spiral for both modes of operation is relatively steady, shown in Figure 3-8.

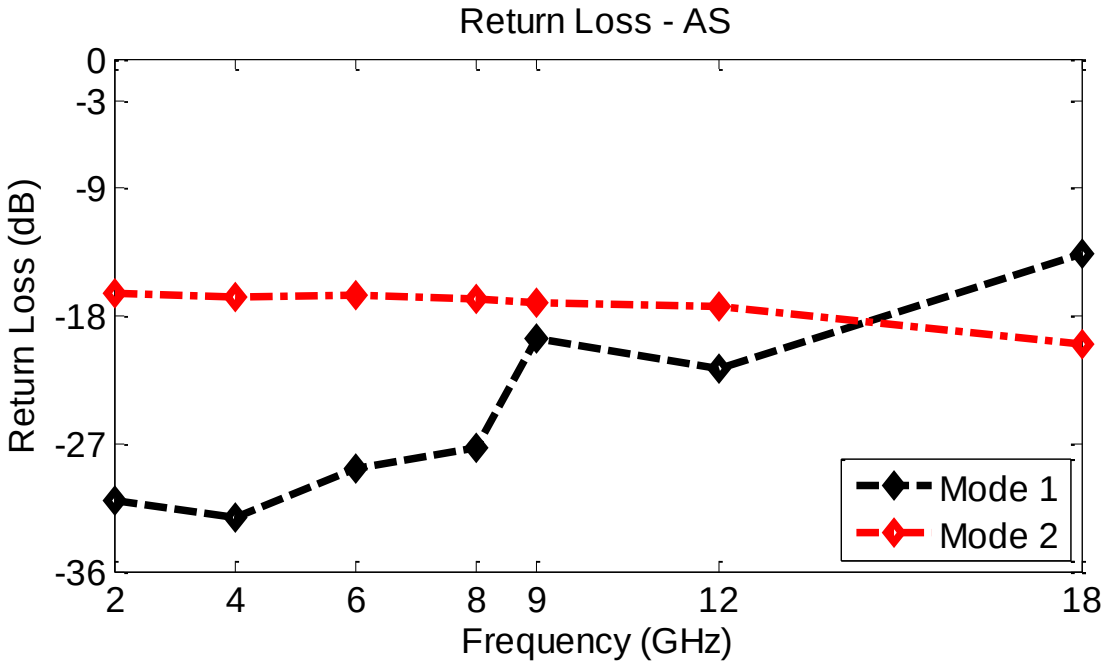

FIGURE 3-8: ARCHIMEDEAN SPIRAL MODAL RETURN LOSS

The Archimedean spiral is well matched across the entire frequency band for the first mode where it steadily increases from around -30dB up to -15dB. In the second mode, the return loss is nearly constant at around -18dB across most of the frequency band.

The modal return loss of the circular log-periodic antennas for both modes of operation is more erratic than the spiral models. The π/8-overlap, or short tooth version, can be seen in Figure 3-9 and the π/12-overlap, or long-tooth version, in Figure 3-10. Both modes of operation for both antennas have the trend of good matching at the lowest frequencies around -18dB with an unsteady increasing to around -9dB at the highest frequencies. A special case occurs with the long-tooth version at 18.0GHz where its match reaches -27dB, which will be explained when the broadband results are compared.

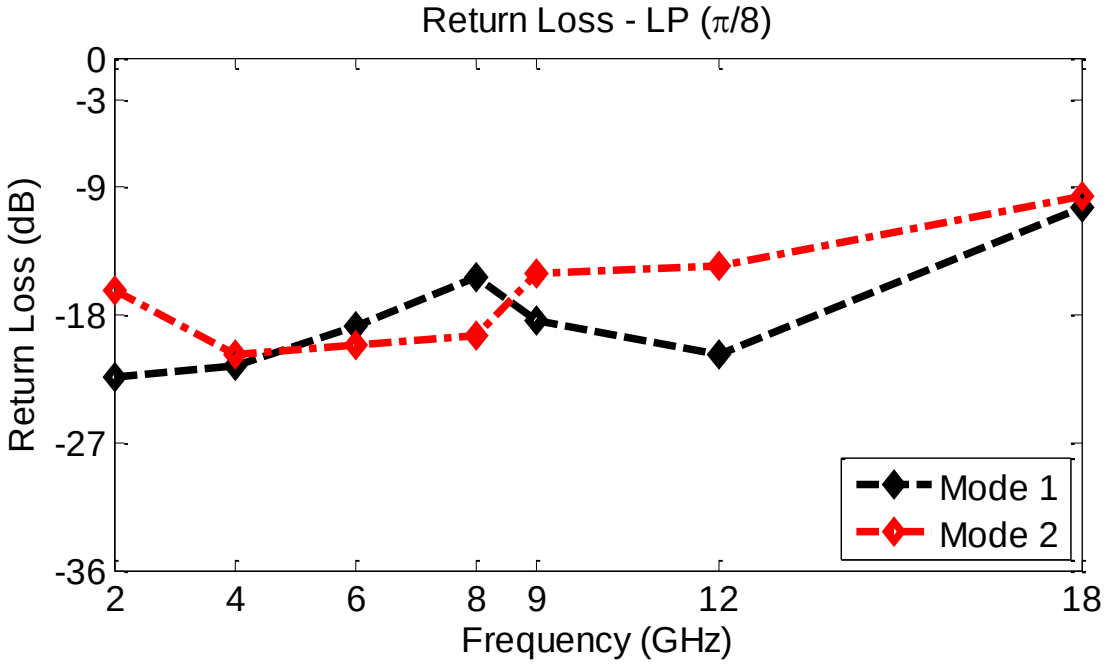

FIGURE 3-9: CIRCULAR LOG-PERIODIC [Π/8] MODAL RETURN LOSS

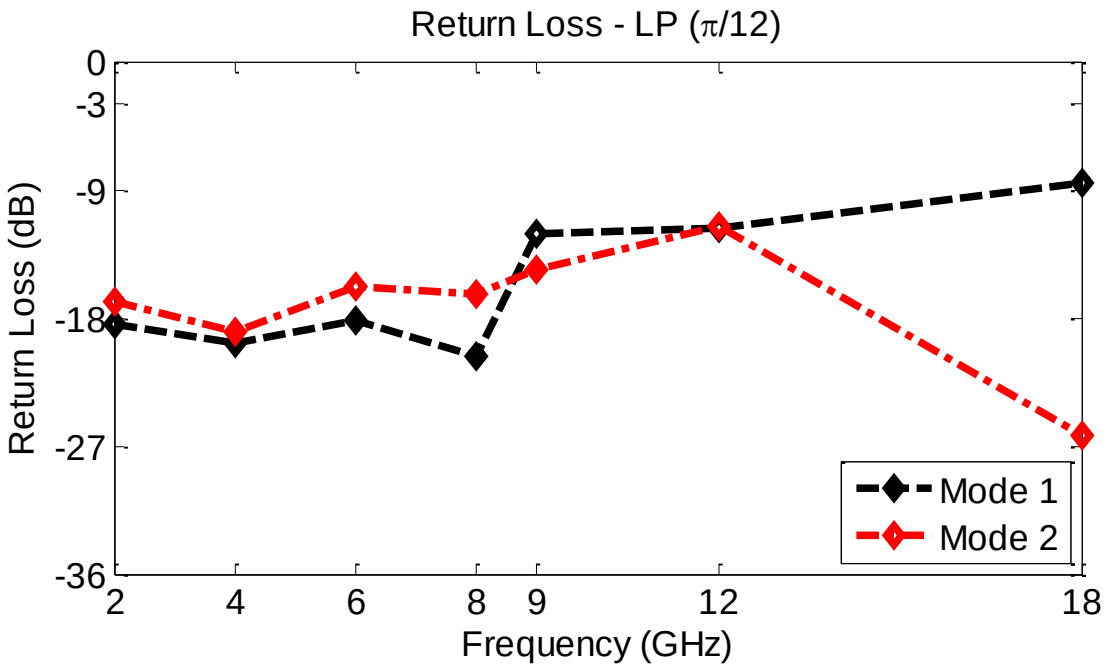

FIGURE 3-10: CIRCULAR LOG-PERIODIC [Π/12] MODAL RETURN LOSS

The modal return loss for the circular sinuous antennas for both modes is chaotic and less well matched than any other antenna. The π/4-interleave version can be seen in Figure 3-11 and the π/3-interleave version in Figure 3-12. Both modes of operation for both antennas are matched around -9dB across the frequency band. Exceptions occur in the case of the π/4-interleave version at 18.0GHz where it reaches -18dB for both modes as well as for the π/3-interleave version at 12.0GHz where it reaches at -18dB for the first mode. These exceptions are better explained when comparing directly with the broadband results.

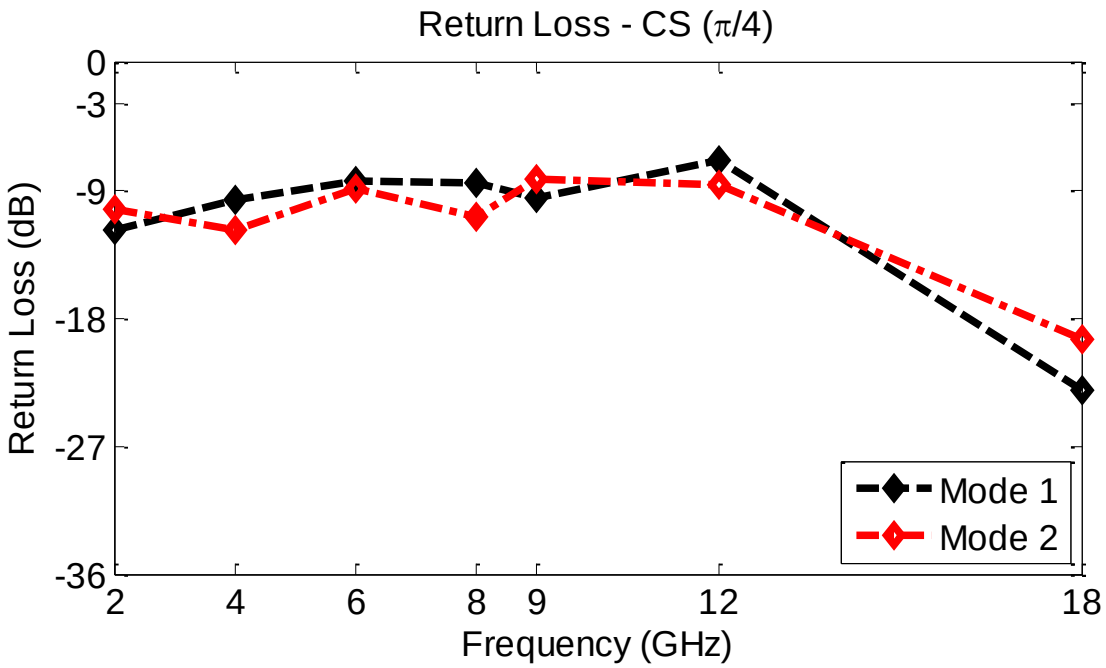

FIGURE 3-11: CIRCULAR SINUOUS [Π/4] MODAL RETURN LOSS

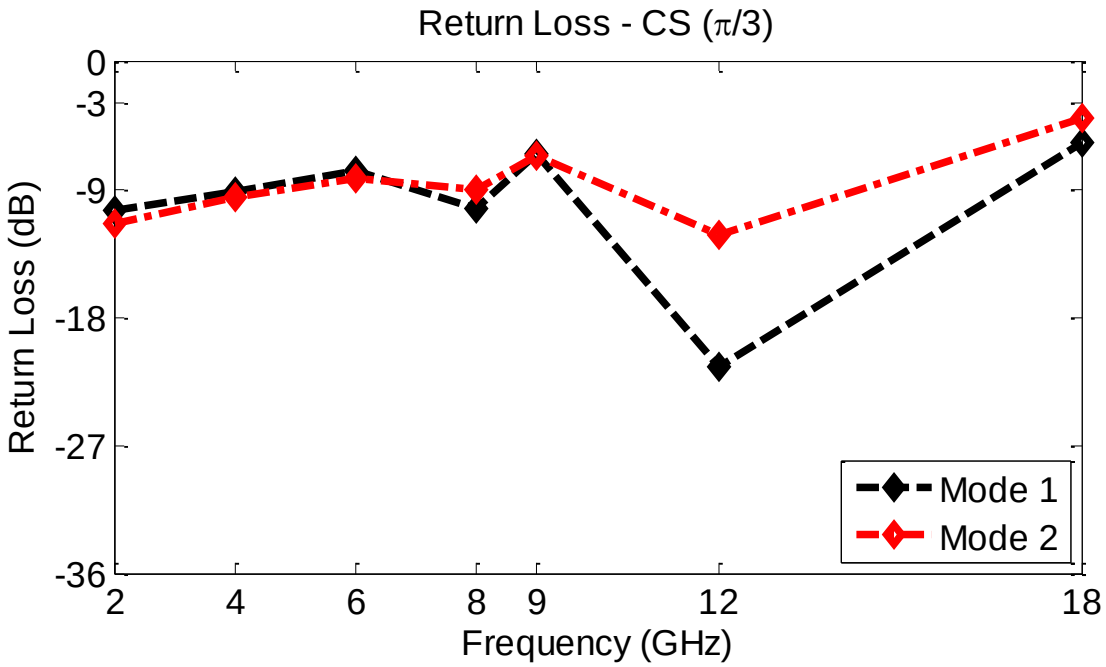

FIGURE 3-12: CIRCULAR SINUOUS [Π/3] MODAL RETURN LOSS

The broadband modal return loss for the logarithmic spiral in the second mode of operation is just as steady as the connected individual simulations. Shown in Figure 3-13 are both responses, the broadband response in black and the individual simulations

overlain in red with diamonds marking the frequencies simulated. There is a slight ripple found at the lowest frequencies, beginning at 2.0GHz and out to around 4.0GHz, which is an effect of truncation. Energy, traveling outward along the spiral arm, is being reflected from the end and disrupting the impedance. This occurs at the lowest frequencies which require the fewest number of wavelengths to reach the end of the arm.

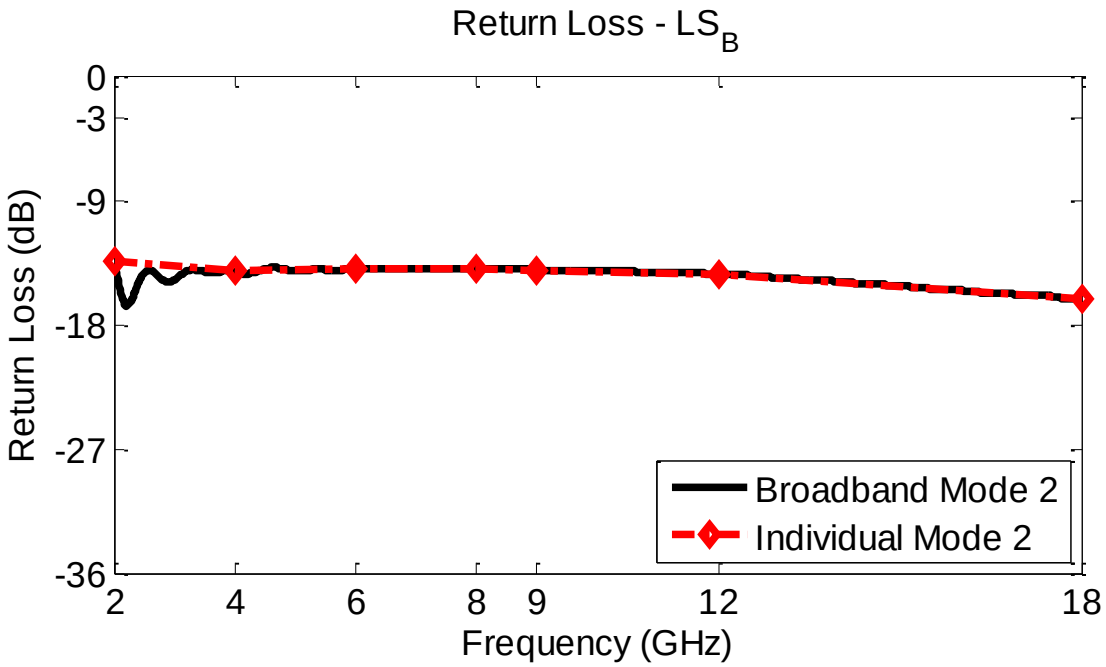

FIGURE 3-13: LOGARITHMIC SPIRAL MODE 2 RETURN LOSS COMPARISON

The broadband modal return loss for the Archimedean spiral in the second mode of operation, shown in Figure 3-14, is again just as steady as the connected individual simulations. Just as with the logarithmic spiral, there is a slight ripple at the lowest frequencies between 2.0 and 4.0GHz that can be attributed to truncation.

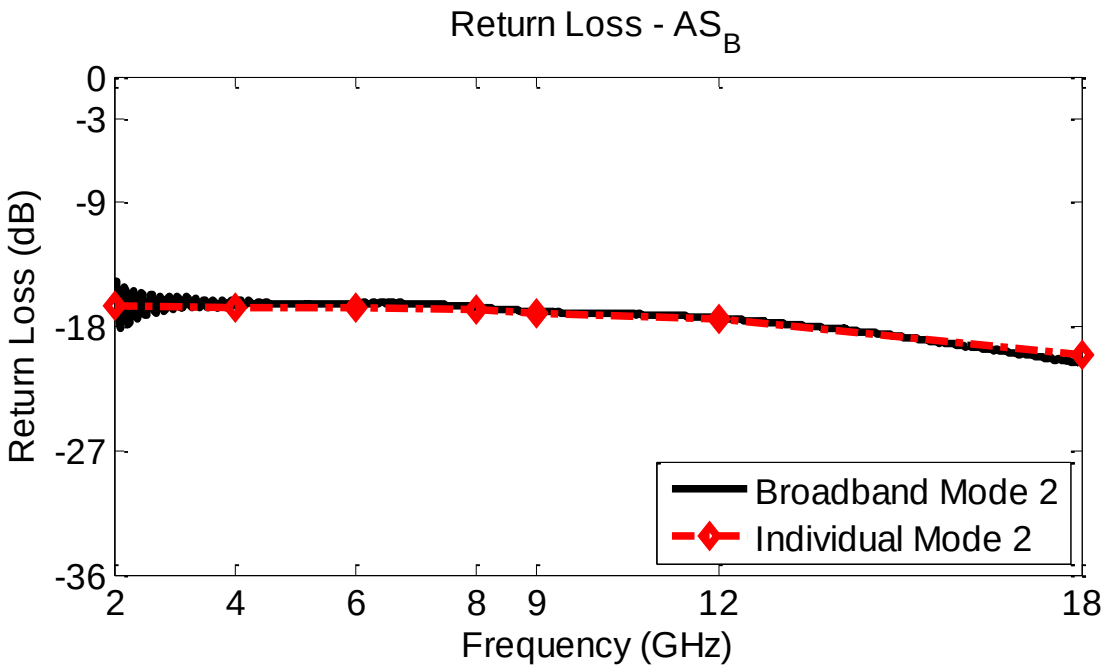

FIGURE 3-14: ARCHIMEDEAN SPIRAL MODE 2 RETURN LOSS COMPARISON

The originally erratic response of the individual circular log-periodic simulations is shown to relate to whether or not the frequency points are within a characteristic dip. The individual simulations show the same trend of better matching at the lowest frequencies and unsteady increasing toward the highest frequencies. Shown in Figure 3-15 is the broadband modal return loss for the π/8-overlap, or short tooth version, with the individual simulations overlain and shown to align at the simulation frequencies. The first dip in the return loss occurs at 3.1GHz and is directly linked with a tooth of the antenna as the higher frequency dips occur at the logarithmic growth rate a property that holds for both designs. The π/12-overlap or long-tooth version is shown in Figure 3-16 where the first dip occurs at a lower frequency of 2.5GHz. The broadband modal return loss is viewed as normal behavior for a quasi-frequency-independent structure. As the teeth become longer, the characteristic dips shift lower in frequency. Finally, only seven (π/8) and eight (π/12) dips are shown in the frequency band selected. This suggests that if the simulations

were run at higher frequencies more dips should occur up to the total number of teeth, but the response in between the dips may prove to be unusable.

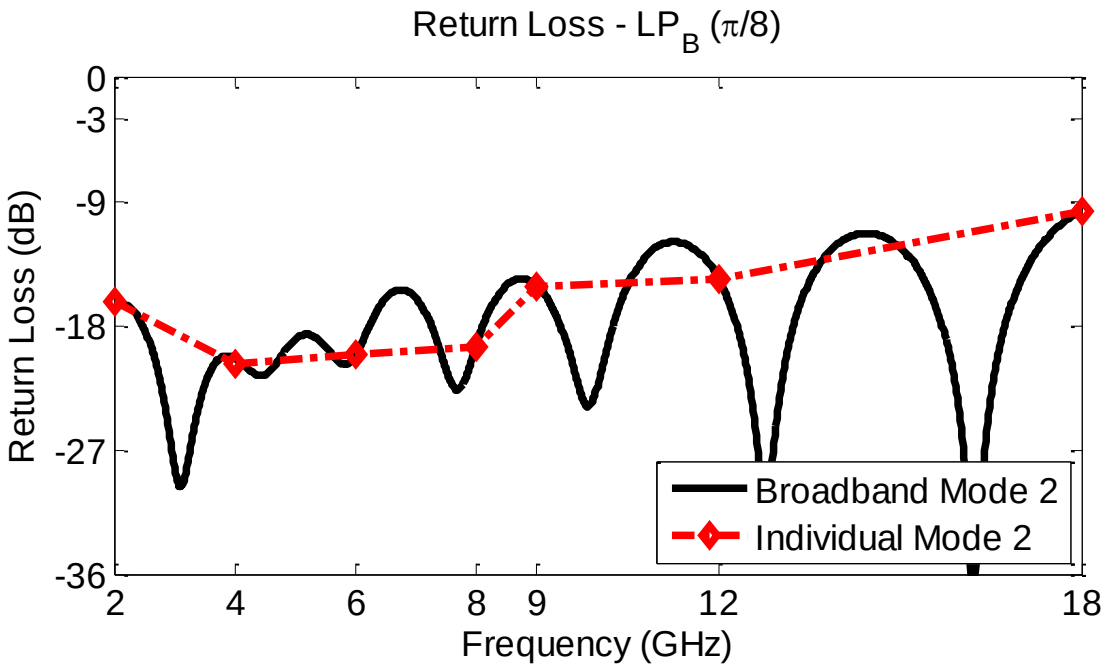

FIGURE 3-15: CIRCULAR LOG-PERIODIC [Π/8] MODE 2 RETURN LOSS COMPARISON

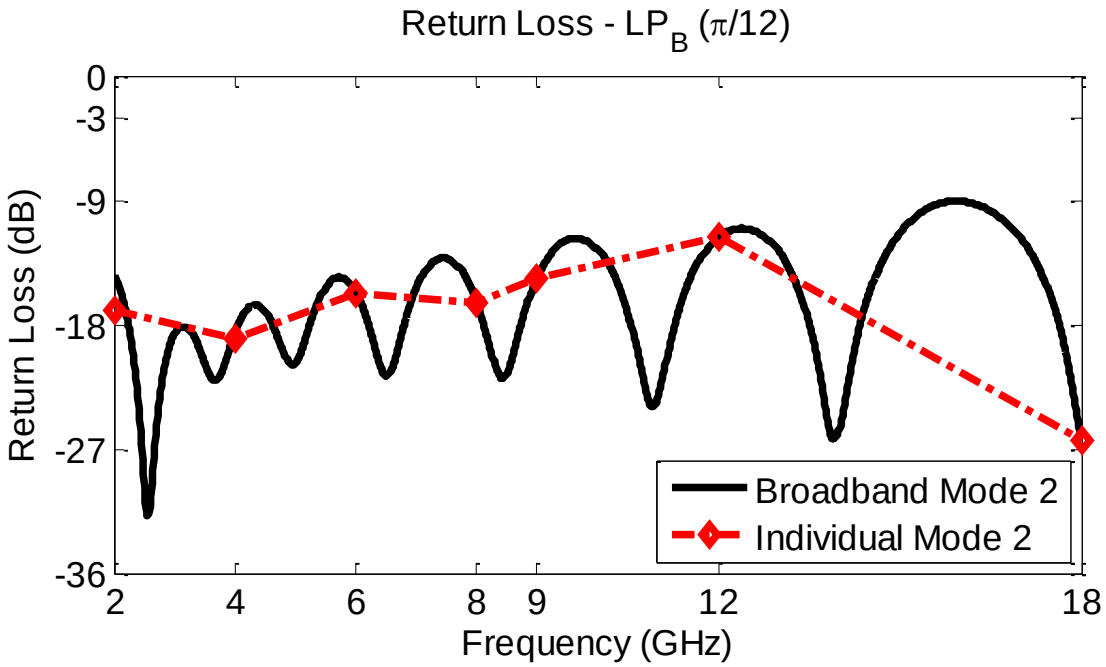

FIGURE 3-16: CIRCULAR LOG-PERIODIC [Π/12] MODE 2 RETURN LOSS COMPARISON

The individual circular sinuous results were chaotic and not as well matched as other antennas, particularly lower in the spectrum. The broadband modal return loss ripples throughout the frequency band, but the dips do not reach the same low levels as the log-periodic. Still, when the interleave is extended from π/4 to π/3 the ripples shift slightly in frequency. The π/4-interleave version can be seen in Figure 3-17 and the π/3-interleave version in Figure 3-18. The dips in the return loss occur appear to begin under 2.0GHz for both versions and when increasing in frequency each dip occurs a logarithmic rate. The circular sinuous designs have nine cells, or wraps, and correspondingly eight lengths between wraps. They also have two extra lengths, one beginning the first wrap and one ending the final wrap, but only six (π/4) to seven (π/3) dips are shown in the figures. The highest frequency for both antennas dip is related to the beginning length and the increasing lengths can be associated with the dips that decrease through the spectrum.

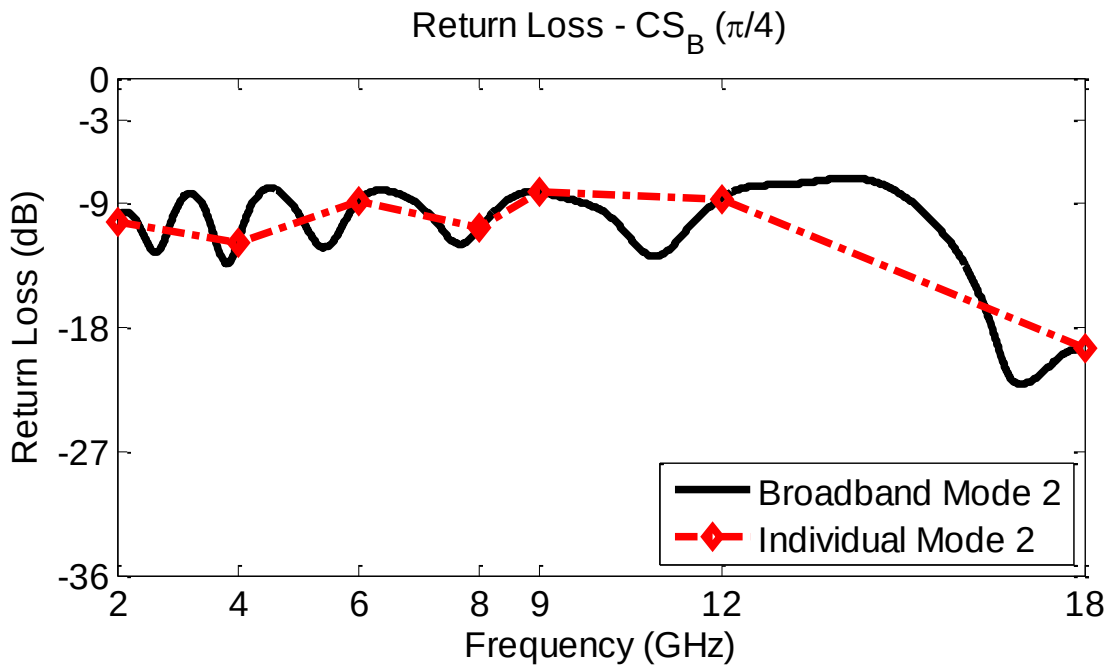

FIGURE 3-17: CIRCULAR SINUOUS [Π/4] MODE 2 RETURN LOSS COMPARISON

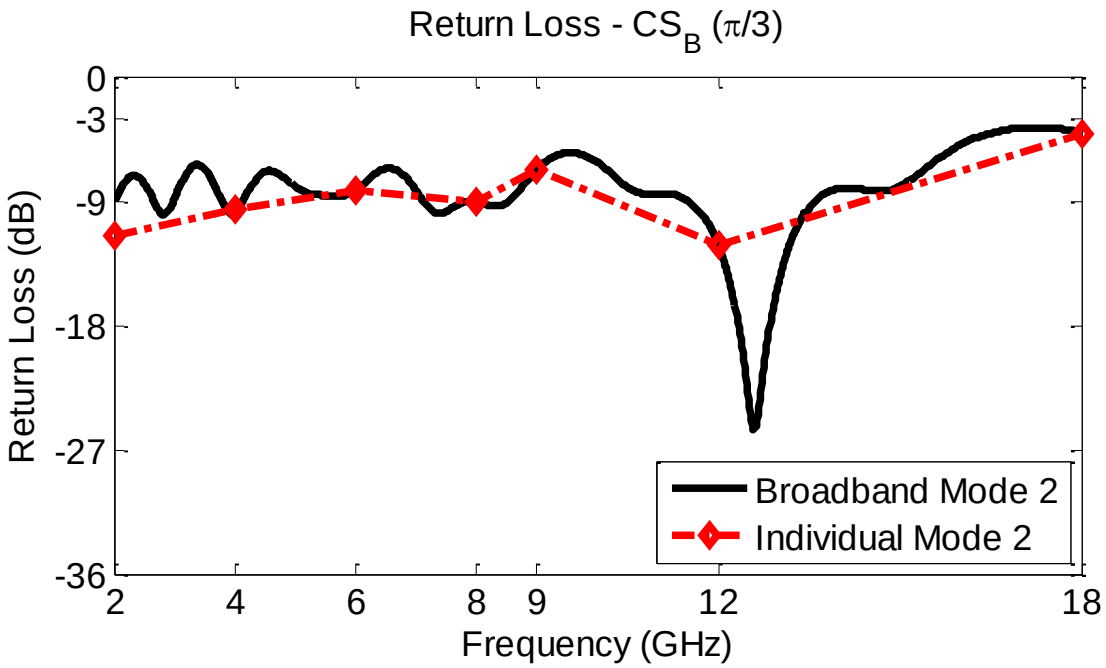

FIGURE 3-18: CIRCULAR SINUOUS [Π/3] MODE 2 RETURN LOSS COMPARISON

3.2.2 FARFIELD RADIATION PATTERNS

Specific cuts about azimuth and across elevation have been taken for both modes of operation at the same seven frequency points. The results for 2.0GHz, 6.0GHz, 9.0GHz and 18.0GHz are presented. The 6.0GHz and 9.0GHz cuts represent the most ideal response as they are located in the center of the designed frequency band. In this region, the effects of truncation are minimal for both modes. 2.0GHz, in the second mode for the spirals, and 18.0GHz show the response of the spiral antennas at the extremes of their operational bandwidth. The farfield radiation pattern response and bandwidth of the circular log-periodic and sinuous will be characterized.

Conical cuts taken about azimuth at fixed elevation angles of 20°, 40°, 45° and 60° span all 360° and are combined into single plots. Cuts taken across elevation begin at boresight, or 0°, and span to the horizon, or 90°. The cuts document the variation within a single quadrant and are fixed at azimuth angles of 0°, 22.5°, 45°, 67.5°. Quadrants are

identical and the response between any 90°-rotation is indistinguishable, shown in the azimuth cuts. The magnitude, or directivity in dBi, and the phase, in degrees, as well as the axial ratio, in dB, are shown for all cuts.

Sub-subsections are used to separate the results of the six antennas due to the volume of data. Within a sub-subsection there is an introduction to the first mode results. After, the first mode results are summarized and the second mode results are introduced. Finally, the second mode results are summarized. For both modes of operation, the magnitude about azimuth is expected to be flat and any variation will be documented as the magnitude ripple which will also be visible as variation in the elevation cuts. For the first mode, the magnitude across elevation is expected to peak at boresight and diminish toward the horizon. For the second mode, it is expected to have a null at boresight, a peak near 40° and to degrade toward the horizon. Similarly, the phase about azimuth is expected to be linear with a slope of -1°/1° for the first mode and -2°/1° for the second mode and any variation will be called the phase ripple. Finally, the axial ratio is expected to be near zero.

3.2.2.1 LOGARITHMIC SPIRAL

For the logarithmic spiral, feed points are located at azimuth angles of 22.5°, 112.5°, 202.5° and 292.5°. Within the first mode of operation results include: the azimuth cuts' magnitude in Figures 3-19 & 3-20, the azimuth cuts' phase in Figures 3-21 & 3-22, the elevation cuts' magnitude in Figures 3-23 & 3-24, the elevation cuts' phase in Figures 3-25 & 3-26 and the axial ratio of the azimuth cuts in Figures 3-27 & 3-28 and of the elevation cuts in Figures 3-29 & 3-30.

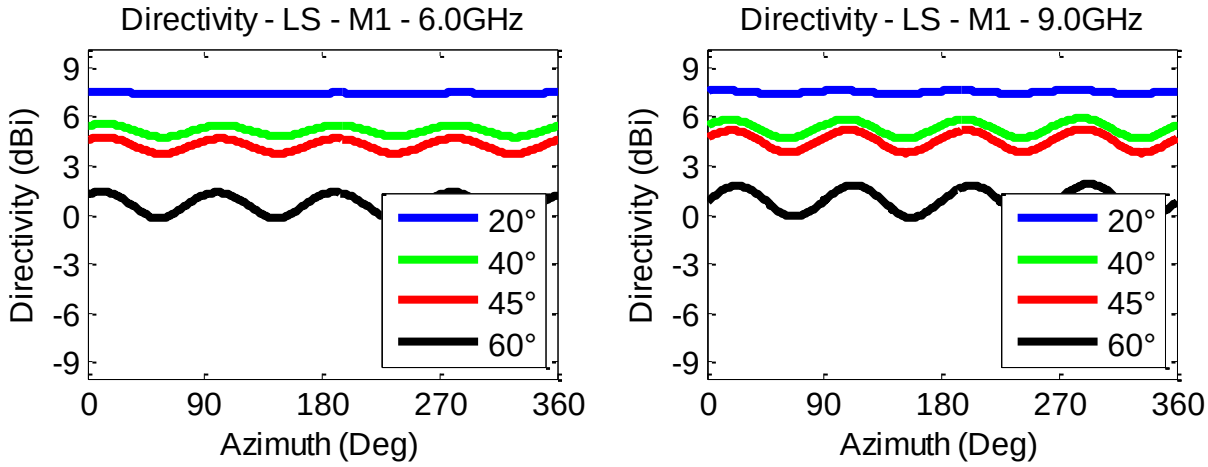

FIGURE 3-19: RADIATION PATTERNS – LS – AZ – M1 – MAG [6 (A) & 9 (B) GHZ]

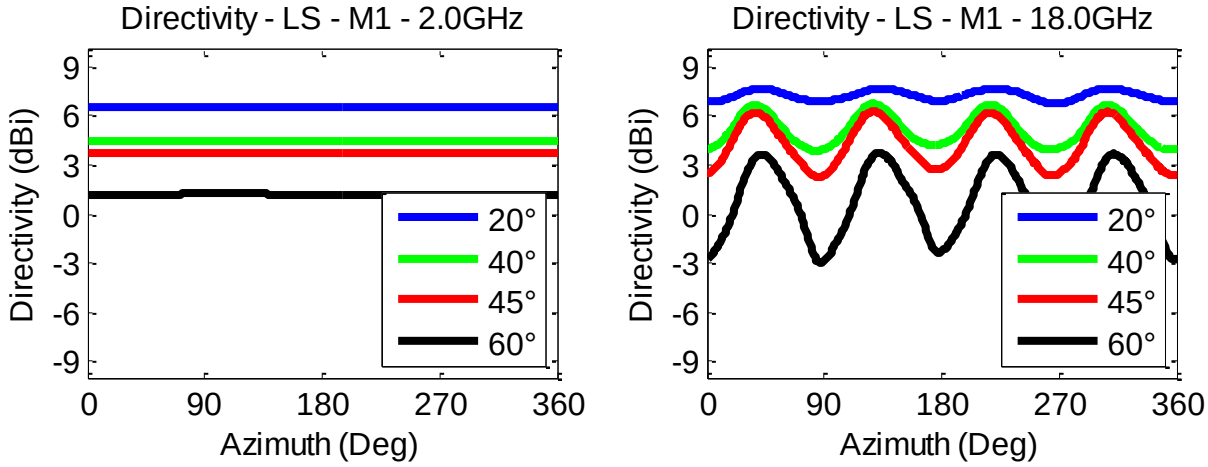

FIGURE 3-20: RADIATION PATTERNS – LS – AZ – M1 – MAG [2 (A) & 18 (B) GHZ]

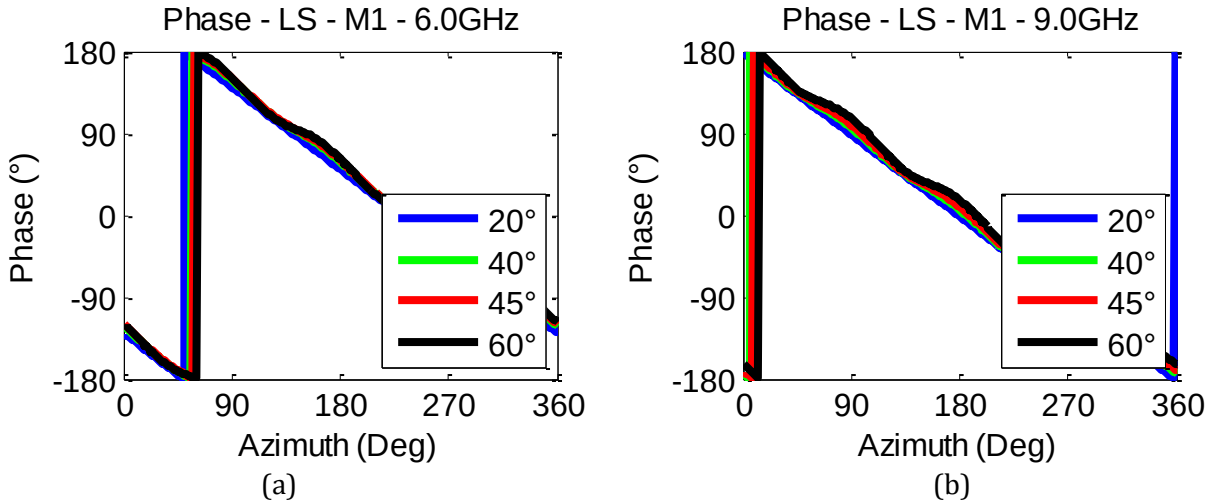

FIGURE 3-21: RADIATION PATTERNS – LS – AZ – M1 – PHA [6 (A) & 9 (B) GHZ]

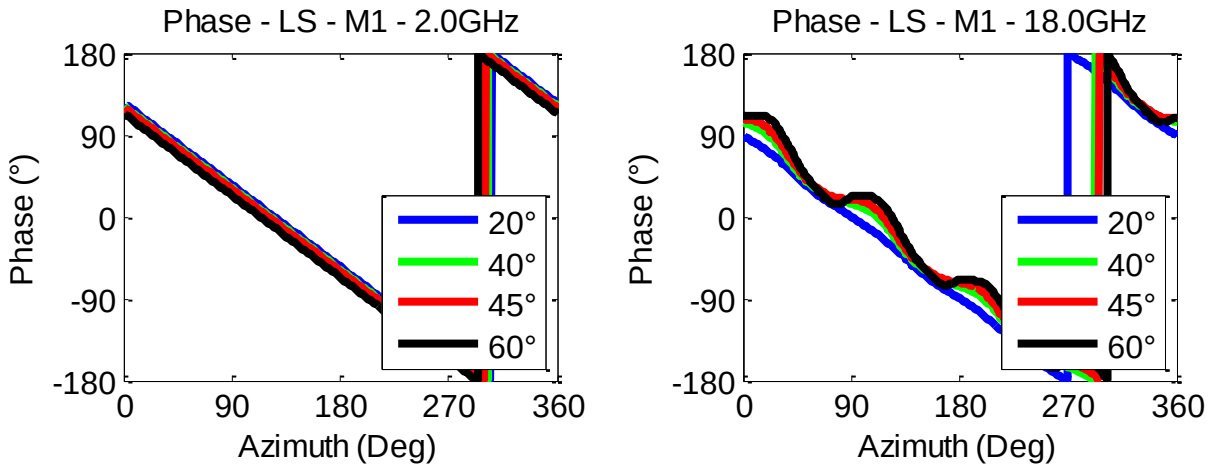

(a) (b)

FIGURE 3-22: RADIATION PATTERNS – LS – AZ – M1 – PHA [2 (A) & 18 (B) GHZ]

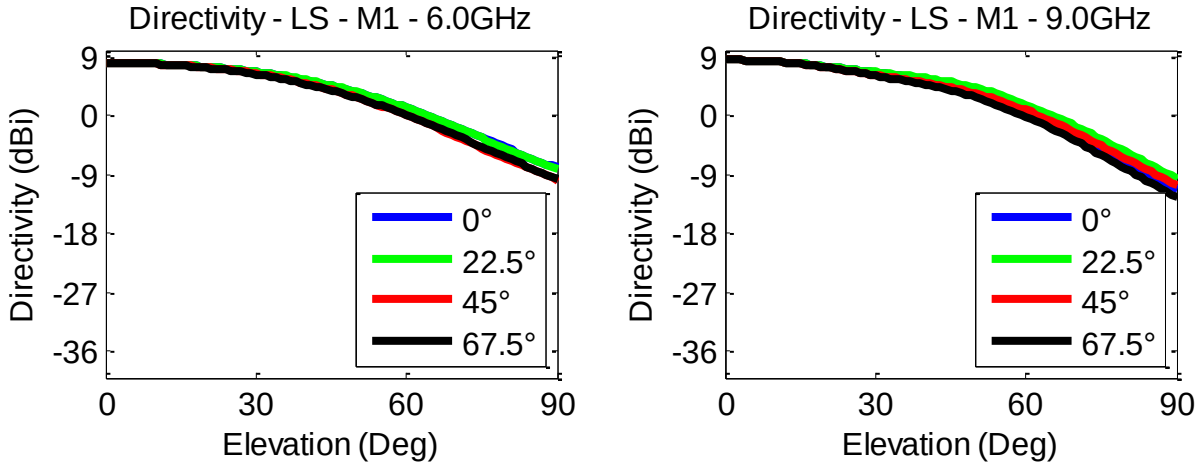

(a) (b)

FIGURE 3-23: RADIATION PATTERNS – LS – EL – M1 – MAG [6 (A) & 9 (B) GHZ]

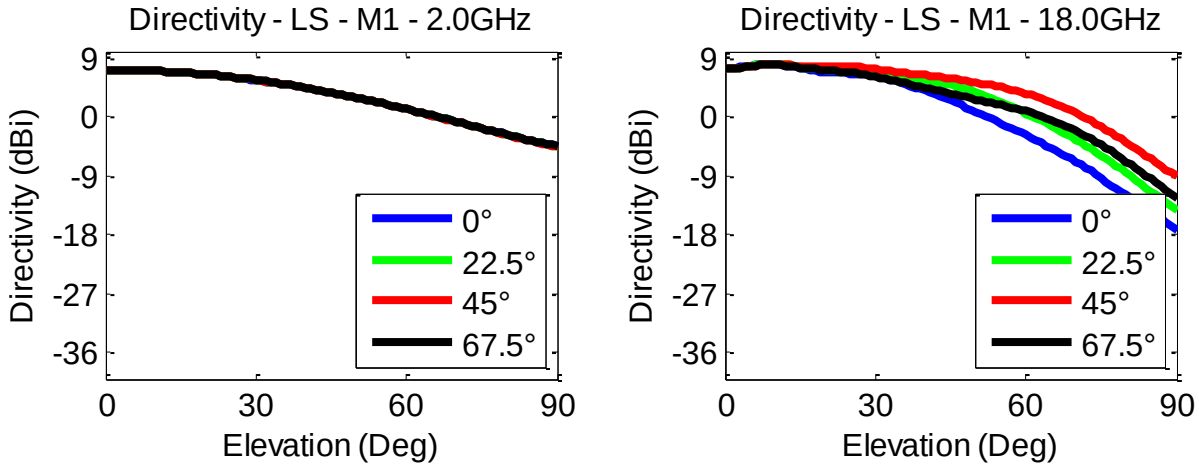

(a) (b)

FIGURE 3-24: RADIATION PATTERNS – LS – EL – M1 – MAG [2 (A) & 18 (B) GHZ]

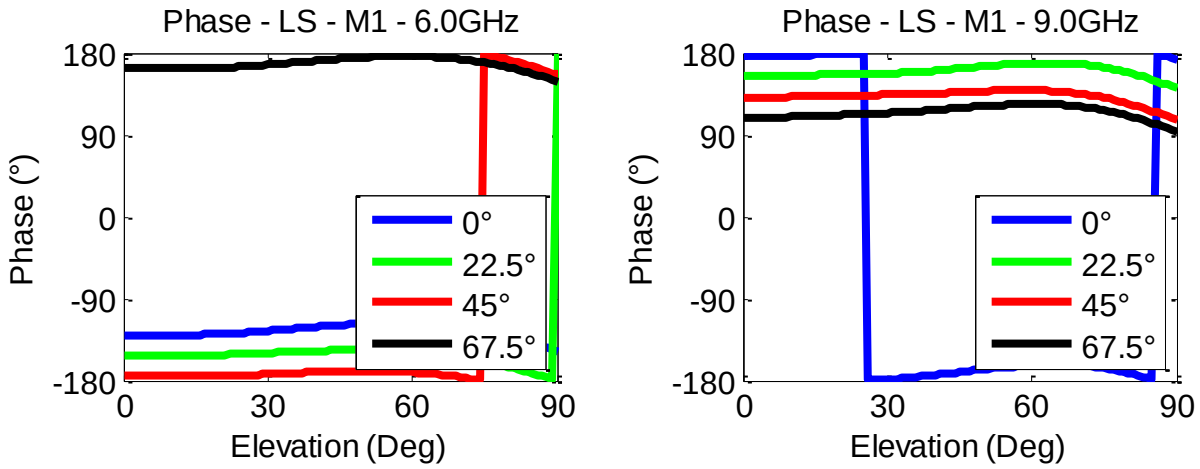

(a) (b)

FIGURE 3-25: RADIATION PATTERNS – LS – EL – M1 – PHA [6 (A) & 9 (B) GHZ]

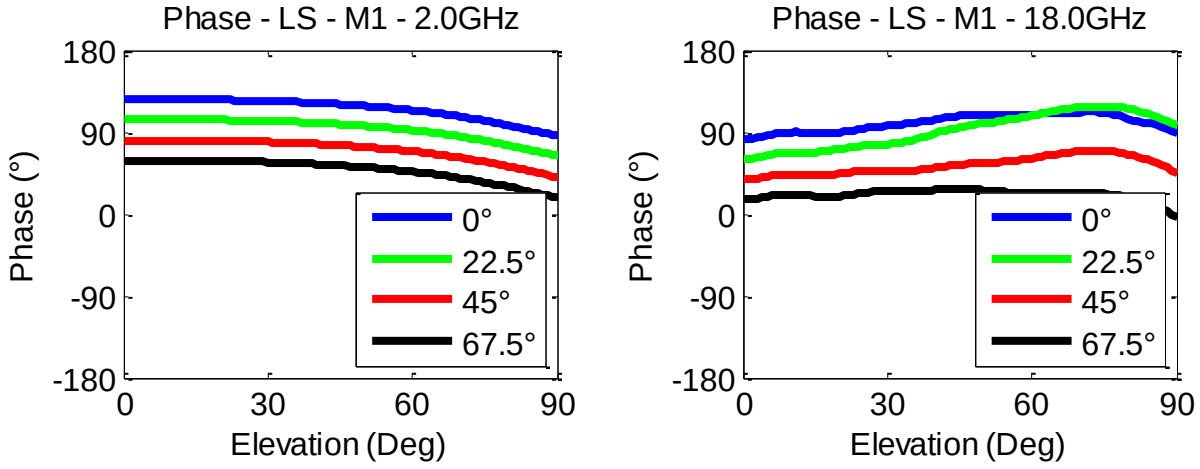

(a) (b)

FIGURE 3-26: RADIATION PATTERNS – LS – EL – M1 – PHA [2 (A) & 18 (B) GHZ]

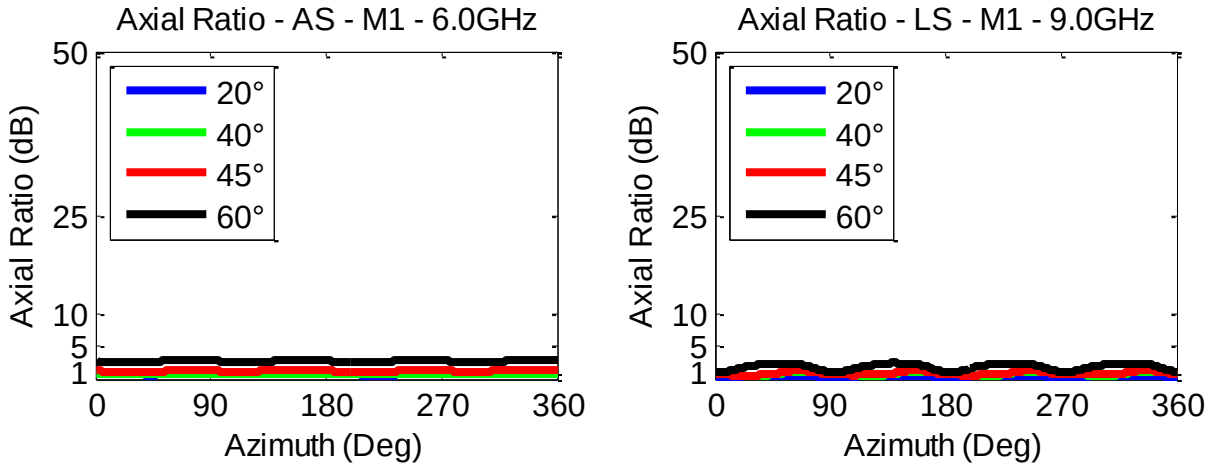

(a) (b)

FIGURE 3-27: AXIAL RATIOS – LS – AZ – M1 [6 (A) & 9 (B) GHZ]

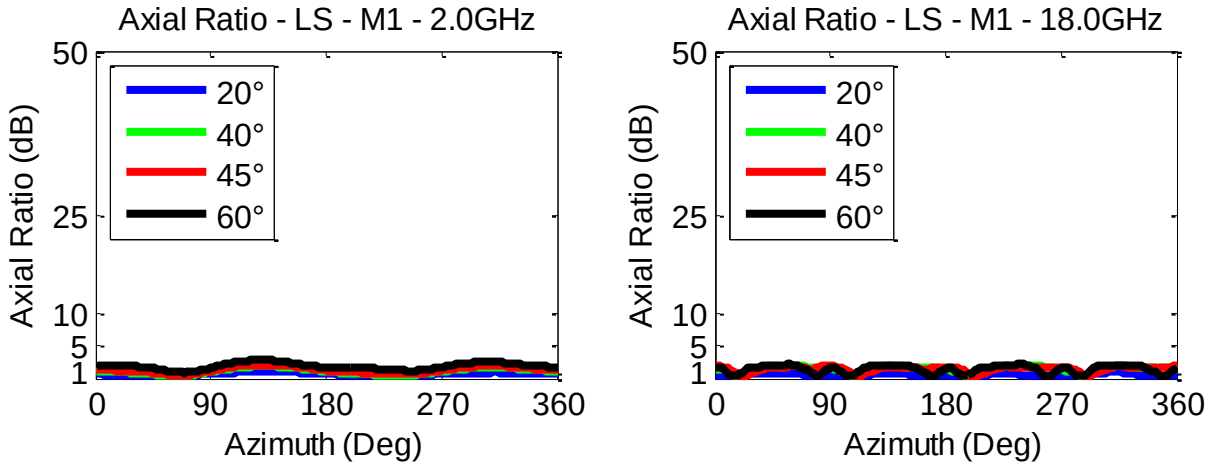

(a) (b)

FIGURE 3-28: AXIAL RATIOS – LS – AZ – M1 [2 (A) & 18 (B) GHZ]

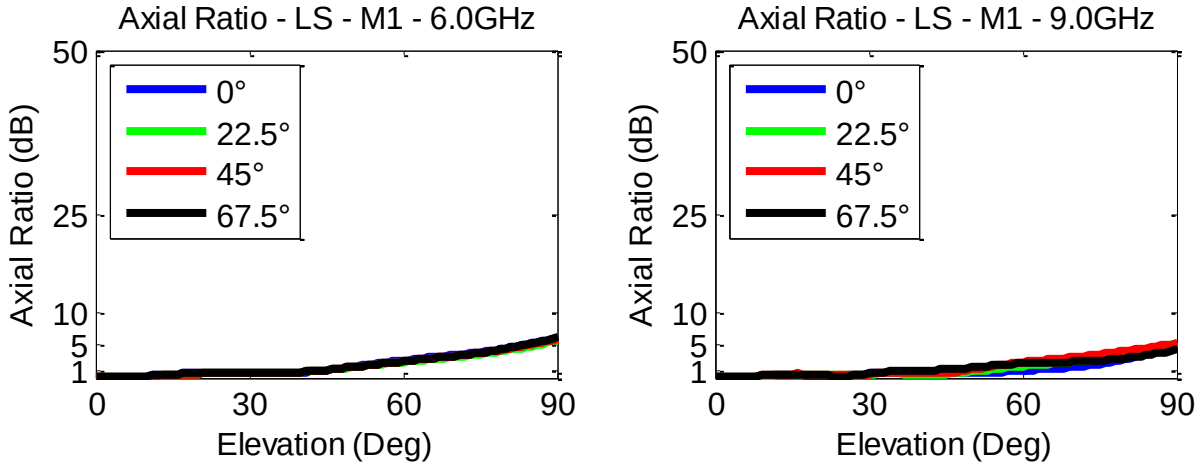

(a) (b)

FIGURE 3-29: AXIAL RATIOS – LS – EL – M1 [6 (A) & 9 (B) GHZ]

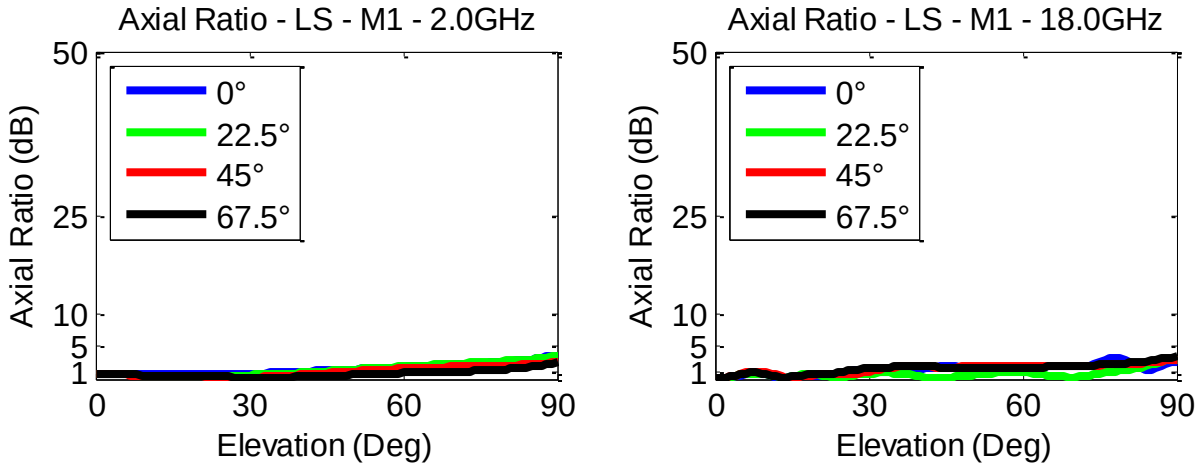

(a) (b)

FIGURE 3-30: AXIAL RATIOS – LS – EL – M1 [2 (A) & 18 (B) GHZ]

For the first mode of operation, the magnitude of the azimuth cuts, from Figures 3-19 & 3-20, are used to view the magnitude ripple. The trend for the first mode is for the ripple to increase as both the frequency increases and the elevation angle increases from boresight to the horizon. In the best case, at the lowest frequency of 2.0GHz, the spiral has ripple of ±0.01dB at 20° in elevation. While in the worst, at the highest frequency of 18.0GHz and 60° in elevation, the ripple is ±3.5dB. At 20° of elevation and 6.0GHz the performance is expected to be the typical mid-band response removed from any truncation effects and here the ripple is ±0.08dB. The magnitude of the elevation cuts, from Figures 3-23 & 3-24, are primarily used to show the maximum directivity at boresight and the -3dB beamwidth. The maximum directivity of 8.5dBi occurs at 9.0GHz and the -3dB beamwidth extends out to 36° in elevation.

Similar to the magnitude ripple, the phase ripple, from Figures 3-21 & 3-22, increases with both increasing frequency and elevation angle. The phase ripple is ±0.1° at 2.0GHz and 20°. However for 18.0GHz at 60°, there is ripple of ±21°. In the mid-band case, 20° of elevation at 6.0GHz, the ripple is ±0.6°. The phase of the elevation cuts, from Figures 3-25 & 3-26, would ideally be equally spaced but most importantly would not overlap. At 18.0GHz, an overlap occurs above 60° in elevation, this would lead to ambiguity in the angle of arrival estimation.

The trend for the axial ratio about azimuth, from Figures 3-27 & 3-28, is for the lowest values at boresight and increasing values toward the horizon while the ripple increases with frequency. In the mid-band at 6.0GHz and 20° in elevation, the average is 0.7dB and the peak is 0.8dB. There is also variation across elevation, from Figures 3-29 &3-30, that increases from boresight toward the horizon. Interestingly, the lowest and peak

cases occur for the 6.0GHz which begin at less than 0.01dB at boresight and reach 6.4dB at the horizon.

Within the second mode of operation results include: the azimuth cuts' magnitude in Figures 3-31 & 3-32, the azimuth cuts' phase in Figures 3-33 & 3-34, the elevation cuts' magnitude in Figures 3-35 & 3-36, the elevation cuts' phase in Figures 3-37 & 3-38 and the axial ratio of the azimuth cuts in Figures 3-39 & 3-40 and of the elevation cuts in Figures 3-41 & 3-42.

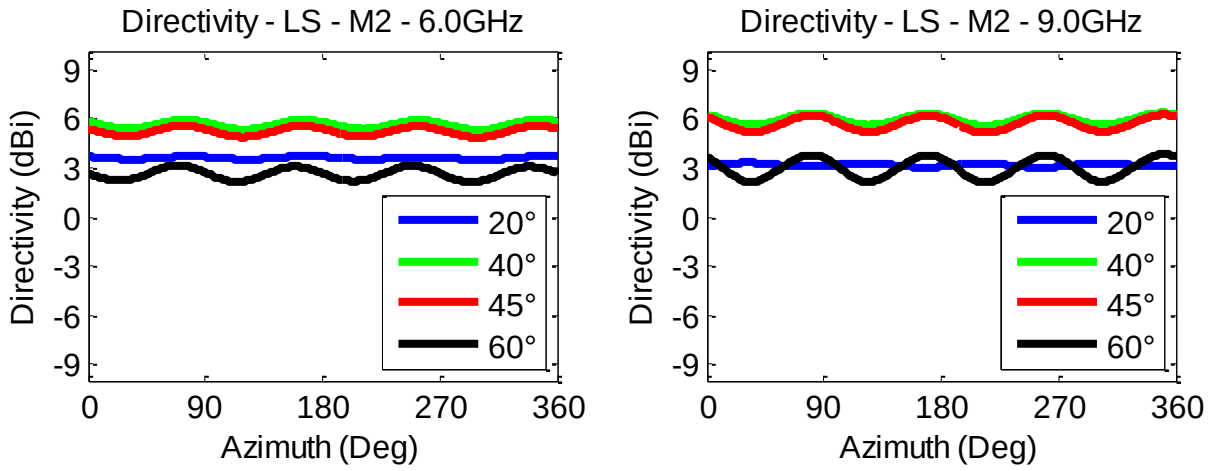

FIGURE 3-31: RADIATION PATTERNS – LS – AZ – M2 – MAG [6 (A) & 9 (B) GHZ]

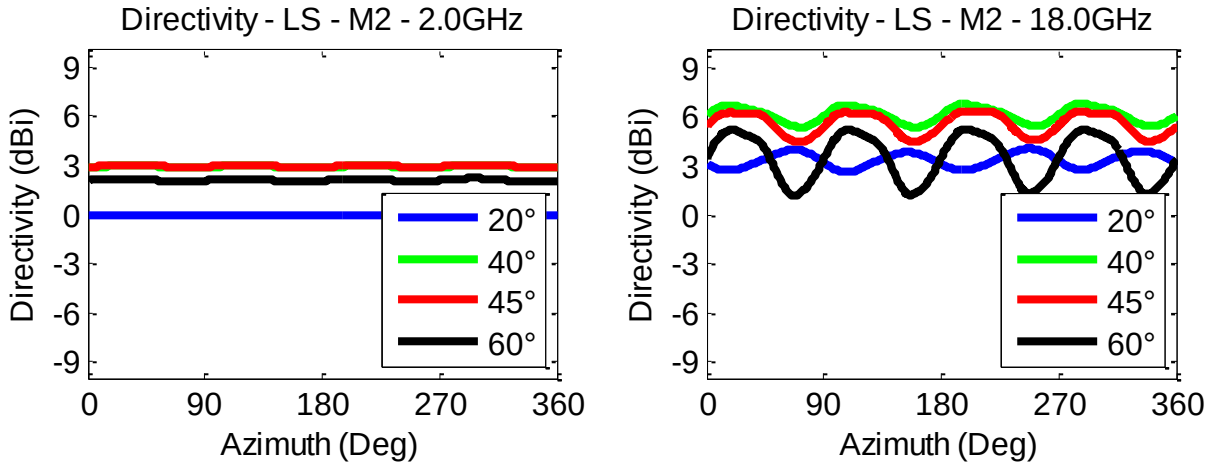

FIGURE 3-32: RADIATION PATTERNS – LS – AZ – M2 – MAG [2 (A) & 18 (B) GHZ]

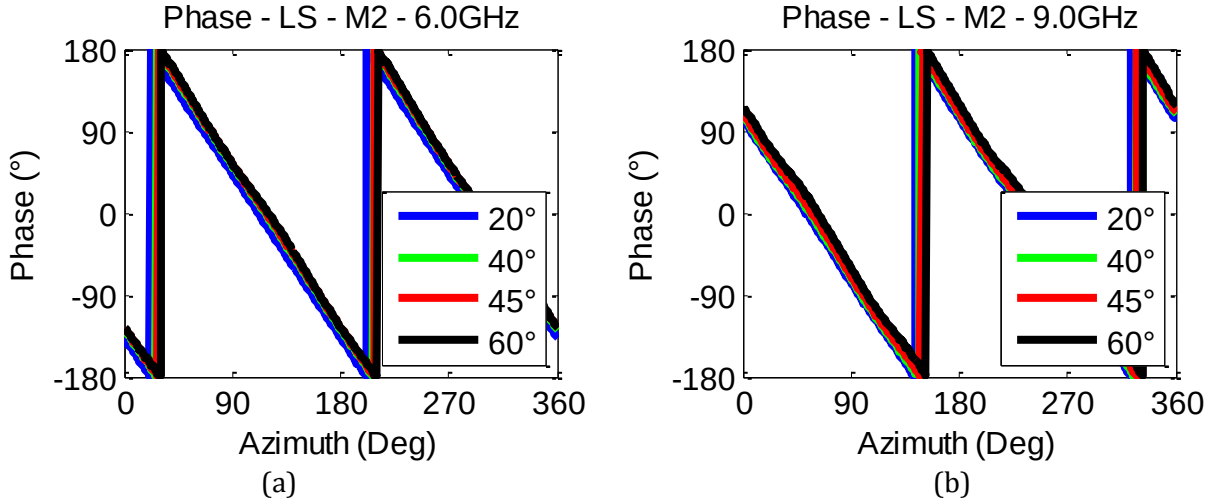

FIGURE 3-33: RADIATION PATTERNS – LS – AZ – M2 – PHA [6 (A) & 9 (B) GHZ]

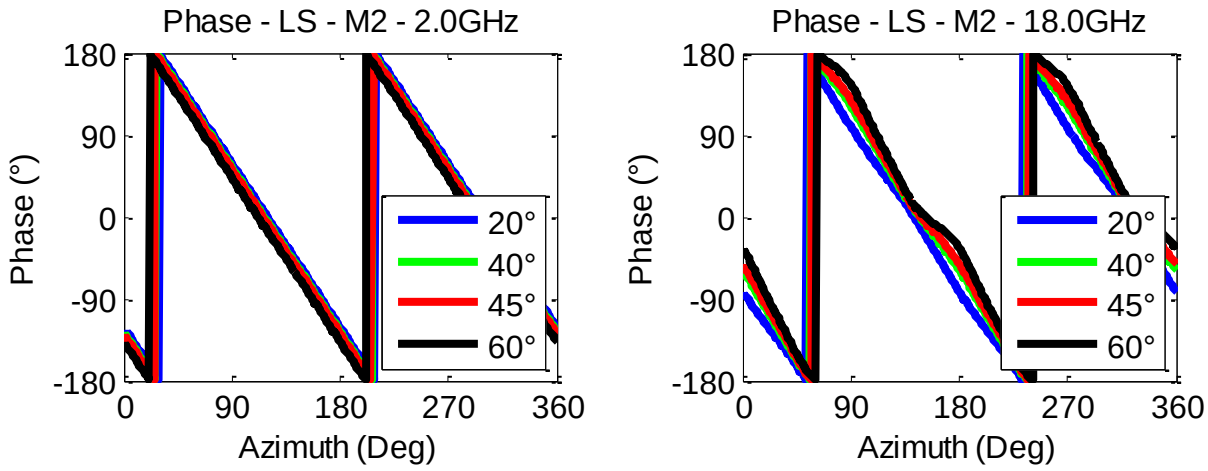

(a) (b)

FIGURE 3-34: RADIATION PATTERNS – LS – AZ – M2 – PHA [2 (A) & 18 (B) GHZ]

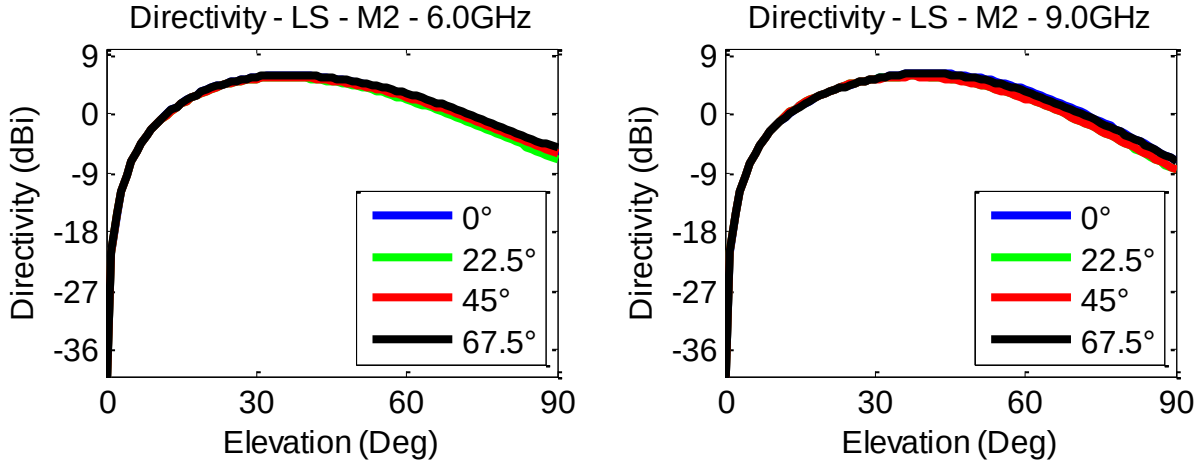

(a) (b)

FIGURE 3-35: RADIATION PATTERNS – LS – EL – M2 – MAG [6 (A) & 9 (B) GHZ]

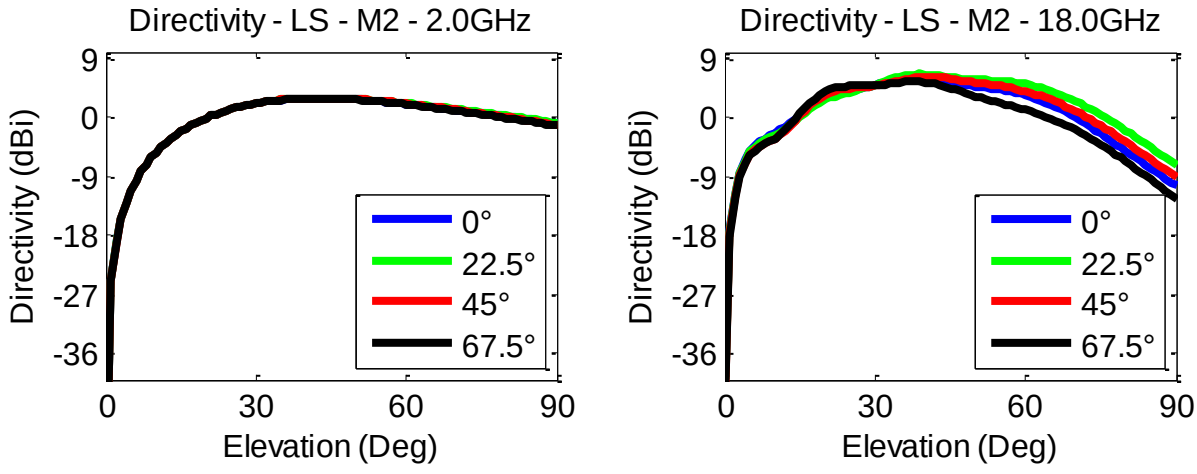

(a) (b)

FIGURE 3-36: RADIATION PATTERNS – LS – EL – M2 – MAG [2 (A) & 18 (B) GHZ]

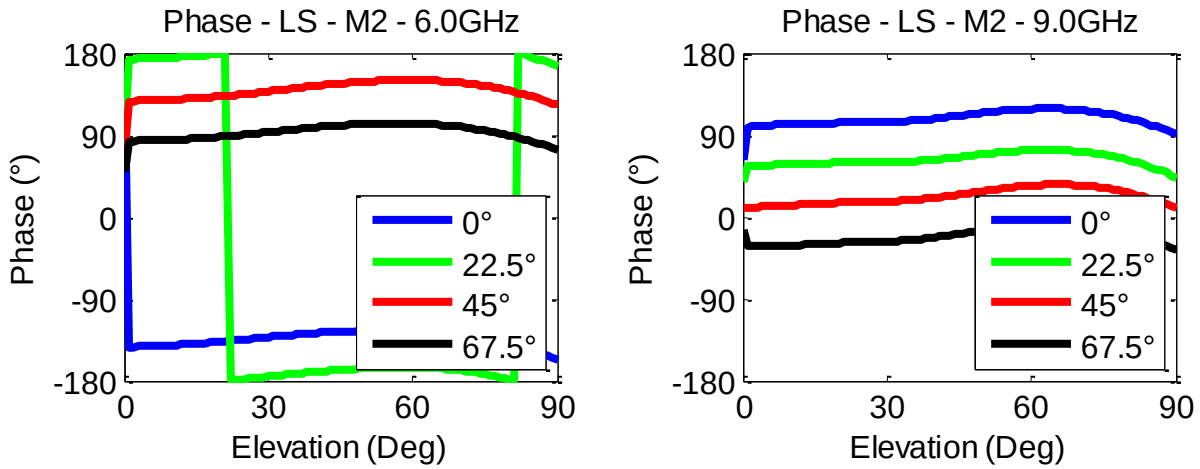

FIGURE 3-37: RADIATION PATTERNS – LS – EL – M2 – PHA [6 (A) & 9 (B) GHZ]

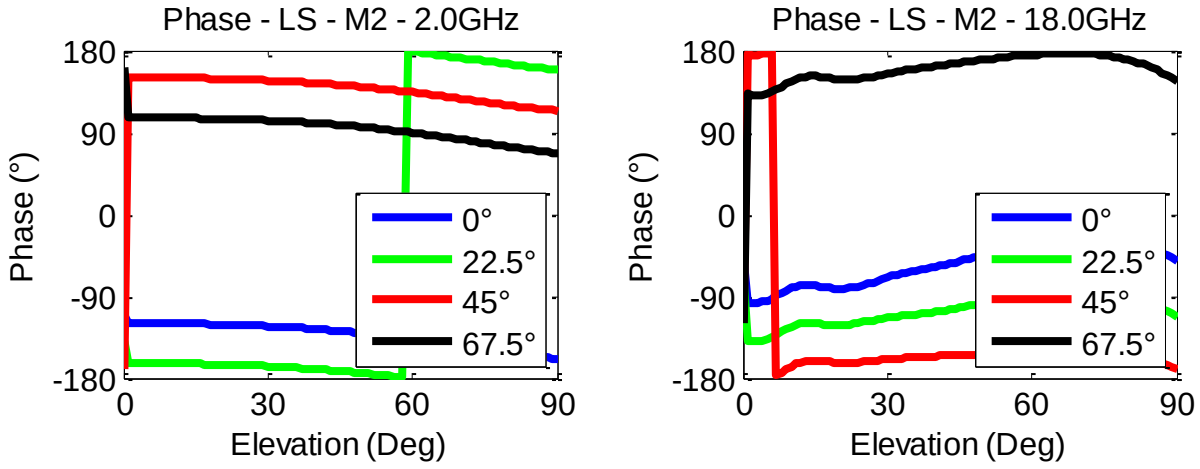

FIGURE 3-38: RADIATION PATTERNS – LS – EL – M2 – PHA [2 (A) & 18 (B) GHZ]

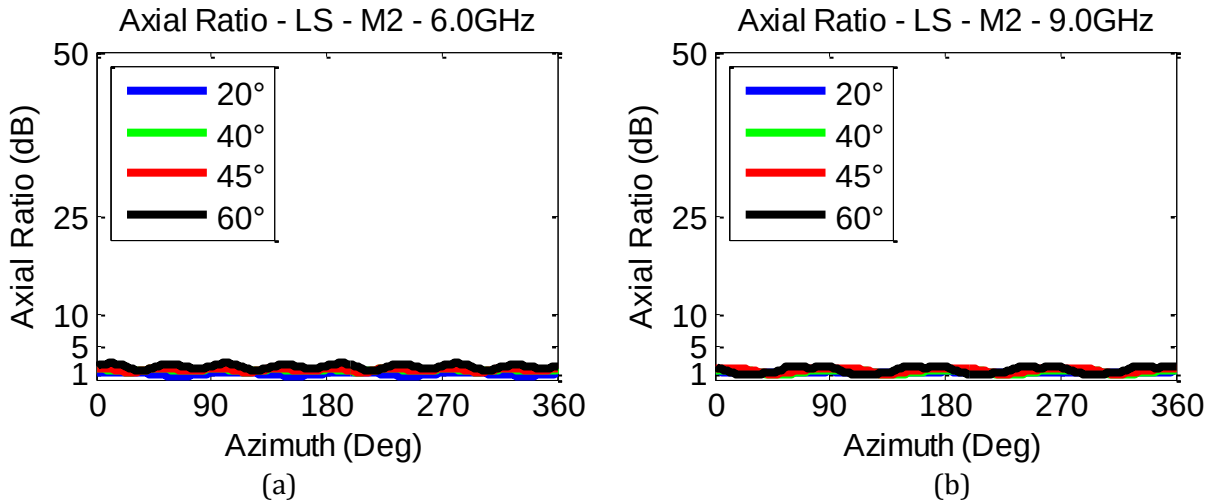

FIGURE 3-39: AXIAL RATIOS – LS – AZ – M2 [6 (A) & 9 (B) GHZ]

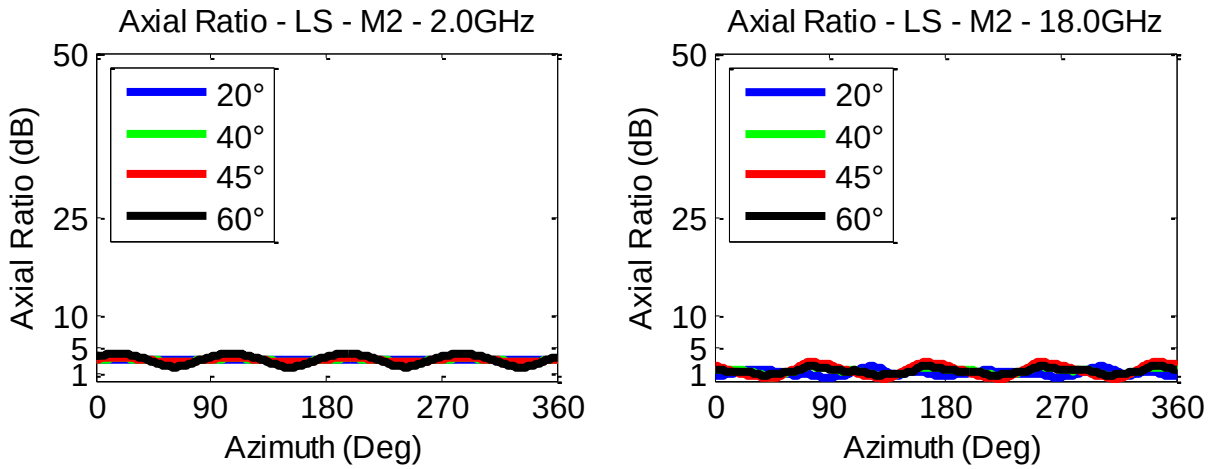

(a) (b)

FIGURE 3-40: AXIAL RATIOS – LS – AZ – M2 [2 (A) & 18 (B) GHZ]

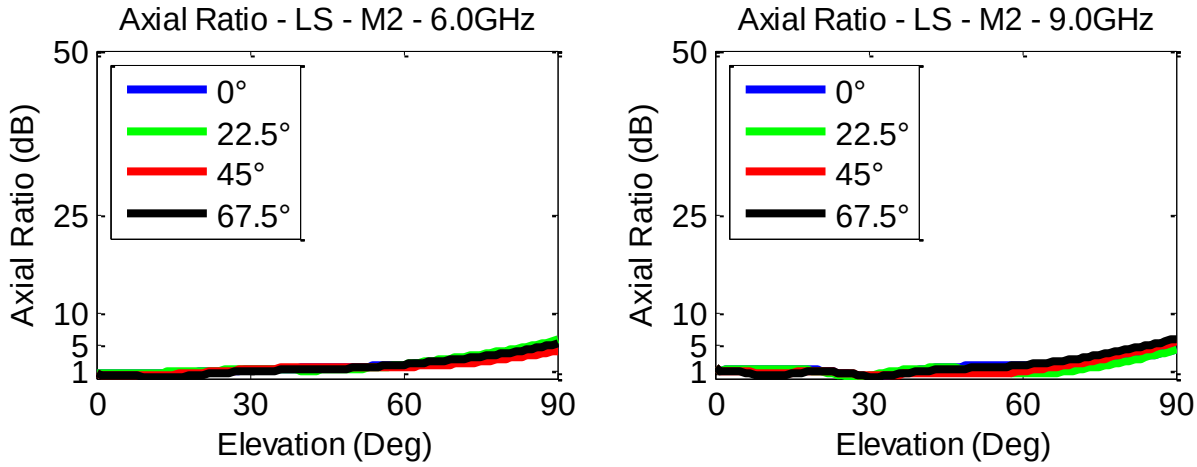

(a) (b)

FIGURE 3-41: AXIAL RATIOS – LS – EL – M2 [6 (A) & 9 (B) GHZ]

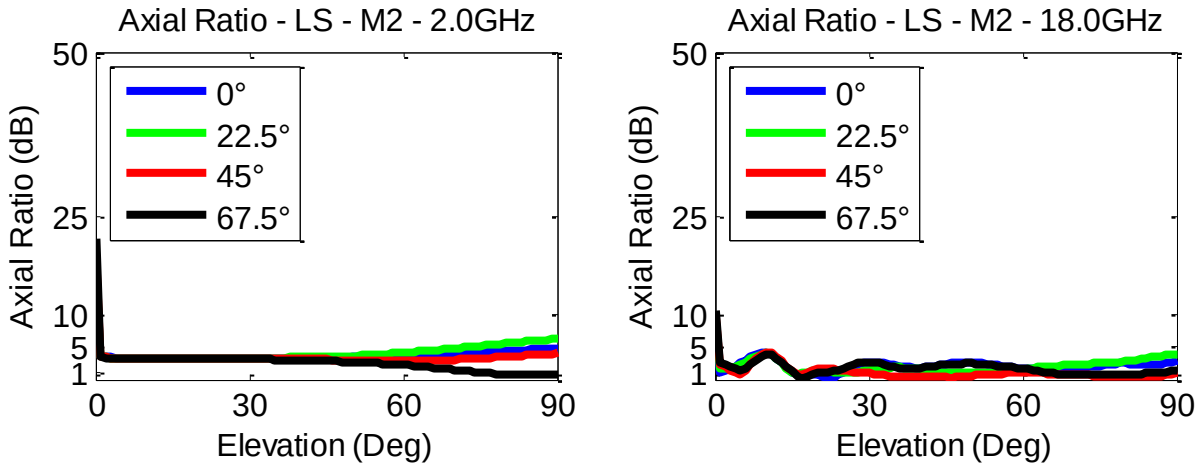

(a) (b)

FIGURE 3-42: AXIAL RATIOS – LS – EL – M2 [2 (A) & 18 (B) GHZ]

For the second mode of operation, the magnitude of the azimuth cuts, from Figures 3-31 & 3-32, are again used to view the magnitude ripple. The same trend holds from the first mode, being that the ripple increases both with the frequency and with an increase in elevation angle. At the lowest frequency of 2.0GHz, the spiral has minimal ripple of ±0.05dB at 40° in elevation. While at the highest frequency of 18.0GHz and 60° in elevation, the ripple is ±2.0dB. For the mid-band case, 6.0GHz and 40° in elevation, the ripple is ±0.3dB. The magnitude of the elevation cuts, from Figures 3-35 & 3-36, are primarily used to show the peak directivity angle and the -3dB beamwidth. The maximum directivity of 6.4dBi for 9.0GHz occurs at 41° in elevation and the -3dB beamwidth extends from 21° to 61°.

The phase ripple about azimuth, from Figures 3-33 & 3-34, increases with frequency, similar to the magnitude ripple. However, different from the magnitude ripple, it is minimal at the elevation angle of maximum directivity. Minimal ripple, of ±0.3° is found at 2GHz and 40° in elevation, while at 18.0GHz and 60° in elevation the ripple is ±14°. In the mid-band case of 40° in elevation at 6.0GHz, the ripple is ±1.5°. The phase of the elevation cuts, from Figures 3-37 & 3-38, would ideally be equally spaced and most importantly would not overlap, which does not occur at any frequency.

The trend for the axial ratio about azimuth, from Figures 3-39 & 3-40, is to remain low toward boresight and increase toward the horizon. There is also variation about azimuth, but for 6.0GHz and 40° in elevation the average is 1.4dB and the peak is under 1.7dB. There is also variation across elevation, from Figures 3-41 & 3-42, that increases from boresight toward the horizon. Again, the lowest and peak cases occur for 6.0GHz which begin around 1dB, dip under 0.01dB and reach 6.1dB at the horizon.

3.2.2.2 ARCHIMEDEAN SPIRAL

For the Archimedean spiral, feed points are again located at azimuth angles of 22.5°, 112.5°, 202.5° and 292.5°. Within the first mode of operation results include: the azimuth cuts' magnitude in Figures 3-43 & 3-44, the azimuth cuts' phase in Figures 3-45 & 3-46, the elevation cuts' magnitude in Figures 3-47 & 3-48, the elevation cuts' phase in Figures 3-49 & 3-50 and the axial ratio of the azimuth cuts in Figures 3-51 & 3-52 and of the elevation cuts in Figures 3-53 & 3-54.

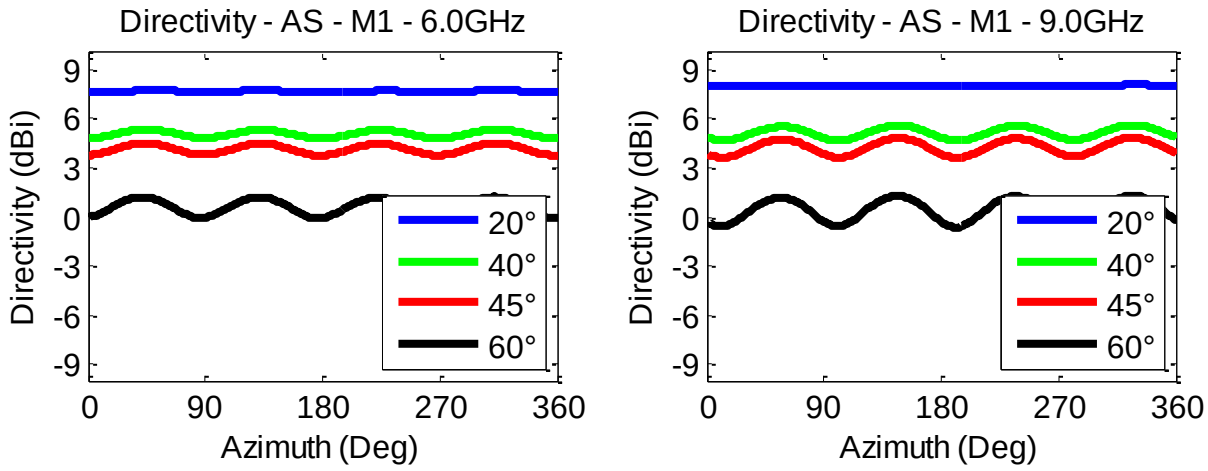

(a) (b)

FIGURE 3-43: RADIATION PATTERNS – AS – AZ – M1 – MAG [6 (A) & 9 (B) GHZ]

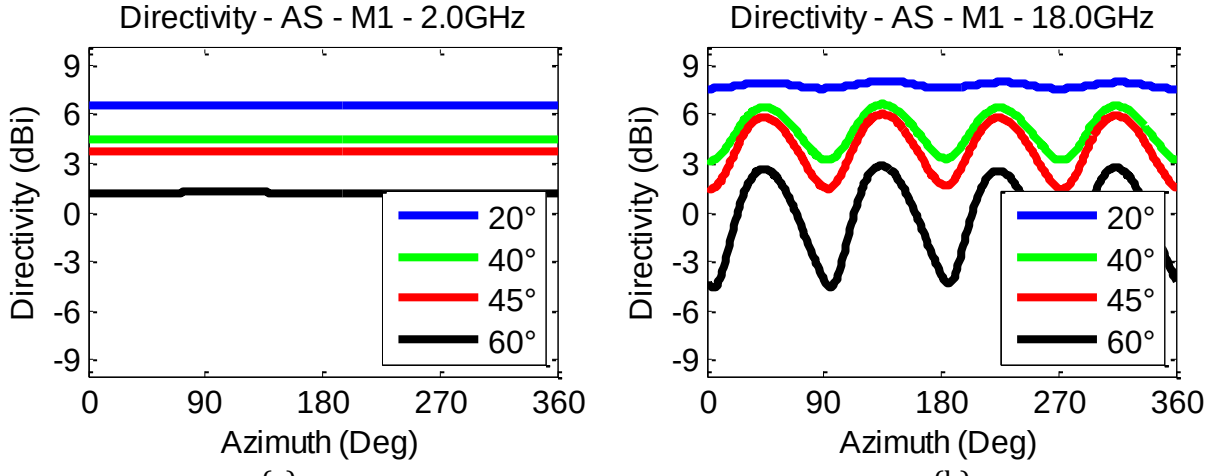

(a) (b)

FIGURE 3-44: RADIATION PATTERNS – AS – AZ – M1 – MAG [2 (A) & 18 (B) GHZ]

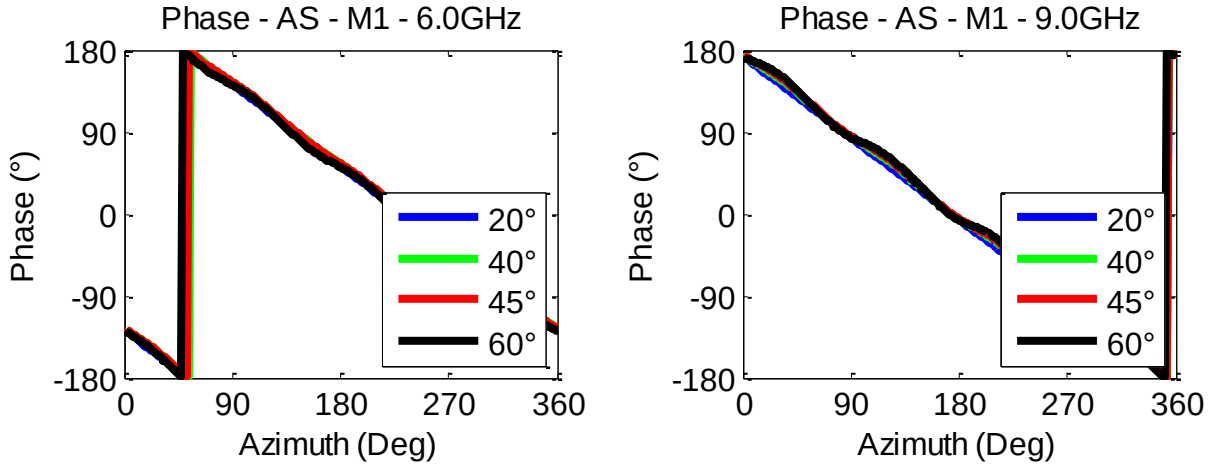

(a) (b)

FIGURE 3-45: RADIATION PATTERNS – AS – AZ – M1 – PHA [6 (A) & 9 (B) GHZ]

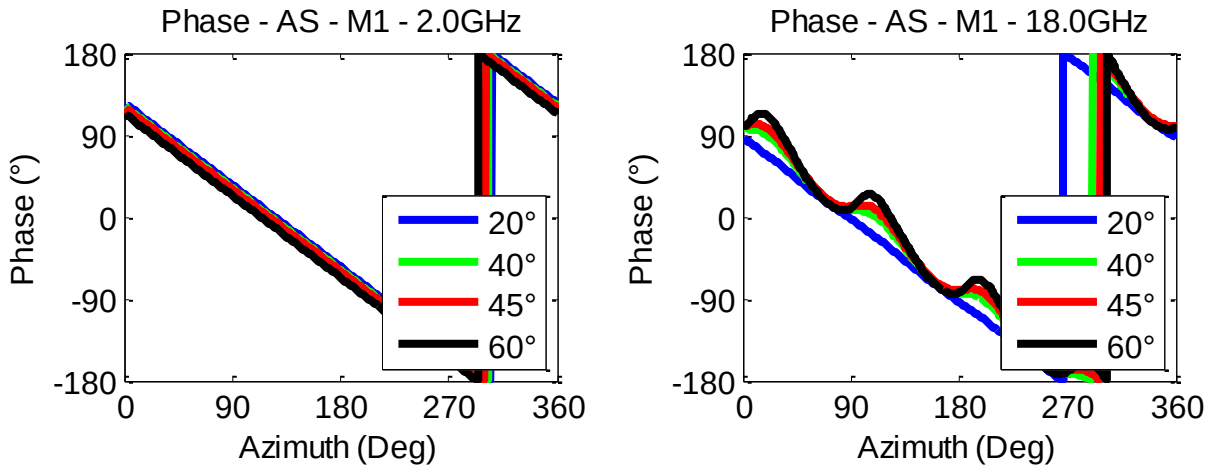

(a) (b)

FIGURE 3-46: RADIATION PATTERNS – AS – AZ – M1 – PHA [2 (A) & 18 (B) GHZ]

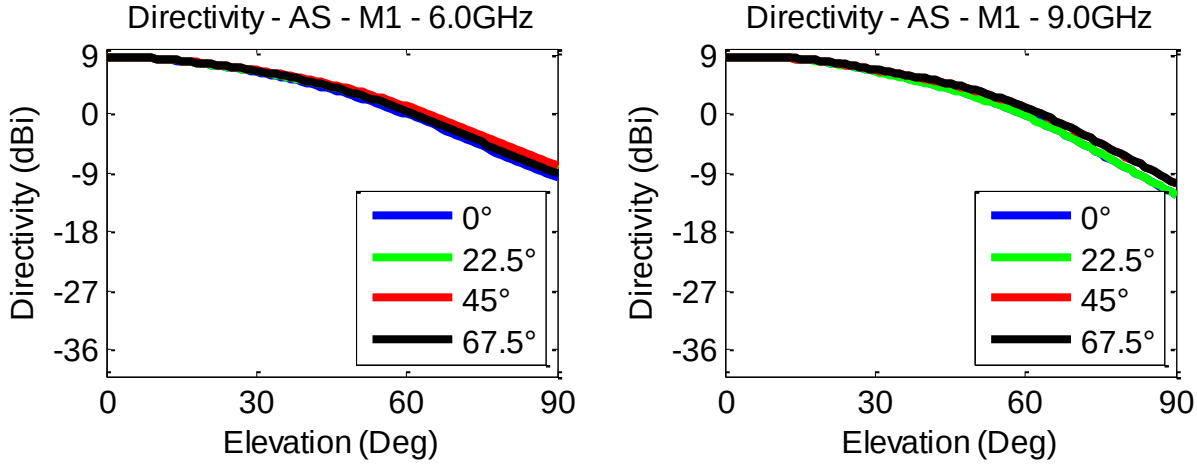

(a) (b)

FIGURE 3-47: RADIATION PATTERNS – AS – EL – M1 – MAG [6 (A) & 9 (B) GHZ]

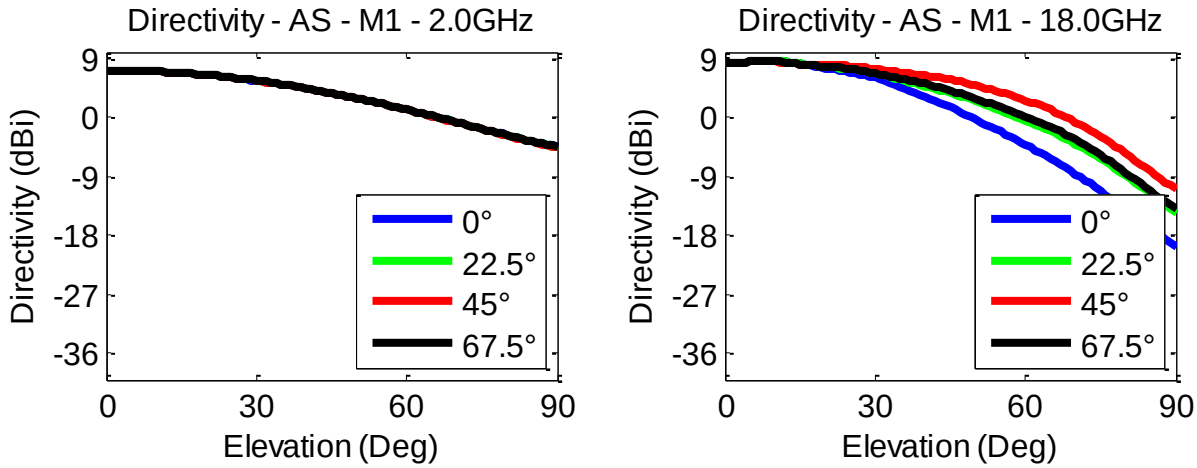

(a) (b)

FIGURE 3-48: RADIATION PATTERNS – AS – EL – M1 – MAG [2 (A) & 18 (B) GHZ]

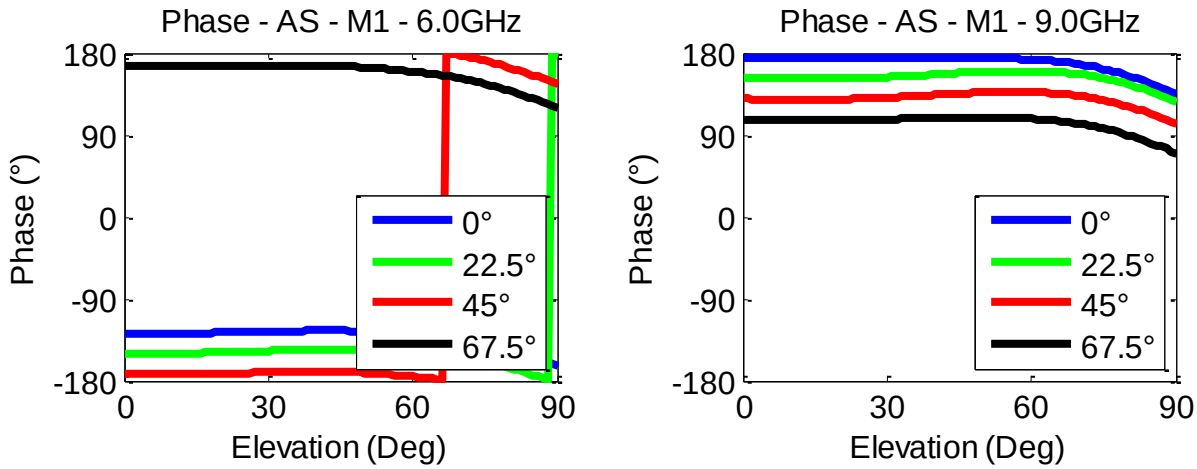

FIGURE 3-49: RADIATION PATTERNS – AS – EL – M1 – PHA [6 (A) & 9 (B) GHZ]

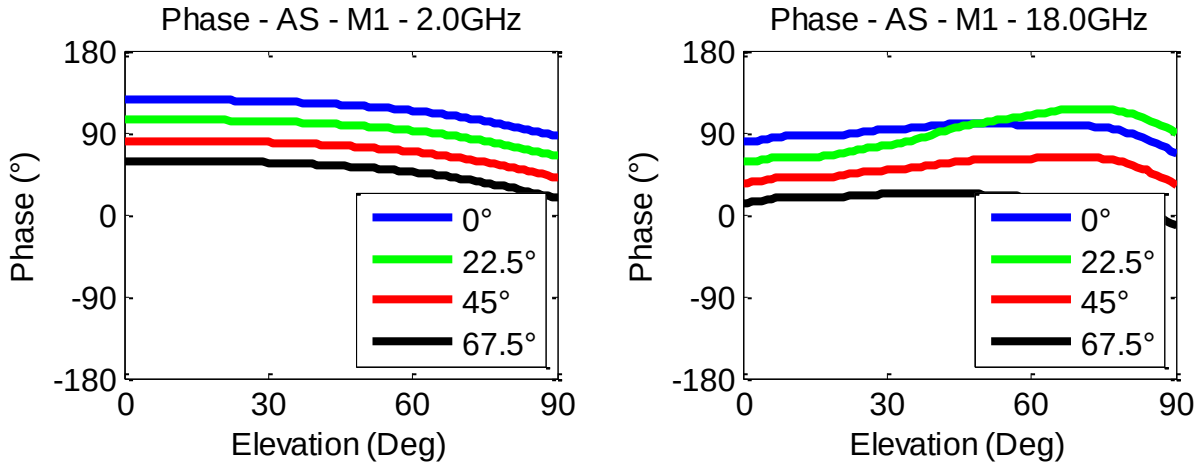

FIGURE 3-50: RADIATION PATTERNS – AS – EL – M1 – PHA [2 (A) & 18 (B) GHZ]

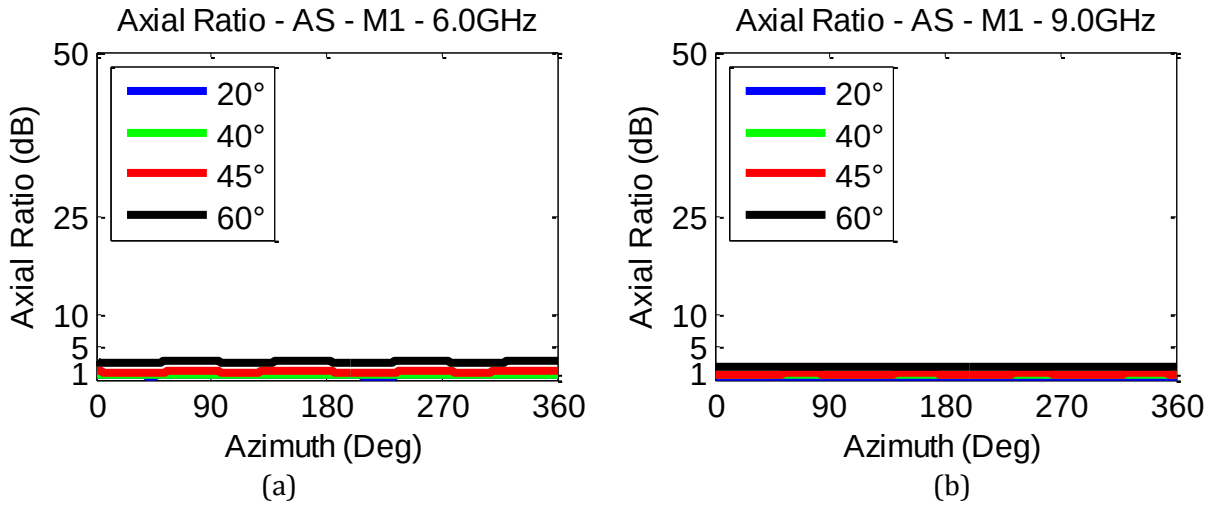

FIGURE 3-51: AXIAL RATIOS – AS – AZ – M1 [6 (A) & 9 (B) GHZ]

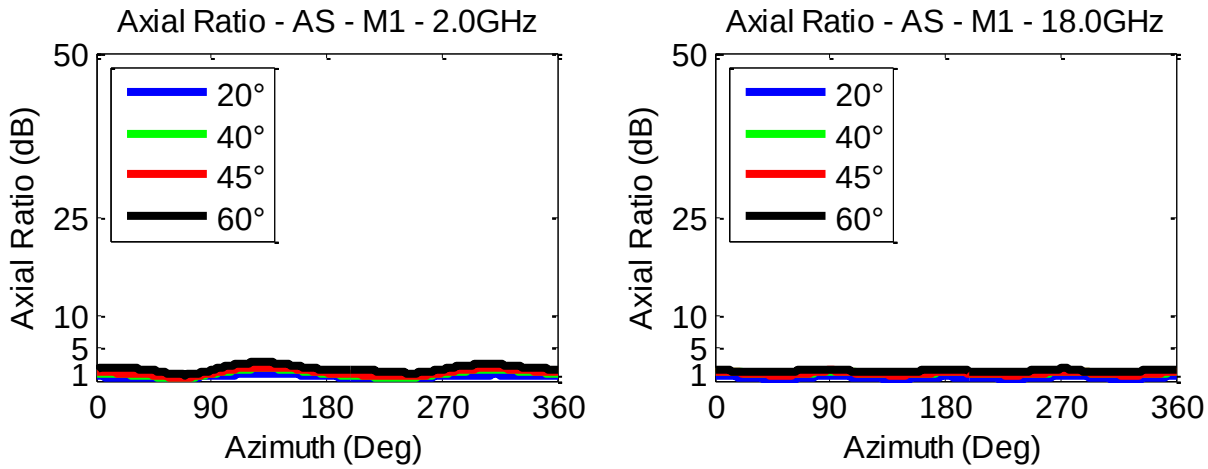

(a) (b)

FIGURE 3-52: AXIAL RATIOS – AS – AZ – M1 [2 (A) & 18 (B) GHZ]

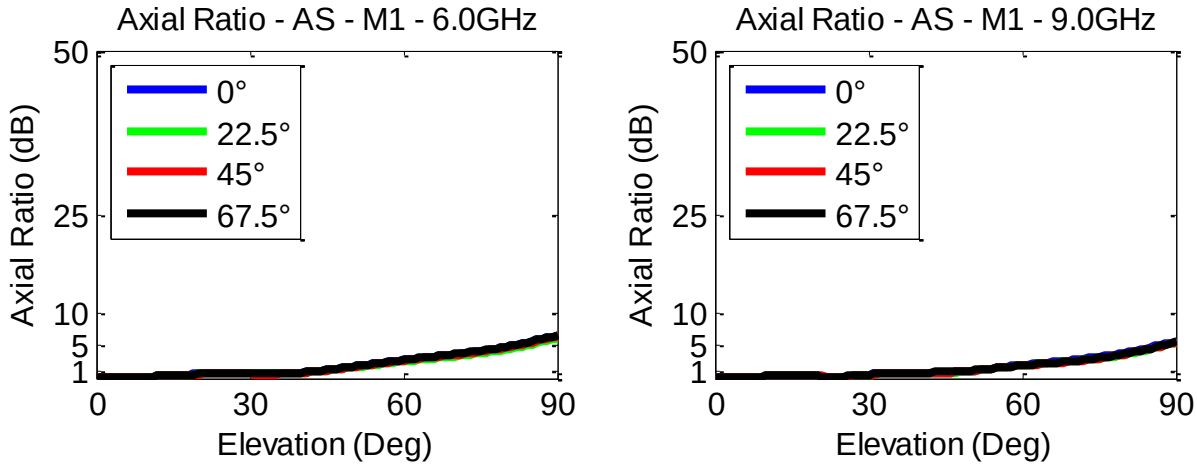

(a) (b)

FIGURE 3-53: AXIAL RATIOS – AS – EL – M1 [6 (A) & 9 (B) GHZ]

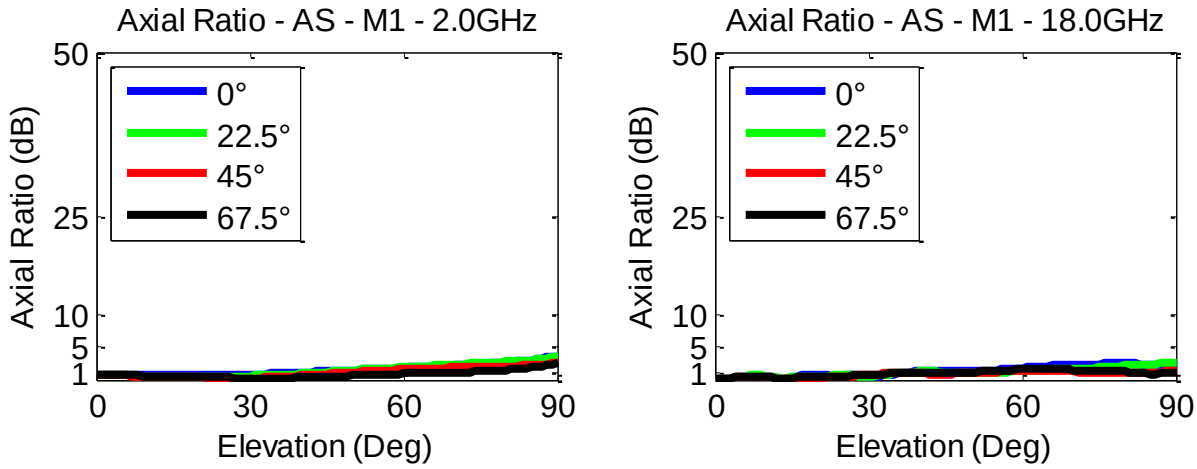

(a) (b)

FIGURE 3-54: AXIAL RATIOS – AS – EL – M1 [2 (A) & 18 (B) GHZ]

For the first mode of operation, the magnitude of the azimuth cuts, from Figures 3-43 & 3-44, are used to view the magnitude ripple. The trend for the first mode is for the ripple to increase as both the frequency increases and the elevation angle increases from boresight to the horizon. In the best case, at the lowest frequency of 2.0GHz, the spiral has ripple of ±0.01dB at 20° in elevation. While in the worst, at the highest frequency of 18.0GHz and 60° in elevation, the ripple is ±3.75dB. At 20° of elevation and 6.0GHz the performance is expected to be the typical mid-band response removed from any truncation effects and here the ripple is ±0.04dB. The magnitude of the elevation cuts, 3-47 & 3-48, are primarily used to show the maximum directivity at boresight and the -3dB beamwidth. The maximum directivity of 8.75dBi occurs at 9.0GHz and the -3dB beamwidth extends to 34°.

Similar to the magnitude ripple, the phase ripple, from Figures 3-45 & 3-46, increases with both increasing frequency and elevation angle. . The phase ripple is ±0.1° at 2.0GHz and 20°. However for 18.0GHz at 60°, there is ripple of ±24°. In the mid-band case, 20° of elevation at 6.0GHz, the ripple is ±0.25°. The phase of the elevation cuts, from Figures 3-49 & 3-50, would ideally be equally spaced but most importantly would not overlap. At 18.0GHz, an overlap occurs above 60° in elevation, which would lead to ambiguity in the angle of arrival estimation.

The trend for the axial ratio about azimuth, from Figures 3-51 & 3-52, is for the lowest values at boresight and increasing values toward the horizon while the ripple increases with frequency. In the mid-band at 6.0GHz and 20° in elevation, the average is 0.6dB and the peak is 0.7dB. There is also variation across elevation, from Figures 3-53 & 3-54, that increases from boresight toward the horizon. As with the logarithmic spiral, the

lowest and peak cases occur for the 6.0GHz which begin at less than 0.01dB at boresight and reach 6.8dB at the horizon.

Within the second mode of operation results include: the azimuth cuts' magnitude in Figures 3-55 & 3-56, the azimuth cuts' phase in Figures 3-57 & 3-58, the elevation cuts' magnitude in Figures 3-59 & 3-60, the elevation cuts' phase in Figures 3-61 & 3-62 and the axial ratio of the azimuth cuts in Figures 3-63 & 3-64 and of the elevation cuts in Figures 3-65 & 3-66.

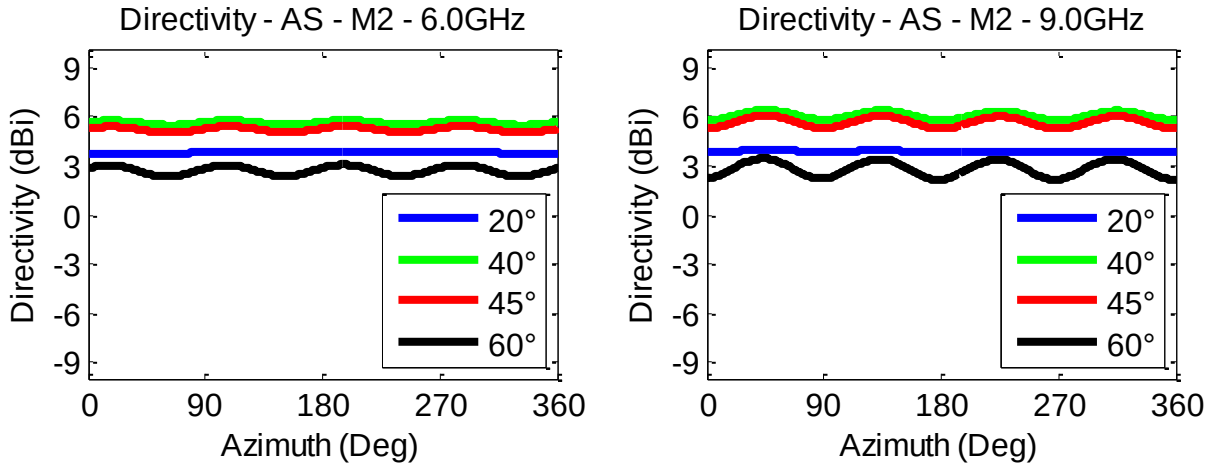

FIGURE 3-55: RADIATION PATTERNS – AS – AZ – M2 – MAG [6 (A) & 9 (B) GHZ]

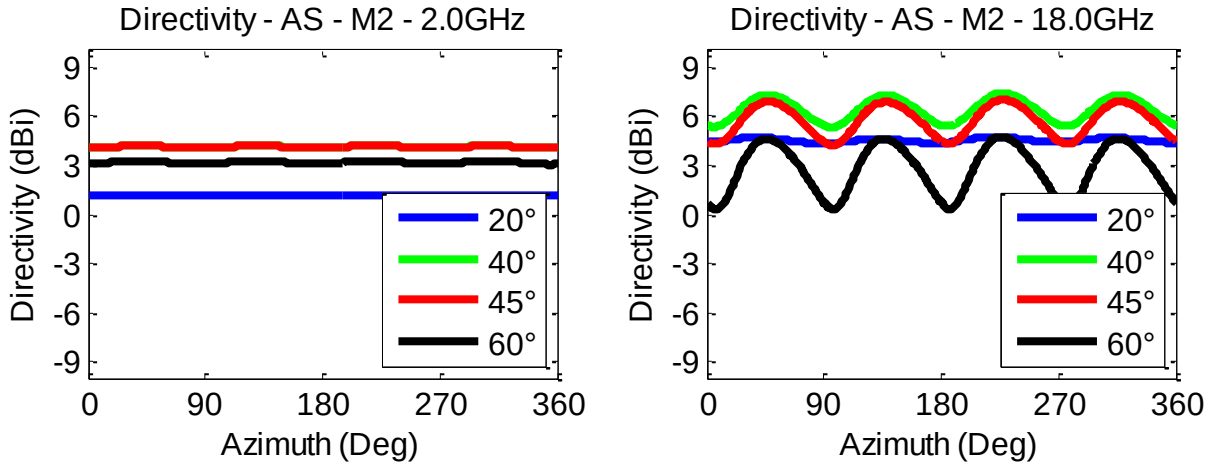

FIGURE 3-56: RADIATION PATTERNS – AS – AZ – M2 – MAG [2 (A) & 18 (B) GHZ]

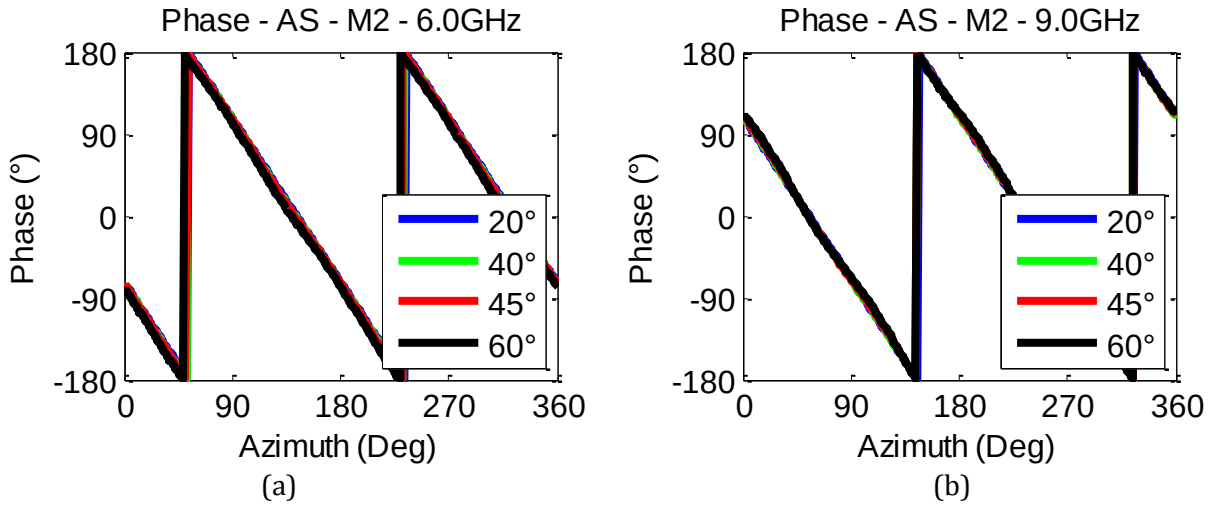

FIGURE 3-57: RADIATION PATTERNS – AS – AZ – M2 – PHA [6 (A) & 9 (B) GHZ]

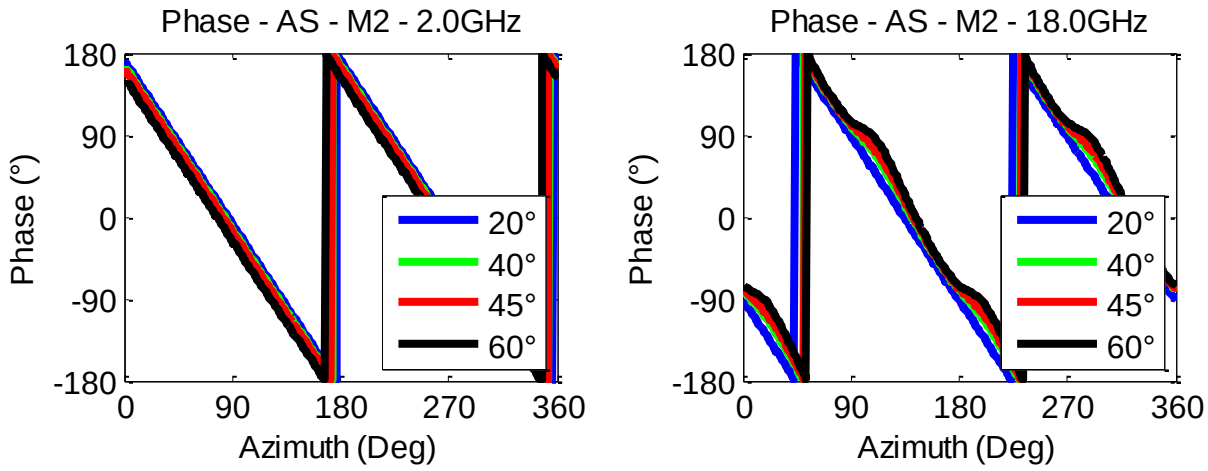

(a) (b)

FIGURE 3-58: RADIATION PATTERNS – AS – AZ – M2 – PHA [2 (A) & 18 (B) GHZ]

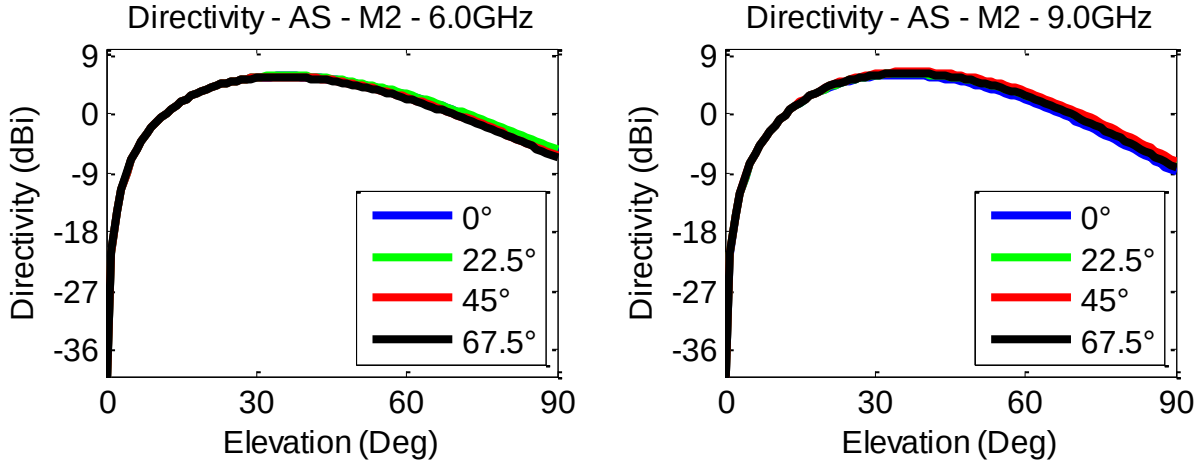

(a) (b)

FIGURE 3-59: RADIATION PATTERNS – AS – EL – M2 – MAG [6 (A) & 9 (B) GHZ]

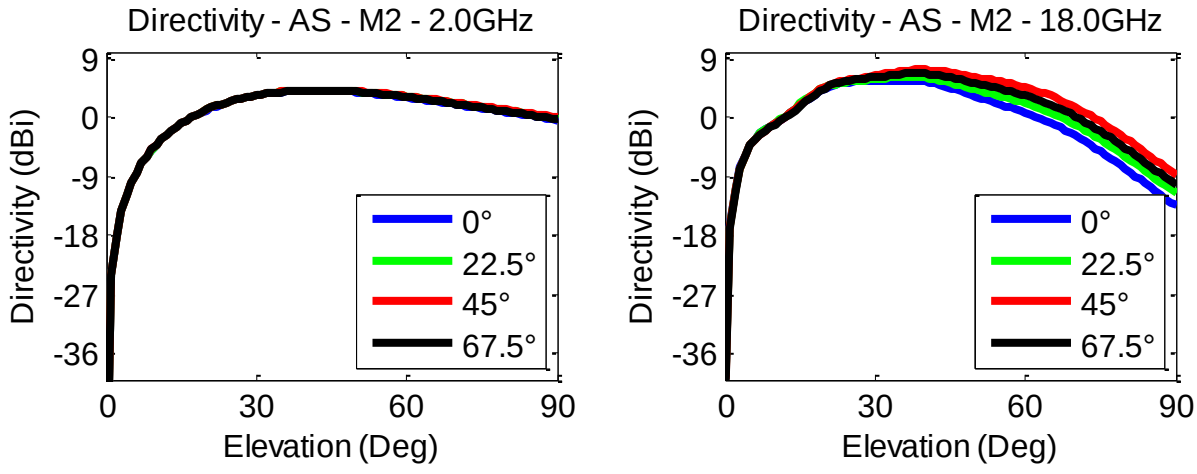

(a) (b)

FIGURE 3-60: RADIATION PATTERNS – AS – EL – M2 – MAG [2 (A) & 18 (B) GHZ]

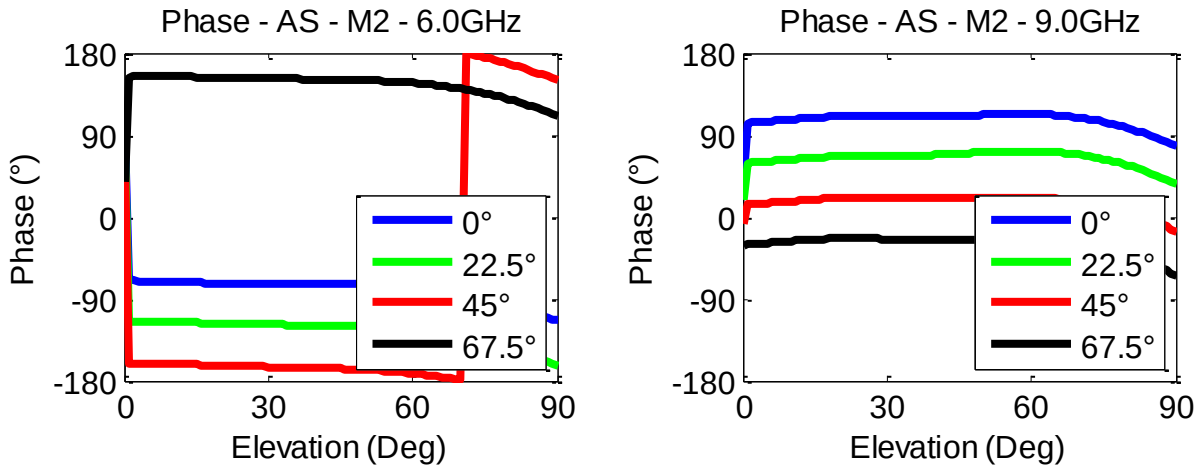

FIGURE 3-61: RADIATION PATTERNS – AS – EL – M2 – PHA [6 (A) & 9 (B) GHZ]

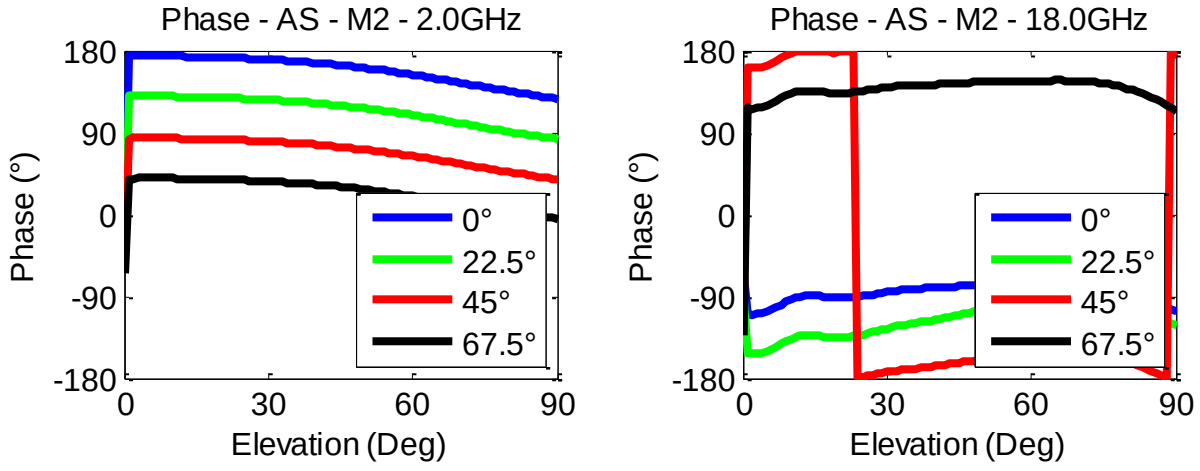

FIGURE 3-62: RADIATION PATTERNS – AS – EL – M2 – PHA [2 (A) & 18 (B) GHZ]

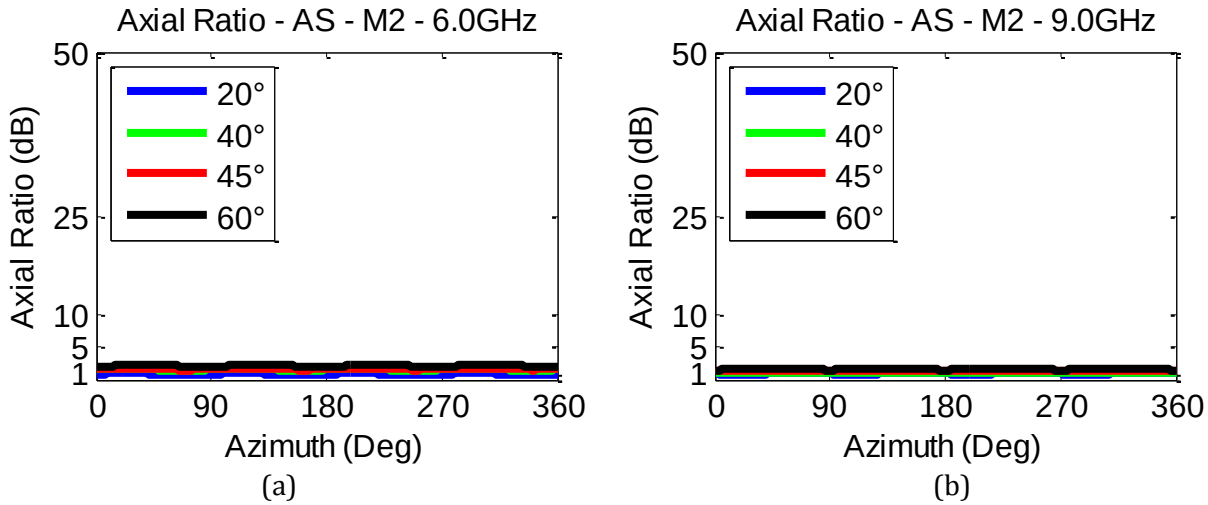

FIGURE 3-63: AXIAL RATIOS – AS – AZ – M2 [6 (A) & 9 (B) GHZ]

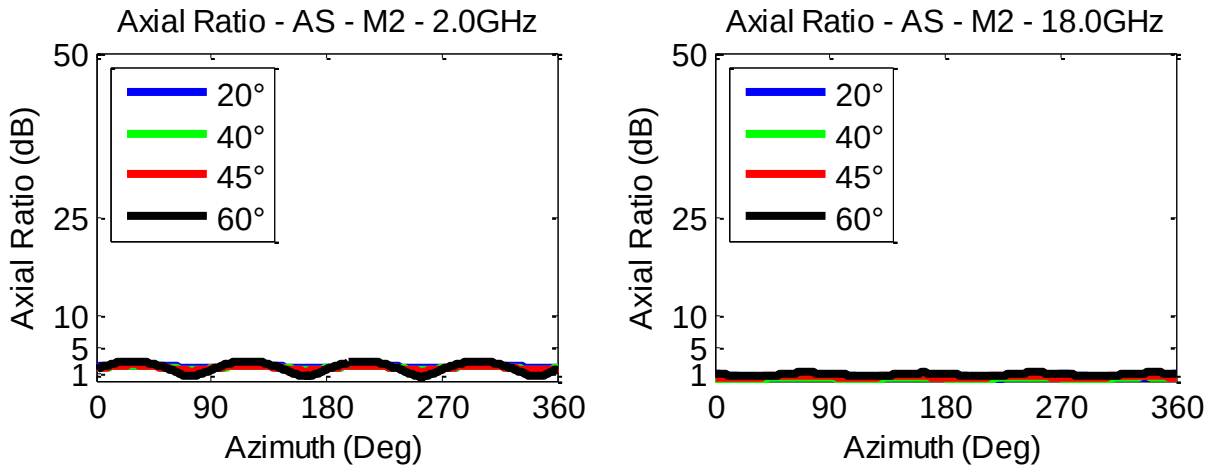

(a) (b)

FIGURE 3-64: AXIAL RATIOS – AS – AZ – M2 [2 (A) & 18 (B) GHZ]

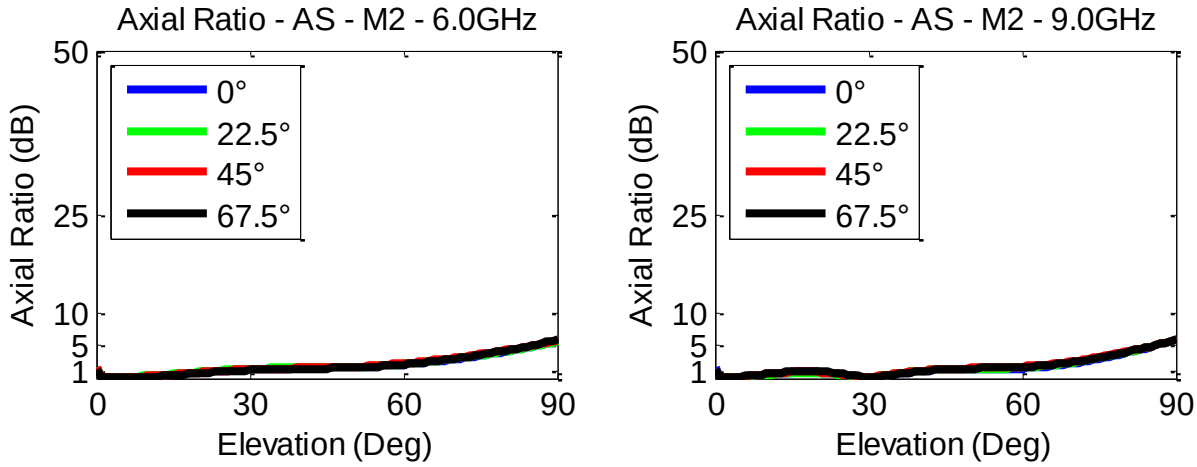

(a) (b)

FIGURE 3-65: AXIAL RATIOS – AS – EL – M2 [6 (A) & 9 (B) GHZ]

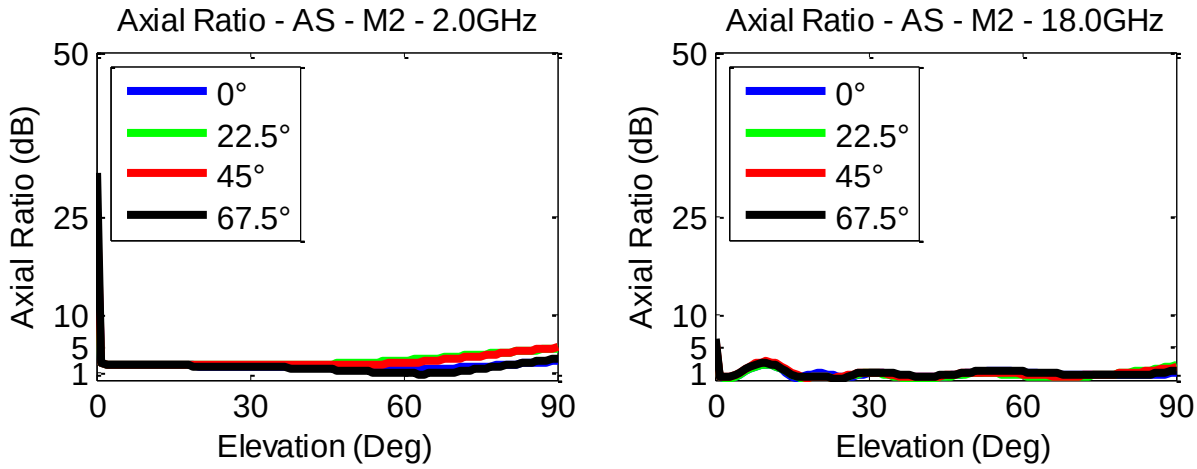

(a) (b)

FIGURE 3-66: AXIAL RATIOS – AS – EL – M2 [2 (A) & 18 (B) GHZ]

For the second mode of operation, the magnitude of the azimuth cuts, from Figures 3-55 & 3-56, are used to view the magnitude ripple. The same trend holds from the first mode, being for the ripple to increase both as the frequency is increases and as the elevation angle increases from boresight to the horizon. At the lowest frequency of 2.0GHz and 40° in elevation, the spiral exhibits minimal ripple at ±0.05dB at elevation angles above 20°. While at the highest frequency of 18.0GHz and 60° of elevation, the ripple is ±2.25dB. For the mid-band case, 6.0GHz and 40° in elevation, the ripple is ±0.15dB. The magnitude of the elevation cuts, from Figures 3-59 & 3-60, show the peak directivity angle and the -3dB beamwidth. The maximum directivity of 6.5dBi for 9.0GHz occurs at 37° in elevation and the -3dB beamwidth extends from 19° to 59°.

The phase ripple about azimuth, from Figures 3-57 & 3-58, increases with frequency, similar to the magnitude ripple. However, different from the magnitude ripple, it is minimal at the elevation angle of maximum directivity. Minimal ripple, of ±0.3° is found at 2GHz and 40° in elevation, while at 18.0GHz and 60° in elevation the ripple is ±14°. In the mid-band case of 40° in elevation at 6.0GHz, the ripple is ±1.0°. The phase of the elevation cuts, from Figures 3-61 & 3-62, are the closest to ideal for any antenna presented and no overlaps occur at any frequency.

The trend for the axial ratio about azimuth, from Figures 3-63 & 3-64, is to remain low toward boresight and increase toward the horizon. There is also variation about azimuth, but for 6.0GHz and 40° in elevation the average is 1.5dB and the peak is under 1.6dB. There is also variation across elevation, from Figures 3-65 & 3-66, that increases from boresight toward the horizon. Again, the lowest and peak cases occur for 6.0GHz which begin around 1dB, dip under 0.001dB and reach 6.0dB at the horizon.

3.2.2.3 CIRCULAR LOG-PERIODIC [Π/8]

For the circular log-periodic with π/8-overlap, feed points are in line with the middle of the elements and are located at azimuth angles of 45°, 135°, 225° and 315°. Within the first mode of operation results include: the azimuth cuts' magnitude in Figures 3-67 & 3-68, the azimuth cuts' phase in Figures 3-69 & 3-70, the elevation cuts' magnitude in Figures 3-71 & 3-72, the elevation cuts' phase in Figures 3-73 & 3-74 and the axial ratio of the azimuth cuts in Figures 3-75 & 3-76 and of the elevation cuts in Figures 3-77 & 3-78.

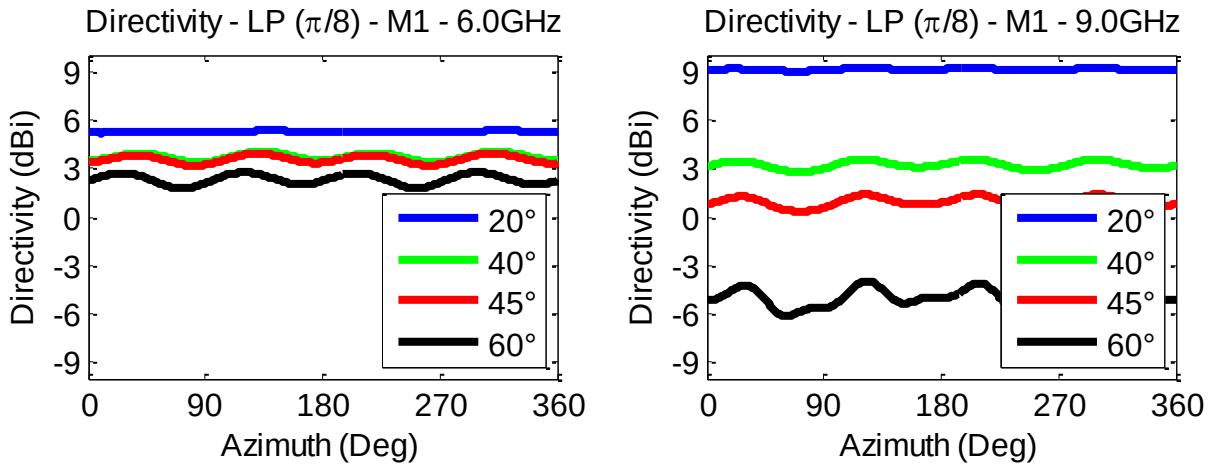

FIGURE 3-67: RADIATION PATTERNS – LP [Π/8] – AZ – M1 – MAG [6 (A) & 9 (B) GHZ]

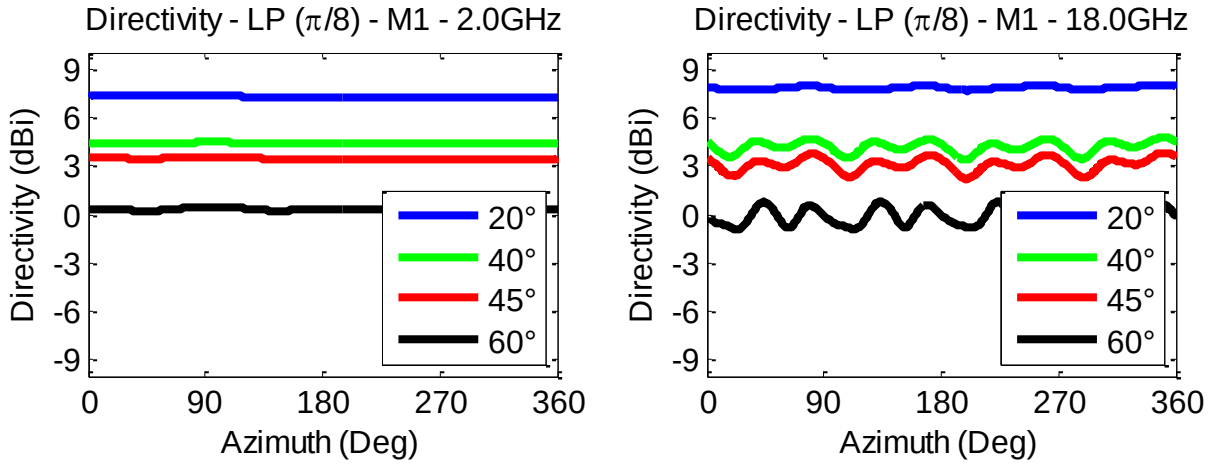

FIGURE 3-68: RADIATION PATTERNS – LP [Π/8] – AZ – M1 – MAG [2 (A) & 18 (B) GHZ]

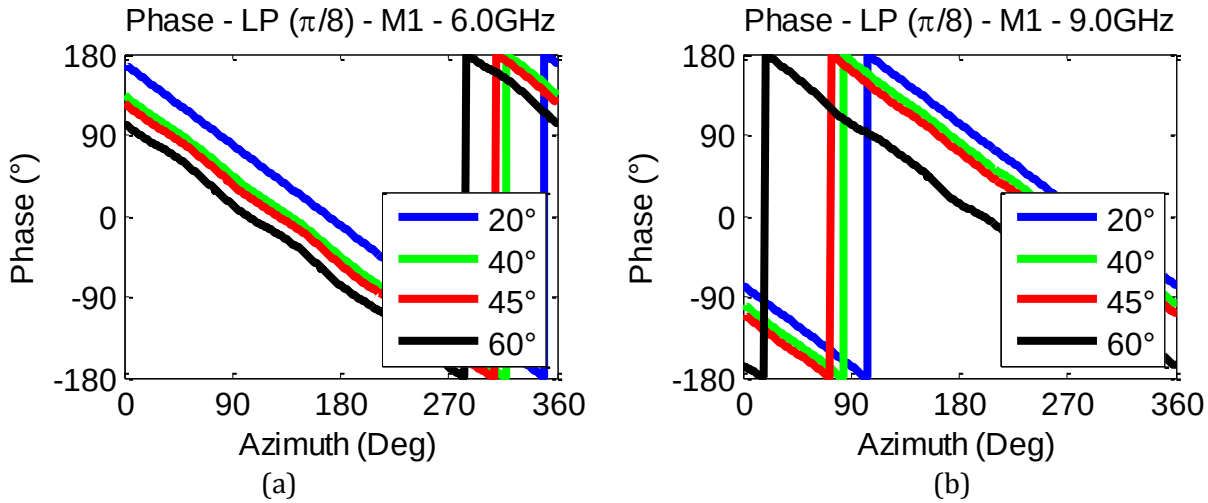

FIGURE 3-69: RADIATION PATTERNS – LP [Π/8] – AZ – M1 – PHA [6 (A) & 9 (B) GHZ]

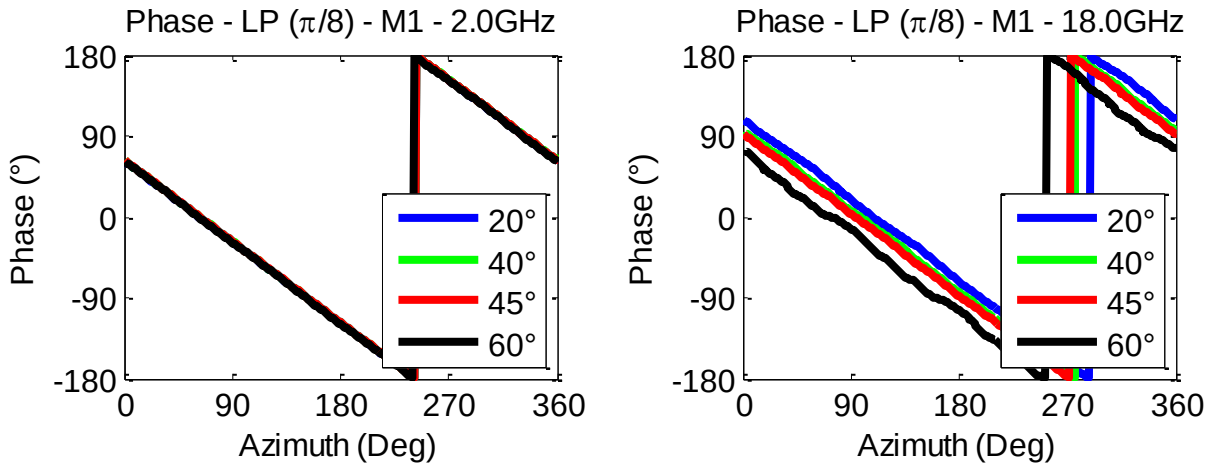

(a) (b)

FIGURE 3-70: RADIATION PATTERNS – LP [Π/8] – AZ – M1 – PHA [2 (A) & 18 (B) GHZ]

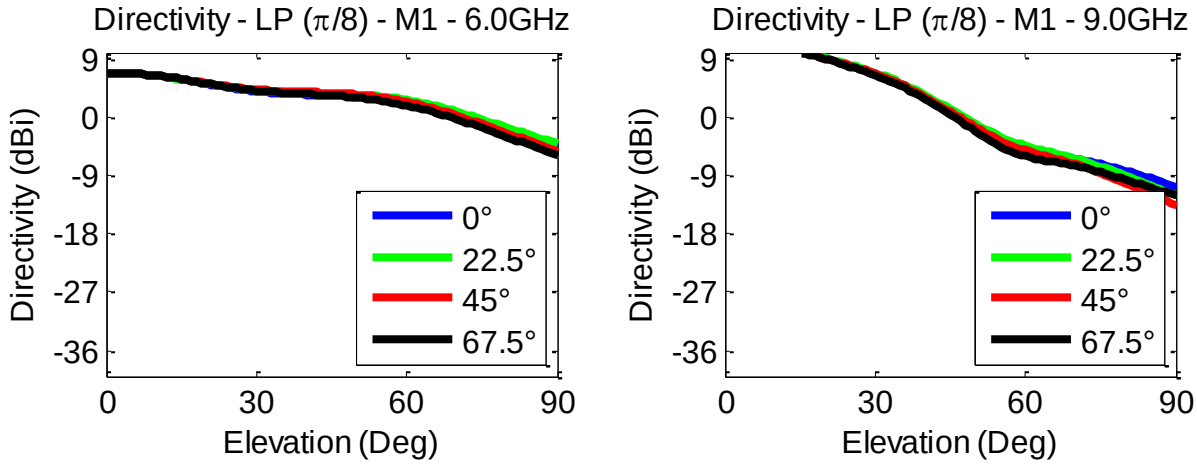

(a) (b)

FIGURE 3-71: RADIATION PATTERNS – LP [Π/8] – EL – M1 – MAG [6 (A) & 9 (B) GHZ]

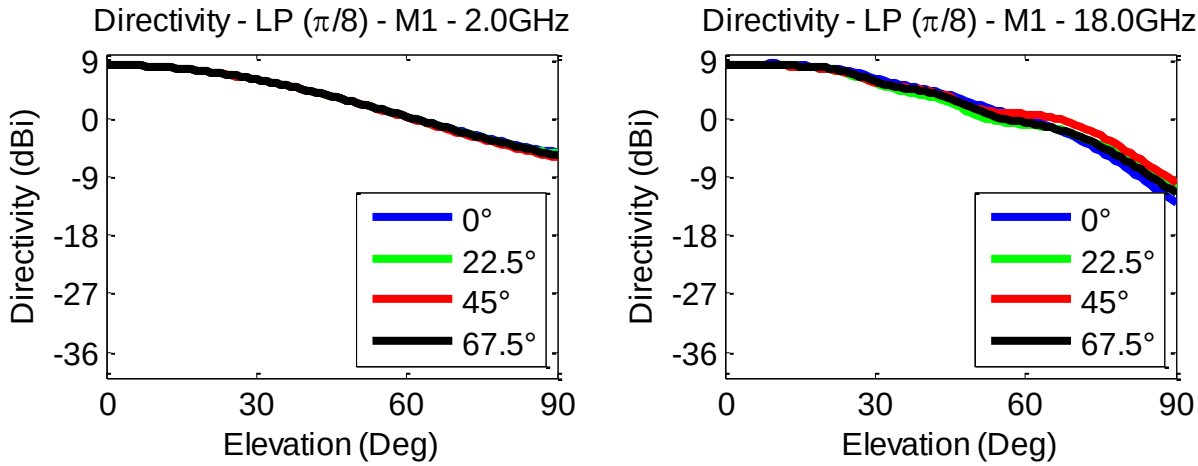

(a) (b)

FIGURE 3-72: RADIATION PATTERNS – LP [Π/8] – EL – M1 – MAG [2 (A) & 18 (B) GHZ]

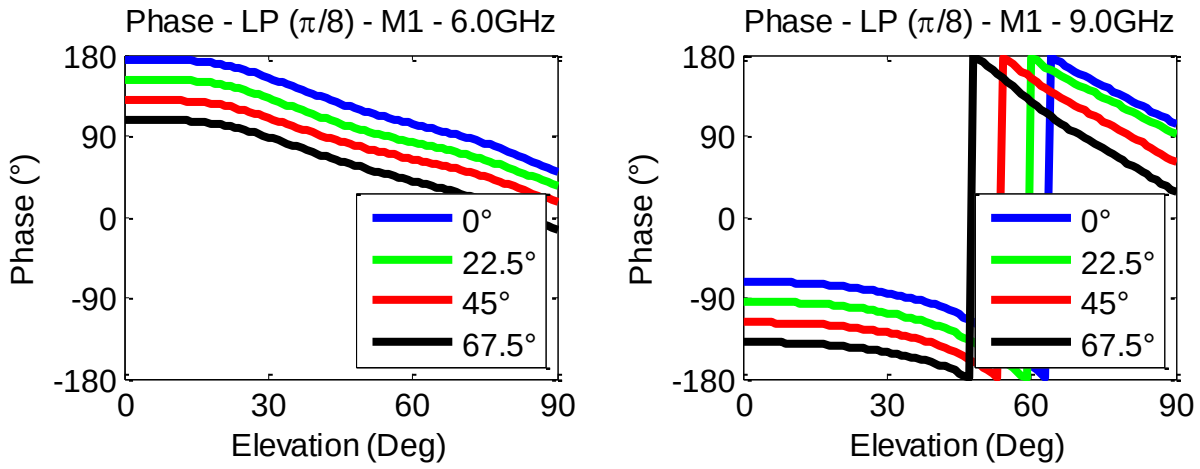

(a) (b)

FIGURE 3-73: RADIATION PATTERNS – LP [Π/8] – EL – M1 – PHA [6 (A) & 9 (B) GHZ]

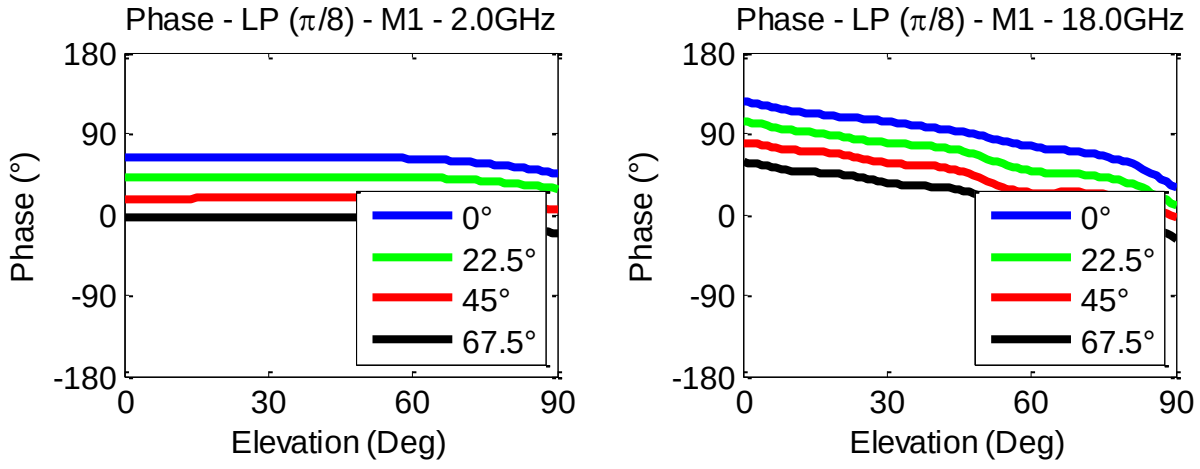

(a) (b)

FIGURE 3-74: RADIATION PATTERNS – LP [Π/8] – EL – M1 – PHA [2 (A) & 18 (B) GHZ]

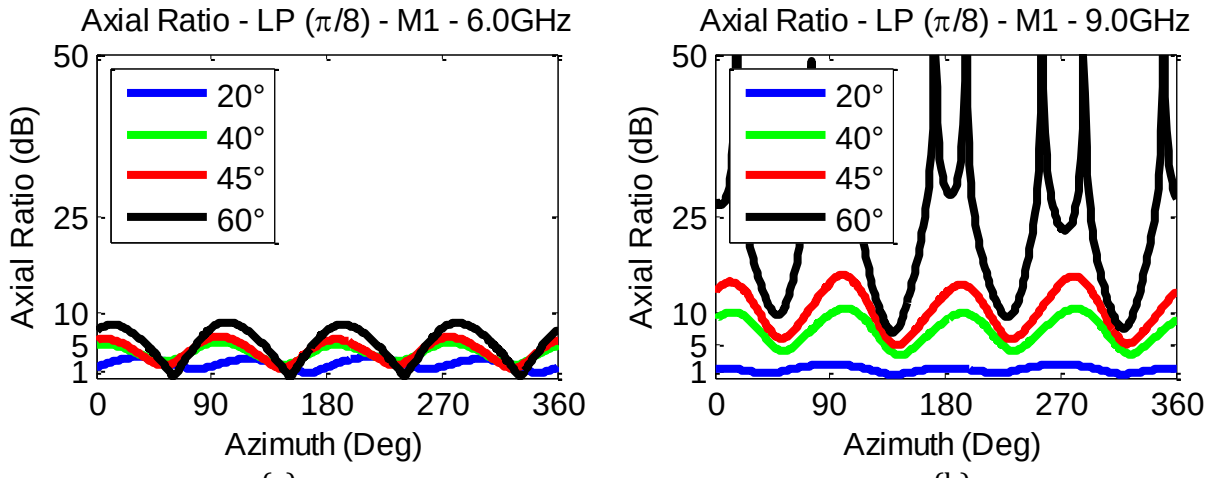

(a) (b)

FIGURE 3-75: AXIAL RATIOS – LP [Π/8] – AZ – M1 [6 (A) & 9 (B) GHZ]

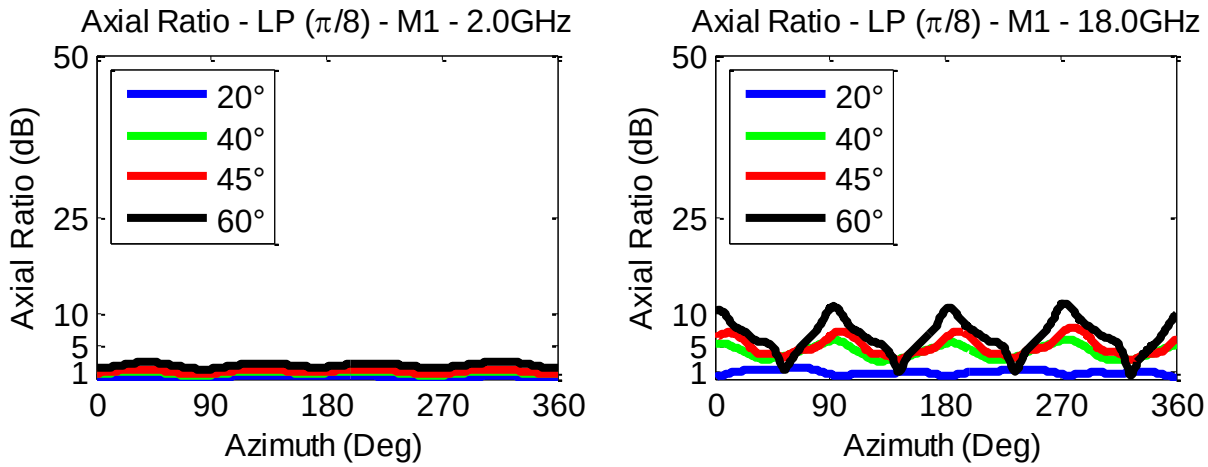

(a) (b)

FIGURE 3-76: AXIAL RATIOS – LP [Π/8] – AZ – M1 [2 (A) & 18 (B) GHZ]

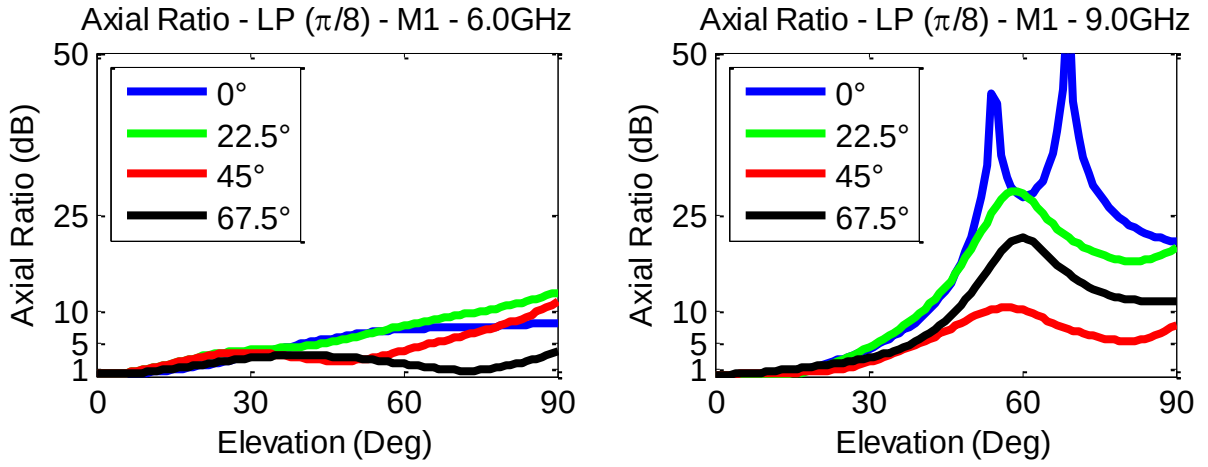

(a) (b)

FIGURE 3-77: AXIAL RATIOS – LP [Π/8] – EL – M1 [6 (A) & 9 (B) GHZ]

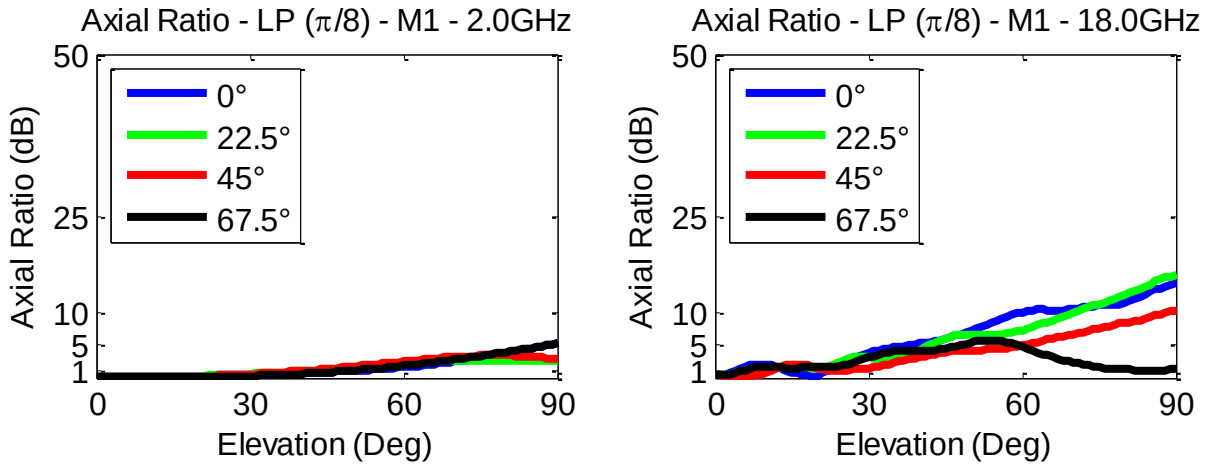

(a) (b)

FIGURE 3-78: AXIAL RATIOS – LP [Π/8] – EL – M1 [2 (A) & 18 (B) GHZ]

For the first mode of operation for the circular log-periodic with π/8-overlap, the trend for the magnitude ripple, from Figures 3-67 & 3-68, is to increase both as the frequency increases and as the elevation angle increases from boresight out to the horizon. At 2.0GHz and 20° in elevation, it has minimal ripple of ±0.02dB. While at the highest frequency of 18.0GHz and 60° in elevation, the ripple is ±1.0dB, which is again much less than it was for either spiral. For the mid-band case of 6GHz at 20° in elevation, the ripple is ±0.07dB. The magnitude of the elevation cuts, from Figures 3-71 & 3-72, show the maximum directivity at boresight, 11.8dBi at 9GHz, and the -3dB beamwidth, that extends out to 21° in elevation for the same frequency.

Similar to the magnitude ripple, the phase ripple, from Figures 3-69 & 3-70, increases with both increasing frequency and increasing elevation angle. The phase ripple is ±0.2° at 2.0GHz and 20° and for 18.0GHz at 60° the ripple is ±4.5°, which again is much lower than it was for either spiral case at this frequency. In the mid-band case, 20° of elevation at 6.0GHz, the ripple is ±0.3°. The phase of the elevation cuts, from Figures 3-73 & 3-74, are well spaced and do not overlap.

The trend for the axial ratio about azimuth, from Figures 3-75 & 3-76, is for the lowest values at boresight and increasing values toward the horizon while the ripple increases with frequency. In the mid-band at 6GHz and 20° in elevation, the average is 2.1dB and the peak is 3.1dB. There is also variation across elevation, from Figures 3-77 & 3-78, that increases from boresight toward the horizon. For 6.0GHz, the axial ratio increases from boresight toward the horizon beginning at less than 0.25dB and reaching 13.6dB. At 9.0GHz the axial ratio begins to exhibit peaks above 25dB from 45° to 75° in elevation at azimuth angles in between the elements.

Within the second mode of operation results include: the azimuth cuts' magnitude in Figures 3-79 & 3-80, the azimuth cuts' phase in Figures 3-81 & 3-82, the elevation cuts' magnitude in Figures 3-83 & 3-84, the elevation cuts' phase in Figures 3-85 & 3-86 and the axial ratio of the azimuth cuts in Figures 3-87 & 3-88 and of the elevation cuts in Figures 3-89 & 3-90.

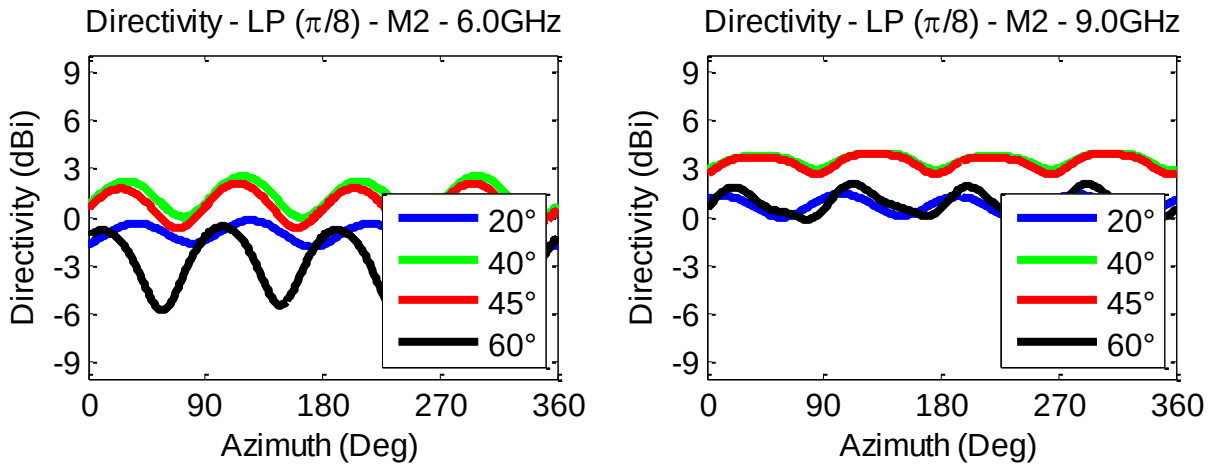

(a) (b)

FIGURE 3-79: RADIATION PATTERNS – LP [Π/8] – AZ – M2 – MAG [6 (A) & 9 (B) GHZ]

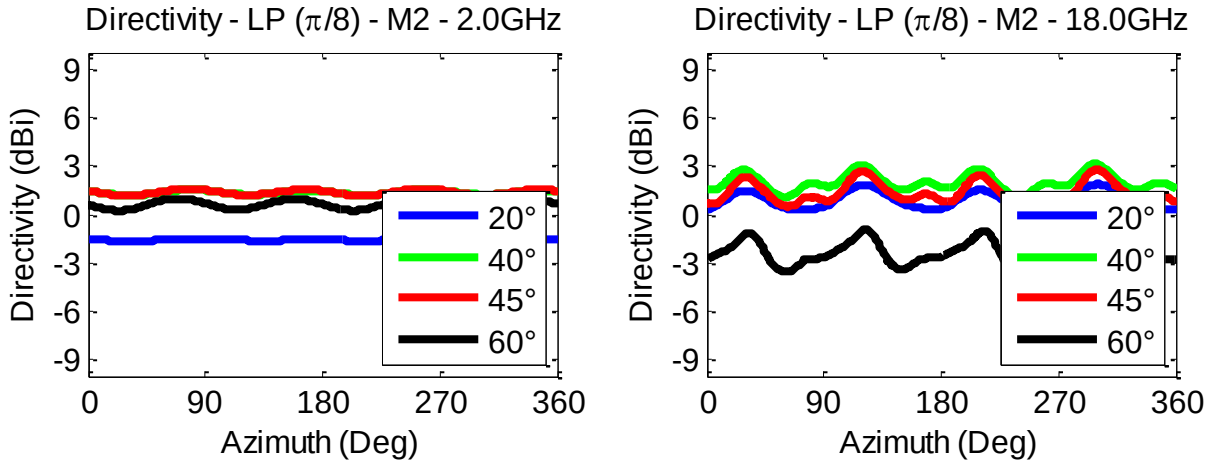

(a) (b)

FIGURE 3-80: RADIATION PATTERNS – LP [Π/8] – AZ – M2 – MAG [2 (A) & 18 (B) GHZ]

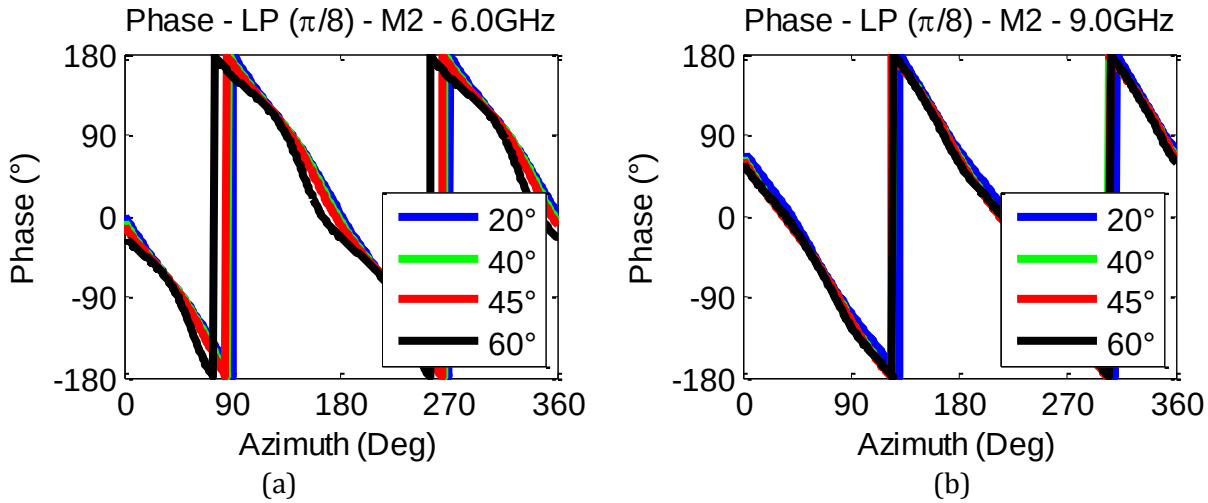

(a) (b)

FIGURE 3-81: RADIATION PATTERNS – LP [Π/8] – AZ – M2 – PHA [6 (A) & 9 (B) GHZ]

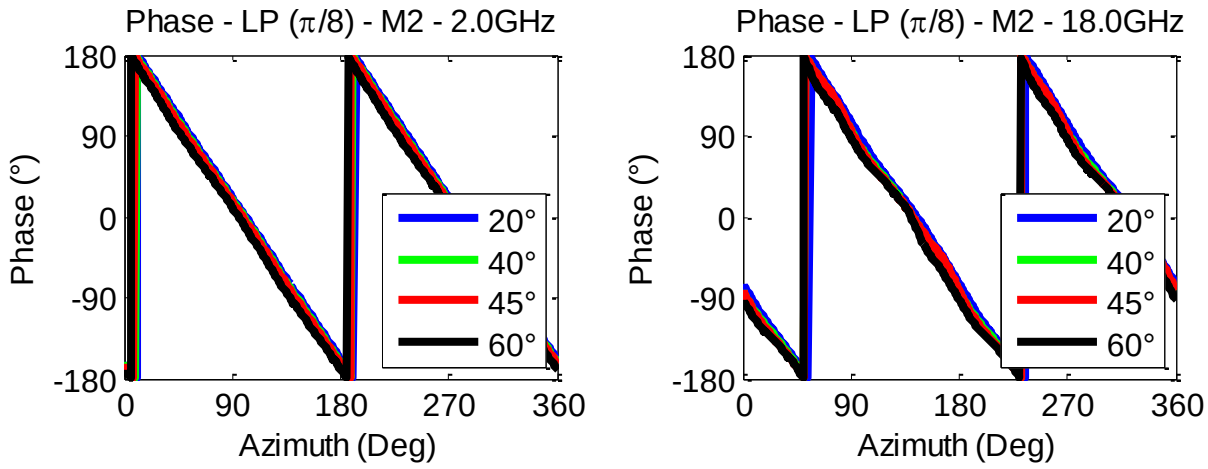

(a) (b)

FIGURE 3-82: RADIATION PATTERNS – LP [Π/8] – AZ – M2 – PHA [2 (A) & 18 (B) GHZ]

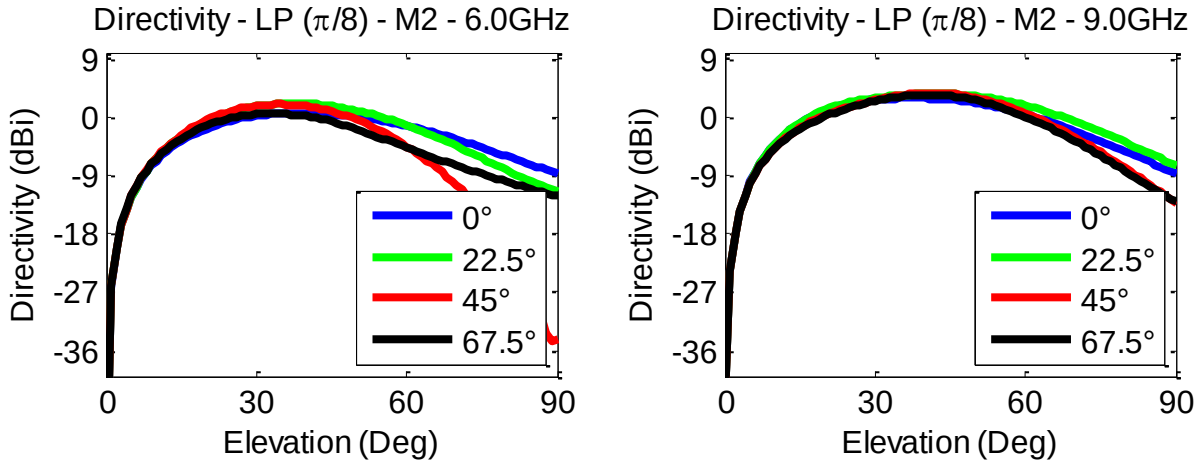

(a) (b)

FIGURE 3-83: RADIATION PATTERNS – LP [Π/8] – EL – M2 – MAG [6 (A) & 9 (B) GHZ]

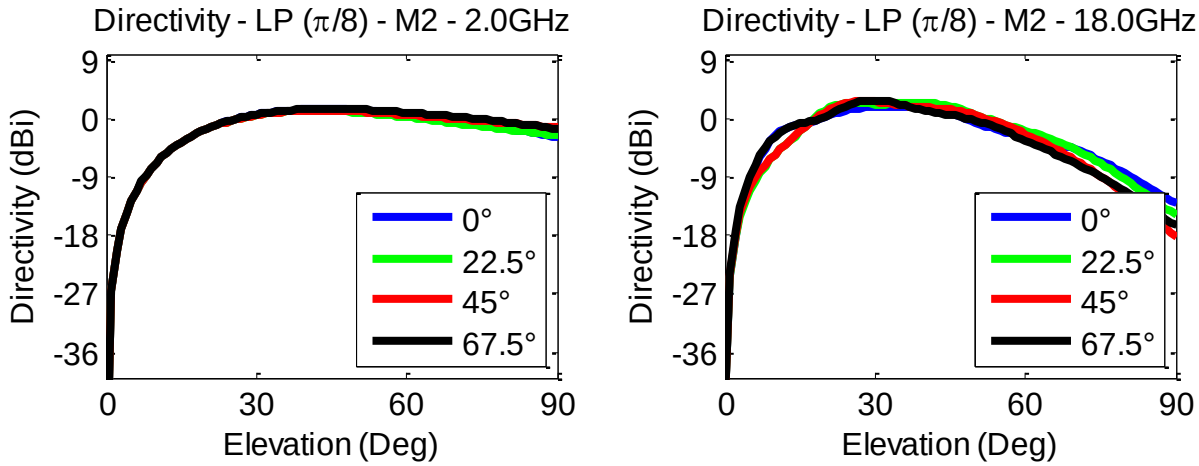

(a) (b)

FIGURE 3-84: RADIATION PATTERNS – LP [Π/8] – EL – M2 – MAG [2 (A) & 18 (B) GHZ]

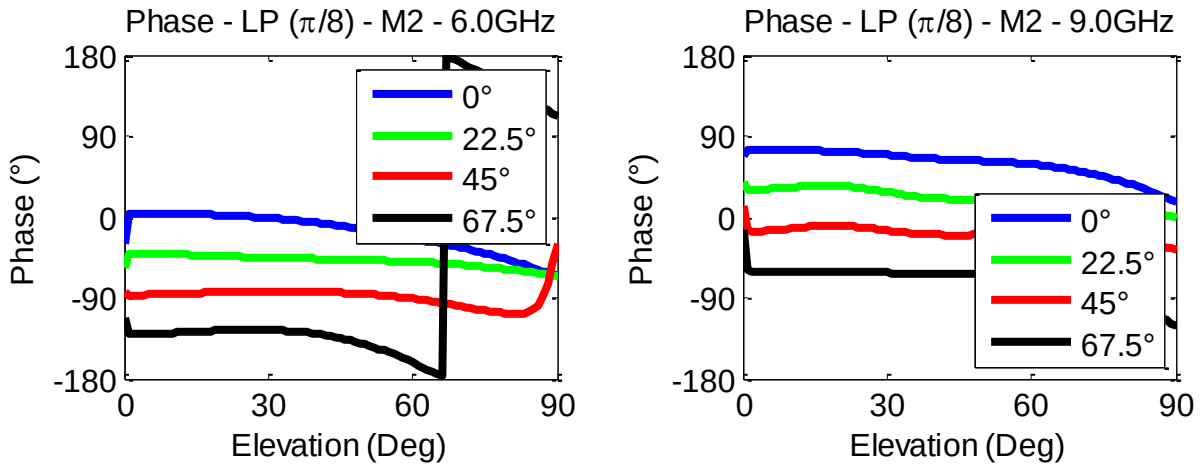

(a) (b)

FIGURE 3-85: RADIATION PATTERNS – LP [Π/8] – EL – M2 – PHA [6 (A) & 9 (B) GHZ]

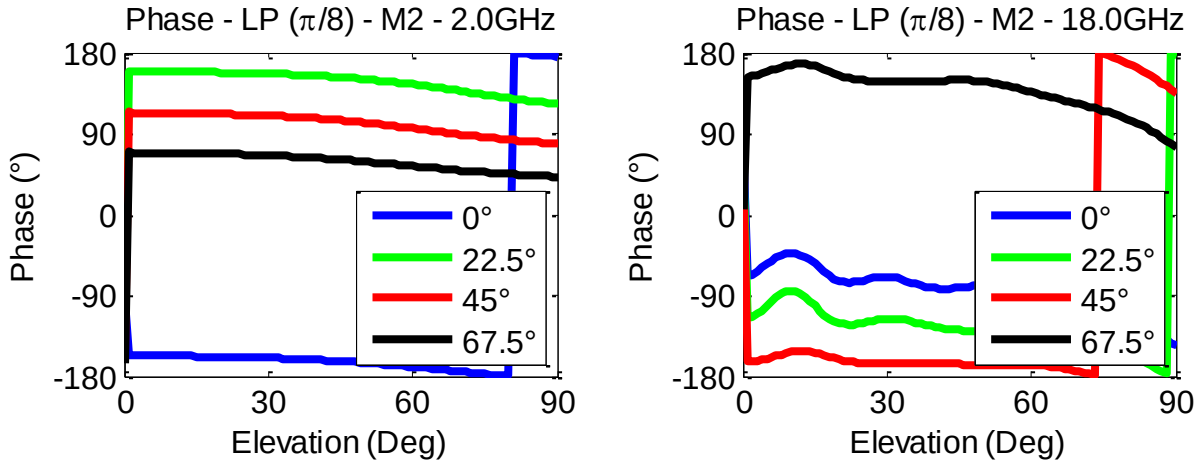

(a) (b)

FIGURE 3-86: RADIATION PATTERNS – LP [Π/8] – EL – M2 – PHA [2 (A) & 18 (B) GHZ]

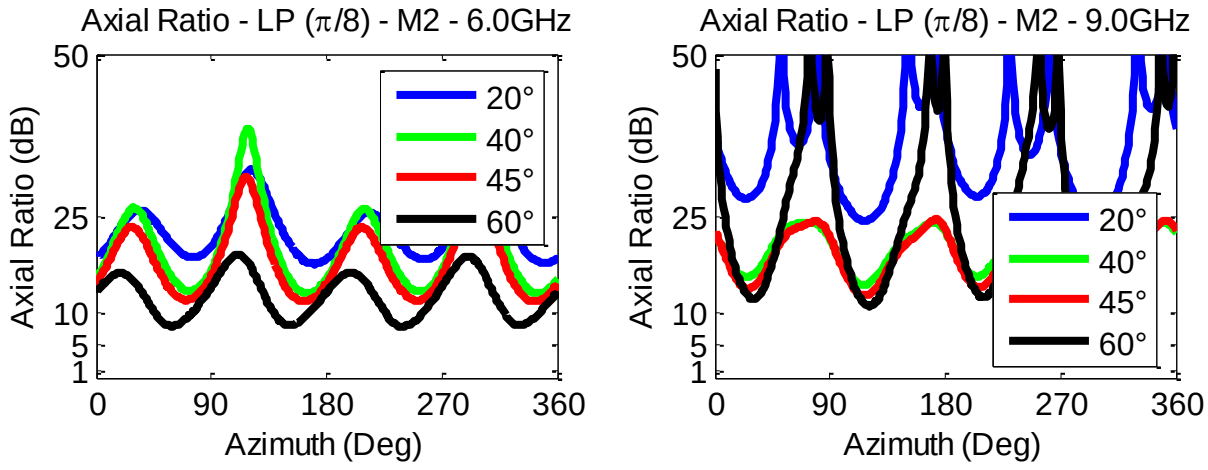

(a) (b)

FIGURE 3-87: AXIAL RATIOS – LP [Π/8] – AZ – M2 [6 (A) & 9 (B) GHZ]

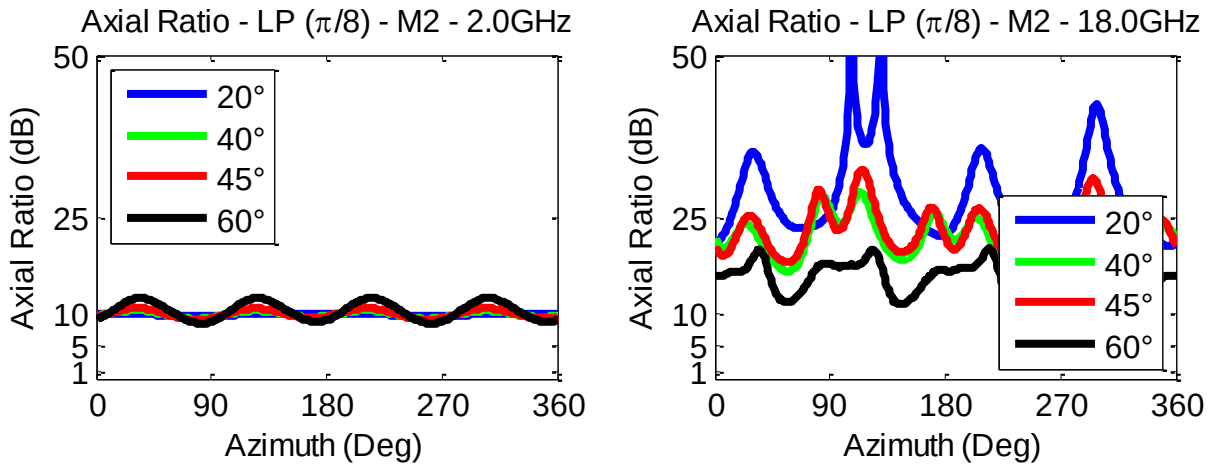

(a) (b)

FIGURE 3-88: AXIAL RATIOS – LP [Π/8] – AZ – M2 [2 (A) & 18 (B) GHZ]

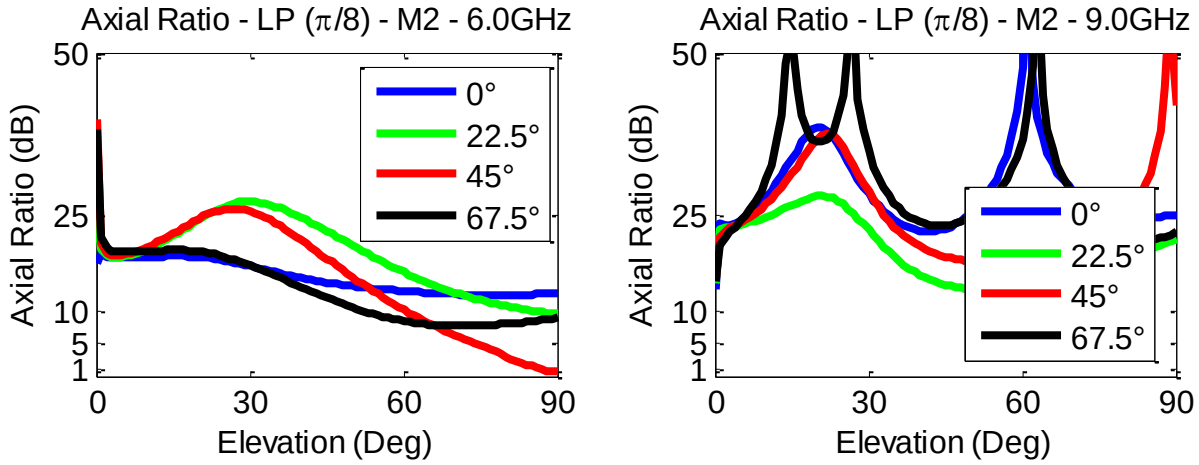

(a) (b)

FIGURE 3-89: AXIAL RATIOS – LP [Π/8] – EL – M2 [6 (A) & 9 (B) GHZ]

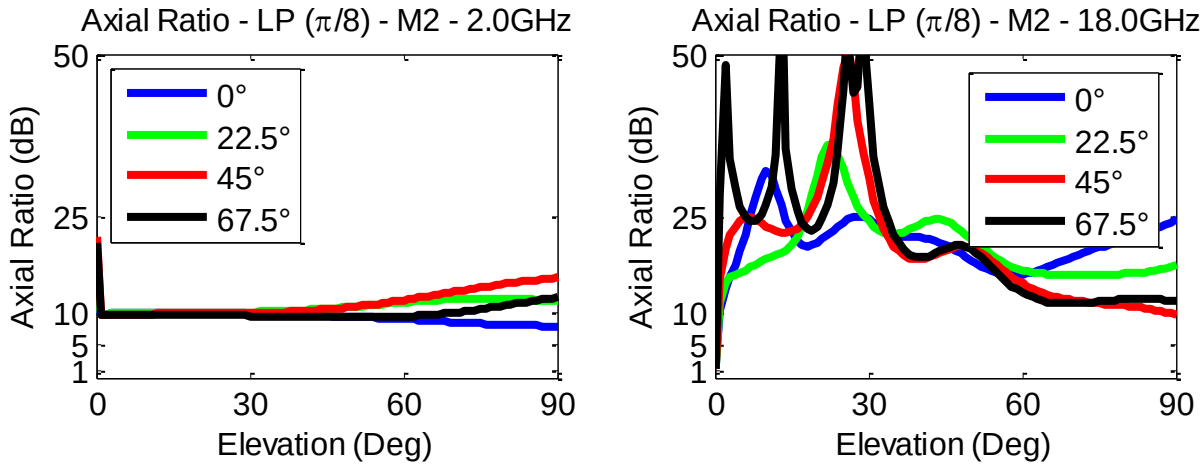

(a) (b)

FIGURE 3-90: AXIAL RATIOS – LP [Π/8] – EL – M2 [2 (A) & 18 (B) GHZ]

For the second mode for the circular log-periodic with π/8-overlap, the ripple of the magnitude of the azimuth cuts, from Figures 3-79 & 3-80, increases as the elevation angle increases, but not necessarily as the frequency increases. At 2.0GHz, the log-periodic has minimal ripple of ±0.2dB at 40° in elevation, while at 18.0GHz and 60° in elevation, the ripple is ±1.25 dB. For 6.0GHz and 40° in elevation, the ripple is ±1.3 dB which is actually more than the higher frequency case. The magnitude of the elevation cuts, from Figures 3-83 & 3-84, show the peak directivity angle and the -3dB beamwidth. The maximum directivity of 4.0dBi for 9.0GHz occurs at 42° in elevation and the -3dB beamwidth extends from 22° to 60°.

The phase ripple about azimuth, from Figures 3-81 & 3-82, again increases with elevation angle. The ripple is ±1.1° at 2.0GHz and 40° in elevation, ±9.0° at 18.0GHz and 60° and in the mid-band is ±8.5° for 6.0GHz and 40° in elevation. The phase of the elevation cuts, from Figures 3-85 & 3-86, are acceptable and an overlap occurs above 80° in elevation for the 6.0GHz case.

There is no trend for the axial ratio in the second mode of operation, from Figures 3-87 & 3-88. There is significant variation about azimuth and for 6.0GHz and 40° in elevation where the average is 20dB but the peak is 39dB. There is also significant variation across elevation, from Figures 3-65 & 3-66. At the mid-band frequency of 6.0GHz the values show less variation than for the higher frequencies and begin around 20dB, peak up to 30dB for the elevation angles selected and slope down to about 10dB at the horizon. The peak axial ratio in the forward hemisphere is 75dB.

3.2.2.4 CIRCULAR LOG-PERIODIC [Π/12]

For the circular log-periodic with π/12-overlap, feed points are located at azimuth angles of 45°, 135°, 225° and 315°. Within the first mode of operation results include: the azimuth cuts' magnitude in Figures 3-91 & 3-92, the azimuth cuts' phase in Figures 3-93 & 3-94, the elevation cuts' magnitude in Figures 3-95 & 3-96, the elevation cuts' phase in Figures 3-97 & 3-98 and the axial ratio of the azimuth cuts in Figures 3-99 & 3-100 and of the elevation cuts in Figures 3-101 & 3-102.

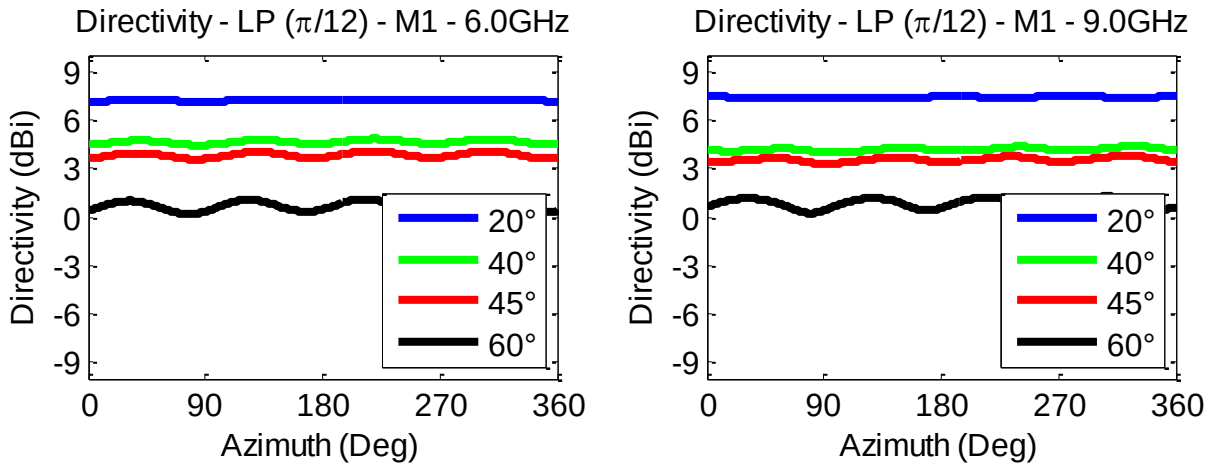

(a) (b)

FIGURE 3-91: RADIATION PATTERNS – LP [Π/12] – AZ – M1 – MAG [6 (A) & 9 (B) GHZ]

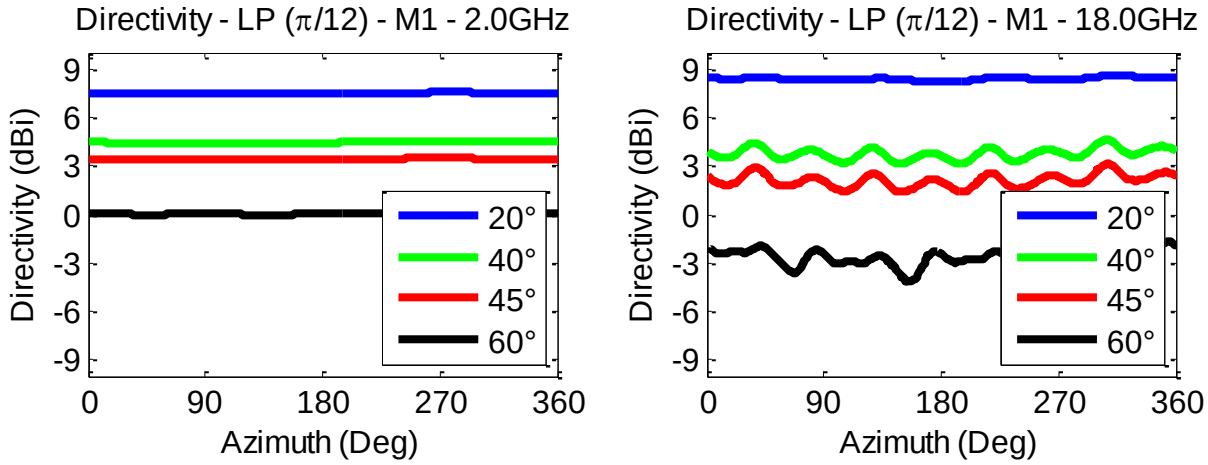

(a) (b)

FIGURE 3-92: RADIATION PATTERNS – LP [Π/12] – AZ – M1 – MAG [2 (A) & 18 (B) GHZ]

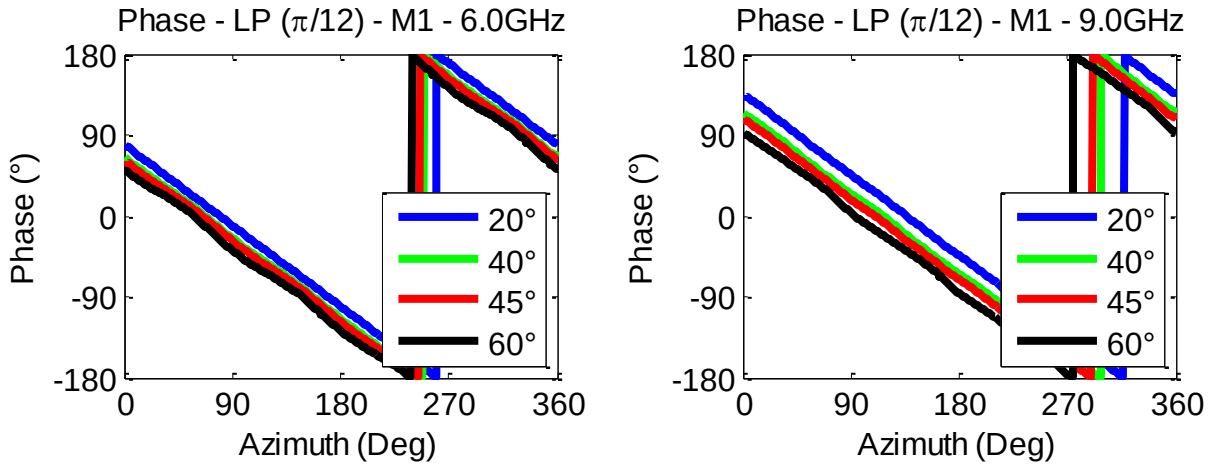

(a) (b)

FIGURE 3-93: RADIATION PATTERNS – LP [Π/12] – AZ – M1 – PHA [6 (A) & 9 (B) GHZ]

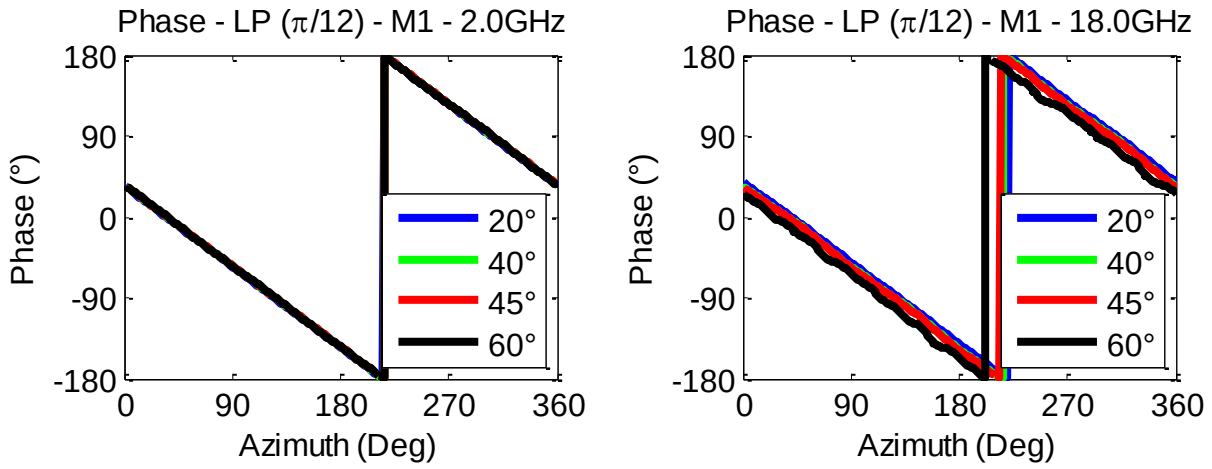

(a) (b)

FIGURE 3-94: RADIATION PATTERNS – LP [Π/12] – AZ – M1 – PHA [2 (A) & 18 (B) GHZ]

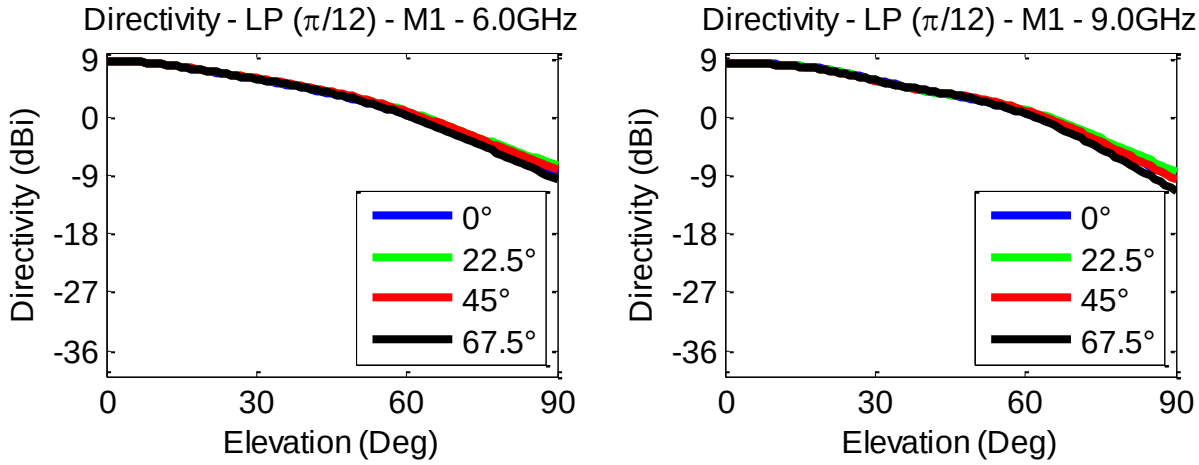

(a) (b)

FIGURE 3-95: RADIATION PATTERNS – LP [Π/12] – EL – M1 – MAG [6 (A) & 9 (B) GHZ]

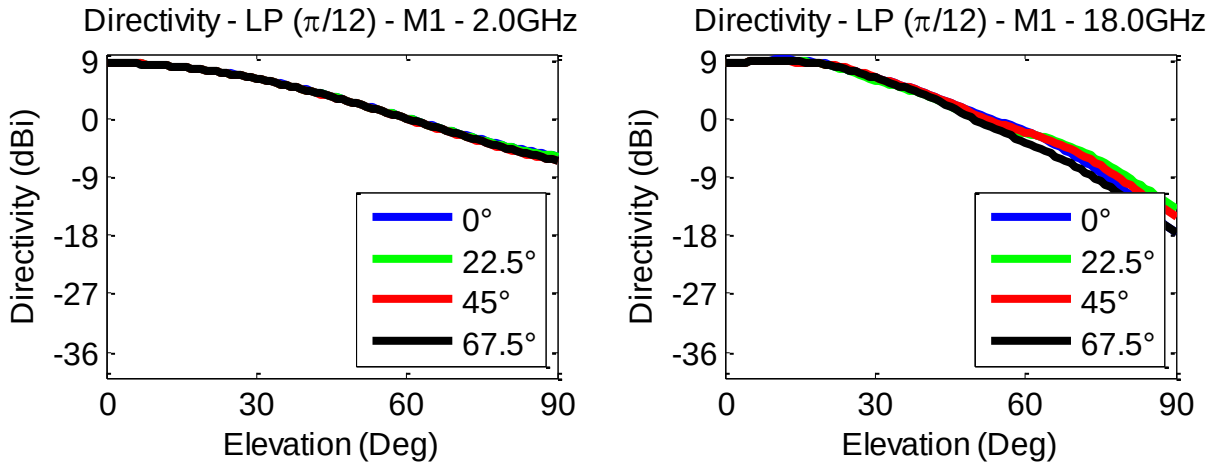

(a) (b)

FIGURE 3-96: RADIATION PATTERNS – LP [Π/12] – EL – M1 – MAG [2 (A) & 18 (B) GHZ]

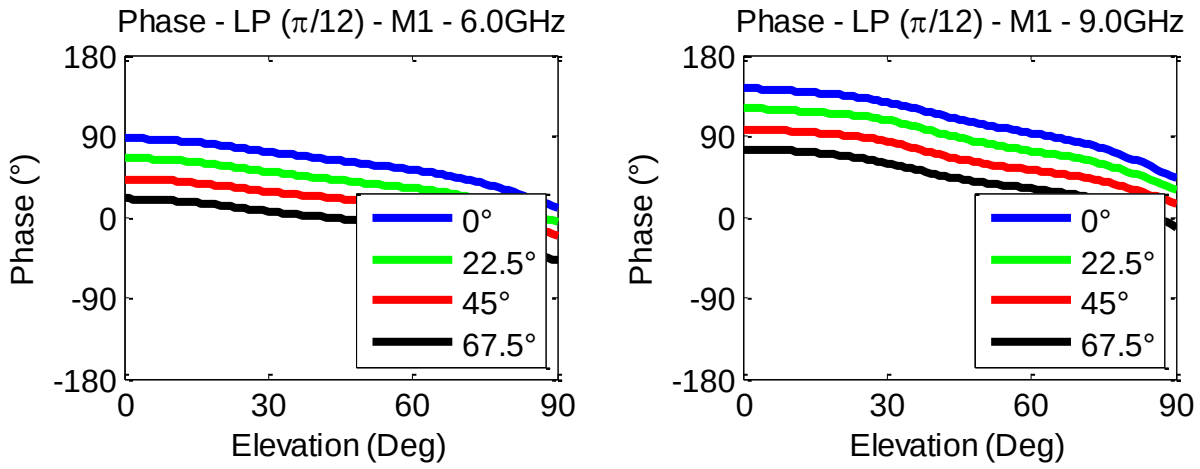

(a) (b)

FIGURE 3-97: RADIATION PATTERNS – LP [Π/12] – EL – M1 – PHA [6 (A) & 9 (B) GHZ]

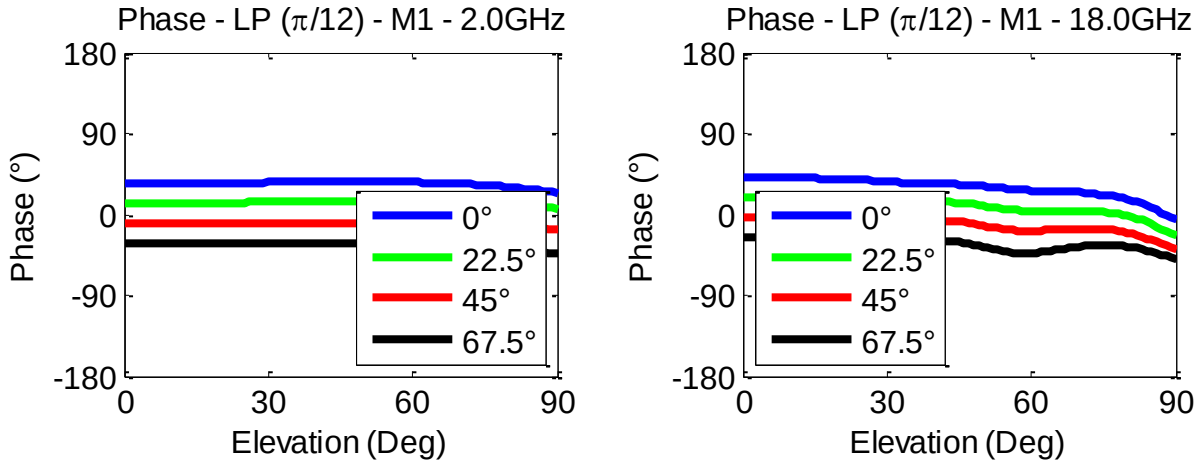

(a) (b)

FIGURE 3-98: RADIATION PATTERNS – LP [Π/12] – EL – M1 – PHA [2 (A) & 18 (B) GHZ]

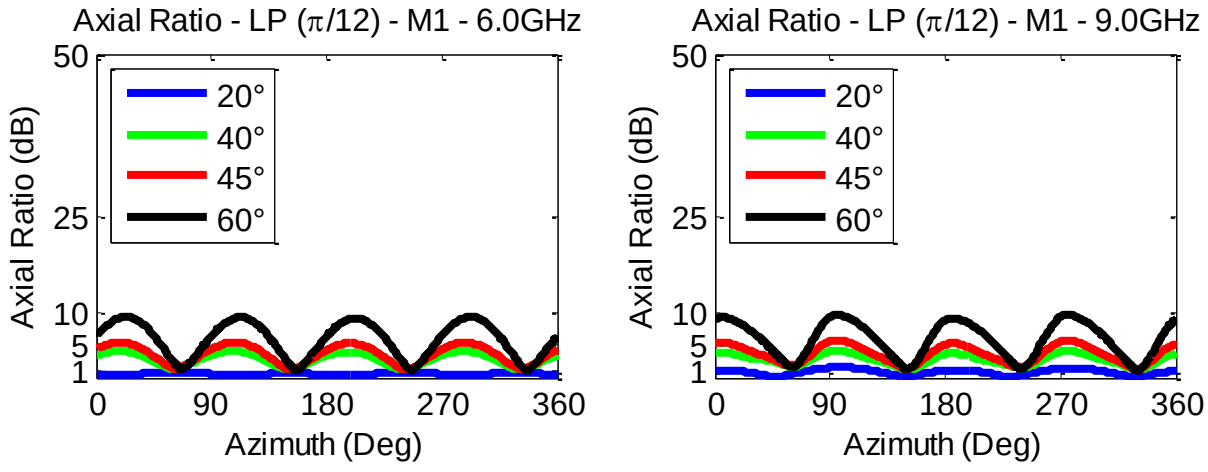

(a) (b)

FIGURE 3-99: AXIAL RATIOS – LP [Π/12] – AZ – M1 [6 (A) & 9 (B) GHZ]

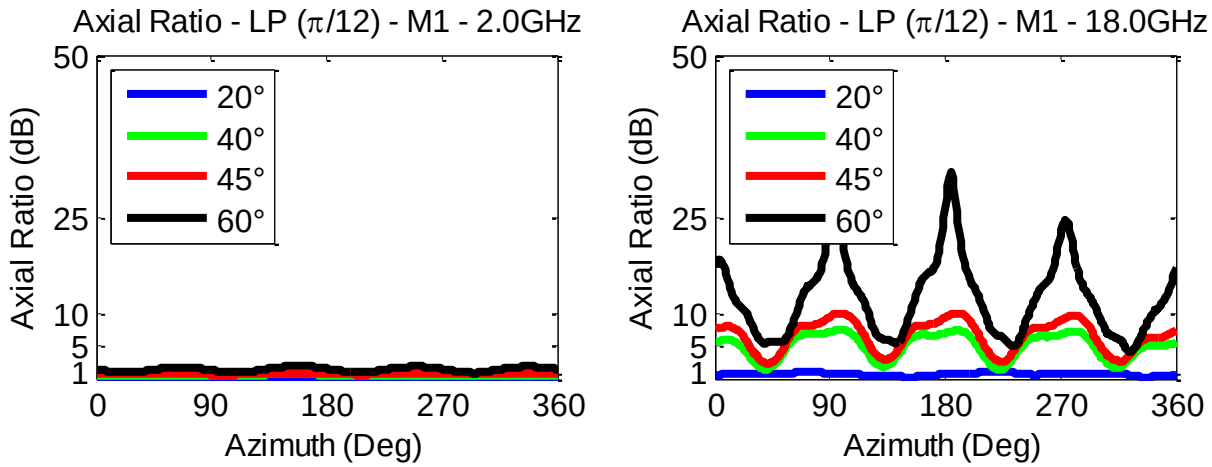

(a) (b)

FIGURE 3-100: AXIAL RATIOS – LP [Π/12] – AZ – M1 [2 (A) & 18 (B) GHZ]

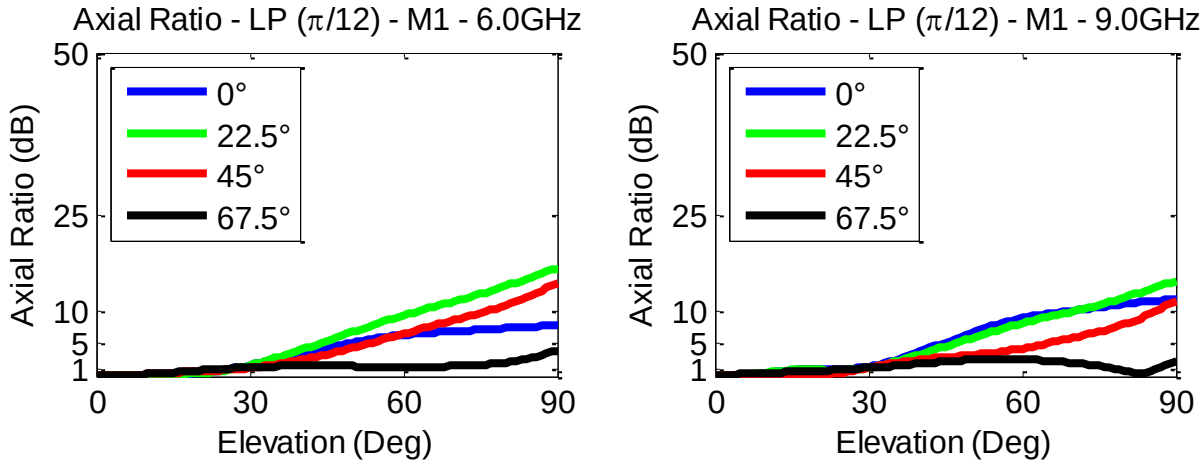

(a) (b)

FIGURE 3-101: AXIAL RATIOS – LP [Π/12] – EL – M1 [6 (A) & 9 (B) GHZ]

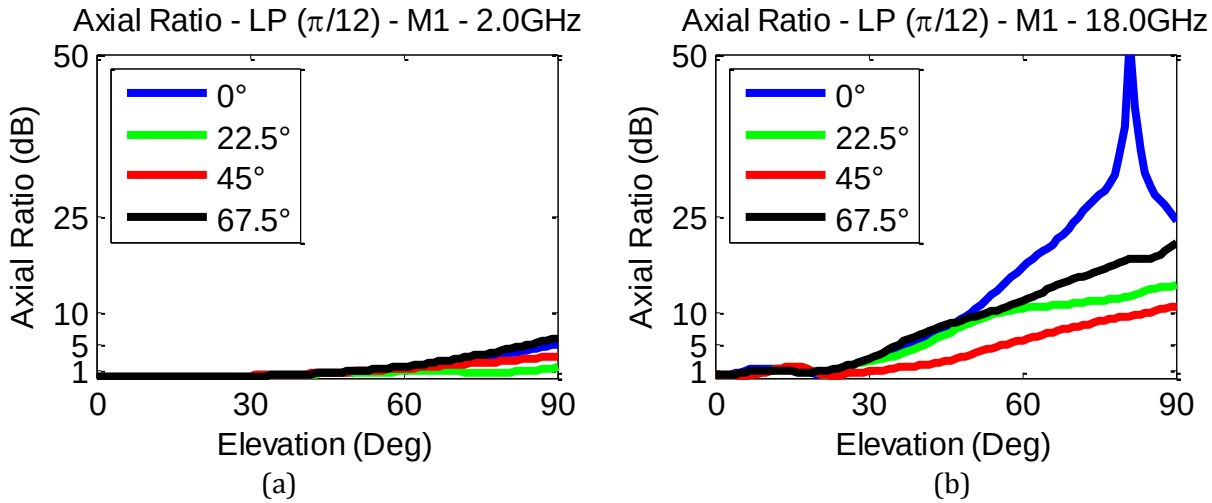

(a) (b)

FIGURE 3-102: AXIAL RATIOS – LP [Π/12] – EL – M1 [2 (A) & 18 (B) GHZ]

For the first mode of operation for the circular log-periodic with π/12-overlap, the trend for the magnitude ripple, from Figures 3-91 & 3-92, to increase both as the frequency increases and as the elevation angle increases from boresight out to the horizon. At the lowest frequency of 2.0GHz and 20° in elevation, it shows minimal ripple of ±0.02dB. While at the highest frequency of 18.0GHz and 60° in elevation, the ripple is ±1.25dB. The ripple at the highest frequency is much less than it was for either spiral. The mid-band case of 6GHz at 40° in elevation, the ripple is ±0.05dB. The magnitude of the elevation cuts, from Figures 3-95 & 3-96, show the maximum directivity at boresight, 8.3dBi at 9GHz, and the -3dB beamwidth, that extends out to 33° in elevation for the same frequency.

Similar to the magnitude ripple, the phase ripple, from Figures 3-93 & 3-94, increases with both increasing frequency and increasing elevation angle. The phase ripple is ±0.1° at 2.0GHz and 20° in elevation and for 18.0GHz at 60° the ripple is ±5.5°, which again is much lower than it was for either spiral case at this frequency. In the mid-band case, 20° of elevation at 6.0GHz at 20° in elevation, the ripple is ±0.3°. The phase of the elevation cuts, from Figures 3-97 & 3-98, are well spaced and do not overlap.

The trend for the axial ratio about azimuth, from Figures 3-99 & 3-100, is for the lowest values at boresight and increasing values toward the horizon while the ripple increases with frequency. In the mid-band at 6GHz and 20° in elevation, the average is 0.6dB and the peak is 0.9dB. There is also variation across elevation, from Figures 3-101 & 3-102, that increases from boresight toward the horizon. For 6.0GHz, the axial ratio increases from boresight toward the horizon beginning at less than 0.01dB and reaching 17.5dB. At 18.0GHz the axial ratio exhibits peaks above 50dB above 75° in elevation at azimuth angles in between the elements.

Within the second mode of operation results include: the azimuth cuts' magnitude in Figures 3-103 & 3-104, the azimuth cuts' phase in Figures 3-105 & 3-106, the elevation cuts' magnitude in Figures 3-107 & 3-108, the elevation cuts' phase in Figures 3-109 & 3-110 and the axial ratio of the azimuth cuts in Figures 3-111 & 3-112 and of the elevation cuts in Figures 3-113 & 3-114.

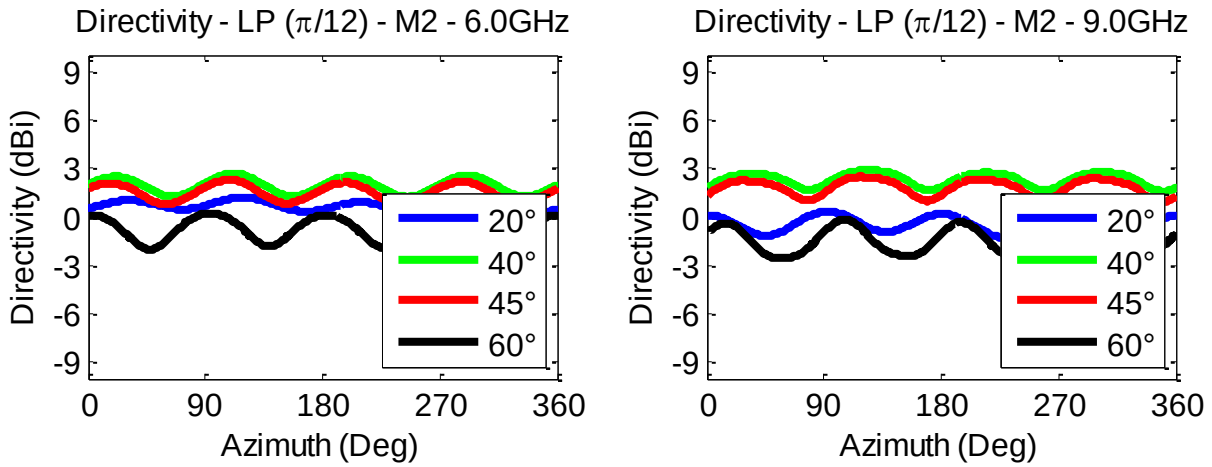

(a) (b)

FIGURE 3-103: RADIATION PATTERNS – LP [Π/12] – AZ – M2 – MAG [6 (A) & 9 (B) GHZ]

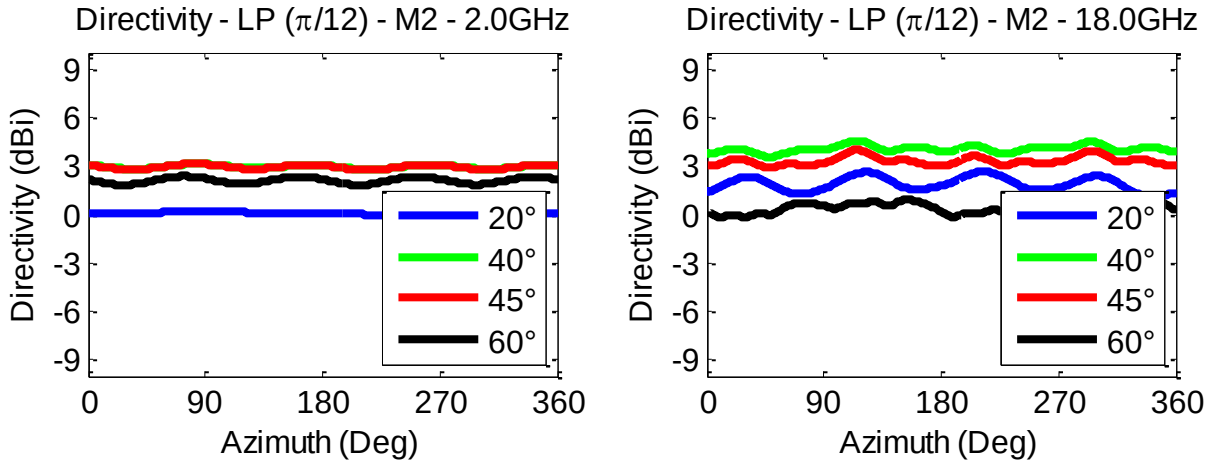

(a) (b)

FIGURE 3-104: RADIATION PATTERNS – LP [Π/12] – AZ – M2 – MAG [2 (A) & 18 (B) GHZ]

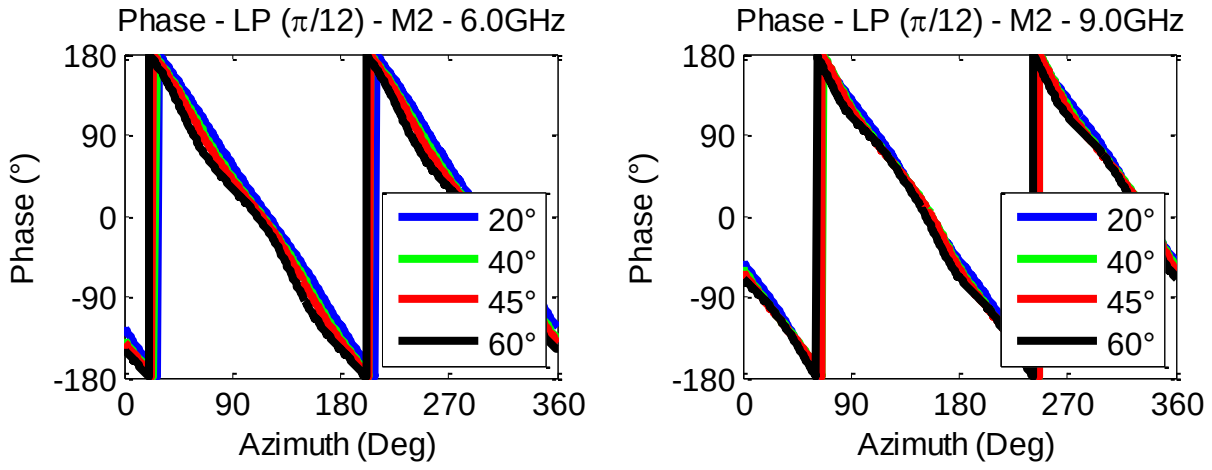

(a) (b)

FIGURE 3-105: RADIATION PATTERNS – LP [Π/12] – AZ – M2 – PHA [6 (A) & 9 (B) GHZ]

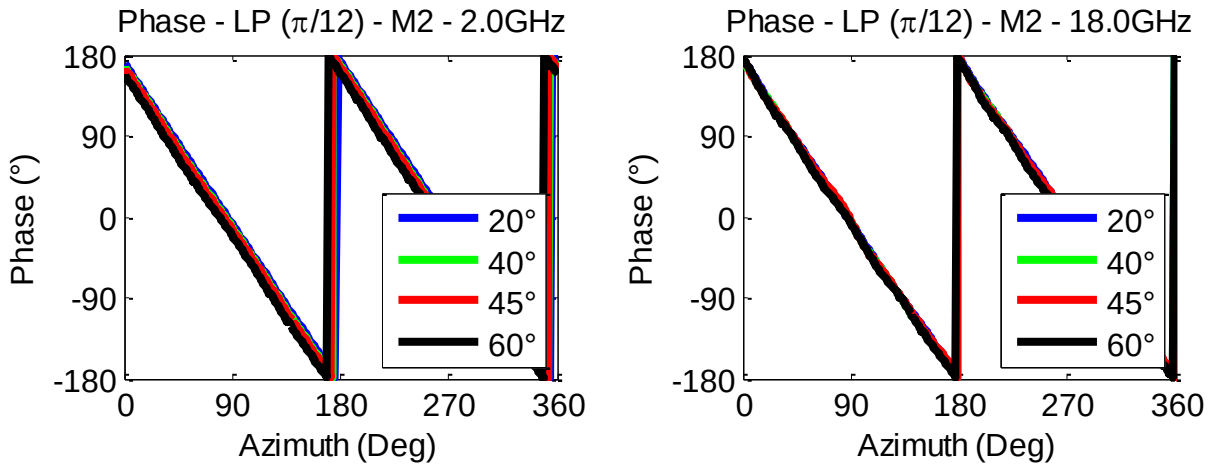

FIGURE 3-106: RADIATION PATTERNS – LP [Π/12] – AZ – M2 – PHA [2 (A) & 18 (B) GHZ]

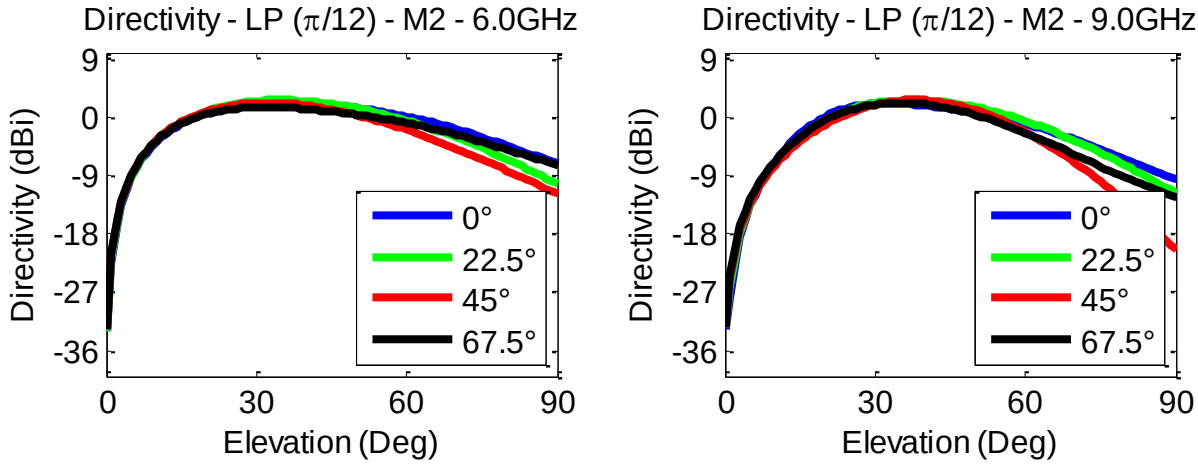

FIGURE 3-107: RADIATION PATTERNS – LP [Π/12] – EL – M2 – MAG [6 (A) & 9 (B) GHZ]

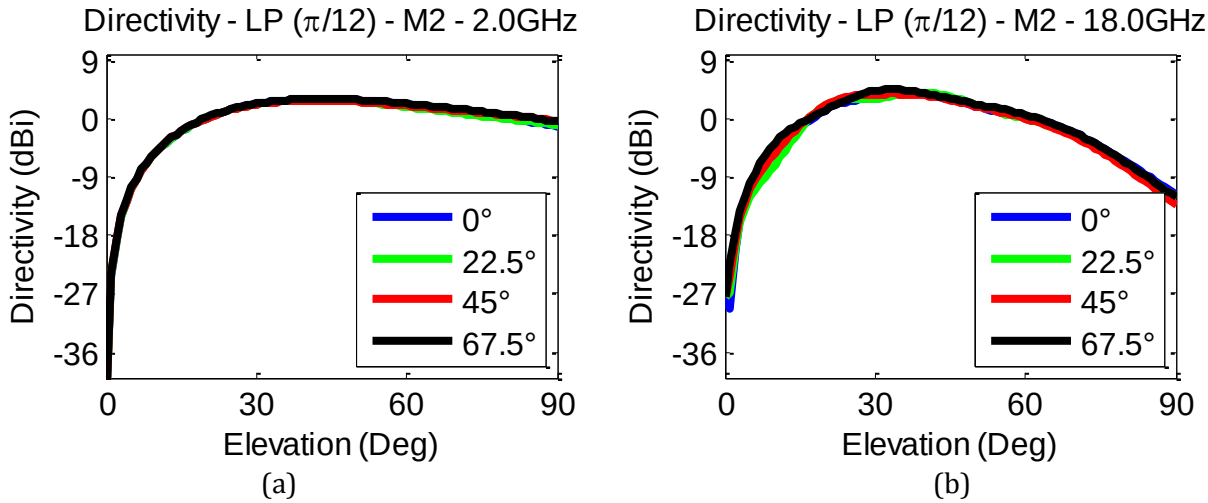

FIGURE 3-108: RADIATION PATTERNS – LP [Π/12] – EL – M2 – MAG [2 (A) & 18 (B) GHZ]

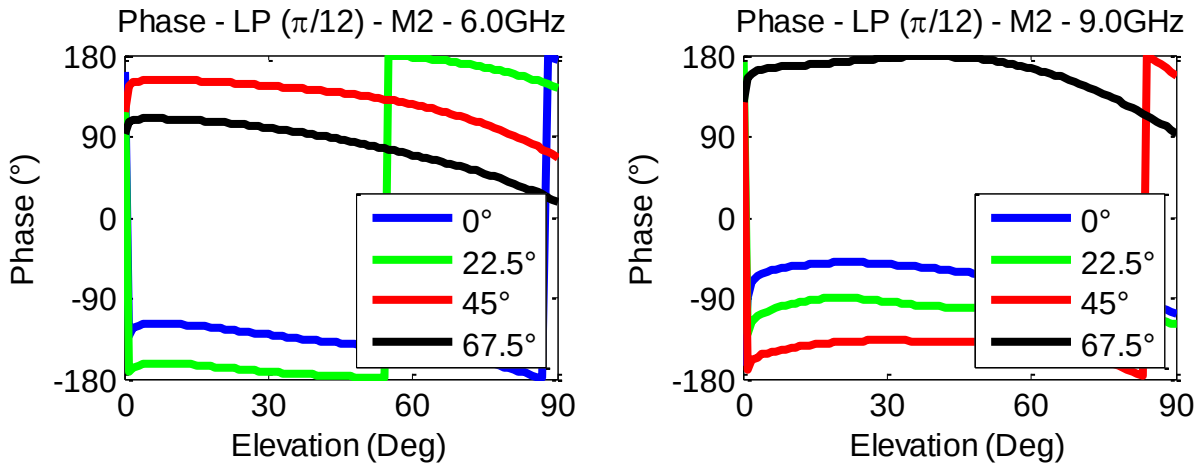

FIGURE 3-109: RADIATION PATTERNS – LP [Π/12] – EL – M2 – PHA [6 (A) & 9 (B) GHZ]

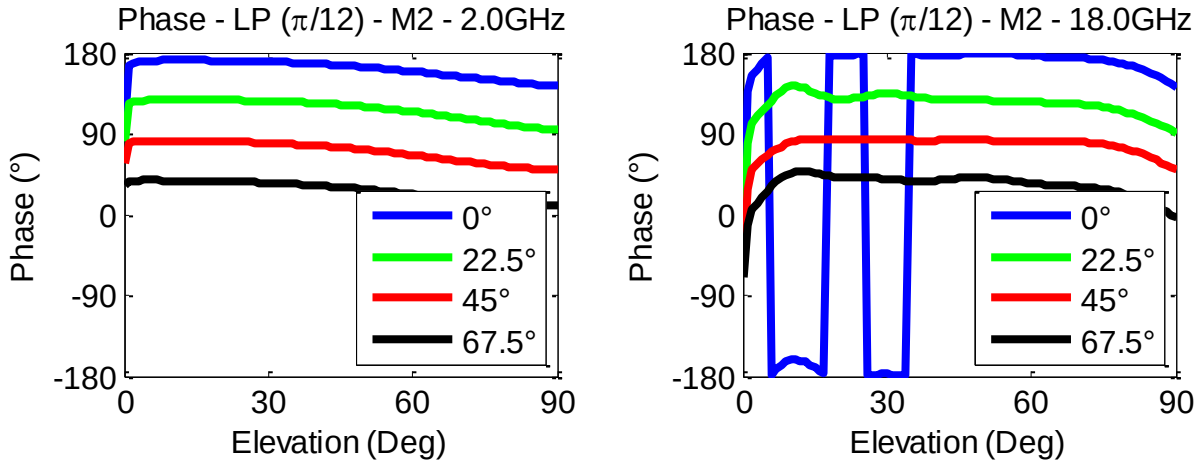

FIGURE 3-110: RADIATION PATTERNS – LP [Π/12] – EL – M2 – PHA [2 (A) & 18 (B) GHZ]

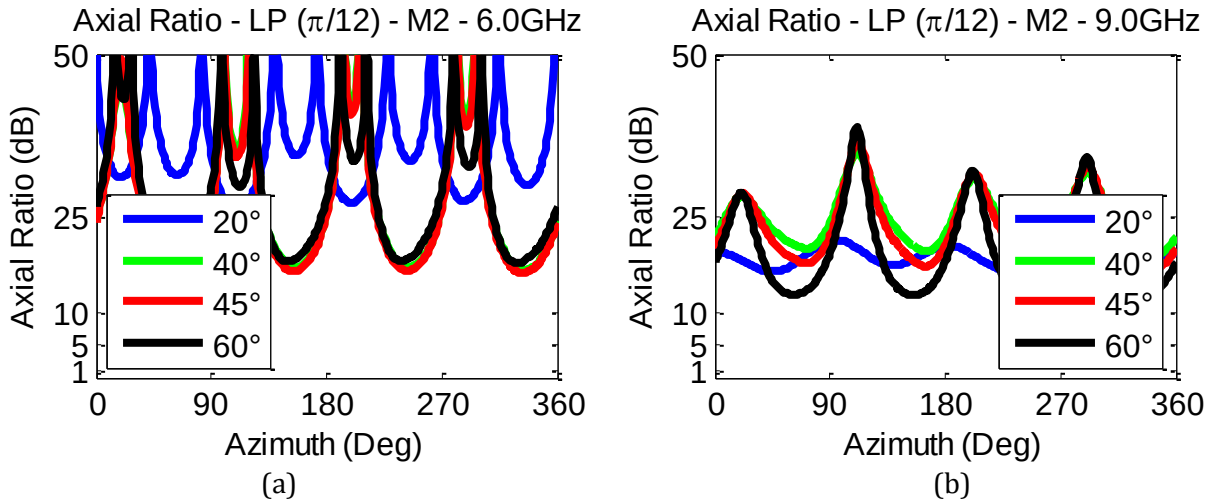

FIGURE 3-111: AXIAL RATIOS – LP [Π/12] – AZ – M2 [6 (A) & 9 (B) GHZ]

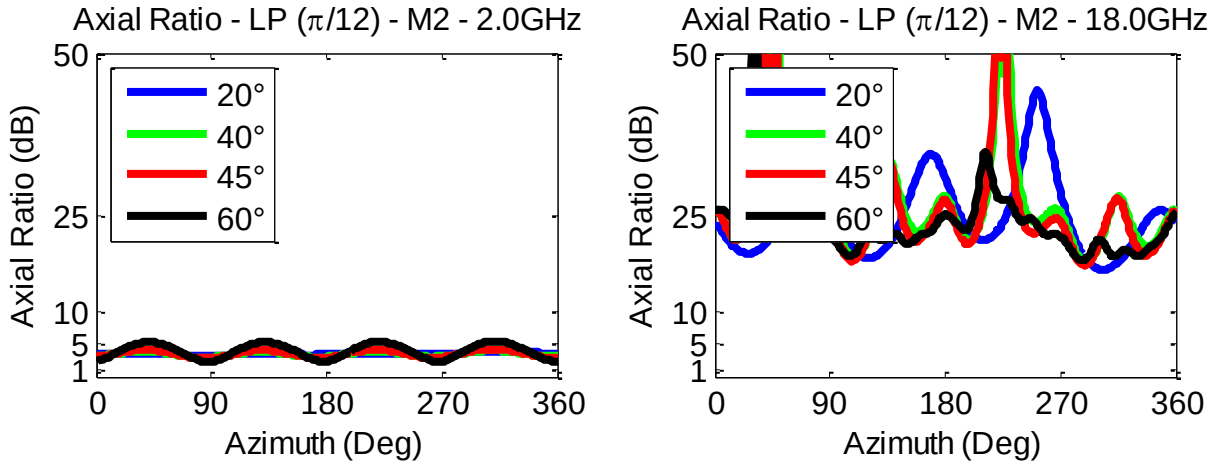

(a) (b)

FIGURE 3-112: AXIAL RATIOS – LP [Π/12] – AZ – M2 [2 (A) & 18 (B) GHZ]

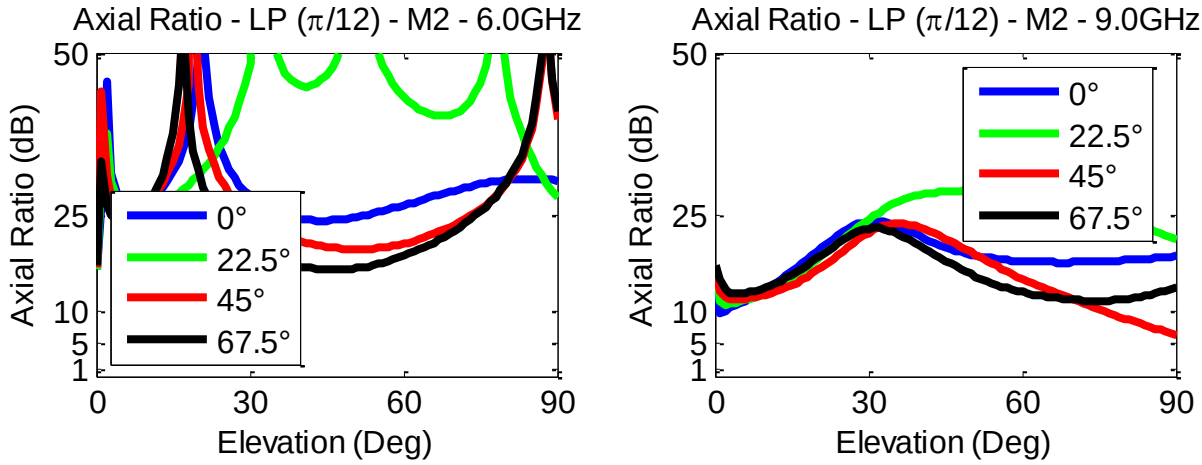

(a) (b)

FIGURE 3-113: AXIAL RATIOS – LP [Π/12] – EL – M2 [6 (A) & 9 (B) GHZ]

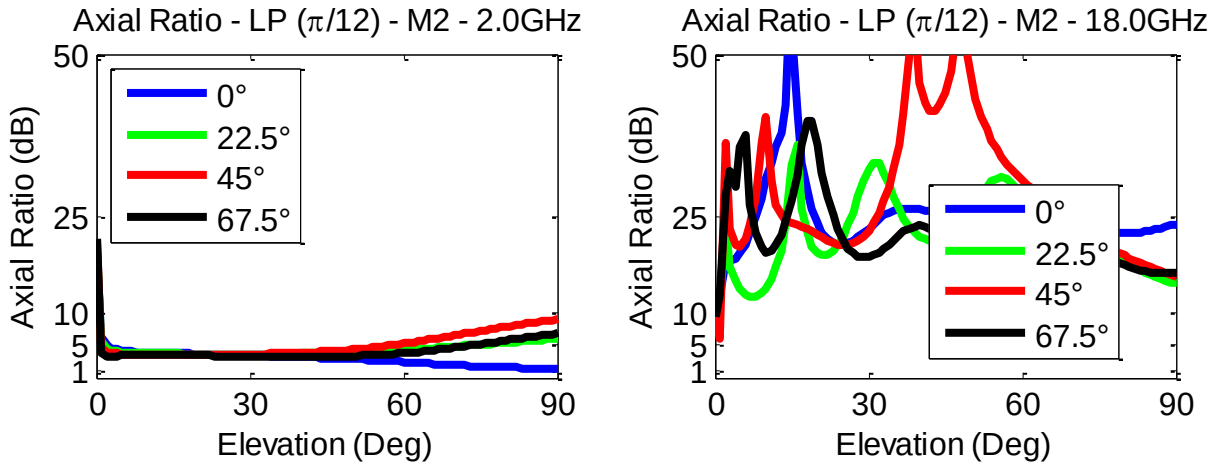

(a) (b)

FIGURE 3-114: AXIAL RATIOS – LP [Π/12] – EL – M2 [2 (A) & 18 (B) GHZ]

For the second mode for the circular log-periodic with π/8-overlap, the ripple of the magnitude of the azimuth cuts, from Figures 3-103 & 3-104, increases as the elevation angle increases. At 2.0GHz and 40° in elevation, the log-periodic has minimal ripple of ±0.2dB, while at 18.0GHz and 60° in elevation, the ripple is ±0.75dB. For 6.0GHz and 40° in elevation, the ripple is ±0.7dB which is actually more than the higher frequency case. The magnitude of the elevation cuts, from Figures 3-107 & 3-108, show the peak directivity angle and the -3dB beamwidth. The maximum directivity of 2.9dBi for 9.0GHz occurs at 38° in elevation and the -3dB beamwidth extends from 22° to 56°.

The phase ripple about azimuth, from Figures 3-105 & 3-106, again increases with elevation angle. The ripple is ±1.1° at 2.0GHz and 40° in elevation, ±4.5° at 18.0GHz and 60° and in the mid-band it is the worst at ±5.5° for 6.0GHz and 40° in elevation. The phase of the elevation cuts, from Figures 3-109 & 3-110, are acceptable and no overlaps occur.

There is no trend for the axial ratios in the second mode of operation, Figures 3-111 & 3-112. There is significant variation about azimuth and for 6.0GHz and 40° in elevation where the average is 28dB but the peak is 78dB. There is also significant variation across elevation, from Figures 3-113 & 3-114. At the mid-band frequency of 6.0GHz the values show less variation than for the higher frequencies and begin around 25dB and peak well above 50dB with no noticeable trend toward the horizon. The peak axial ratio in the forward hemisphere is 132dB.

3.2.2.5 CIRCULAR SINUOUS [Π/4]

For the circular sinuous with π/4-interleave, feed points are located at azimuth angles of 22°, 112°, 202° and 292°. The elements wrap back-and-forth and are centered about 0°, 90°, 180° and 270°. Within the first mode of operation results include: the azimuth cuts' magnitude in Figures 3-115 & 3-116, the azimuth cuts' phase in Figures 3-117 & 3-118, the elevation cuts' magnitude in Figures 3-119 & 3-120, the elevation cuts' phase in Figures 3-121 & 3-122 and the axial ratio of the azimuth cuts in Figures 3-123 & 3-124 and of the elevation cuts in Figures 3-125 & 3-126.

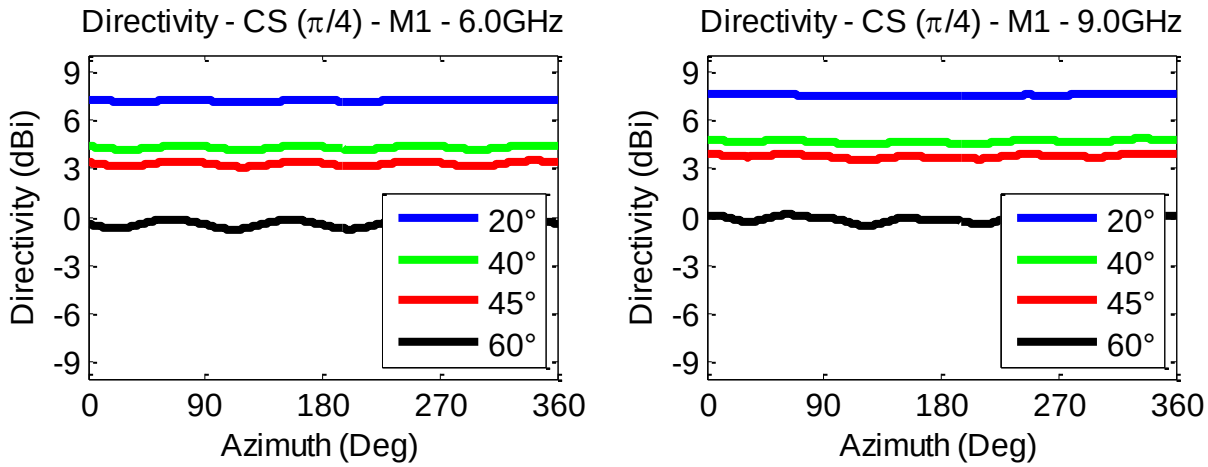

(a) (b)

FIGURE 3-115: RADIATION PATTERNS – CS [Π/4] – AZ – M1 – MAG [6 (A) & 9 (B) GHZ]

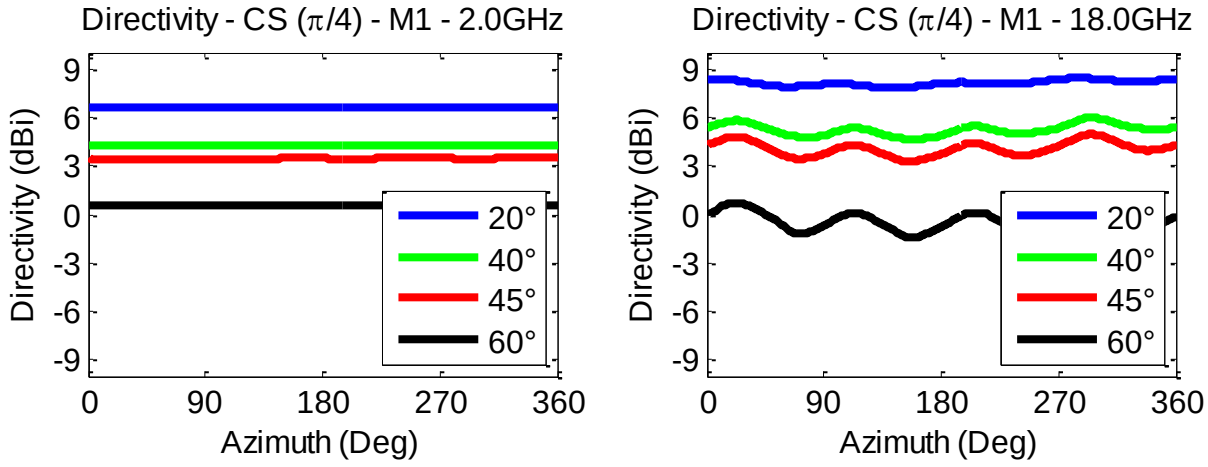

(a) (b)

FIGURE 3-116: RADIATION PATTERNS – CS [Π/4] – AZ – M1 – MAG [2 (A) & 18 (B) GHZ]

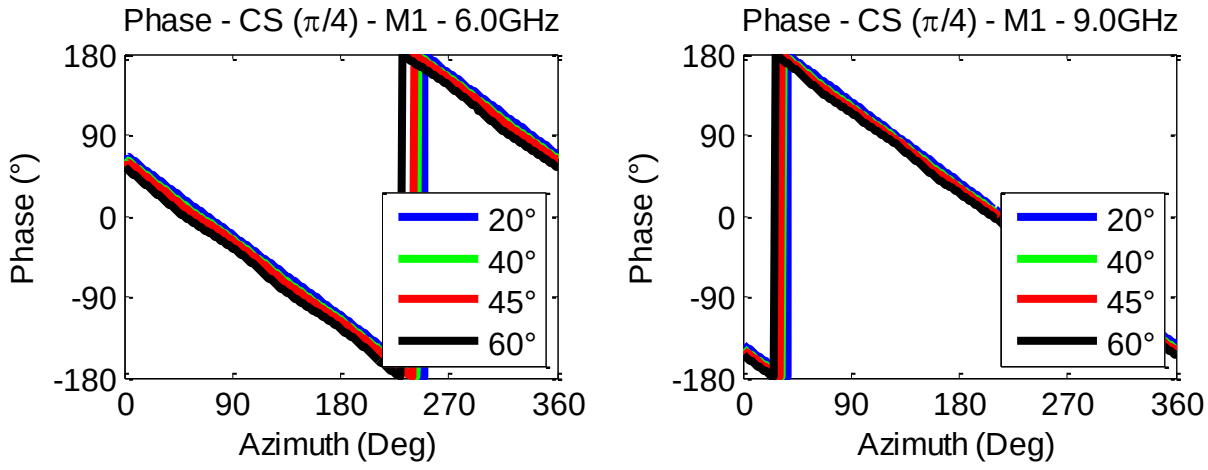

(a) (b)

FIGURE 3-117: RADIATION PATTERNS – CS [Π/4] – AZ – M1 – PHA [6 (A) & 9 (B) GHZ]

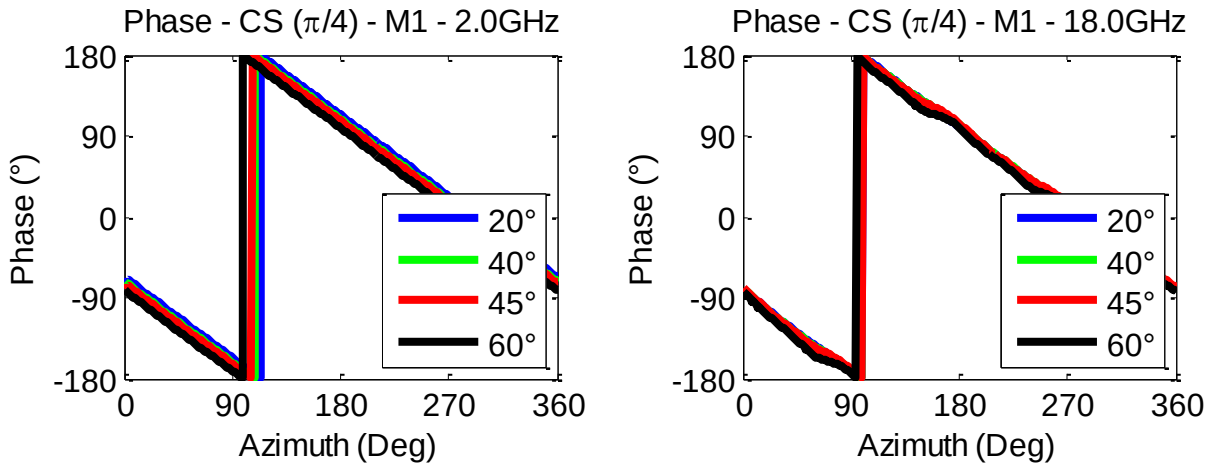

(a) (b)

FIGURE 3-118: RADIATION PATTERNS – CS [Π/4] – AZ – M1 – PHA [2 (A) & 18 (B) GHZ]

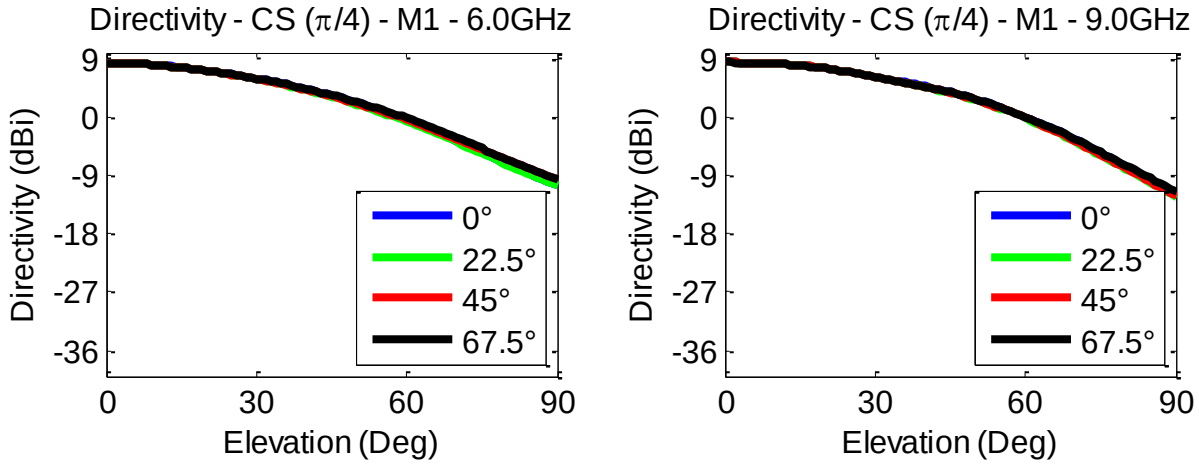

(a) (b)

FIGURE 3-119: RADIATION PATTERNS – CS [Π/4] – EL – M1 – MAG [6 (A) & 9 (B) GHZ]

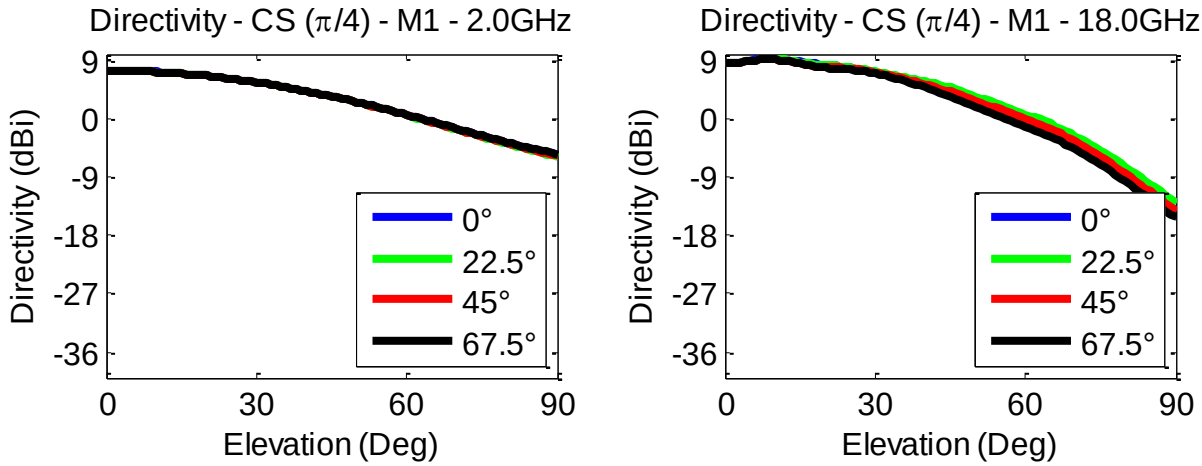

(a) (b)

FIGURE 3-120: RADIATION PATTERNS – CS [Π/4] – EL – M1 – MAG [2 (A) & 18 (B) GHZ]

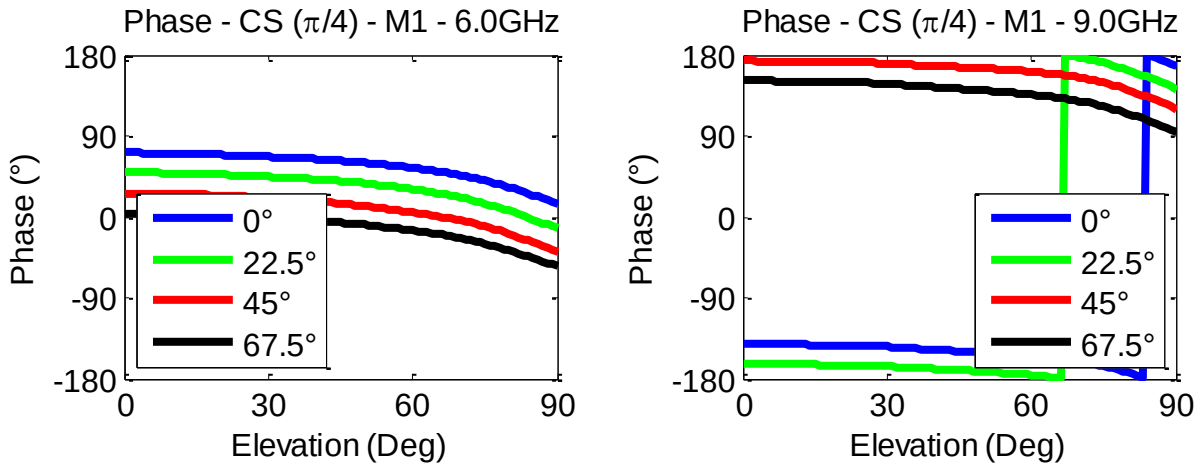

(a) (b)

FIGURE 3-121: RADIATION PATTERNS – CS [Π/4] – EL – M1 – PHA [6 (A) & 9 (B) GHZ]

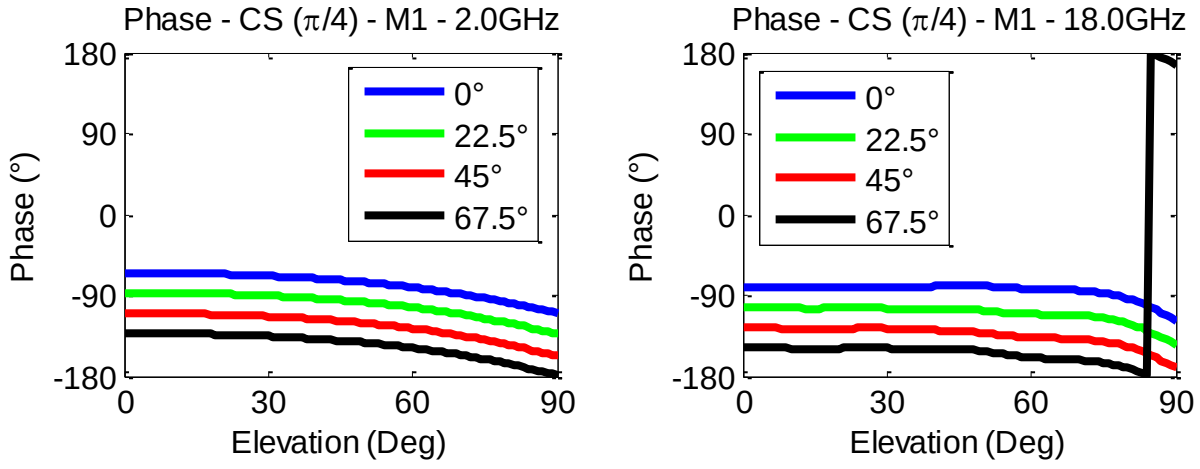

(a) (b)

FIGURE 3-122: RADIATION PATTERNS – CS [Π/4] – EL – M1 – PHA [2 (A) & 18 (B) GHZ]

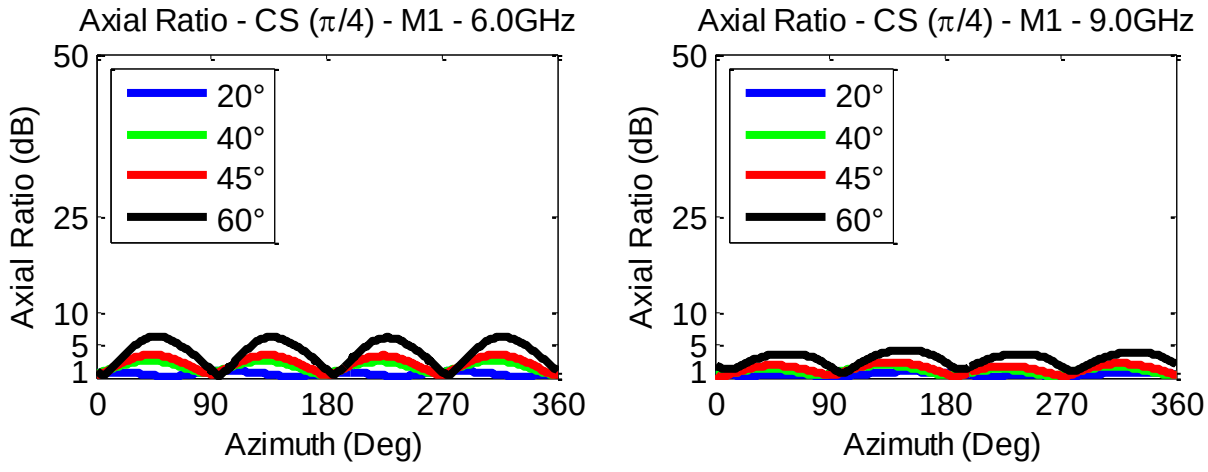

(a) (b)

FIGURE 3-123: AXIAL RATIOS – CS [Π/4] – AZ – M1 [6 (A) & 9 (B) GHZ]

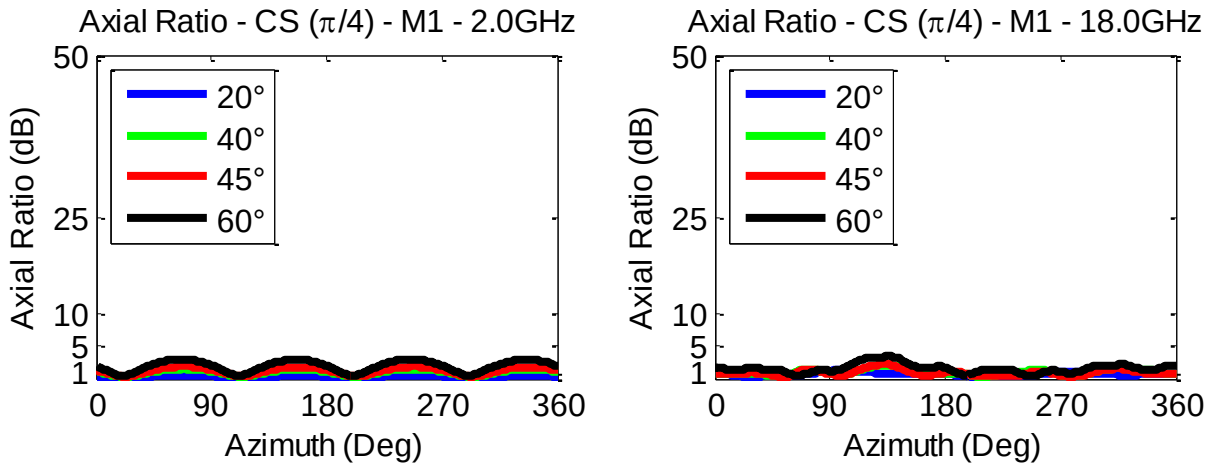

(a) (b)

FIGURE 3-124: AXIAL RATIOS – CS [Π/4] – AZ – M1 [2 (A) & 18 (B) GHZ]

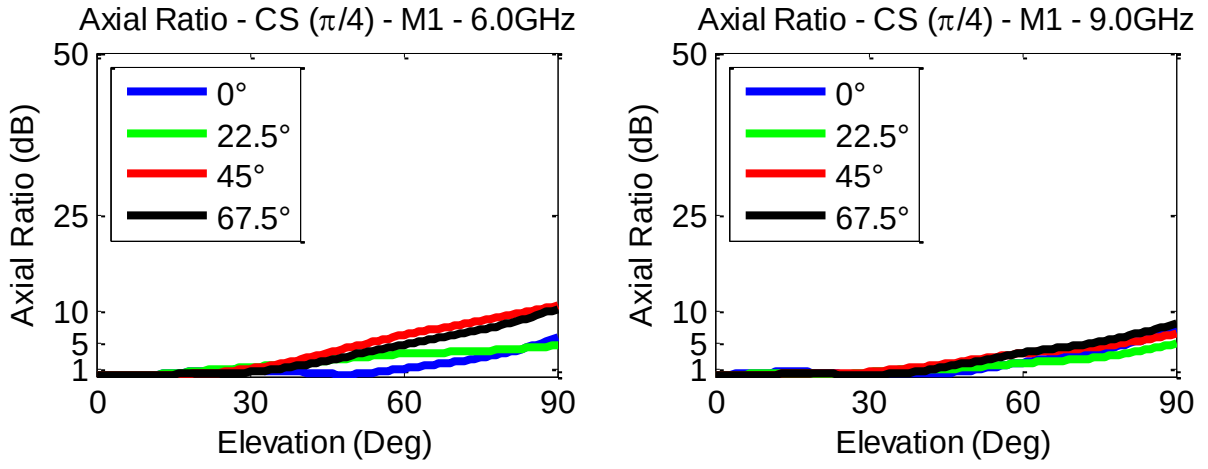

(a) (b)

FIGURE 3-125: AXIAL RATIOS – CS [Π/4] – EL – M1 [6 (A) & 9 (B) GHZ]

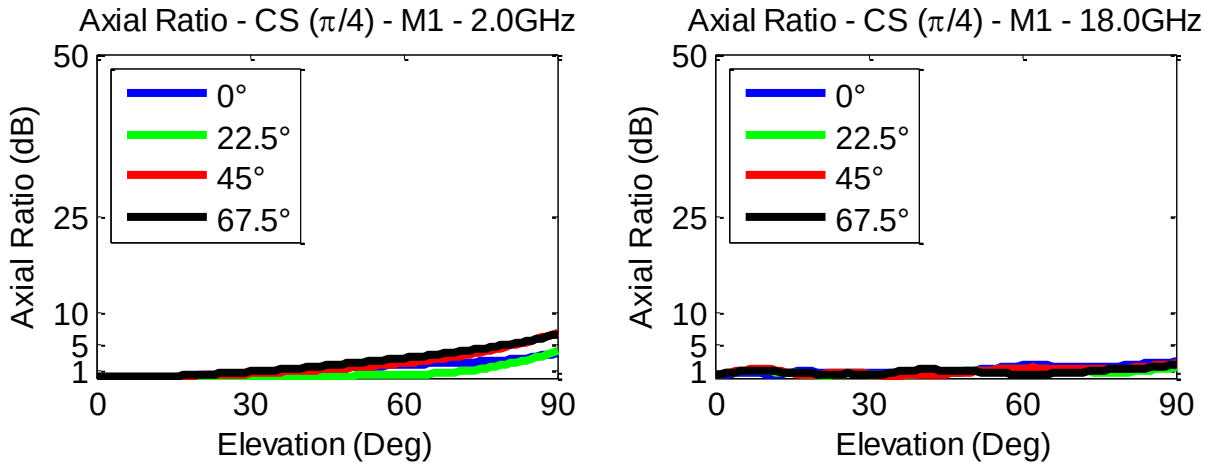

(a) (b)

FIGURE 3-126: AXIAL RATIOS – CS [Π/4] – EL – M1 [2 (A) & 18 (B) GHZ]

For the first mode of operation for the circular sinuous with π/4-interleave, the trend for the magnitude ripple, from Figures 3-115 & 3-116, is to increase both as the frequency increases and as the elevation angle increases from boresight out to the horizon. At 2.0GHz and 20° in elevation, it has minimal ripple of ±0.01dB. While at the highest frequency of 18.0GHz and 60° in elevation, the ripple is ±1.25dB, which is again much less than it was for either spiral. For the mid-band case of 6GHz at 20° in elevation, the ripple is ±0.03dB. The magnitude of the elevation cuts, from Figures 3-119 & 3-120, show the maximum directivity at boresight, 8.5dBi at 9GHz, and the -3dB beamwidth, that extends out to 35° in elevation for the same frequency.

Similar to the magnitude ripple, the phase ripple, from Figures 3-117 & 3-118, increases with both increasing frequency and increasing elevation angle. The phase ripple is ±0.5° at 2.0GHz and 20° and for 18.0GHz at 60° the ripple is ±8.5°, which again is much lower than it was for either spiral case at this frequency. In the mid-band case, 20° of elevation at 6.0GHz, the ripple is ±0.25°. The phase of the elevation cuts, from Figures 3-121 & 3-122, are well spaced and do not overlap.

The trend for the axial ratio about azimuth, from Figures 3-123 & 3-124, is for the lowest values at boresight and increasing values toward the horizon. In the mid-band at 6.0GHz and 20° in elevation, the average is 0.6dB and the peak is 1.0dB. There is also variation across elevation, from Figures 3-125 & 3-126, that increases from boresight toward the horizon. For 6.0GHz, the axial ratio increases from boresight toward the horizon beginning at less than 0.01dB and reaching 11.4dB.

Within the second mode of operation results include: the azimuth cuts' magnitude in Figures 3-127 & 3-128, the azimuth cuts' phase in Figures 3-129 & 3-130, the elevation

cuts' magnitude in Figures 3-131 & 3-132, the elevation cuts' phase in Figures 3-133 & 3-134 and the axial ratio of the azimuth cuts in Figures 3-135 & 3-136 and of the elevation cuts in Figures 3-137 & 3-138.

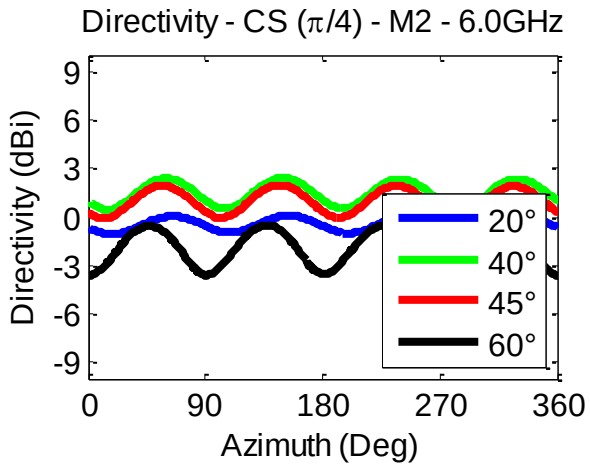

(a)

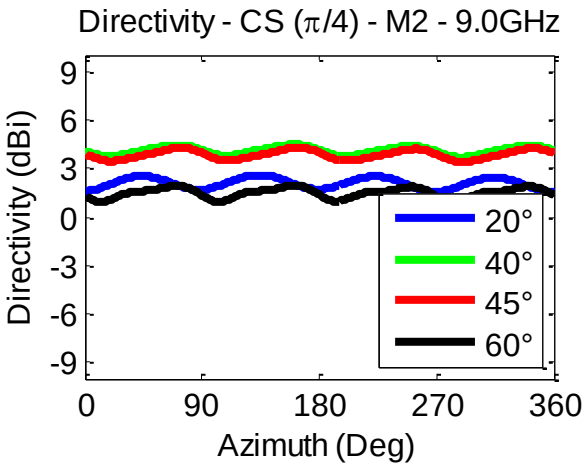

(b)

FIGURE 3-127: RADIATION PATTERNS – CS [Π/4] – AZ – M2 – MAG [6 (A) & 9 (B) GHZ]

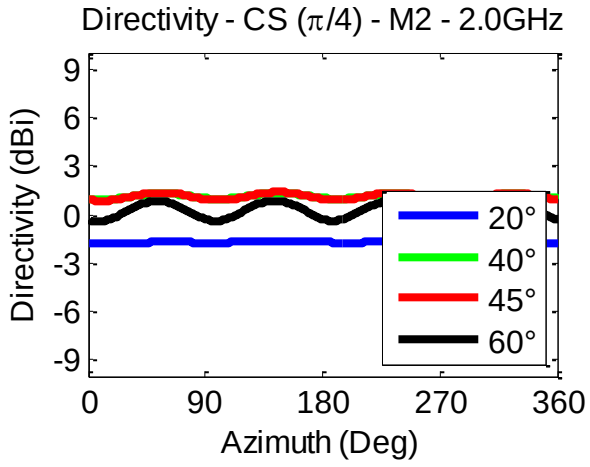

(a)

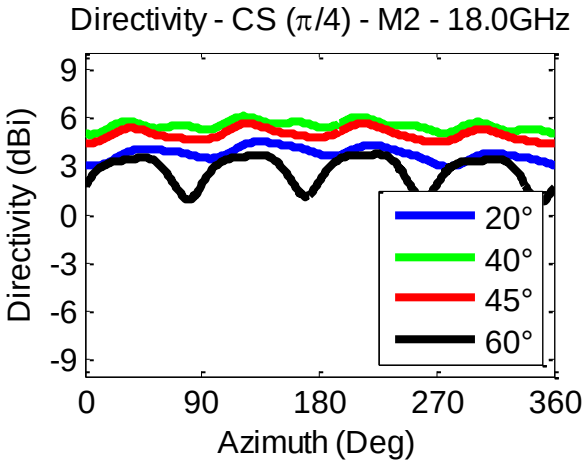

(b)

FIGURE 3-128: RADIATION PATTERNS – CS [Π/4] – AZ – M2 – MAG [2 (A) & 18 (B) GHZ]

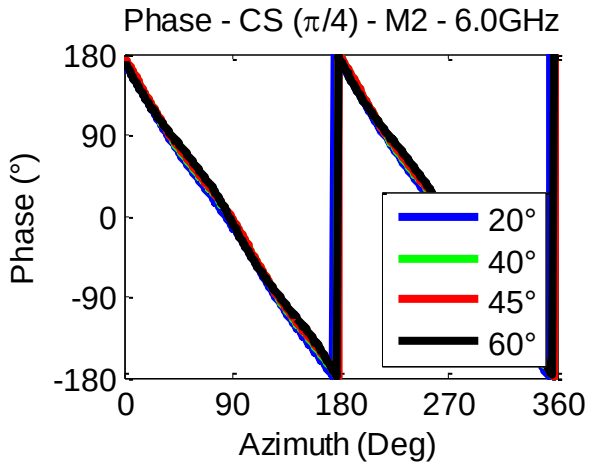

(a)

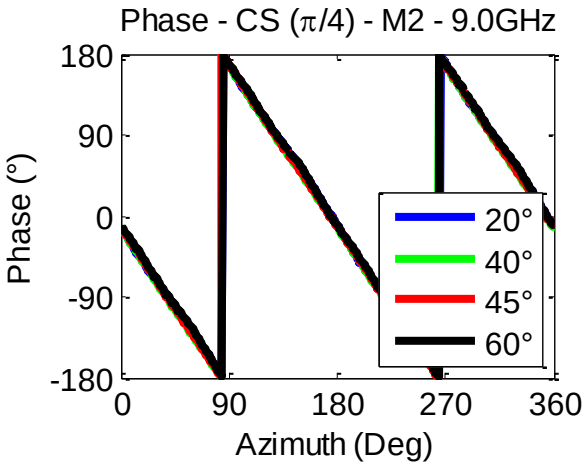

(b)

FIGURE 3-129: RADIATION PATTERNS – CS [Π/4] – AZ – M2 – PHA [6 (A) & 9 (B) GHZ]

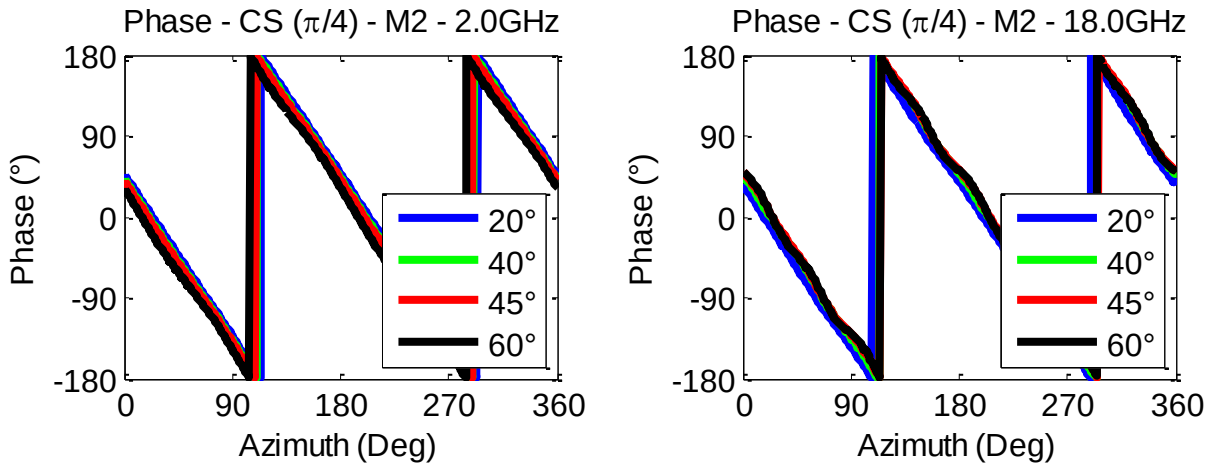

(a) (b)

FIGURE 3-130: RADIATION PATTERNS – CS [Π/4] – AZ – M2 – PHA [2 (A) & 18 (B) GHZ]

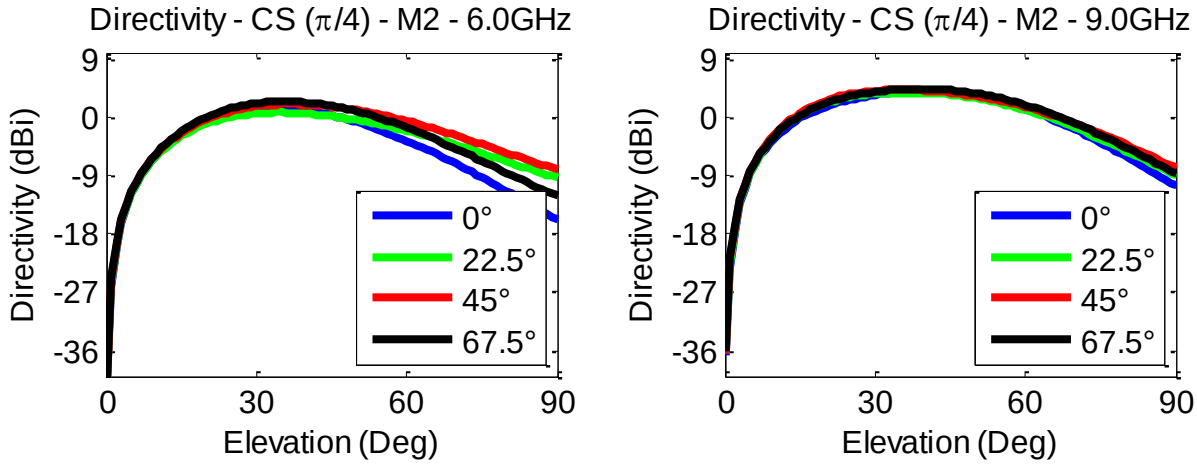

(a) (b)

FIGURE 3-131: RADIATION PATTERNS – CS [Π/4] – EL – M2 – MAG [6 (A) & 9 (B) GHZ]

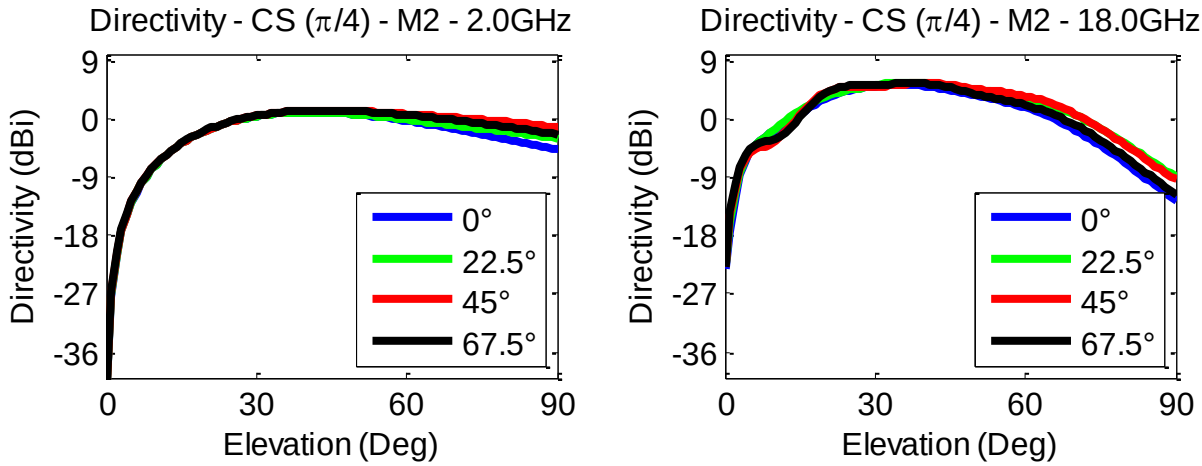

(a) (b)

FIGURE 3-132: RADIATION PATTERNS – CS [Π/4] – EL – M2 – MAG [2 (A) & 18 (B) GHZ]

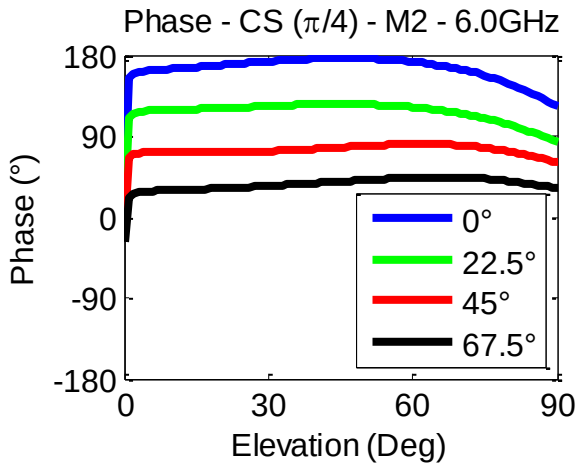

(a)

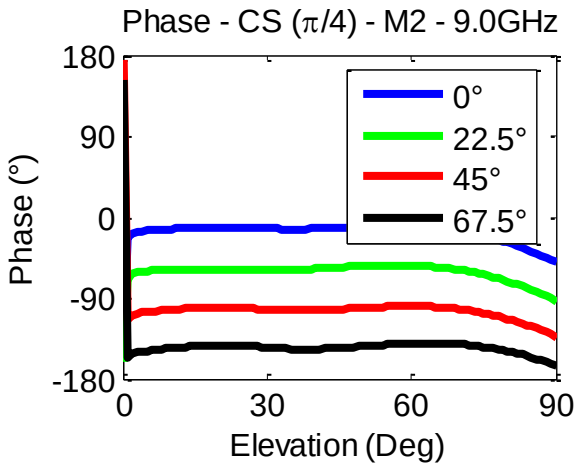

(b)

FIGURE 3-133: RADIATION PATTERNS – CS [Π/4] – EL – M2 – PHA [6 (A) & 9 (B) GHZ]

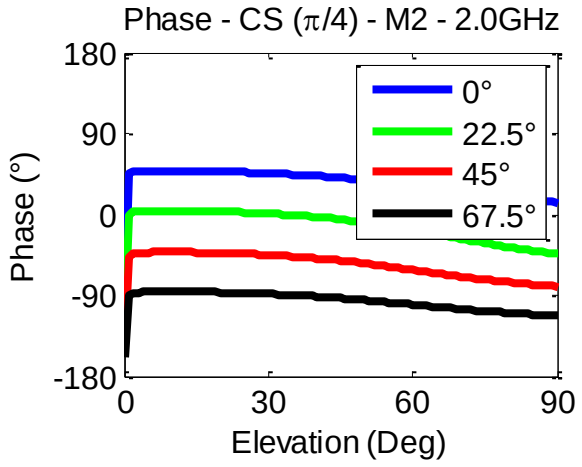

(a)

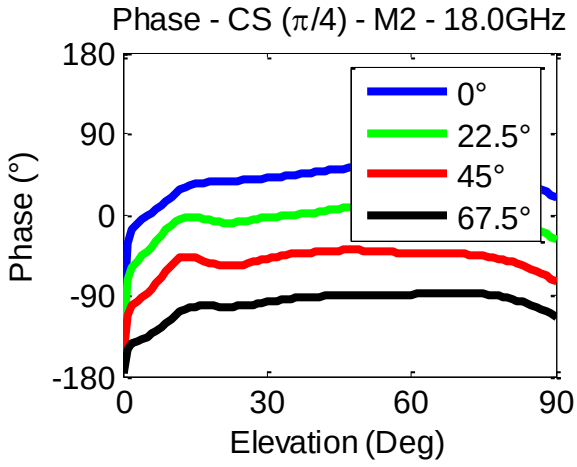

(b)

FIGURE 3-134: RADIATION PATTERNS – CS [Π/4] – EL – M2 – PHA [2 (A) & 18 (B) GHZ]

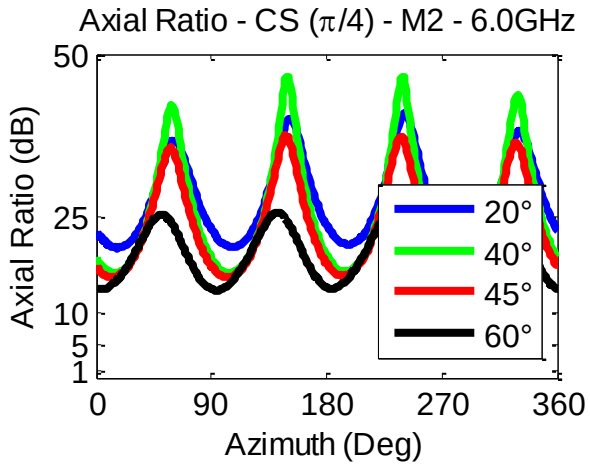

(a)

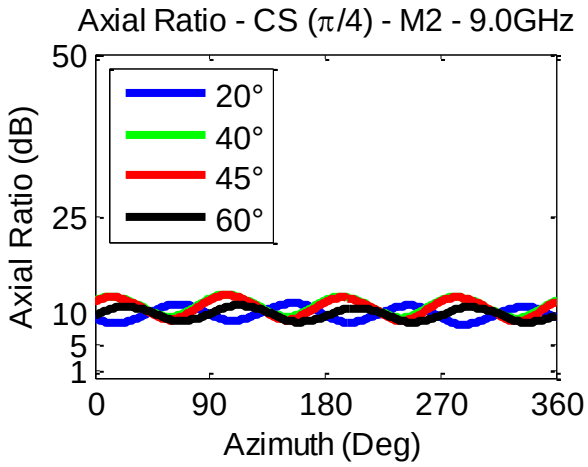

(b)

FIGURE 3-135: AXIAL RATIOS – CS [Π/4] – AZ – M2 [6 (A) & 9 (B) GHZ]

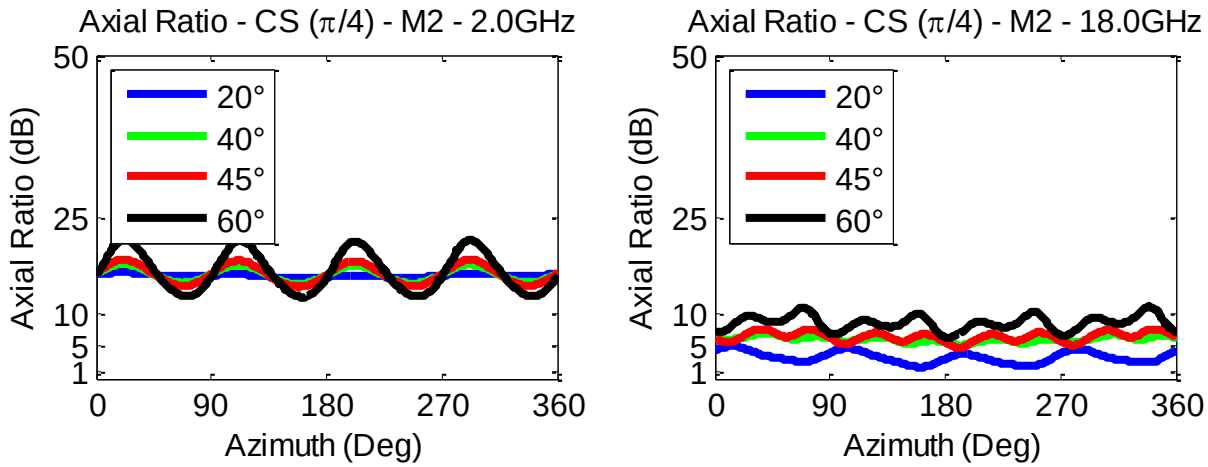

(a) (b)

FIGURE 3-136: AXIAL RATIOS – CS [Π/4] – AZ – M2 [2 (A) & 18 (B) GHZ]

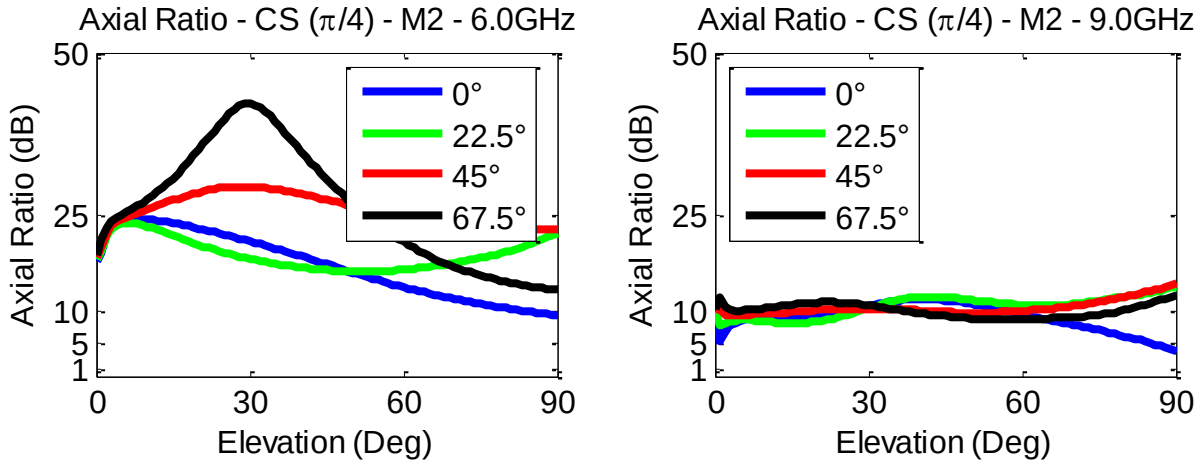

(a) (b)

FIGURE 3-137: AXIAL RATIOS – CS [Π/4] – EL – M2 [6 (A) & 9 (B) GHZ]

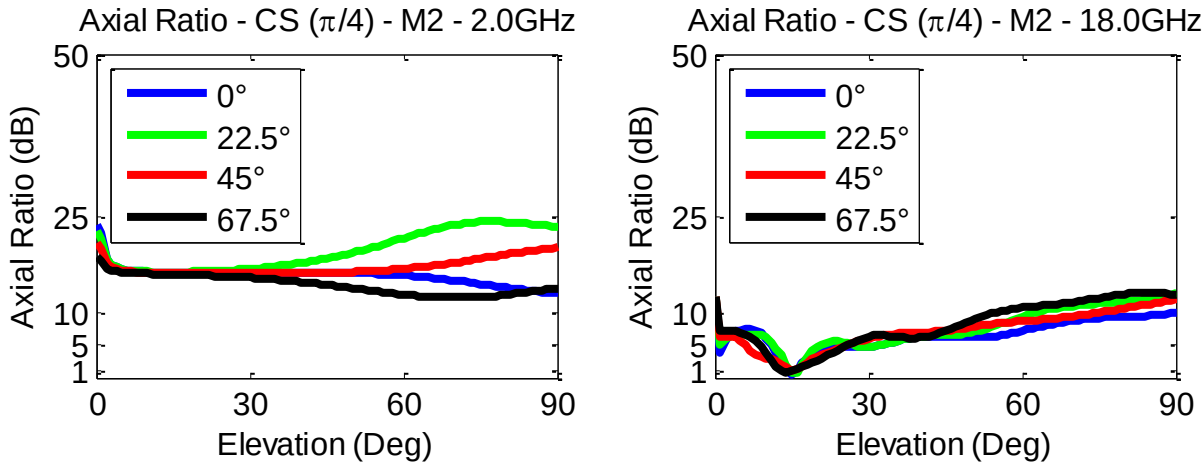

(a) (b)

FIGURE 3-138: AXIAL RATIOS – CS [Π/4] – EL – M2 [2 (A) & 18 (B) GHZ]

For the second mode for the circular sinuous with π/4-interleave, the ripple of the magnitude of the azimuth cuts, from Figures 3-127 & 3-128, increases as the elevation angle increases, but not necessarily as the frequency increases. The sinuous has minimal ripple of ±0.2dB for 2.0GHz at 40° in elevation, ±1.0dB for 6.0GHz at 40° in elevation, and ±1.5dB at 18.0GHz and 60° in elevation. The magnitude of the elevation cuts, from Figures 3-131 & 3-132, show the peak directivity angle and the -3dB beamwidth. The maximum directivity of 4.5dBi for 9.0GHz occurs at 40° in elevation and the -3dB beamwidth extends from 19° to 61°.

The phase ripple about azimuth, from Figures 3-129 & 3-130, again increases with elevation angle. The ripple is ±1.3° at 2.0GHz and 40° in elevation, ±8.5° at 18.0GHz and 60° and in the mid-band it is ±5.5° for 6.0GHz and 40° in elevation. The phase of the elevation cuts, from Figures 3-133 & 3-134, are acceptable and an overlap occurs above 80° in elevation for the 6.0GHz case.

There is no trend for the axial ratio in the second mode of operation, from Figures 3-135 & 3-136. There is significant variation about azimuth and for 6.0GHz and 40° in elevation where the average is 25dB but the peak is 47dB. There is also significant variation across elevation, from Figures 3-137 & 3-138. The mid-band frequency of 6.0GHz shows more variation than any other frequency presented and begins around 20dB, peaks up to 40dB for the elevation angles selected and slopes back down to about 15dB on average at the horizon. The peak axial ratio in the forward hemisphere is 114dB.

3.2.2.6 CIRCULAR SINUOUS [Π/3]

For the circular sinuous with π/3-interleave, feed points are located at azimuth angles of 8°, 98°, 188° and 278°. The elements wrap back-and-forth and are centered about 0°, 90°, 180° and 270°. Within the first mode of operation results include: the azimuth cuts' magnitude in Figures 3-139 & 3-140, the azimuth cuts' phase in Figures 3-141 & 3-142, the elevation cuts' magnitude in Figures 3-143 & 3-144, the elevation cuts' phase in Figures 3-145 & 3-146 and the axial ratio of the azimuth cuts in Figures 3-147 & 3-148 and of the elevation cuts in Figures 3-149 & 3-150.

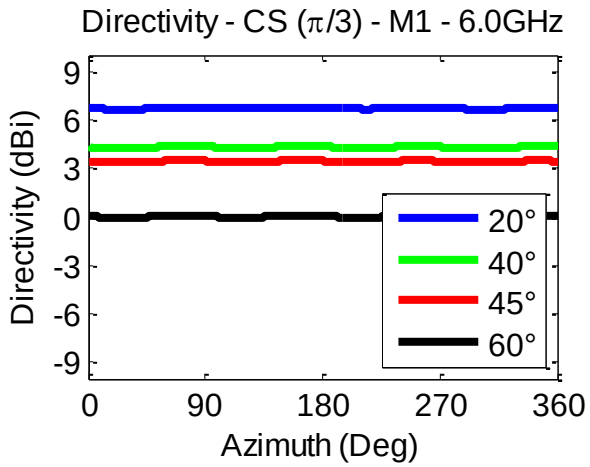

(a)

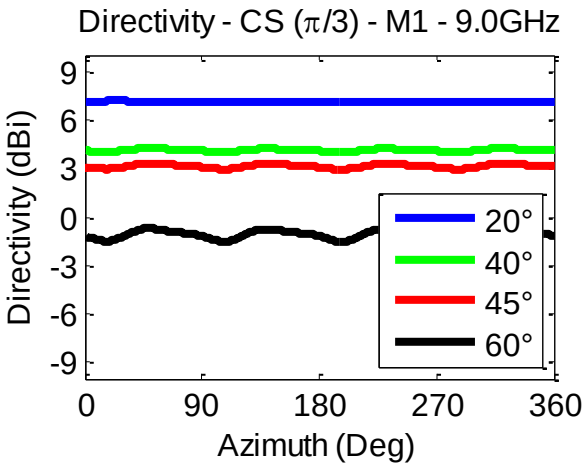

(b)

FIGURE 3-139: RADIATION PATTERNS – CS [Π/3] – AZ – M1 – MAG [6 (A) & 9 (B) GHZ]

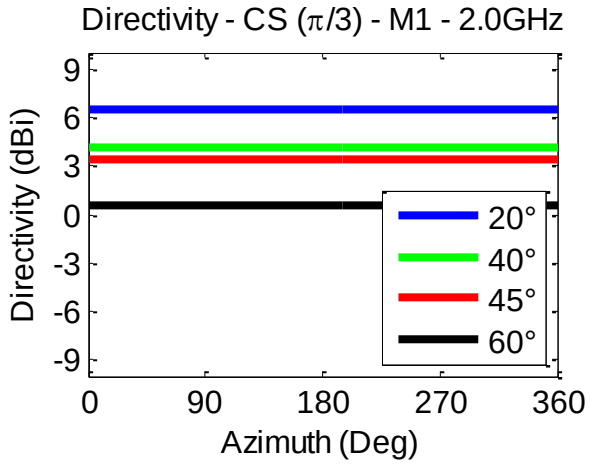

(a)

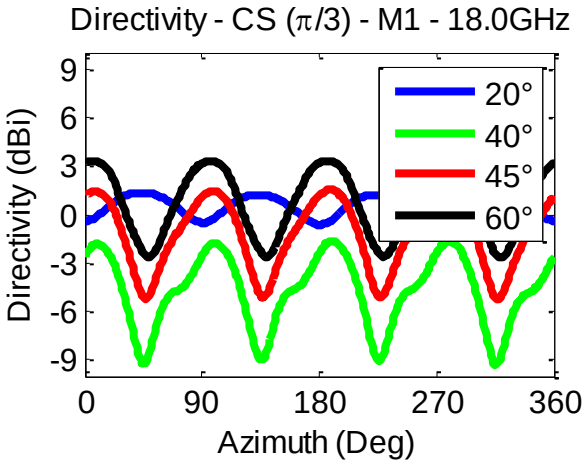

(b)

FIGURE 3-140: RADIATION PATTERNS – CS [Π/3] – AZ – M1 – MAG [2 (A) & 18 (B) GHZ]

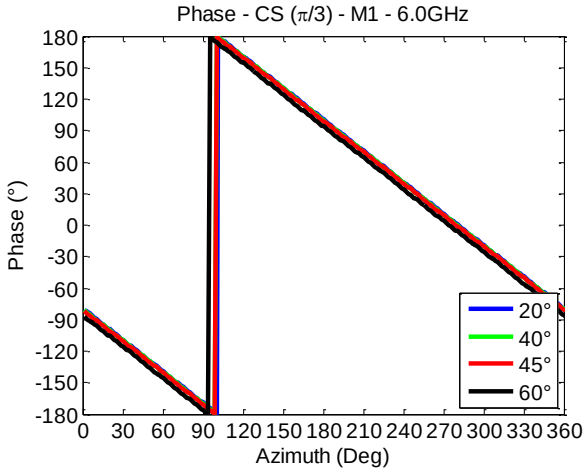

(a)

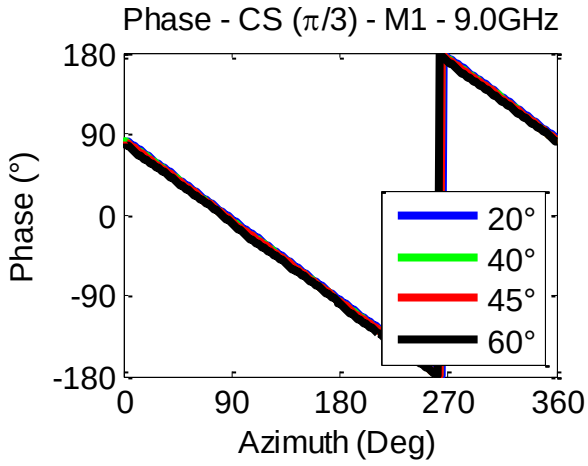

(b)

FIGURE 3-141: RADIATION PATTERNS – CS [Π/3] – AZ – M1 – PHA [6 (A) & 9 (B) GHZ]

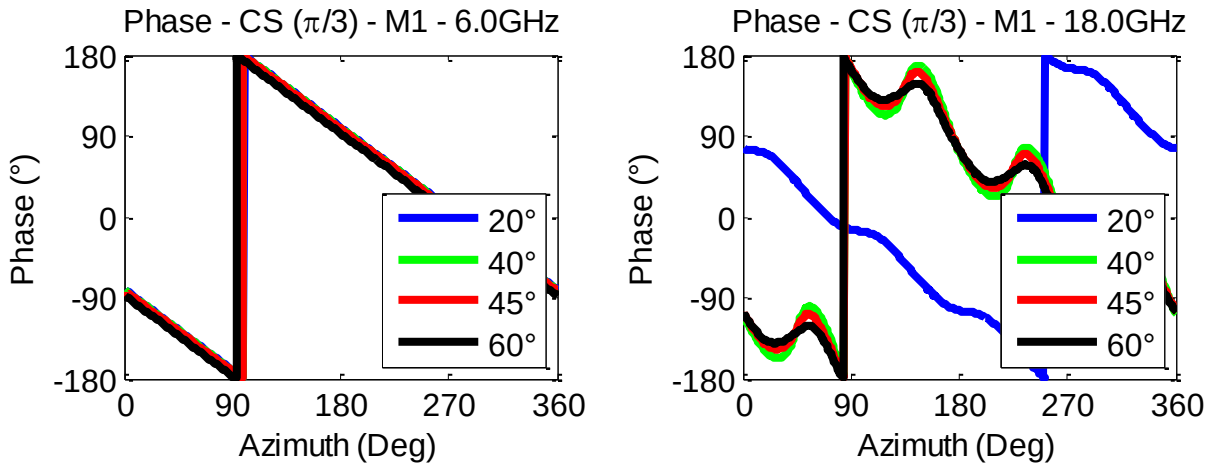

(a) (b)

FIGURE 3-142: RADIATION PATTERNS – CS [Π/3] – AZ – M1 – PHA [2 (A) & 18 (B) GHZ]

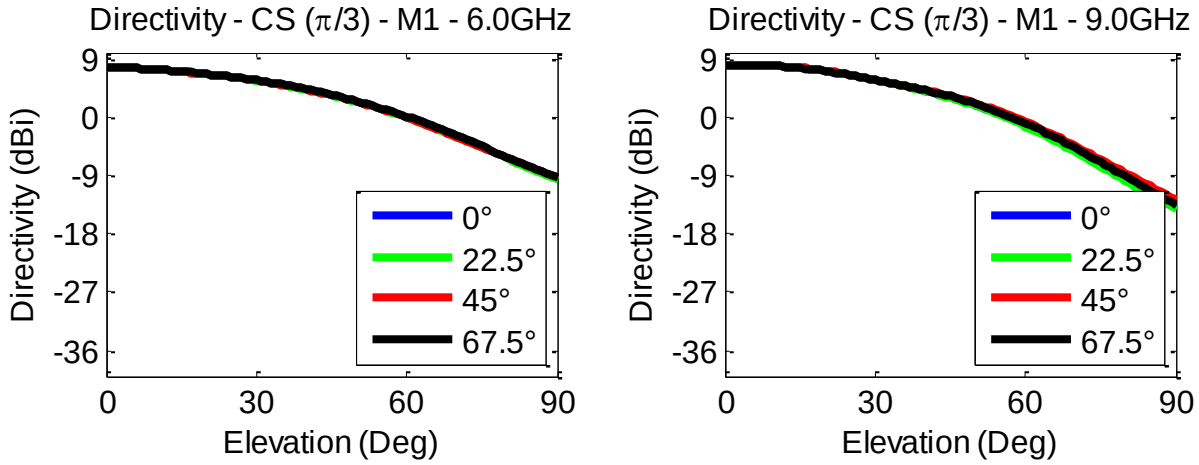

(a) (b)

FIGURE 3-143: RADIATION PATTERNS – CS [Π/3] – EL – M1 – MAG [6 (A) & 9 (B) GHZ]

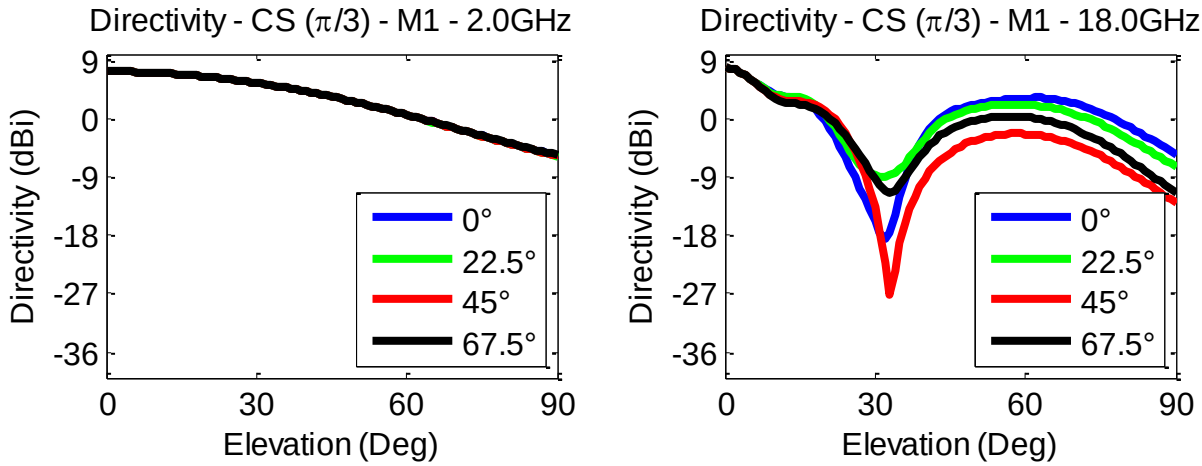

(a) (b)

FIGURE 3-144: RADIATION PATTERNS – CS [Π/3] – EL – M1 – MAG [2 (A) & 18 (B) GHZ]

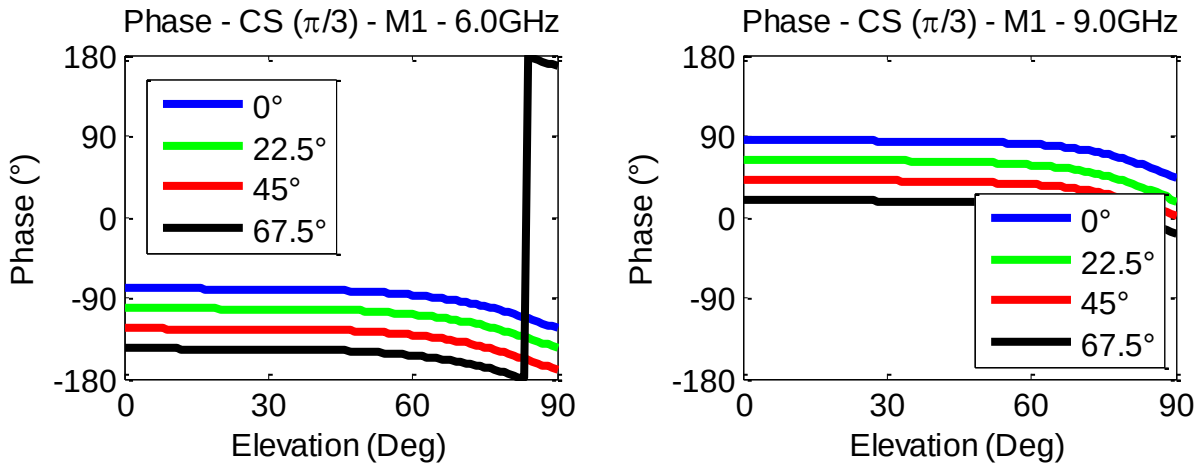

(a) (b)

FIGURE 3-145: RADIATION PATTERNS – CS [Π/3] – EL – M1 – PHA [6 (A) & 9 (B) GHZ]

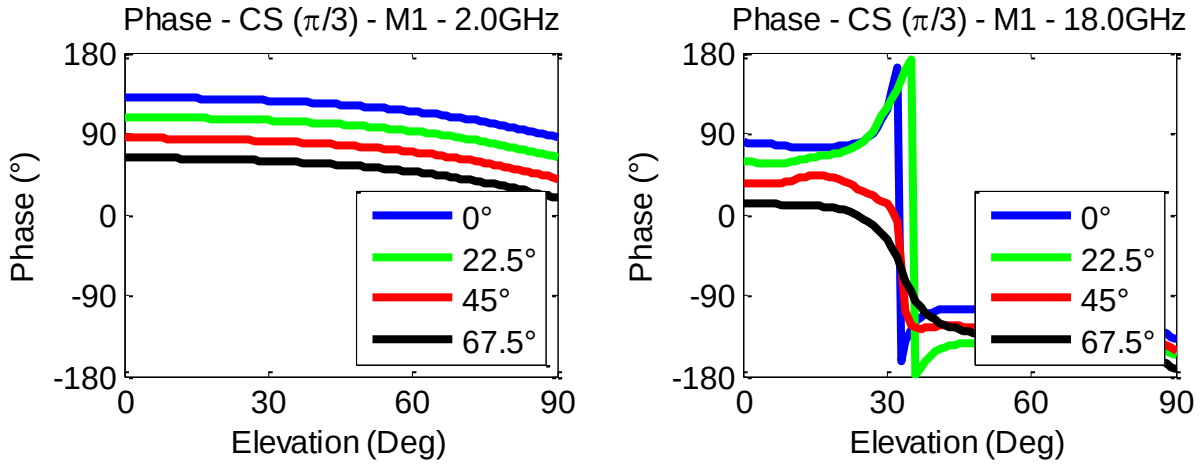

(a) (b)

FIGURE 3-146: RADIATION PATTERNS – CS [Π/3] – EL – M1 – PHA [2 (A) & 18 (B) GHZ]

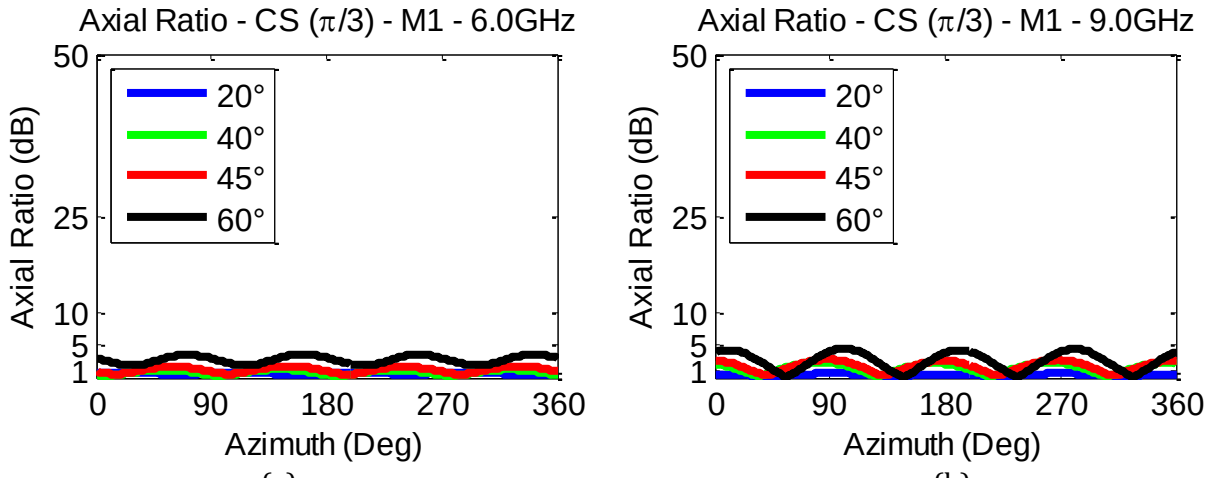

(a) (b)

FIGURE 3-147: AXIAL RATIOS – CS [Π/3] – AZ – M1 [6 (A) & 9 (B) GHZ]

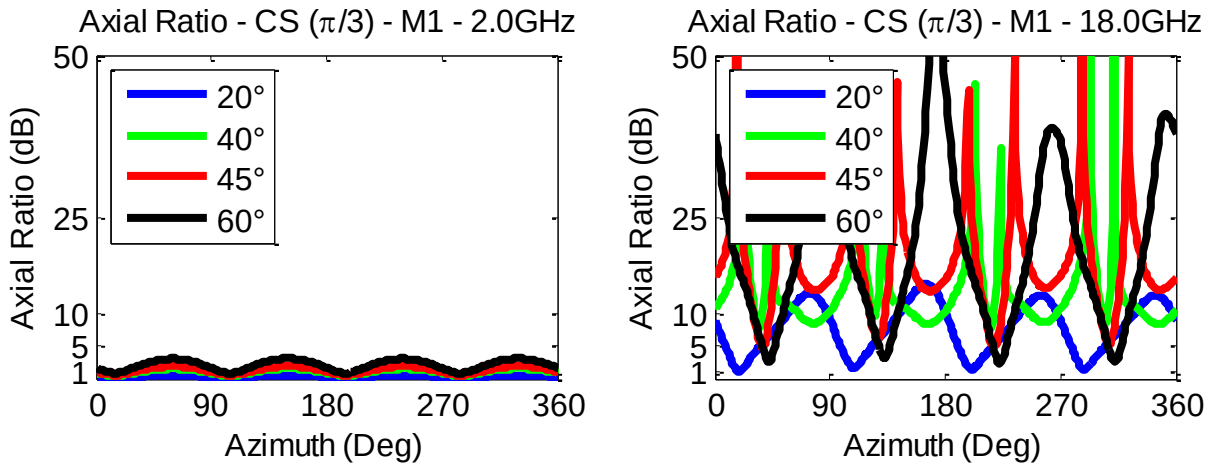

(a) (b)

FIGURE 3-148: AXIAL RATIOS – CS [Π/3] – AZ – M1 [2 (A) & 18 (B) GHZ]

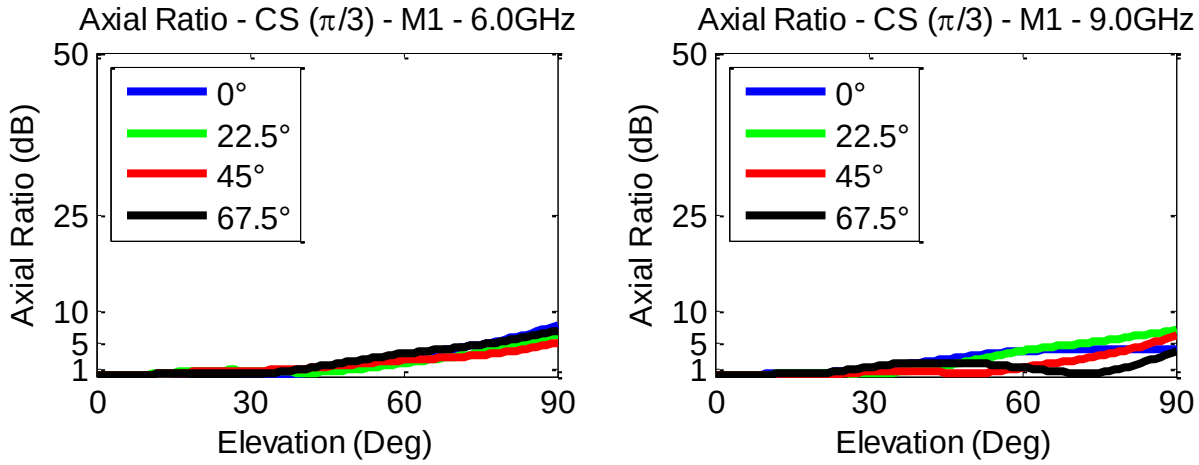

(a) (b)

FIGURE 3-149: AXIAL RATIOS – CS [Π/3] – EL – M1 [6 (A) & 9 (B) GHZ]

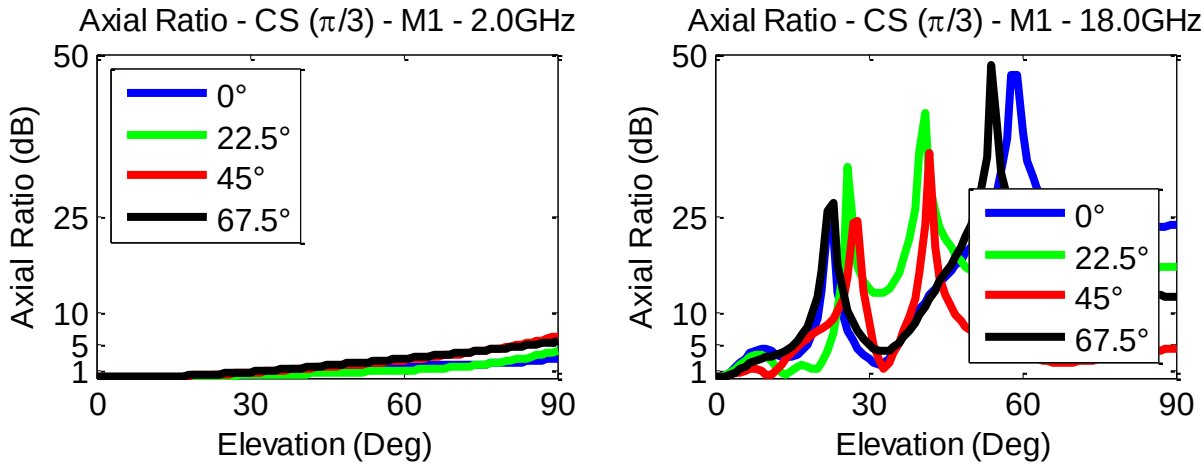

(a) (b)

FIGURE 3-150: AXIAL RATIOS – CS [Π/3] – EL – M1 [2 (A) & 18 (B) GHZ]

For the first mode of operation for the circular sinuous with π/3-interleave, the trend for the magnitude ripple, from Figures 3-139 & 3-140, is to increase both as the frequency increases and as the elevation angle increases from boresight out to the horizon. At 2.0GHz and 20° in elevation, it has minimal ripple of ±0.001dB. While at the highest frequency of 18.0GHz and 60° in elevation, the ripple is ±3.0dB, but the average directivity at 20° in elevation is actually lower than at 60°. The results show that this design does not radiate properly at 18.0GHz and the return loss suggests that this is probably true for any frequency much over 12.0GHz. For the mid-band case of 6GHz at 20° in elevation, the ripple is ±0.01dB. The magnitude of the elevation cuts, from Figures 3-143 & 3-144, show the maximum directivity at boresight, 8.1dBi at 9GHz, and the -3dB beamwidth, that extends out to 34° in elevation for the same frequency.

The phase ripple, from Figures 3-141 & 3-142, is exceedingly low for all frequencies and elevation angles presented with the exception of 18.0GHz, which appears to be outside the operational bandwidth. The phase ripple is ±0.1° at both 2.0GHz and 6.0GHz at 20° in elevation. While for 18.0GHz at 60° in elevation the ripple is ±27°. The phase of the elevation cuts, from Figures 3-145 & 3-146, are very well spaced and do not overlap, again with the exception of 18.0GHz.

The trend for the axial ratio about azimuth, from Figures 3-147 & 3-148, is for the lowest values at boresight and increasing values toward the horizon. In the mid-band at 6.0GHz and 20° in elevation, the average is 0.7dB and the peak is 0.9dB. There is also variation across elevation, from Figures 3-149 & 3-150, that increases from boresight toward the horizon. For 6.0GHz, the axial ratio increases from boresight toward the horizon beginning at less than 0.01dB and reaching 8.0dB.

Within the second mode of operation results include: the azimuth cuts' magnitude in Figures 3-151 & 3-152, the azimuth cuts' phase in Figures 3-153 & 3-154, the elevation cuts' magnitude in Figures 3-155 & 3-156, the elevation cuts' phase in Figures 3-157 & 3-158 and the axial ratio of the azimuth cuts in Figures 3-159 & 3-160 and of the elevation cuts in Figures 3-161 & 3-162.

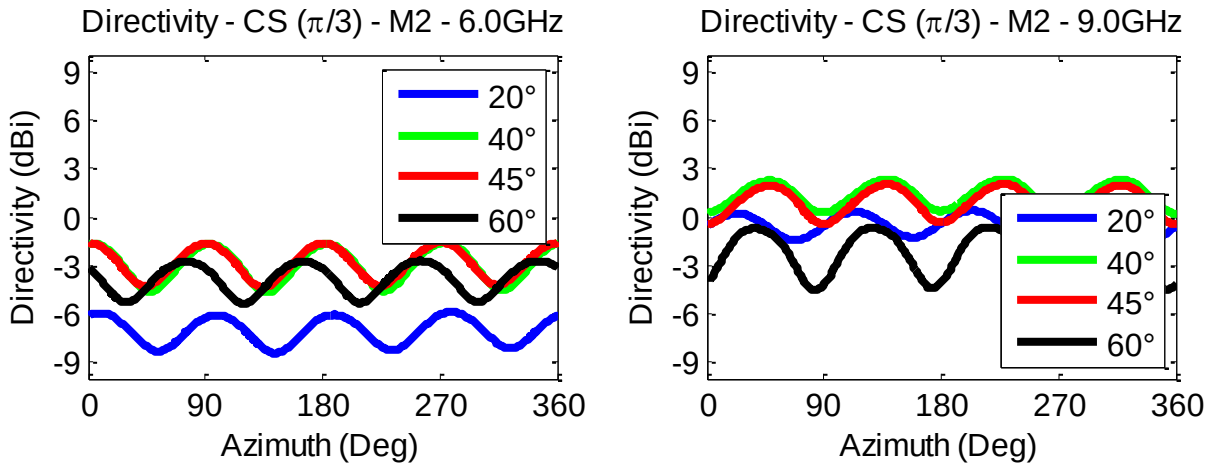

(a) (b)

FIGURE 3-151: RADIATION PATTERNS – CS [Π/3] – AZ – M2 – MAG [6 (A) & 9 (B) GHZ]

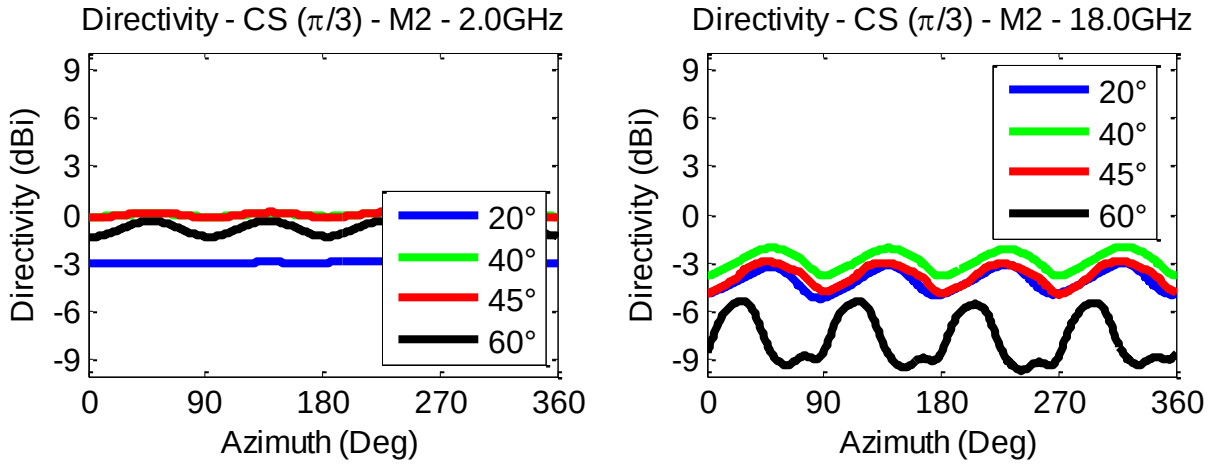

(a) (b)

FIGURE 3-152: RADIATION PATTERNS – CS [Π/3] – AZ – M2 – MAG [2 (A) & 18 (B) GHZ]

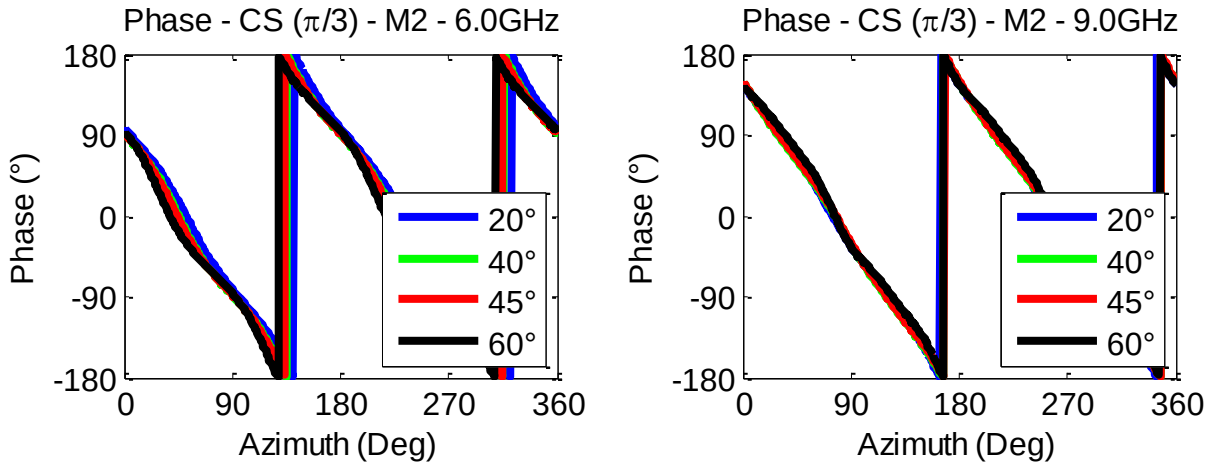

(a) (b)

FIGURE 3-153: RADIATION PATTERNS – CS [Π/3] – AZ – M2 – PHA [6 (A) & 9 (B) GHZ]

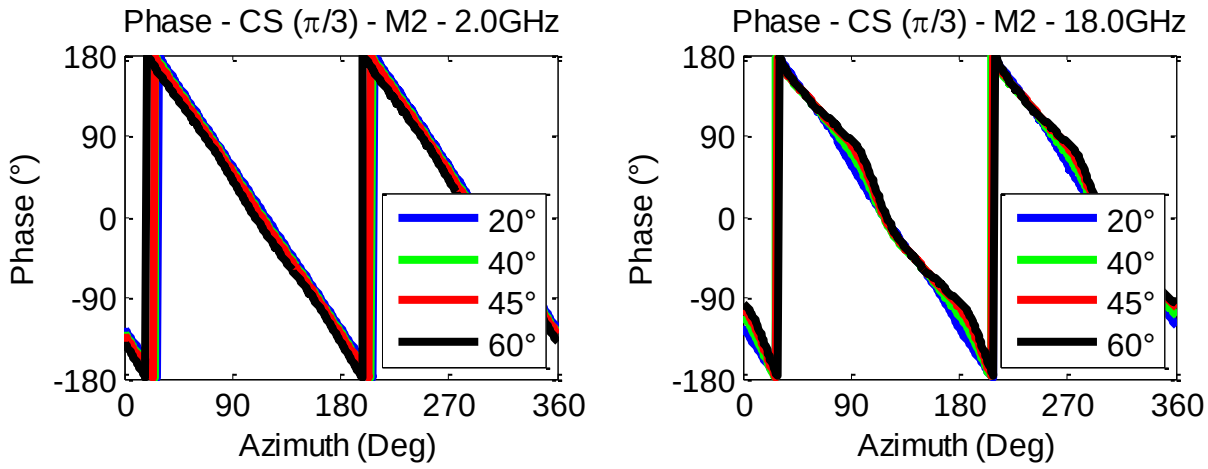

(a) (b)

FIGURE 3-154: RADIATION PATTERNS – CS [Π/3] – AZ – M2 – PHA [2 (A) & 18 (B) GHZ]

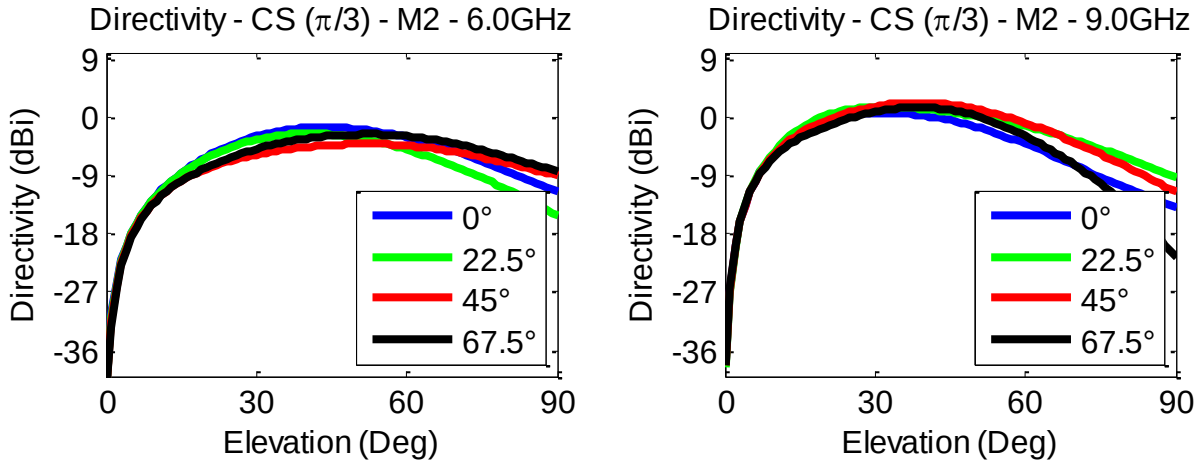

(a) (b)

FIGURE 3-155: RADIATION PATTERNS – CS [Π/3] – EL – M2 – MAG [6 (A) & 9 (B) GHZ]

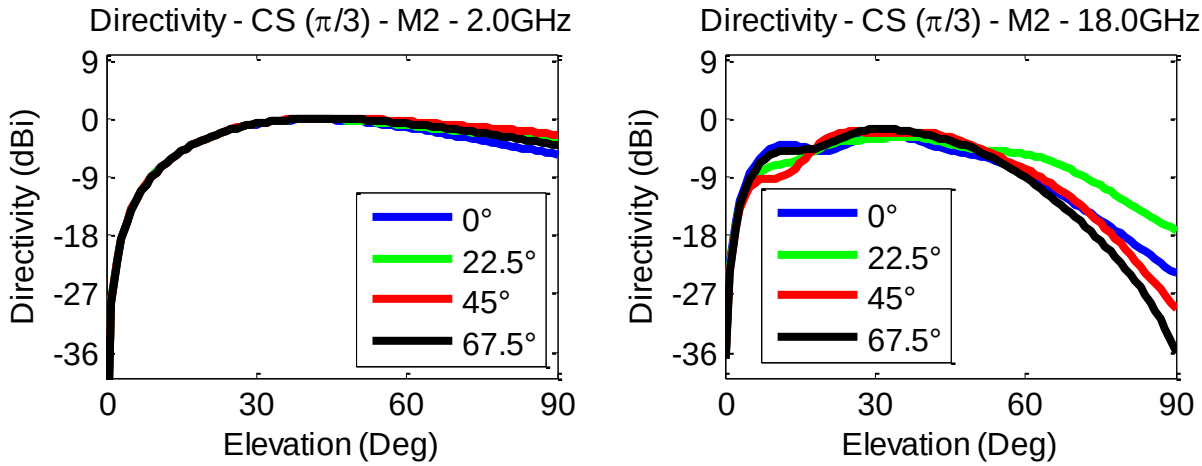

(a) (b)

FIGURE 3-156: RADIATION PATTERNS – CS [Π/3] – EL – M2 – MAG [2 (A) & 18 (B) GHZ]

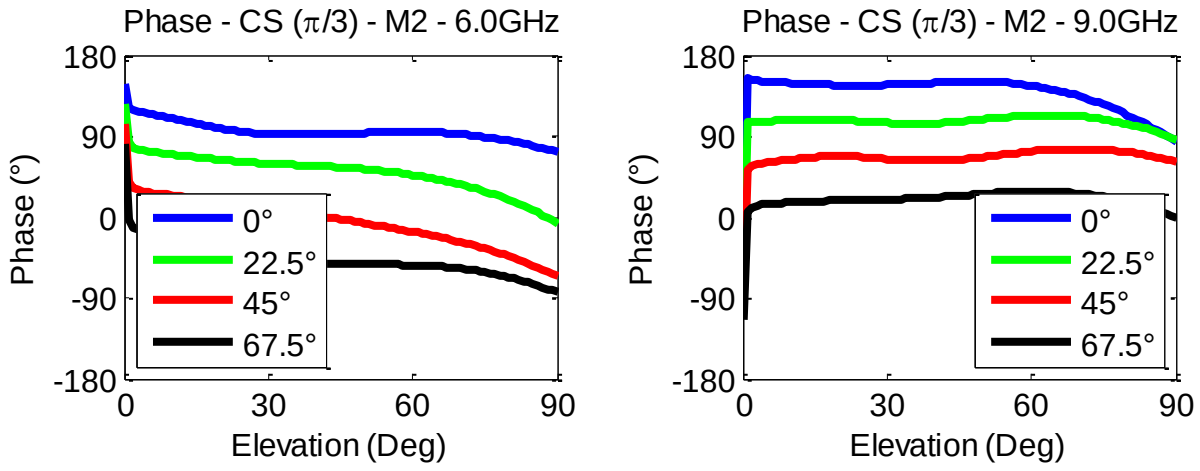

(a) (b)

FIGURE 3-157: RADIATION PATTERNS – CS [Π/3] – EL – M2 – PHA [6 (A) & 9 (B) GHZ]

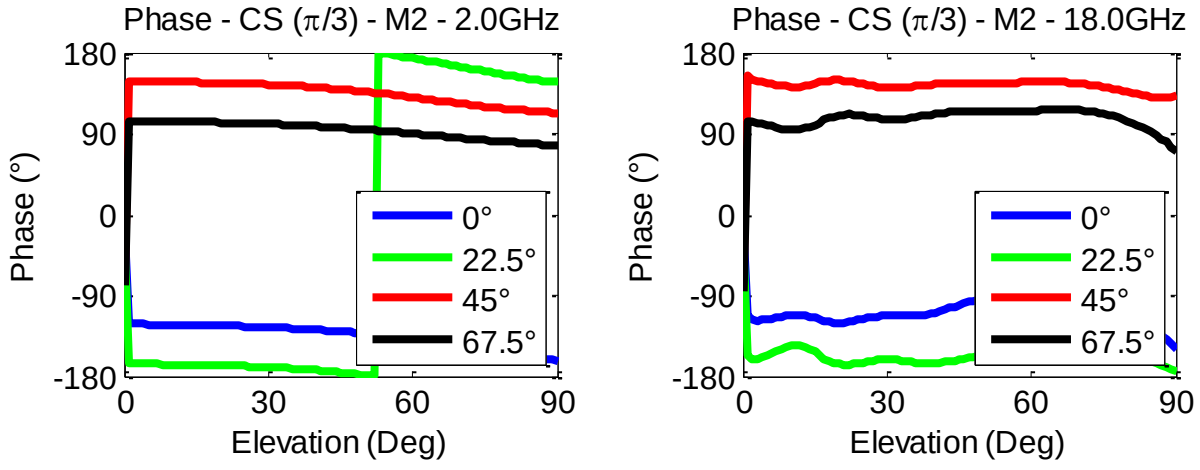

(a) (b)

FIGURE 3-158: RADIATION PATTERNS – CS [Π/3] – EL – M2 – PHA [2 (A) & 18 (B) GHZ]

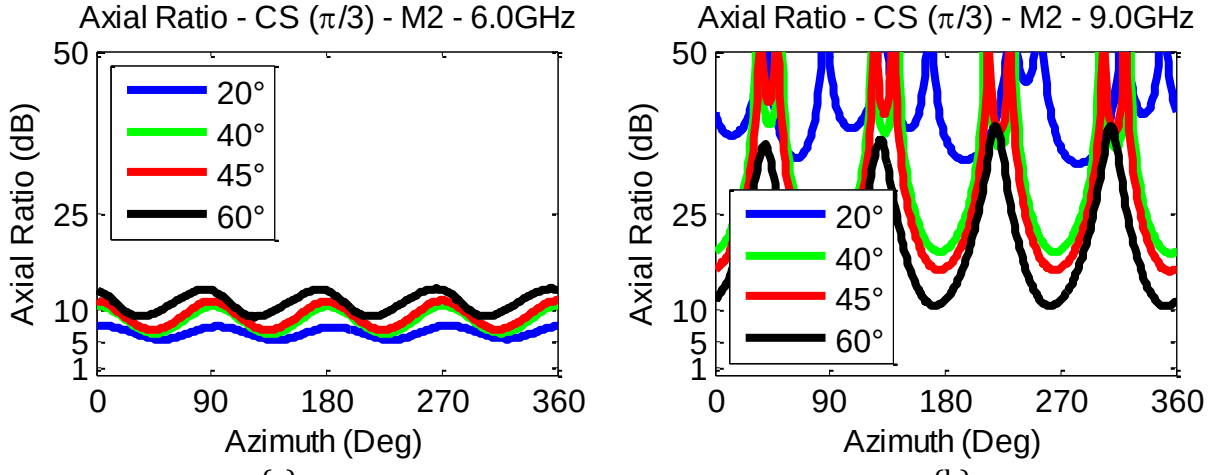

(a) (b)

FIGURE 3-159: AXIAL RATIOS – CS [Π/3] – AZ – M2 [6 (A) & 9 (B) GHZ]

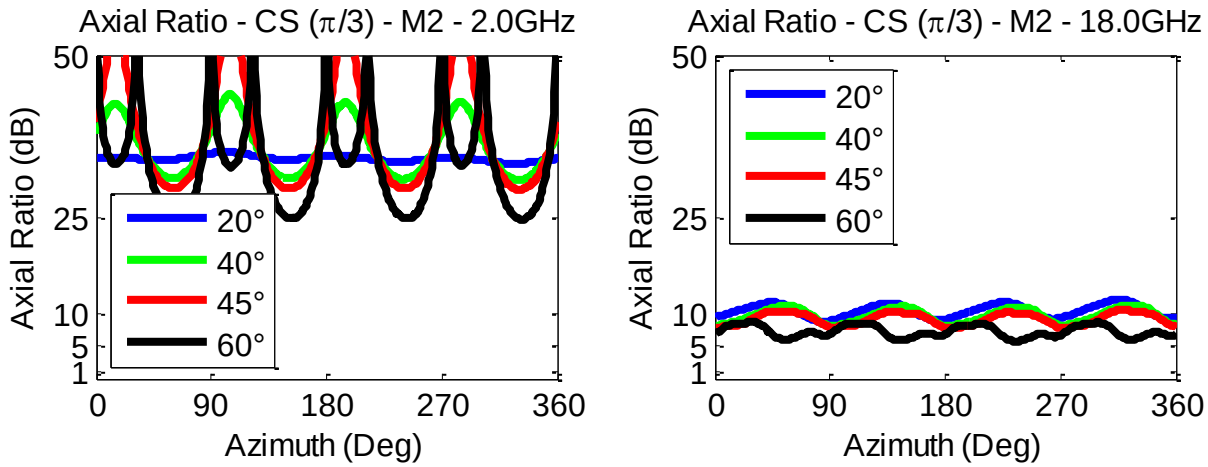

(a) (b)

FIGURE 3-160: AXIAL RATIOS – CS [Π/3] – AZ – M2 [2 (A) & 18 (B) GHZ]

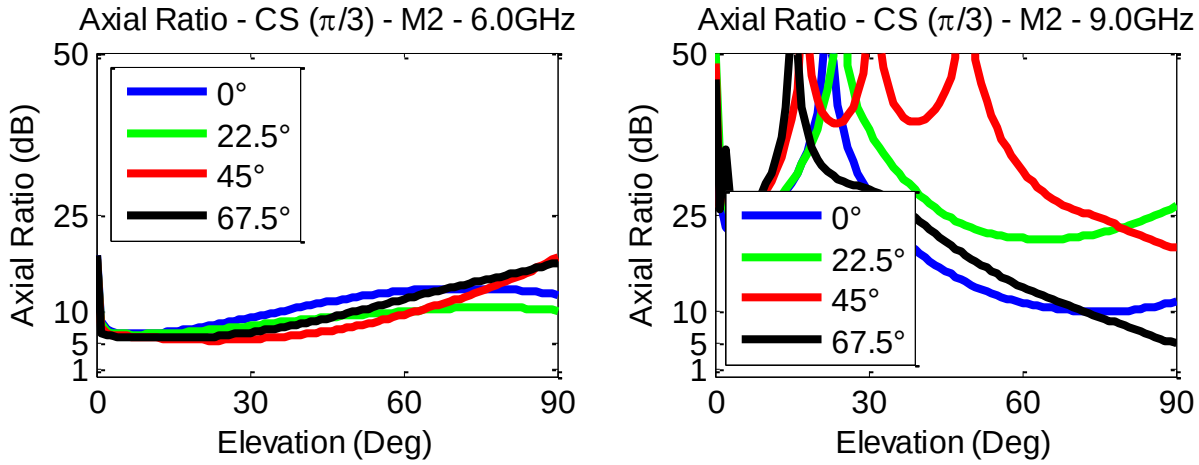

(a) (b)

FIGURE 3-161: AXIAL RATIOS – CS [Π/3] – EL – M2 [6 (A) & 9 (B) GHZ]

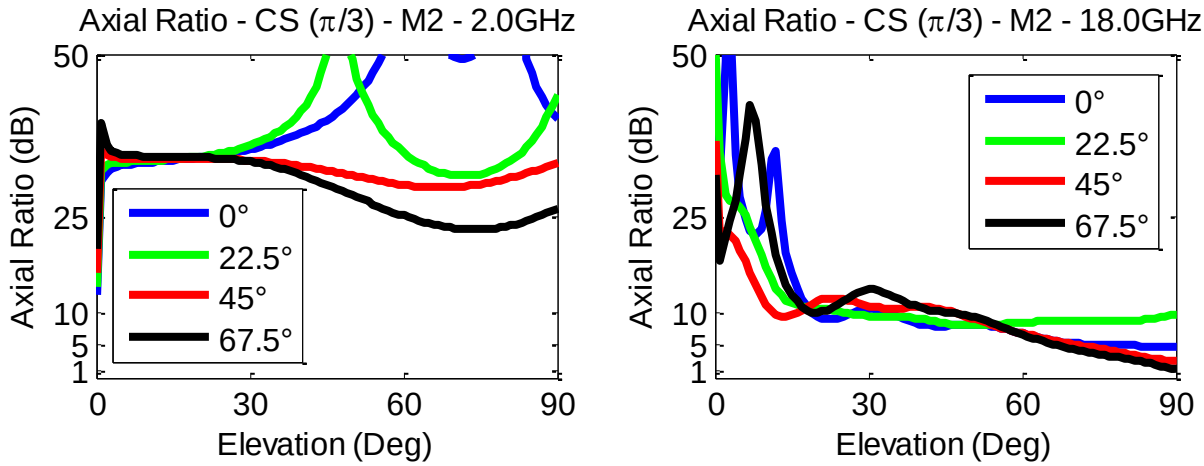

(a) (b)

FIGURE 3-162: AXIAL RATIOS – CS [Π/3] – EL – M2 [2 (A) & 18 (B) GHZ]

For the second mode for the circular sinuous with π/3-interleave, the ripple of the magnitude of the azimuth cuts, from Figures 3-151 & 3-152, increases as the elevation angle increases and as the frequency increases within the operational bandwidth. The sinuous has minimal ripple of ±0.1dB for 2.0GHz at 40° in elevation, ±1.5dB for 6.0GHz at 40° in elevation, and ±2.25dB at 18.0GHz and 60° in elevation. The magnitude of the elevation cuts, from Figures 3-155 & 3-156, show the peak directivity angle and the -3dB beamwidth. The maximum directivity of 2.4dBi for 9.0GHz occurs at 39° in elevation and the -3dB beamwidth extends from 20° to 59°.

The phase ripple about azimuth, from Figures 3-153 & 3-154, again increases with elevation angle. The ripple is ±0.7° at 2.0GHz and 40° in elevation, ±17° at 18.0GHz and 60° and in the mid-band it is ±10° for 6.0GHz and 40° in elevation. The phase of the elevation cuts, from Figures 3-157 & 3-158, are acceptable and an overlap occurs above 85° in elevation for the 9.0GHz case.

There is no trend for the axial ratio in the second mode of operation, from Figures 3-159 & 3-160. There is variation about azimuth and for 6.0GHz and 40° in elevation where the average is 8.5dB but the peak is 11dB. There is also significant variation across elevation, from Figures 3-161 & 3-162, for all but the 6.0GHz case. 6.0GHz shows less variation than any other frequency presented and begins around 7dB and steadily increases up to about 15dB on average at the horizon. The peak axial ratio in the forward hemisphere is 81dB.

3.2.3 MAGNETIC FIELD SURFACE PLOTS

Presented in *Four-arm Spiral Antennas* are the instantaneous current distributions for both modes of operation on an Archimedean four-arm spiral (11). They represent, using black-and-white shading, every half-wavelength phase change of the signal as it travels along the arm. They are used to show the change in size of the active region related to both the frequency and the mode of operation. In an attempt to create a comparison for the Archimedean spiral, the plots are limited to the positive values of the normal magnetic field. The plots are also limited to an amplitude of 5.0 A/m that corresponds to black, while zero and negative correspond to white. Observing the plots, the intent is to view the extent to which the current travels along each element type and to deduce the active region. Comparisons are made between frequency, using 4.0 & 8.0GHz, and mode of operation.

At 4.0GHz, the first mode is expected to operate at one wavelength circumference, or about 75mm (diameter of 24mm) and the second mode at a circumference of around 150mm (diameter of 48mm). The design has a span of three turns and the normal component of the magnetic field has a mean radius of 1.5 turns for the first mode and 2.2 turns for the second mode, that correspond to the theoretical sizes. Figures 3-163 & 3-164 show the normal component of the magnetic field for the logarithmic spiral antennas excited at 4.0GHz in the first and second modes of operation, respectively. The active region is between a single pair of arms for the first mode and instead is symmetric about the center between two pair of arms for the second mode. In both modes of operation the energy in between the arms diminishes at an accelerated rate beyond the active region. Still, at 4.0GHz in the second mode, a small but noticeable amount of energy reaches the end of the arms and builds along the cavity wall; a noticeable effect of truncation.

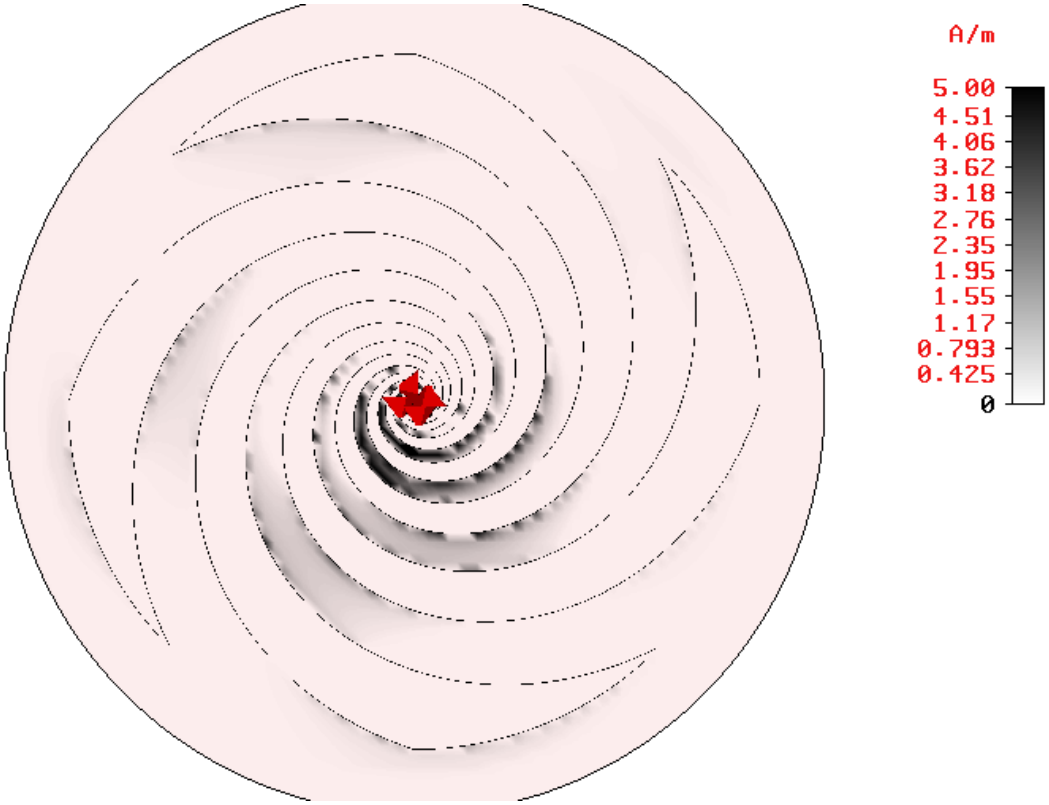

FIGURE 3-163: LOGARITHMIC SPIRAL NORMAL H-FIELD [4.0GHZ - MODE 1]

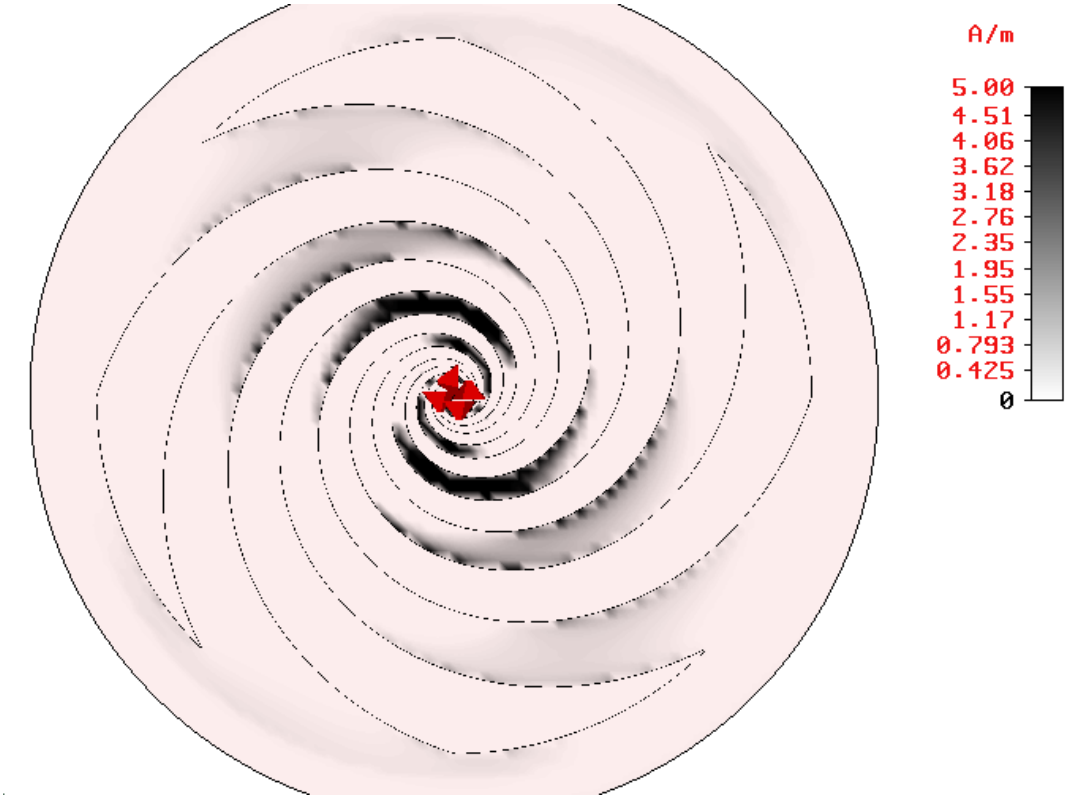

FIGURE 3-164: LOGARITHMIC SPIRAL NORMAL H-FIELD [4.0GHZ - MODE 2]

At 8.0GHz, the first mode is expected to operate at one wavelength circumference, or about 37.5mm (diameter of 12mm) and the second mode at a circumference of around 75mm (diameter of 24mm). The design has a span of three turns and the normal component of the magnetic field has a mean radius of 0.85 turns for the first mode and 1.5 turns for the second mode, that correspond to the theoretical sizes. Figures 3-165 & 3-166 show the normal component of the magnetic field for the logarithmic spiral antennas excited at 8.0GHz in the first and second modes of operation, respectively. Again, the active region is between a single pair of arms for the first mode and instead is symmetric about the center between two pair of arms for the second mode. In both modes of operation the energy in between the arms diminishes at an accelerated rate beyond the active region. At 8.0GHz in the second mode, there is almost no energy remaining by the end of the arms to build along the cavity wall.

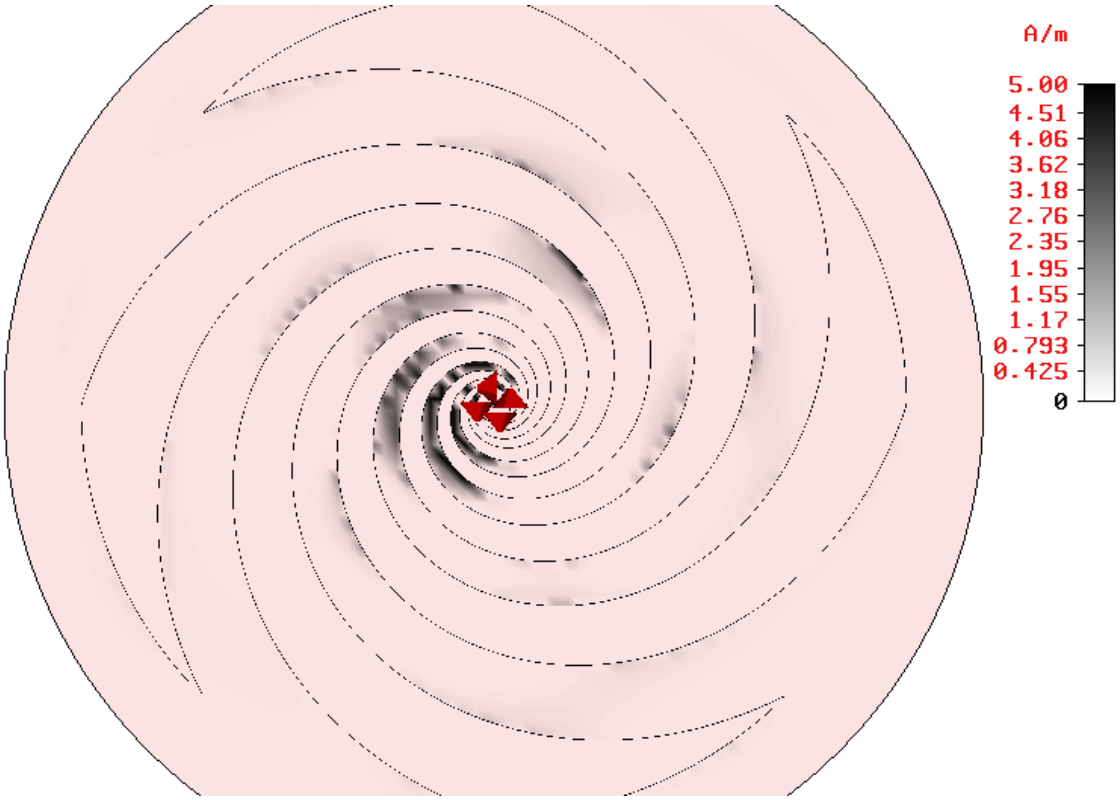

FIGURE 3-165: LOGARITHMIC SPIRAL NORMAL H-FIELD [8.0GHZ - MODE 1]

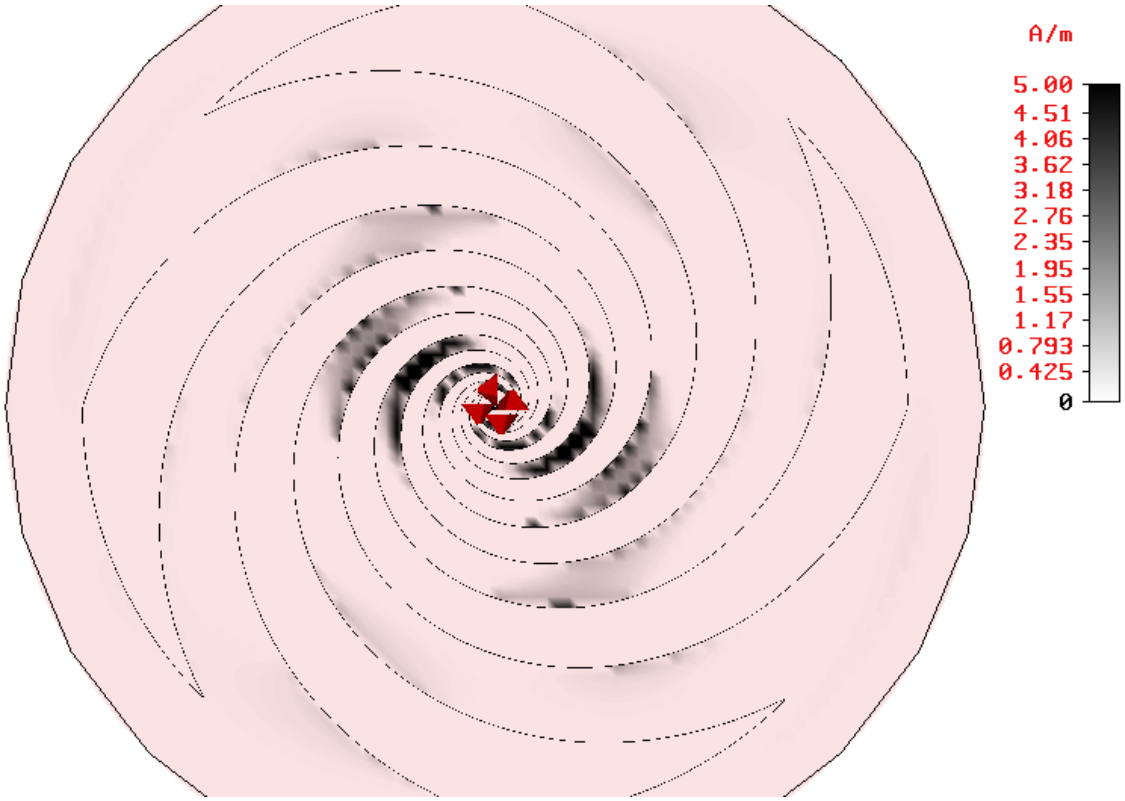

FIGURE 3-166: LOGARITHMIC SPIRAL NORMAL H-FIELD [8.0GHZ - MODE 2]

The Archimedean spiral is expected to exhibit the same active region as the logarithmic spiral. At 4.0GHz, the first mode is expected to operate at one wavelength circumference, or about 75mm (diameter of 24mm) and the second mode at a circumference of around 150mm (diameter of 48mm). The Archimedean design has a span of ten turns and the normal component of the magnetic field has a mean radius of 1.85 turns for the first mode and 4.2 turns for the second mode, that correspond to the theoretical sizes. Figures 3-167 & 3-168 show the normal component of the magnetic field for the Archimedean spiral antenna excited at 4.0GHz in the first and second modes of operation, respectively. The active region is singular for the first mode, or it varies by 360° at the mean radius, and instead is symmetric about the center, or varies by 720° at the mean radius, for the second mode. In both modes of operation the energy in between the arms diminishes at an accelerated rate beyond the active region. At 4.0GHz in the second mode, there is no visible energy reaching the cavity wall. The effects of truncation begin at 4GHz, but it is hard to detect any energy reaching the end of the arms based on the scaling. The Archimedean spiral uses more turns and therefore allows more energy to dissipate beyond the active region before reaching the ends.

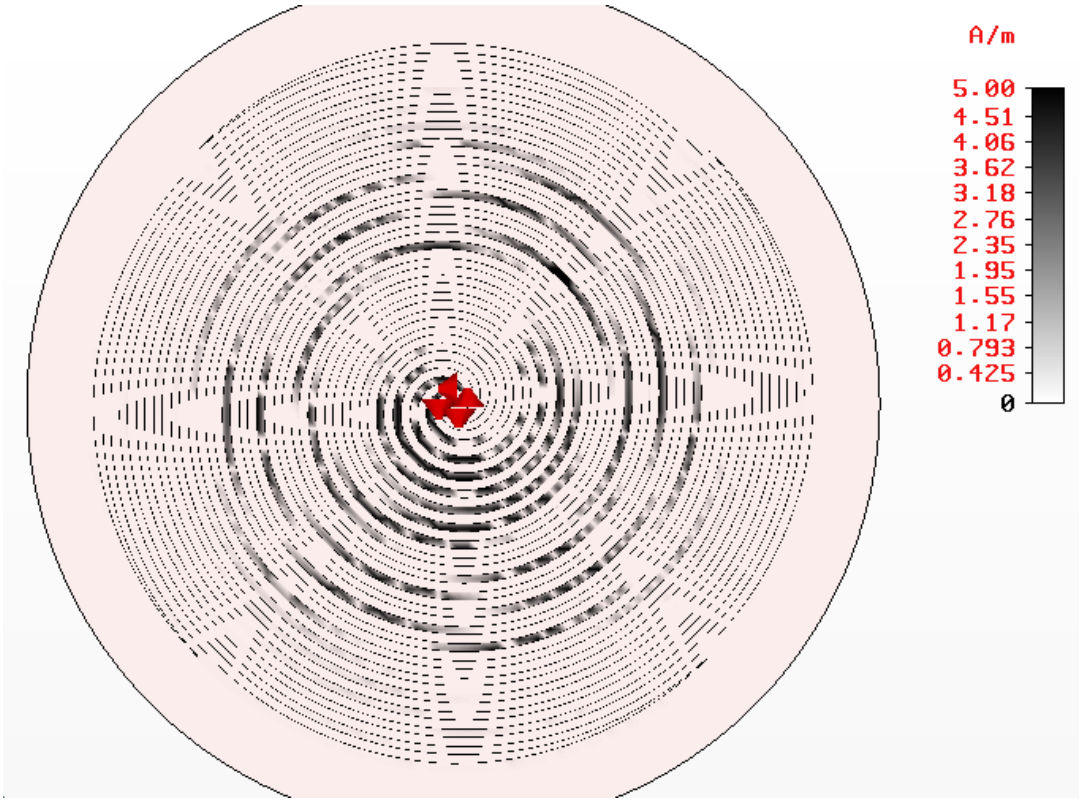

FIGURE 3-167: ARCHIMEDEAN SPIRAL NORMAL H-FIELD [4.0GHZ - MODE 1]

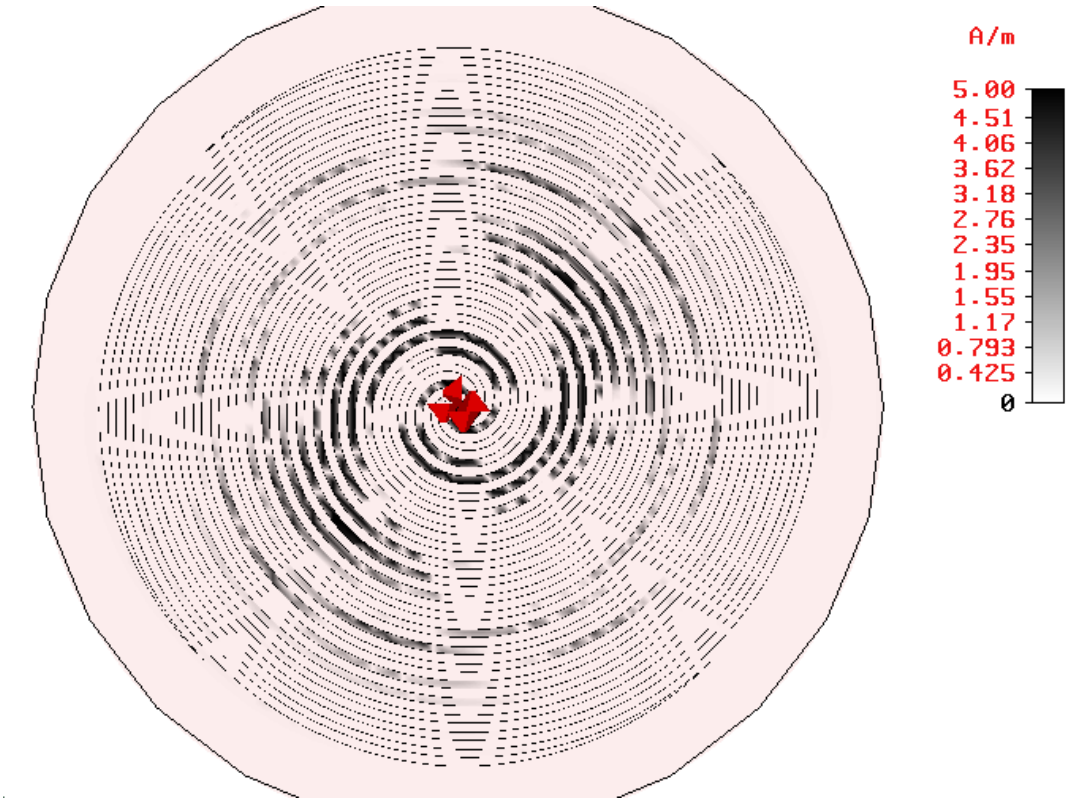

FIGURE 3-168: ARCHIMEDEAN SPIRAL NORMAL H-FIELD [4.0GHZ - MODE 2]

The frequency will scale for the Archimedean spiral in the same way it does for the logarithmic spiral. At 8.0GHz, the first mode is expected to operate at one wavelength circumference, or about 37.5mm (diameter of 12mm) and the second mode at a circumference of around 75mm (diameter of 24mm). The design has a span of ten turns and the normal component of the magnetic field has a mean radius of 0.67 turns for the first mode and 1.85 turns for the second mode, that correspond to the theoretical sizes. Figures 3-169 & 3-170 show the normal component of the magnetic field for the Archimedean spiral antenna excited at 8.0GHz in the first and second modes of operation, respectively. The active region is singular for the first mode, or it varies by 360° at the mean radius, and instead is symmetric about the center, or varies by 720° at the mean radius, for the second mode. In both modes of operation the energy in between the arms diminishes at an accelerated rate beyond the active region. At 8.0GHz in the second mode, there is almost no energy remaining by the end of the arms to build along the cavity wall.

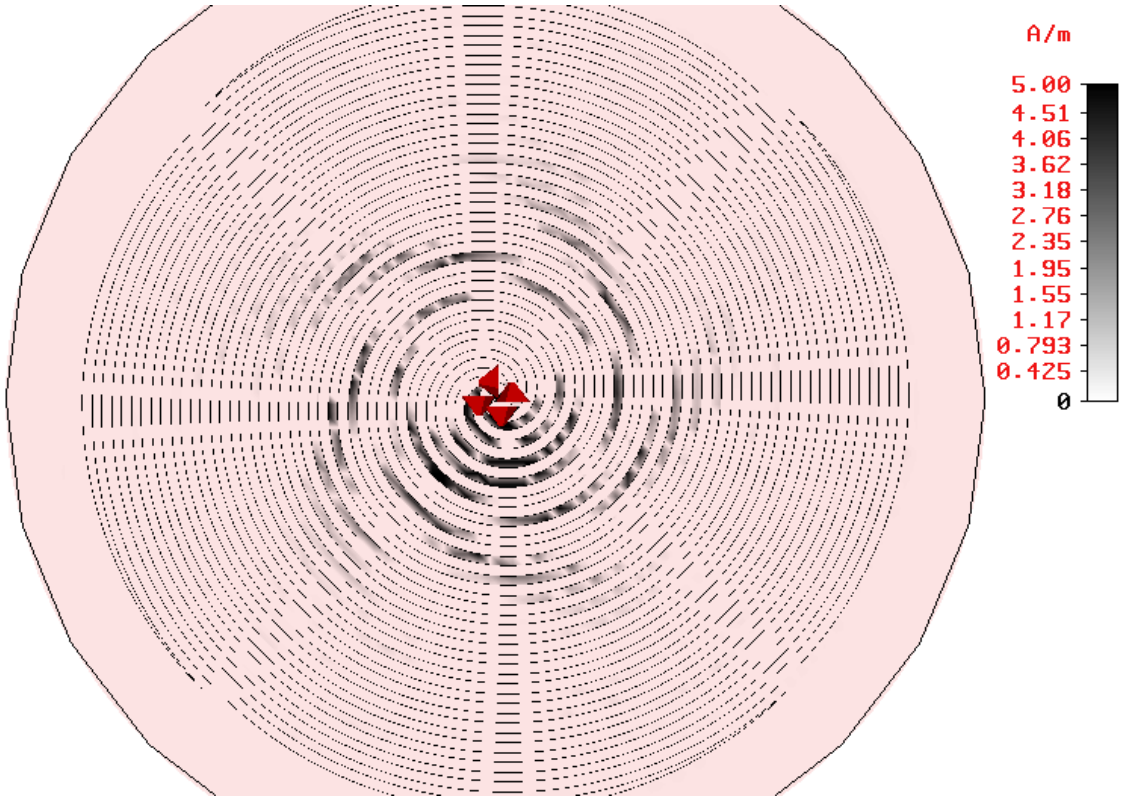

FIGURE 3-169: ARCHIMEDEAN SPIRAL NORMAL H-FIELD [8.0GHZ - MODE 1]

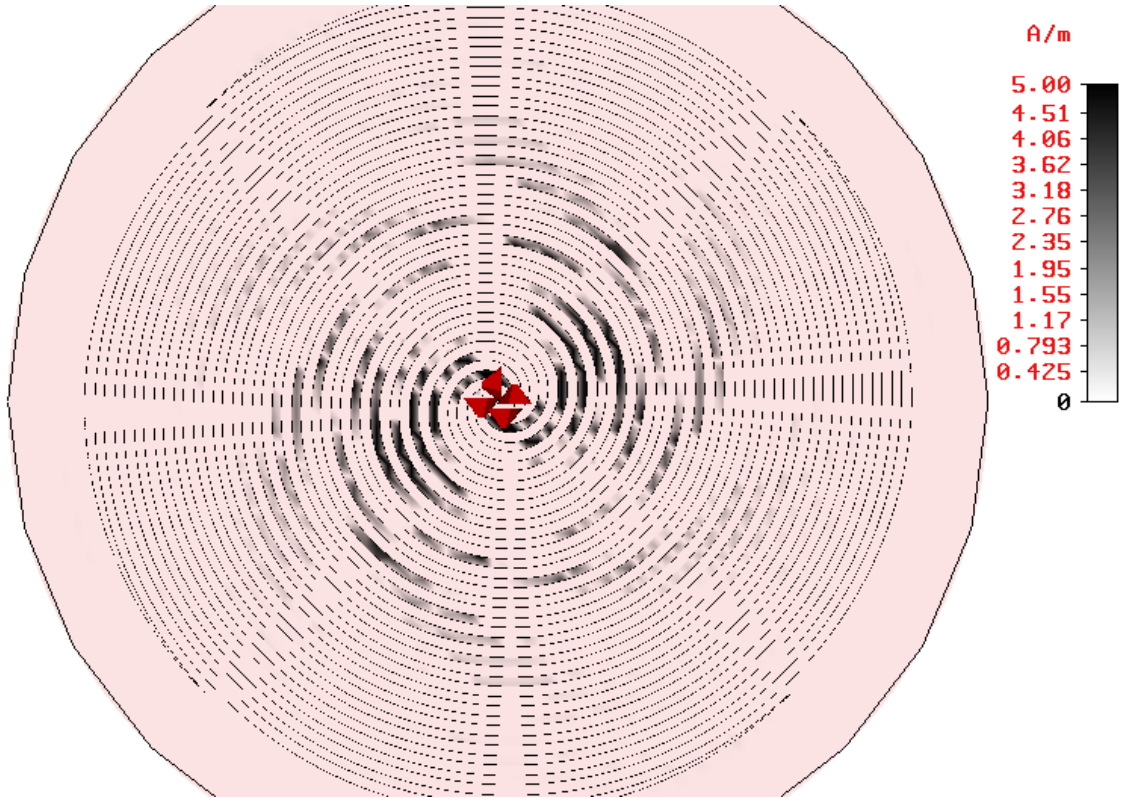

FIGURE 3-170: ARCHIMEDEAN SPIRAL NORMAL H-FIELD [8.0GHZ - MODE 2]

The circular log-periodic, with π/8-overlap, is expected to exhibit the same active region for both modes of operation. At 4.0GHz, the first mode is expected to occur where a ring of current has a phase that varies by 360° for the first mode or 720° for the second mode. The broadband return loss results show 4.0GHz to lie between the first and second dips in the simulated spectrum and the farfield has an increased directivity and decreased beamwidth. This combination suggests that the active region is located at a circumference greater than one wavelength. The circumference of the ninth tooth is between 121-156mm (diameter of 38.5-49.7mm) and equivalent to 1.6-2.0λ. Figures 3-171 & 3-172 show the normal component of the magnetic field for the circular log-periodic antenna with π/8-overlap excited at 4.0GHz in the first and second modes of operation, respectively. From the figure it is clear that there is energy out to about the eleventh tooth. It is not clear whether the energy diminishes rapidly beyond the active region, but similar to the logarithmic spiral there is enough energy to visibly build up along the cavity wall.

The same antenna excited at 8.0GHz is shown in Figures 3-173 & 3-174 for the first and second modes, respectively. The circumference of the sixth tooth is between 56-73mm (diameter of 18-23mm) and equivalent to 1.5-1.9λ. From the figure it is clear that there is energy out to about the ninth tooth but it rapidly diminishes and does not noticeable build up along the cavity wall.

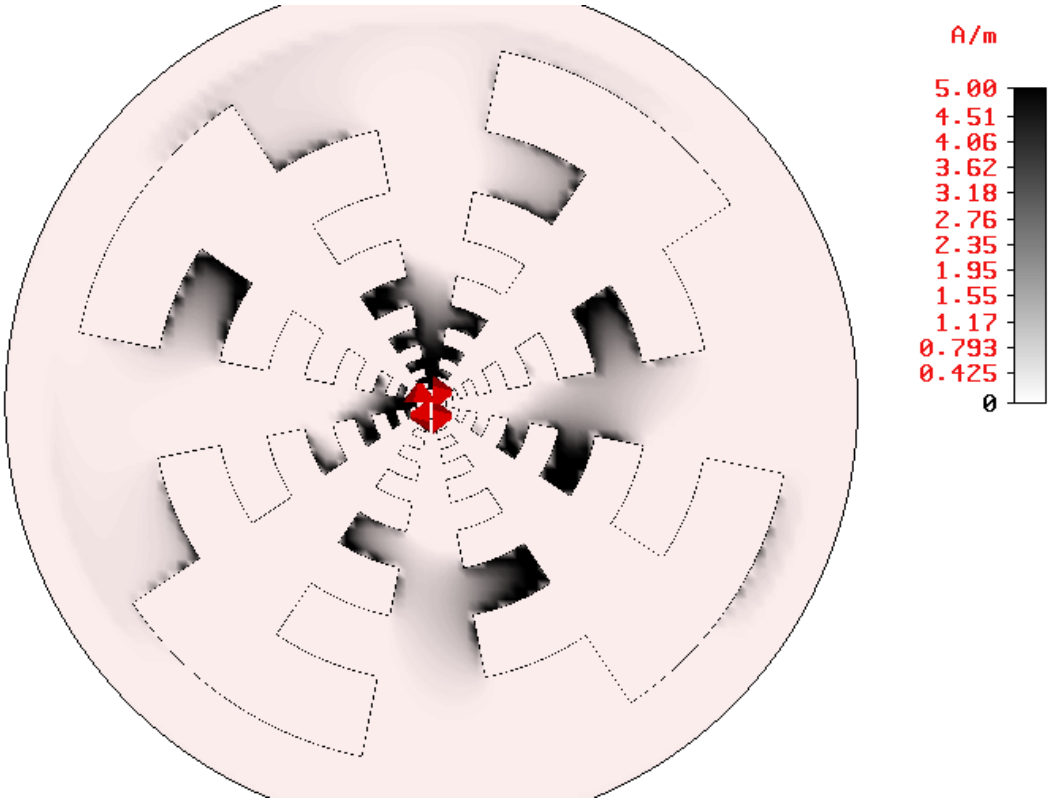

FIGURE 3-171: CIRCULAR LOG-PERIODIC [Π/8] NORMAL H-FIELD [4.0GHZ - MODE 1]

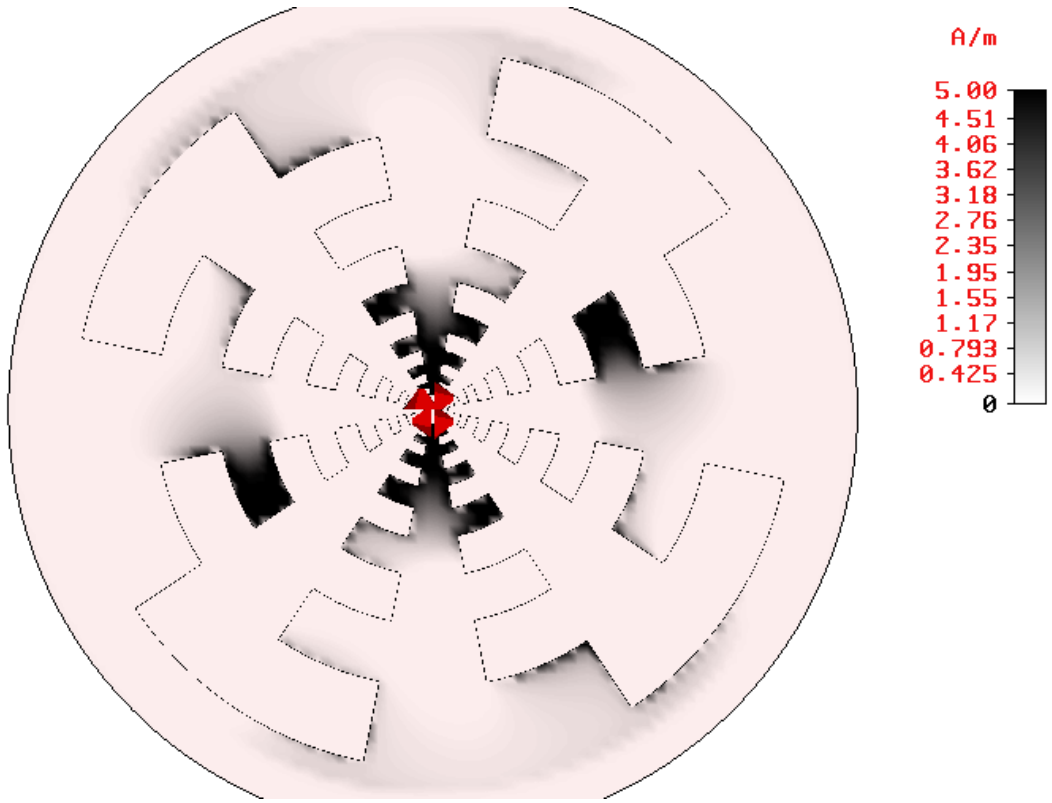

FIGURE 3-172: CIRCULAR LOG-PERIODIC [Π/8] NORMAL H-FIELD [4.0GHZ - MODE 2]

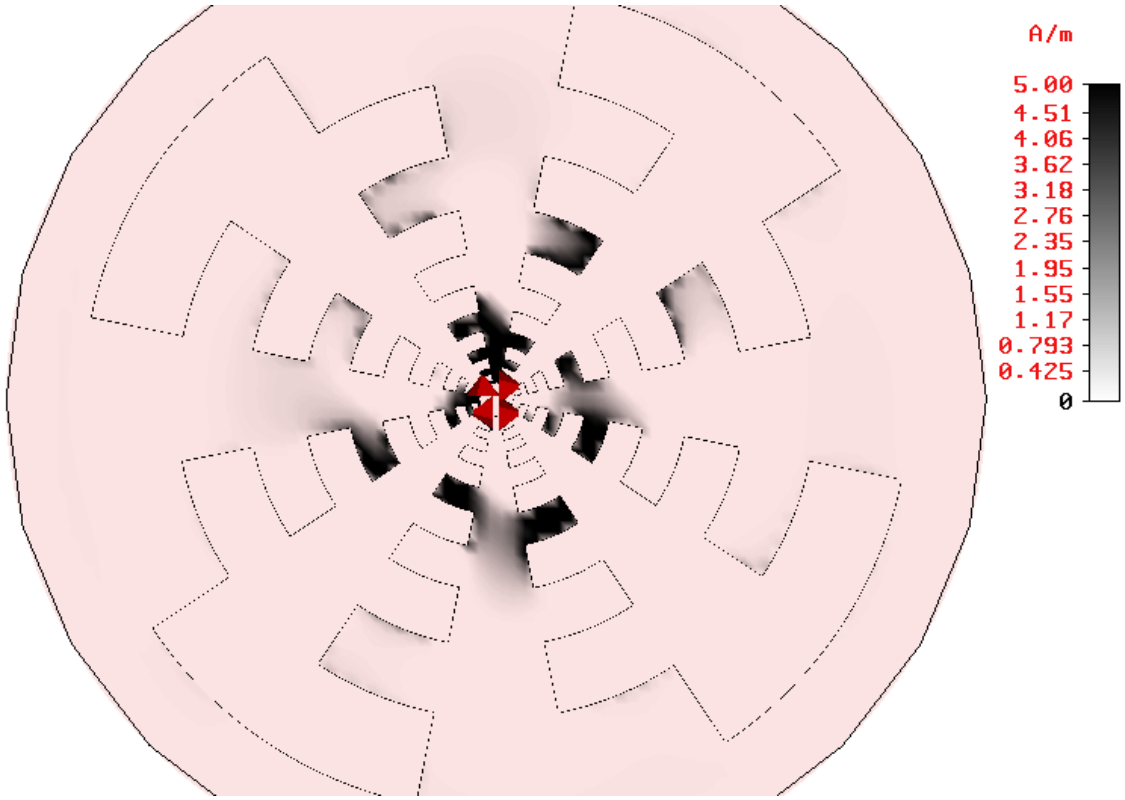

FIGURE 3-173: CIRCULAR LOG-PERIODIC [Π/8] NORMAL H-FIELD [8.0GHZ - MODE 1]

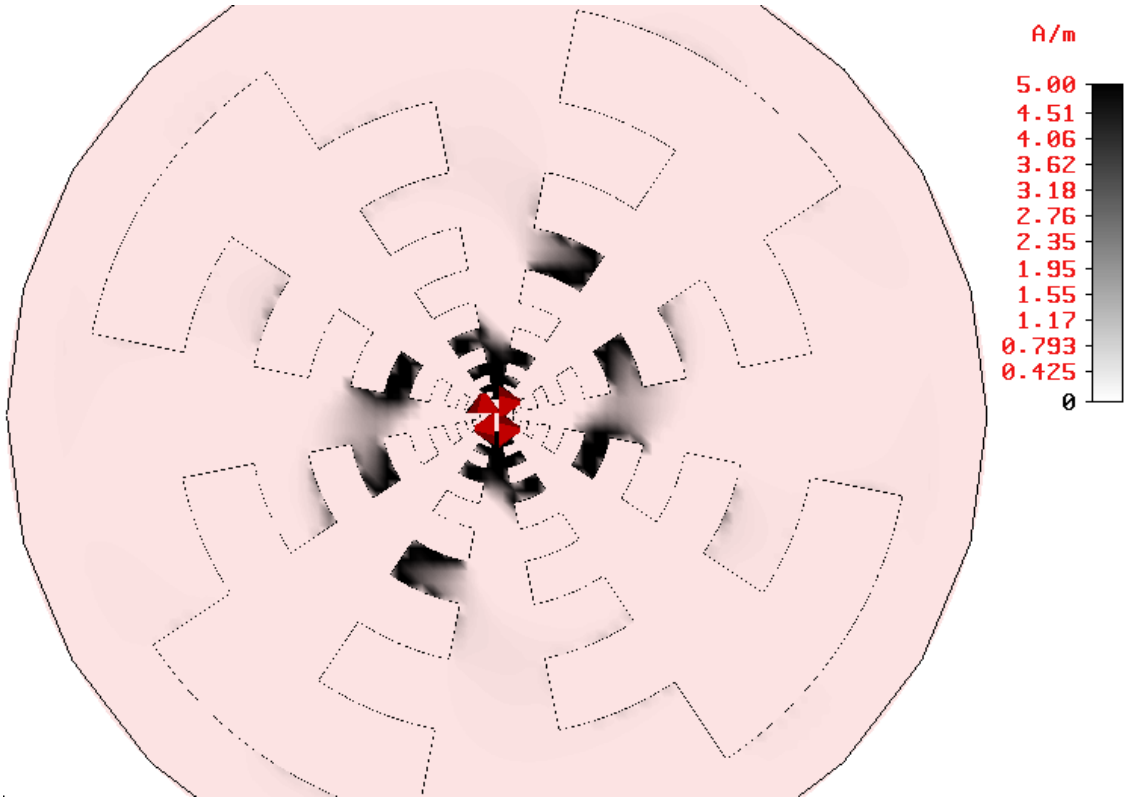

FIGURE 3-174: CIRCULAR LOG-PERIODIC [Π/8] NORMAL H-FIELD [8.0GHZ - MODE 2]

The circular log-periodic, with π/12-overlap, is expected to exhibit the same active region for both modes of operation. At 4.0GHz, the first mode is expected to occur where a ring of current has a phase that varies by 360° for the first mode or 720° for the second mode. The broadband return loss results show 4.0GHz to lie between the second and third dips in the simulated spectrum but the farfield has directivity and beamwidth similar to both spiral antennas. This combination suggests that the active region is located at a circumference closer to one wavelength than the circular long-tooth log-periodic. The circumference of the seventh tooth is between 73-94mm (diameter of 23-30mm) and equivalent to 1.0-1.25λ. Figures 3-175 & 3-176 show the normal component of the magnetic field for the circular log-periodic antenna with π/8-overlap excited at 4.0GHz in the first and second modes of operation, respectively. From the figure it is clear that there is energy out to about the tenth tooth. It is not clear whether the energy diminishes rapidly beyond the active region, but similar to the logarithmic spiral there is enough energy to visibly build up along the cavity wall.

The same antenna excited at 8.0GHz is shown in Figures 3-177 & 3-178 for the first and second modes, respectively. The circumference of the fifth tooth is between 43-56mm (diameter of 14-18mm) and equivalent to 1.1-1.5λ. From the figure it is clear that there is energy out to about the eighth tooth but it rapidly diminishes and does not noticeable build up along the cavity wall.

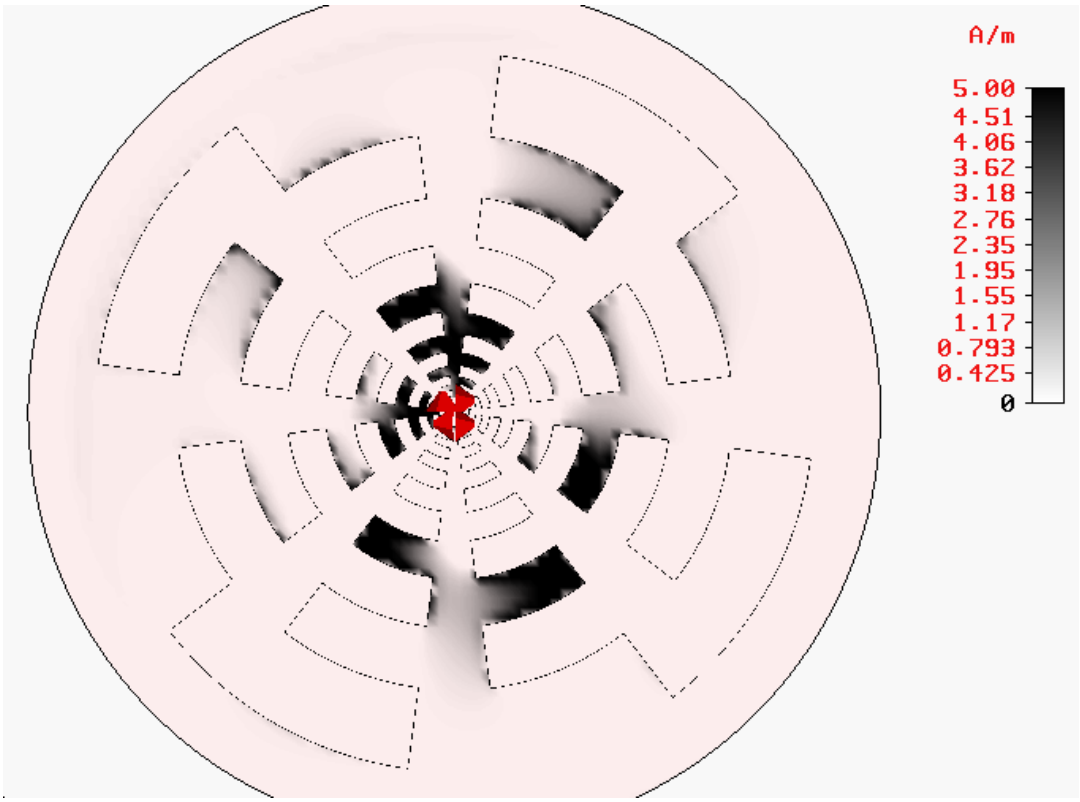

FIGURE 3-175: CIRCULAR LOG-PERIODIC [Π/12] NORMAL H-FIELD [4.0GHZ - MODE 1]

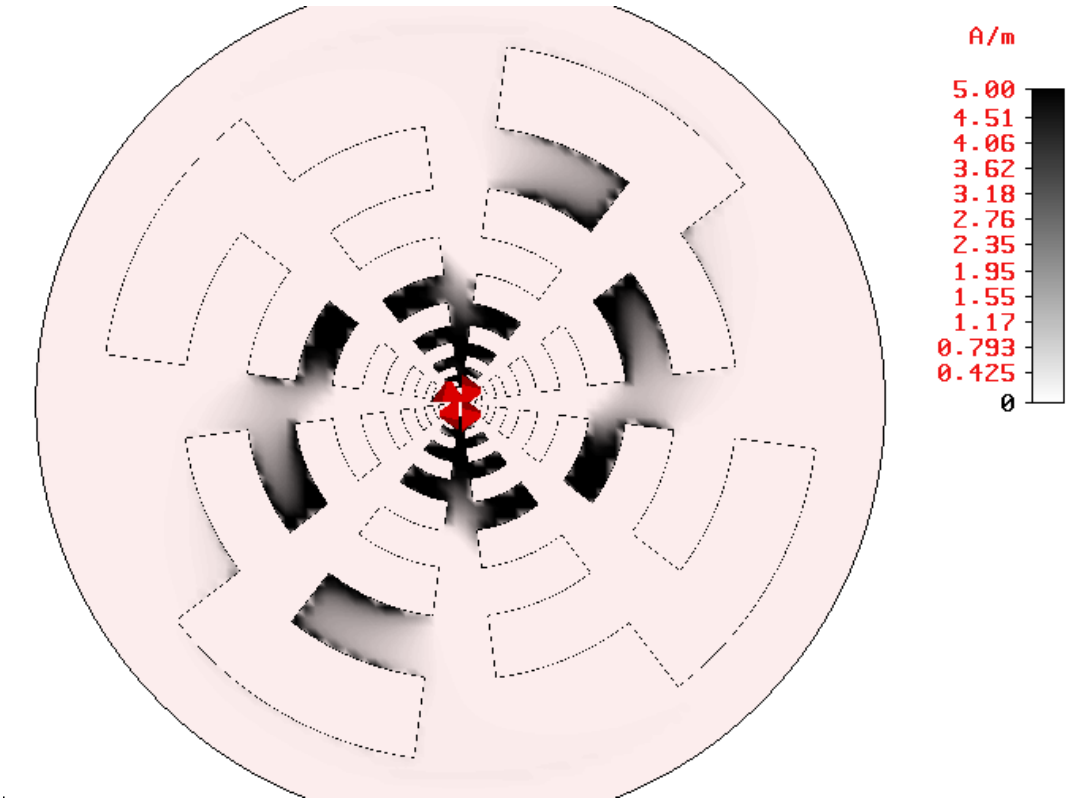

FIGURE 3-176: CIRCULAR LOG-PERIODIC [Π/12] NORMAL H-FIELD [4.0GHZ - MODE 2]

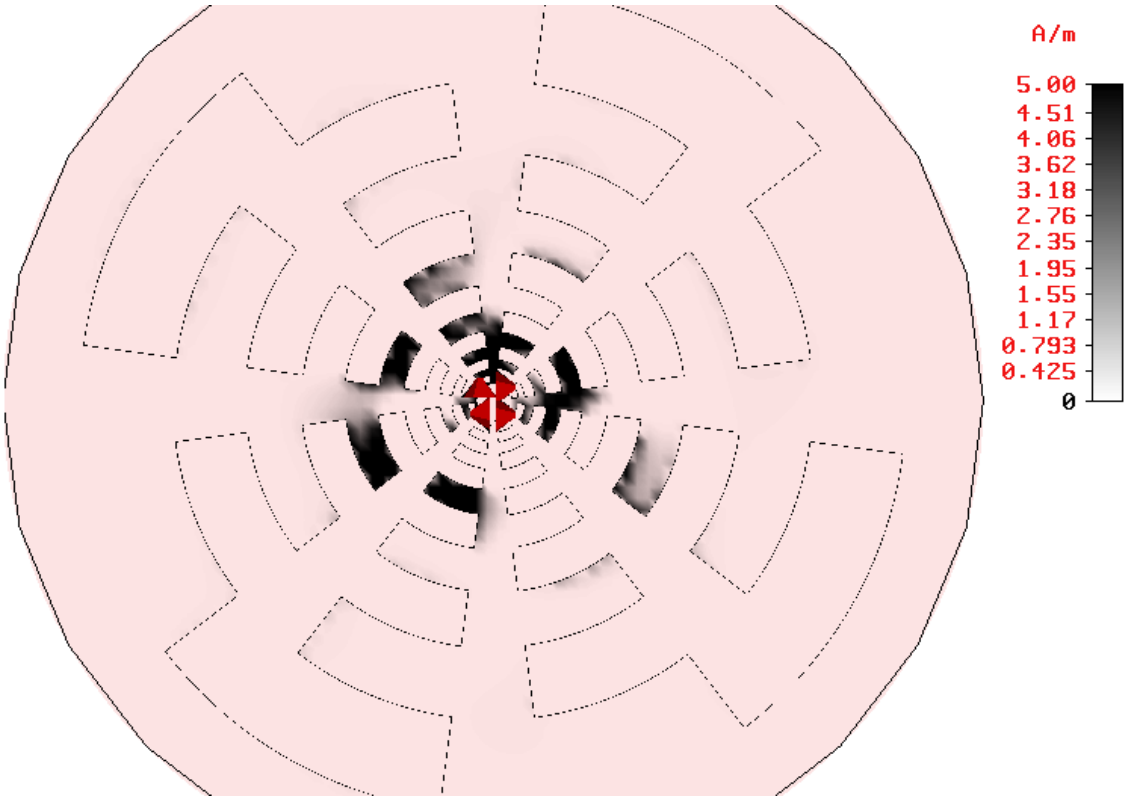

FIGURE 3-177: CIRCULAR LOG-PERIODIC [Π/12] NORMAL H-FIELD [8.0GHZ - MODE 1]

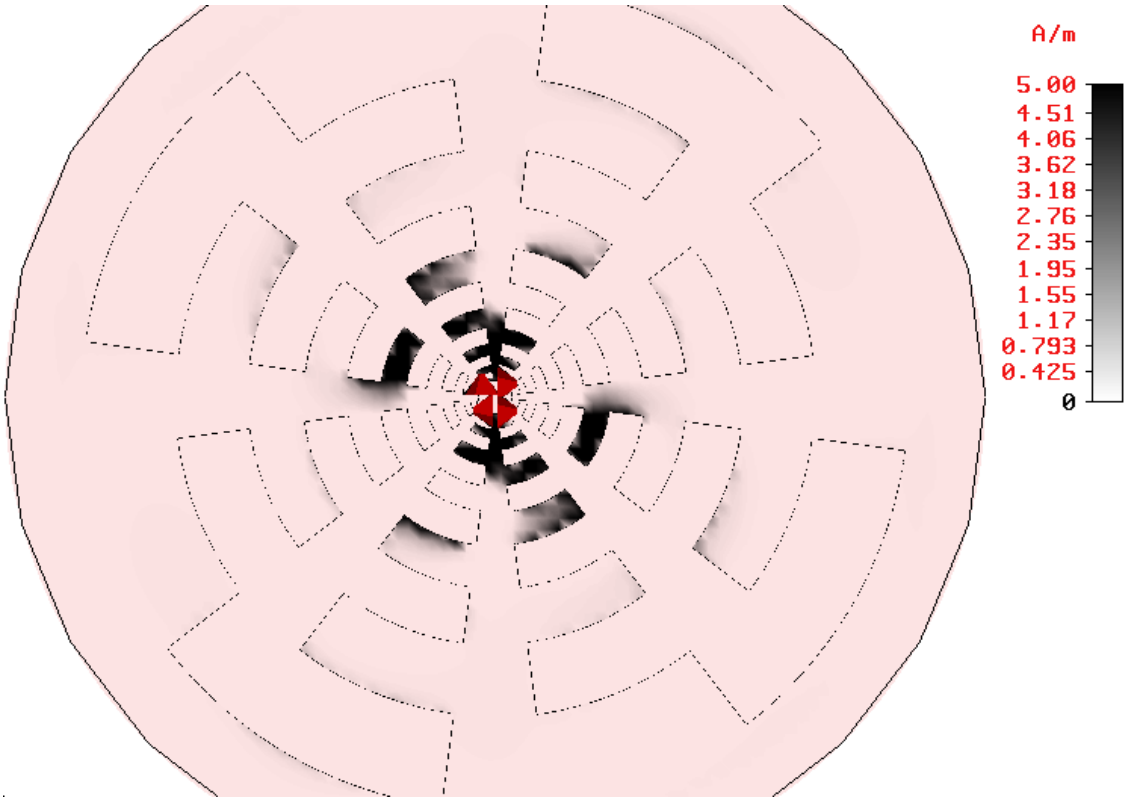

FIGURE 3-178: CIRCULAR LOG-PERIODIC [Π/12] NORMAL H-FIELD [8.0GHZ - MODE 2]

The circular sinuous is often viewed as a hybrid of the circular log-periodic and spiral antennas and there are no specific expectations in terms of active regions. From the broadband return loss simulation results, for the π/4-interleave version, 4.0GHz is located between the fourth and fifth dips from the highest frequency in the spectrum which suggests that the active region occurs along the length between the fourth and fifth wraps. Figures 3-179 & 3-180 show the normal component of the magnetic field for the circular sinuous antenna with π/4-interleave excited at 4.0GHz in the first and second modes of operation, respectively. It is shown that the energy related to the first mode begins to diminish after the sixth cell or during the seventh length. This suggests that while the mean energy in the active region may occur along the fifth length, there is still considerable energy that extends out to the seventh which is similar to both spiral antennas. The fifth length occurs between 0.75-1.0λ and the seventh length occurs between 1.5-2.0λ at 4.0GHz. For the second mode of operation, significant energy is visible out to a greater extent, or about one extra length, than in the first mode. Still, there is minimal energy build up along the cavity wall for both modes. The active region varies by 360° for the first mode and by 720° for the second mode.

The same antenna excited at 8.0GHz is shown in Figures 3-181 & 3-182 for the first and second modes, respectively. The active region scales with frequency as expected and the results are shifted by two wraps which places it between the second and third dips from the highest frequency dip and correlates to being between the second and third cells, or wraps. The third length occurs between 0.75-1.0λ and the fifth length, during which the energy diminishes, occurs between 1.5-2.0λ at 8.0GHz. Passing around the structure at the active region shows it varies by 360° for the first mode and by 720° for the second mode.

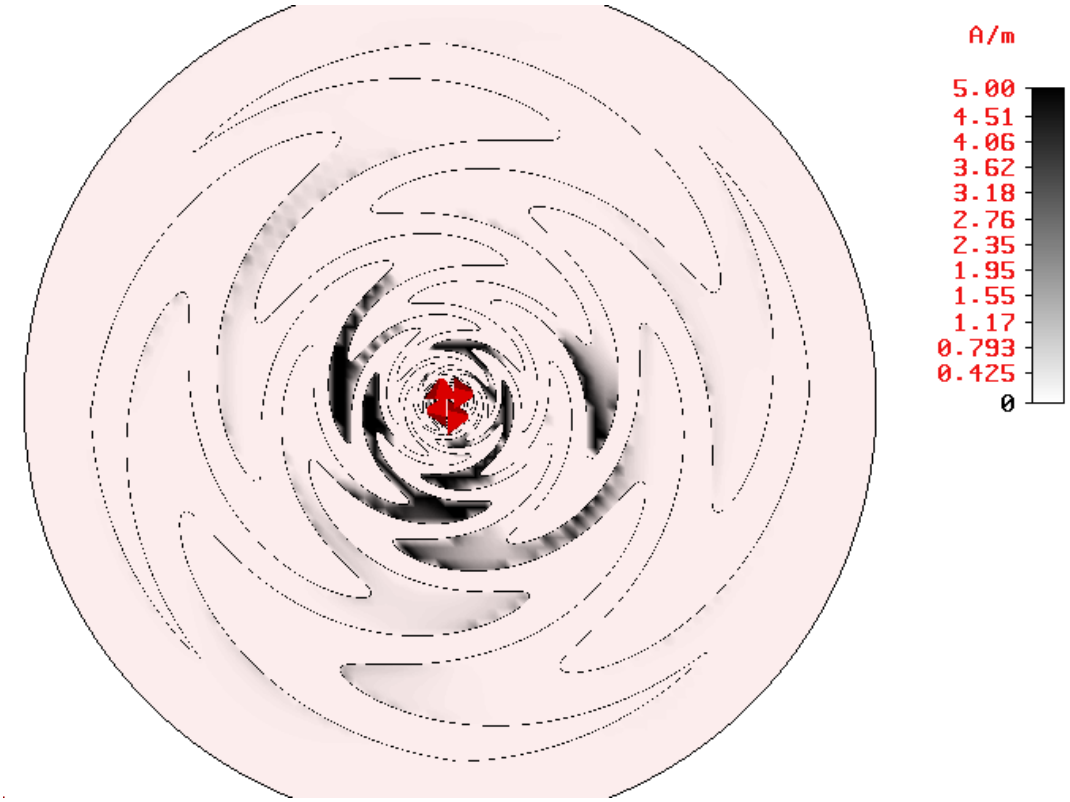

FIGURE 3-179: CIRCULAR SINUOUS [Π/4] NORMAL H-FIELD [4.0GHZ - MODE 1]

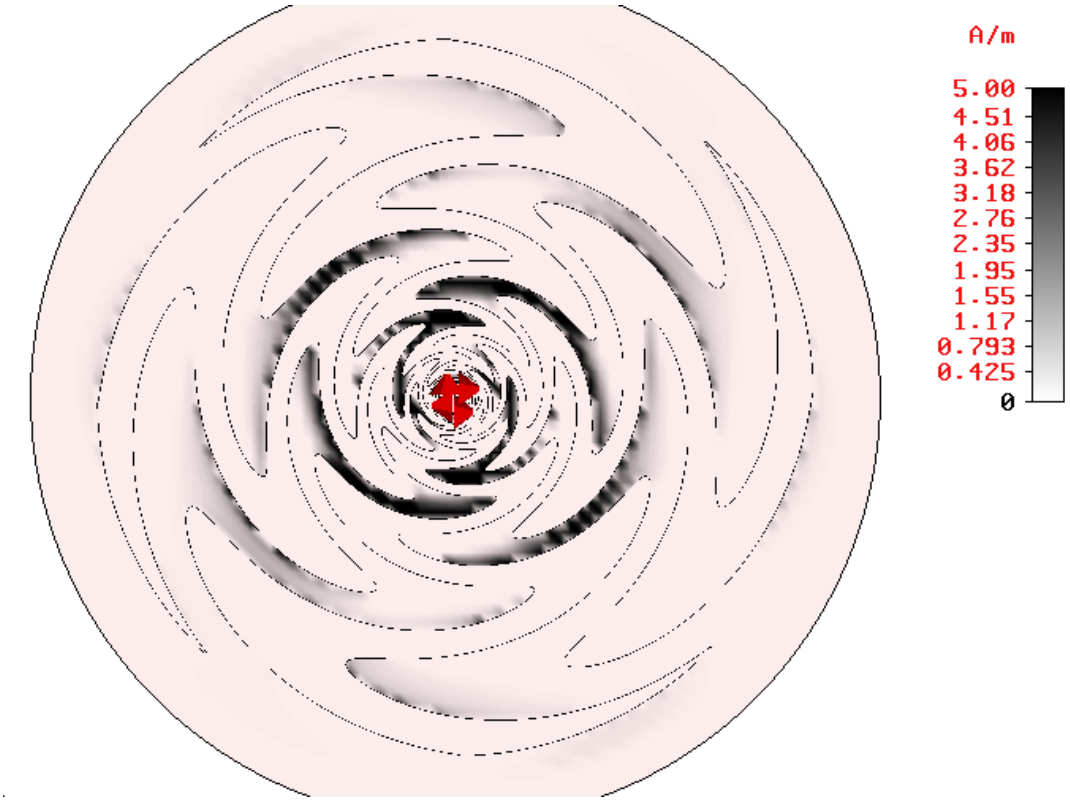

FIGURE 3-180: CIRCULAR SINUOUS [Π/4] NORMAL H-FIELD [4.0GHZ - MODE 2]

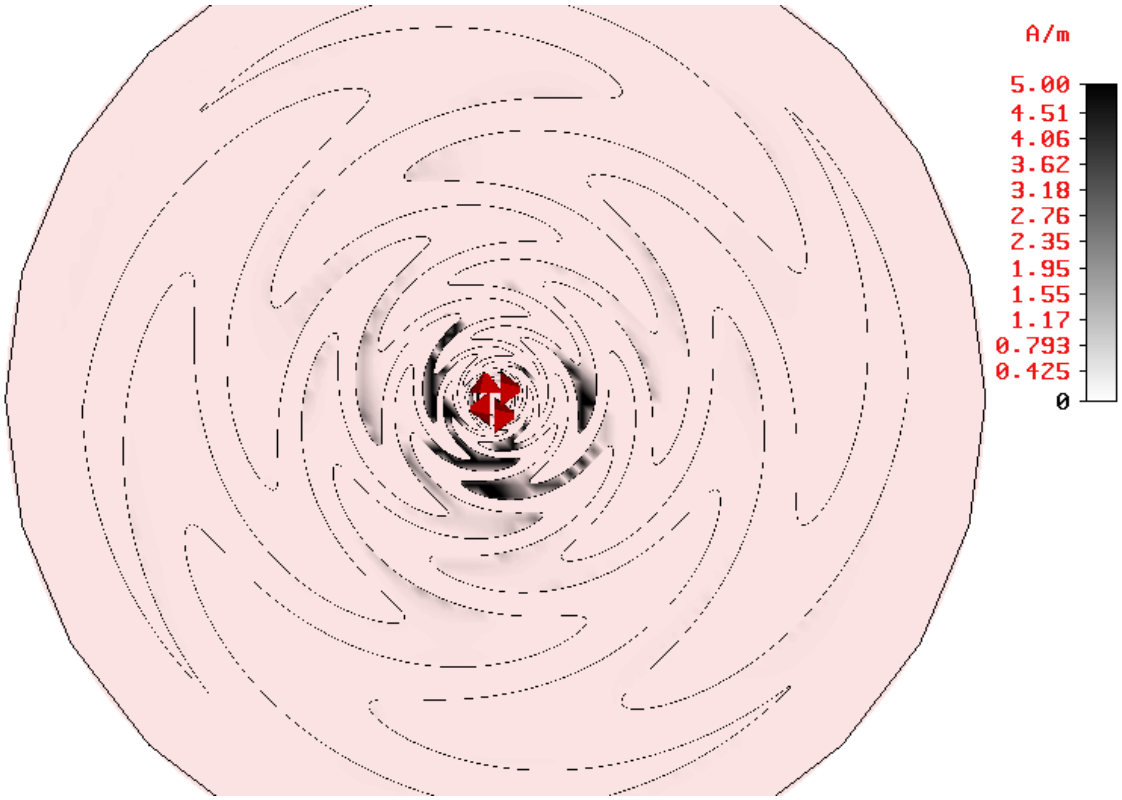

FIGURE 3-181: CIRCULAR SINUOUS [Π/4] NORMAL H-FIELD [8.0GHZ - MODE 1]

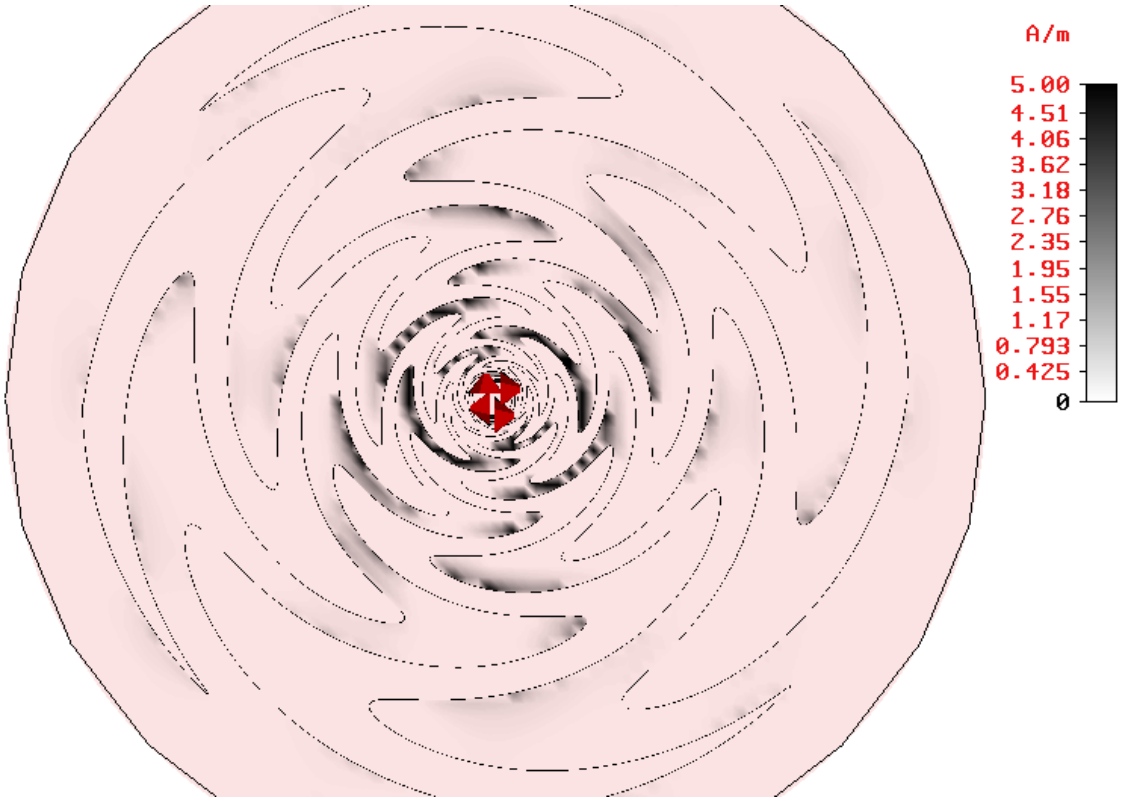

FIGURE 3-182: CIRCULAR SINUOUS [Π/4] NORMAL H-FIELD [8.0GHZ - MODE 2]

From the broadband return loss simulation results, for the π/3-interleave version of the circular sinuous, 4.0GHz is located between the fourth and fifth dips from the highest frequency dip. The frequency point is very nearly at the fifth dip which suggests that the active region occurs along the length between the fourth and fifth wraps or along the fifth length. Figures 3-183 & 3-184 show the normal component of the magnetic field for the circular sinuous antenna with π/4-interleave excited at 4.0GHz in the first and second modes of operation, respectively. It is shown that the energy related to the first mode begins to diminish after the sixth cell or during the seventh length. This suggests that while the mean energy in the active region may occur along the fifth length, there is still considerable energy that extends out to the seventh which is similar to both spiral antennas. The fifth length occurs between 0.75-1.0λ and the seventh length occurs between 1.5-2.0λ at 4.0GHz. For the second mode of operation, significant energy is visible out to a greater extent, or about one extra length, than in the first mode. Still, there is minimal energy build up along the cavity wall for both modes. The active region varies by 360° for the first mode and by 720° for the second mode.

The same antenna excited at 8.0GHz is shown in Figures 3-185 & 3-186 for the first and second modes, respectively. The active region scales with frequency as expected and the results are shifted by two wraps which places it between the second and third dips from the highest frequency dip and correlates to being between the second and third cells, or wraps. The third length occurs between 0.75-1.0λ and the fifth length, during which the energy diminishes, occurs between 1.5-2.0λ at 8.0GHz. Passing around the structure at the active region shows it varies by 360° for the first mode and by 720° for the second mode.

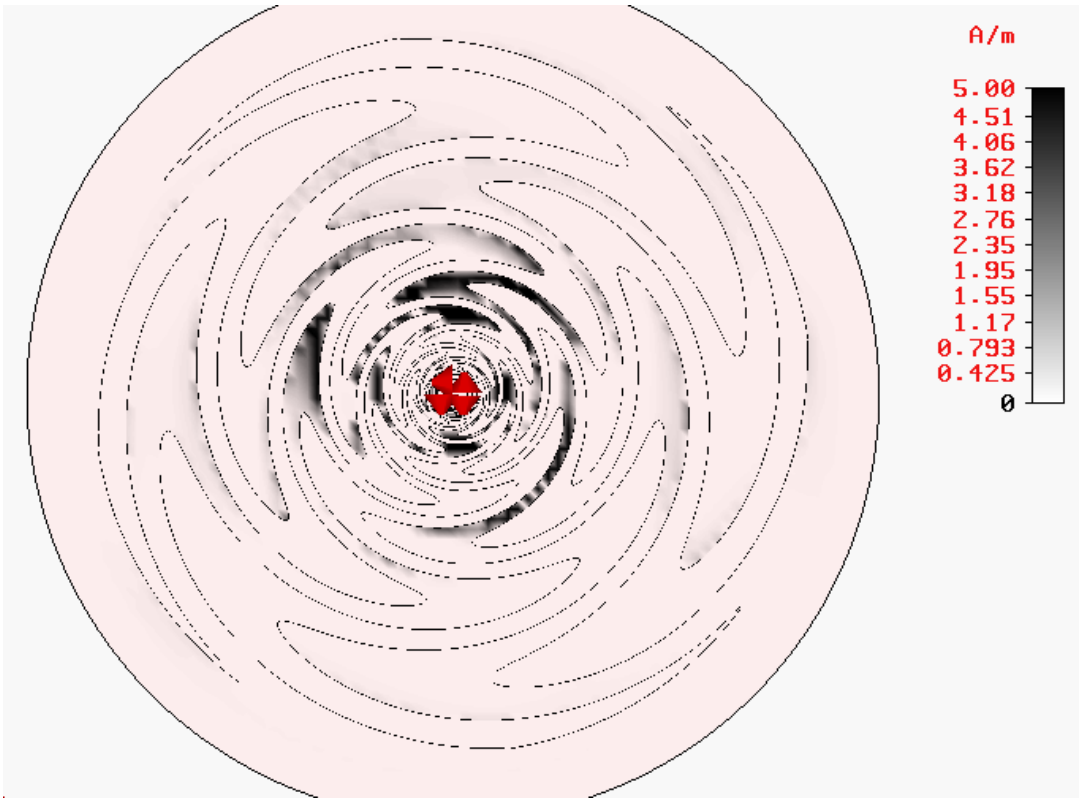

FIGURE 3-183: CIRCULAR SINUOUS [Π/3] NORMAL H-FIELD [4.0GHZ - MODE 1]

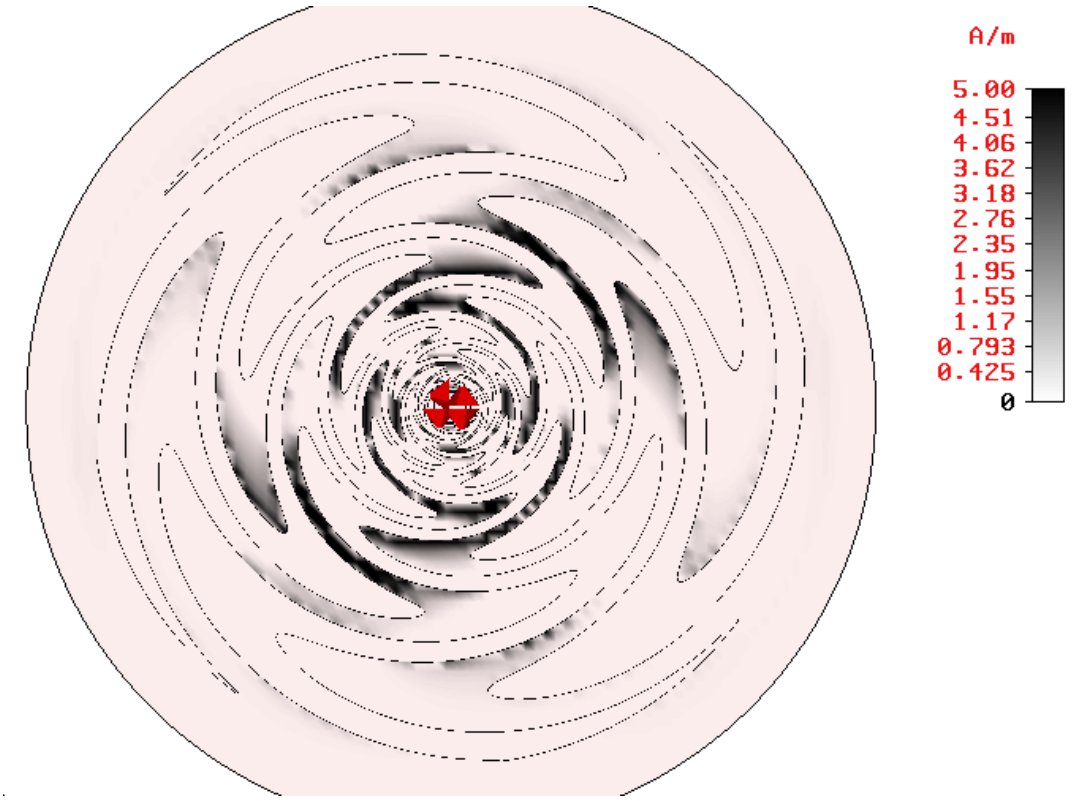

FIGURE 3-184: CIRCULAR SINUOUS [Π/3] NORMAL H-FIELD [4.0GHZ - MODE 2]

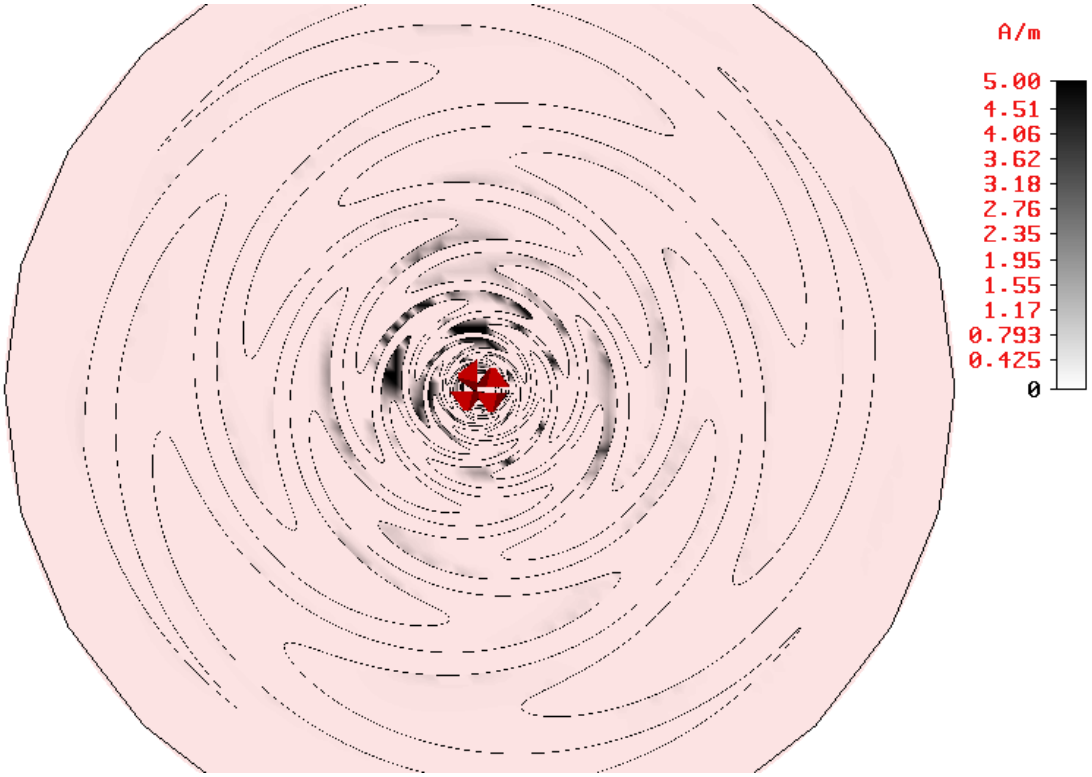

FIGURE 3-185: CIRCULAR SINUOUS [Π/3] NORMAL H-FIELD [8.0GHZ - MODE 1]

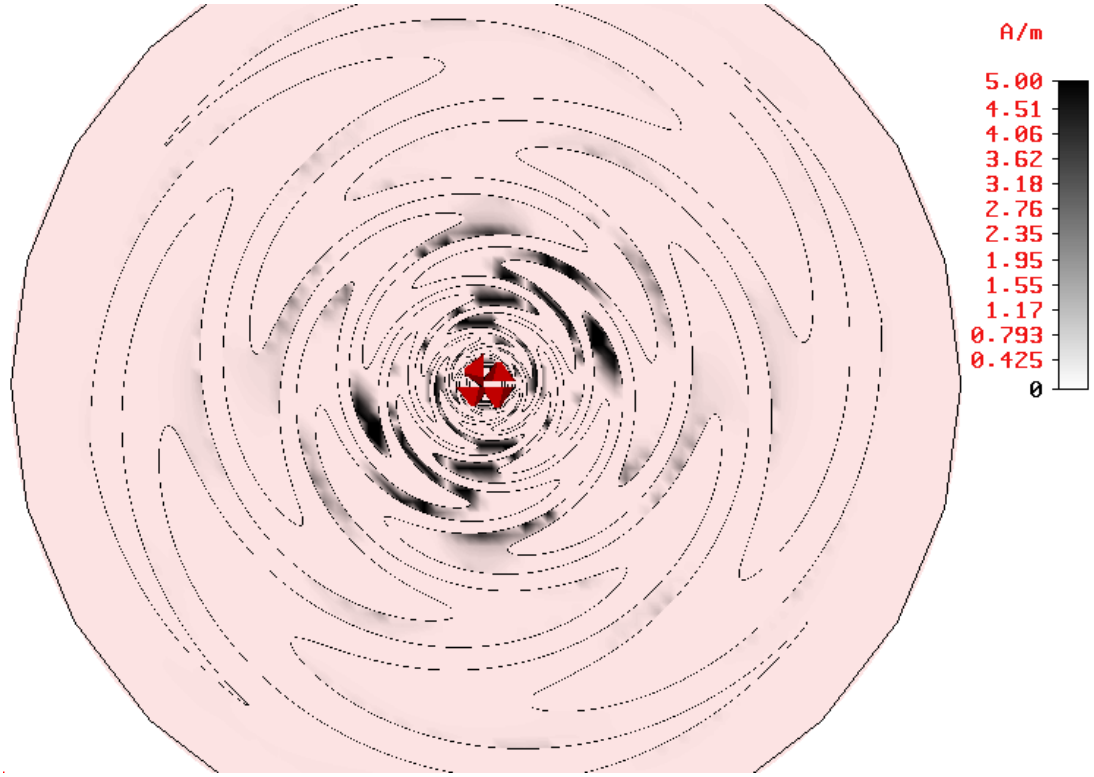

FIGURE 3-186: CIRCULAR SINUOUS [Π/3] NORMAL H-FIELD [8.0GHZ - MODE 2]

3.3 SIMULATION COMPARISON

The results for the previous subsection are tabulated to quickly compare the response of the six designs. The first mode of operation performance is shown in Table 3-1. Directivity, in dBi, is compared at 9.0GHz which is the maximum of the four frequencies presented. Along with directivity, the -3dB elevation angle of the 9GHz pattern shows the beamwidth. Five of the antennas are very similar with directivity between 8-9dBi and -3dB beamwidth out to 33-36°. The exception is for the circular log-periodic with π/8-overlap which has the maximum of 11.8dBi and a beamwidth of only 21°. The magnitude and phase ripples are compared at 2.0, 6.0 and 18.0GHz. For the first mode, 2.0GHz at 20° in elevation is commonly the best case for both the magnitude and phase ripple, while 18.0GHz at 60° in elevation is commonly the worst case. Yet, for both circular log-periodics, the operational bandwidth extends to frequencies higher than 18.0GHz and their magnitude and phase ripple is much lower than other designs. Also, an exception is made for the circular sinuous with π/4-interleave that achieves lower ripple by radiating at 18.0GHz from the first partial length that leads into the first wrap. 6.0GHz is the mid-band case and ripple values at 20° in elevation are typically only slightly higher than for 2.0GHz. All of the antennas seem to radiate effectively at this frequency and it is noted that the logarithmic spiral actually has the highest magnitude and phase ripple. Axial ratios show the circularity of the polarization and are compared at the mid-band. The only anomaly at 20° in elevation is the circular log-periodic with π/8-overlap that has increased values which are the tradeoff for having increased directivity. Finally, the active regions, calculated from the magnetic field plots are compared and a suggestion is made for the minimum design size to cover a desired frequency range.

TABLE 3-1: SIMULATION COMPARISON [MODE 1]

FACTOR	LS	AS	LP (π/8)	LP (π/12)	CS (π/4)	CS (π/3)	UNITS
DIRECTIVITY (9GHz)	8.5	8.75	11.8	8.3	8.5	8.1	dBi
-3dB (9GHz)	36°	34°	21°	33°	35°	34°	El ∠
MAGNITUDE RIPPLE (2GHz @ 20°)	±0.01	±0.01	±0.02	±0.02	±0.01	±0.001	dB
PHASE RIPPLE (2GHz @ 20°)	±0.1	±0.1	±0.2	±0.1	±0.5	±0.1	°
MAGNITUDE RIPPLE (18GHz @ 60°)	±3.5	±3.75	±1.0	±1.25	±1.25	±3.0	dB
PHASE RIPPLE (18GHz @ 60°)	±21	±24	±4.5	±5.5	±8.5	±27	°
MAGNITUDE RIPPLE (6GHz @ 20°)	±0.08	±0.04	±0.07	±0.05	±0.03	±0.01	dB
PHASE RIPPLE (6GHz @ 20°)	±0.6	±0.25	±0.3	±0.3	±0.25	±0.1	°
AVERAGE AXIAL RATIO (6GHz @ 20°)	0.7	0.6	2.1	0.6	0.6	0.7	dB
MAXIUMUM AXIAL RATIO (6GHz @ 20°)	0.8	0.7	3.1	0.9	1.0	0.9	dB
MAXIUMUM AXIAL RATIO (6GHz)	6.4	6.8	13.6	17.5	11.4	8	dB
ACTIVE REGION	1.0	1.0	1.75	1.25	1.0	1.0	λ
SUGGESTED DESIGN SIZE	0.8	0.8	1.25	0.75	0.5	0.5	λ (min)

The second mode of operation performance is shown in Table 3-2. The elevation angle maximum directivity in the second mode can vary and therefore the angle it occurs at is also compared. The -3dB elevation angles on either side of the maximum angle show the beamwidth. The angles of the maximum directivity are relatively uniform between 37-42° in elevation as are the beamwidths spanning 34-42°. The spiral antennas achieve the maximum right-hand circular polarization (RHCP) directivity of around 6.5dBi, but the rest of the antennas suffer from a lack of polarization filtering and only achieve directivity of 2.5-4.5dBi. The magnitude and phase ripples are compared at 2.0, 6.0 and 18.0GHz. For the second mode, 2.0GHz at 40° in elevation is commonly the best case for both the magnitude and phase ripple, while 18.0GHz at 60° in elevation is commonly the worst case. Yet, for both circular log-periodics, the operational bandwidth extends to frequencies higher than 18.0GHz and their magnitude and phase ripple is lower than other designs. The exception made for the circular sinuous with π/4-interleave in the first mode does not exist in the second mode where it has the worst ripple of any design. 6.0GHz is the mid-band case and ripple values at 40° in elevation are only slightly higher for the spiral than for 2.0GHz. Axial ratios show the reason for the worsening ripple, as the average values escalate for the non-spiral designs. The average values for 40° in elevation are over 20 for all but the circular sinuous with π/3-interleave and maximum values in the forward hemisphere all reach over 75. The worst cases for the spiral antennas always occur at the horizon, but for the other designs the worst cases can occur almost anywhere outside the -3dB beamwidth. Finally, the active regions, calculated from the magnetic field plots are compared and a suggestion is made for the maximum design size to cover a desired frequency range.

TABLE 3-2: SIMULATION COMPARISON [MODE 2]

FACTOR	LS	AS	LP (π/8)	LP (π/12)	CS (π/4)	CS (π/3)	UNITS
DIRECTIVITY (9GHz)	6.4	6.5	4.0	2.9	4.5	2.4	dBi
MAXIMUM (9GHz)	41°	37°	42°	38°	40°	39°	El ∠
-3dB (9GHz)	21-61°	19-59°	22-60°	22-56°	19-61°	20-59°	El ∠
MAGNITUDE RIPPLE (2GHz @ 40°)	±0.05	±0.05	±0.2	±0.2	±0.2	±0.1	dB
PHASE RIPPLE (2GHz @ 40°)	±0.3	±0.3	±1.1	±1.1	±1.3	±0.7	°
MAGNITUDE RIPPLE (18GHz @ 60°)	±2.0	±2.25	±1.25	±0.75	±1.5	±2.25	dB
PHASE RIPPLE (18GHz @ 60°)	±14	±14	±9.0	±4.5	±8.5	±17	°
MAGNITUDE RIPPLE (6GHz @ 40°)	±0.3	±0.15	±1.3	±0.7	±1.0	±1.5	dB
PHASE RIPPLE (6GHz @ 40°)	±1.5	±1.0	±8.5	±5.5	±5.5	±10	°
AVERAGE AXIAL RATIO (6GHz @ 40°)	1.4	1.5	20	28	25	8.5	dB
MAXIUMUM AXIAL RATIO (6GHz @ 40°)	1.7	1.6	39	78	47	11	dB
MAXIUMUM AXIAL RATIO (6GHz)	6.1	6.0	75	132	114	81	dB
ACTIVE REGION	2.0	2.0	1.75	1.25	1.0	1.0	λ
SUGGESTED DESIGN SIZE	2.25	2.25	2.25	1.75	1.50	1.50	λ (max)

3.4 LOGARITHMIC SPIRAL WITH A GROUND PLANE

In order to correlate with the experimental results, an infinite PEC ground plane is added to the original logarithmic spiral model and simulated in the second mode of operation with the broadband method. The tradeoff associated with including the ground plane is an increase in simulation time versus a result more closely related to the experimentation. Comparisons between both the modal return loss and farfield plots are made. Figure 3-187 shows the broadband second mode result of the original spiral model in black with the ground plane model overlain in red. The results are nearly identical, but in the region from 2.0-4.0GHz where truncation is noticeable, the ripple is slightly changed.

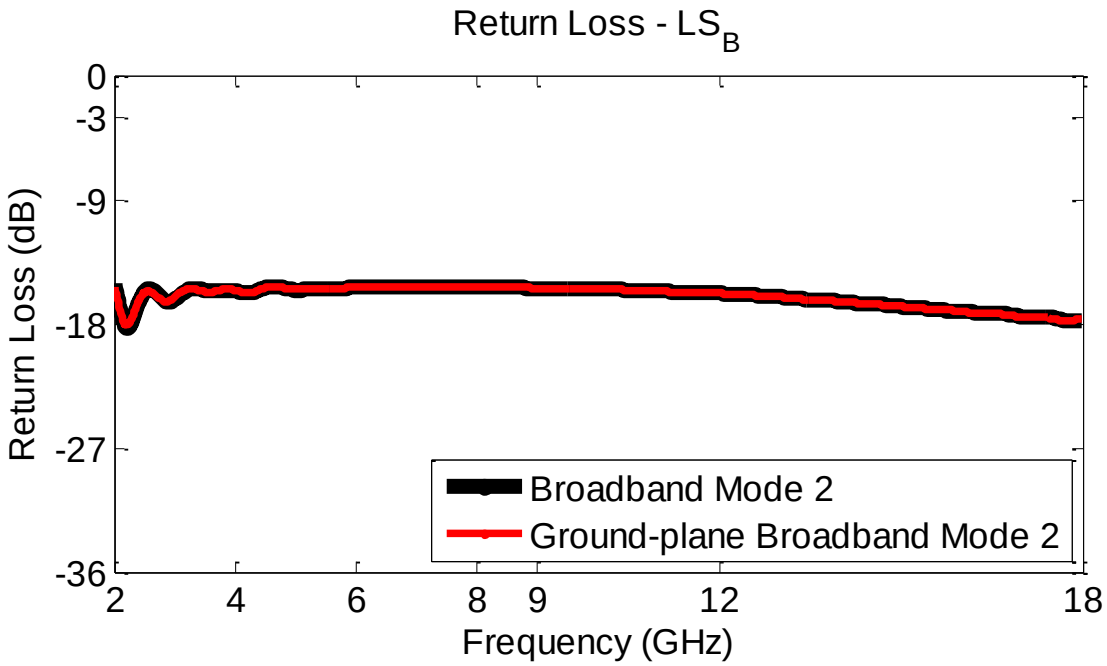

FIGURE 3-187: LOGARITHMIC SPIRAL WITH GROUND PLANE MODAL RETURN LOSS

For the logarithmic spiral ground plane model farfield results, the magnitude of the azimuth cuts, from Figures 3-188 & 3-189, are again used to view the magnitude ripple. The same trend holds from the first mode, being that the ripple increases both with the

frequency and with an increase in elevation angle. At the lowest frequency of 2.0GHz, the spiral has minimal ripple of ±0.07dB at 40° in elevation. While at the highest frequency of 18.0GHz and 60° in elevation, the ripple is ±2.0dB. For the mid-band case, 6.0GHz and 40° in elevation, the ripple is ±0.4dB. The magnitude of the elevation cuts, from Figures 3-192 & 3-193, are primarily used to show the peak directivity angle and the -3dB beamwidth. The maximum directivity of 6.4dBi for 9.0GHz occurs at 37° in elevation and the -3dB beamwidth extends from 22° to 61°.

The phase ripple about azimuth, from Figures 3-190 & 3-191, increases with frequency, similar to the magnitude ripple. However, different from the magnitude ripple, it is minimal at the elevation angle of maximum directivity. Minimal ripple, of ±1.3° is found at 2GHz and 40° in elevation, while at 18.0GHz and 60° in elevation the ripple is ±14°. In the mid-band case of 40° in elevation at 6.0GHz, the ripple is ±1.5°. The phase of the elevation cuts, from Figures 3-194 & 3-195, would ideally be equally spaced and most importantly would not overlap, which does not occur at any frequency.

The trend for the axial ratio about azimuth, from Figures 3-196 & 3-197, is to remain low toward boresight and increase toward the horizon. There is also variation about azimuth, but for 6.0GHz and 40° in elevation the average is 2.0dB and the peak is under 2.6dB. There is also variation across elevation, from Figures 3-198 & 3-199, that increases from boresight toward the horizon. Again, the lowest and peak cases occur for 6.0GHz which begin around 1dB, dip under 0.1dB and reach 7.5dB at the horizon.

The key changes in the farfield pattern are that the phase center is moving more rapidly from boresight to the horizon and the maximum directivity is shifted 4° toward boresight while the pattern is pinched at the horizon.

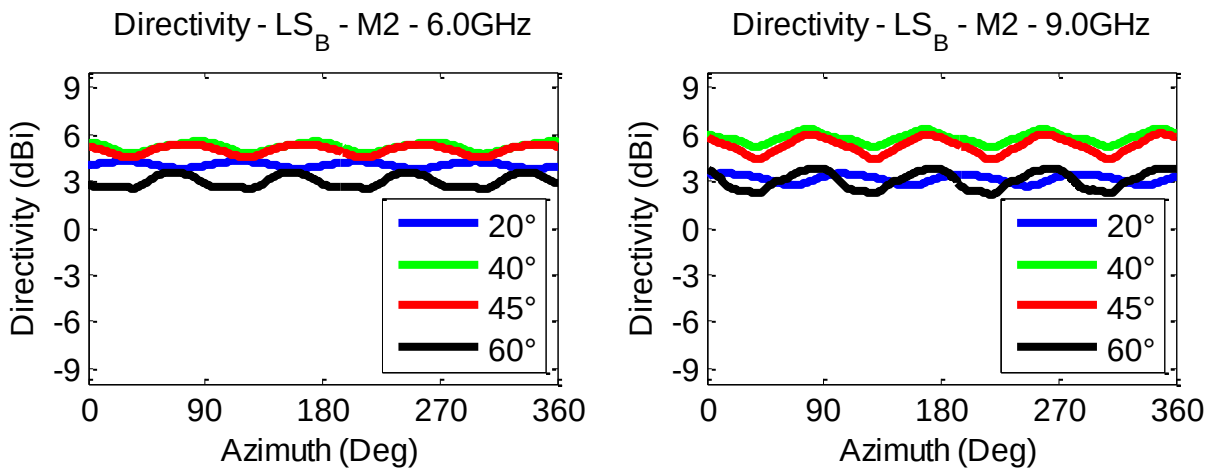

FIGURE 3-188: RADIATION PATTERNS – LS – GND – AZ – M2 – MAG [6 (A) & 9 (B) GHZ]

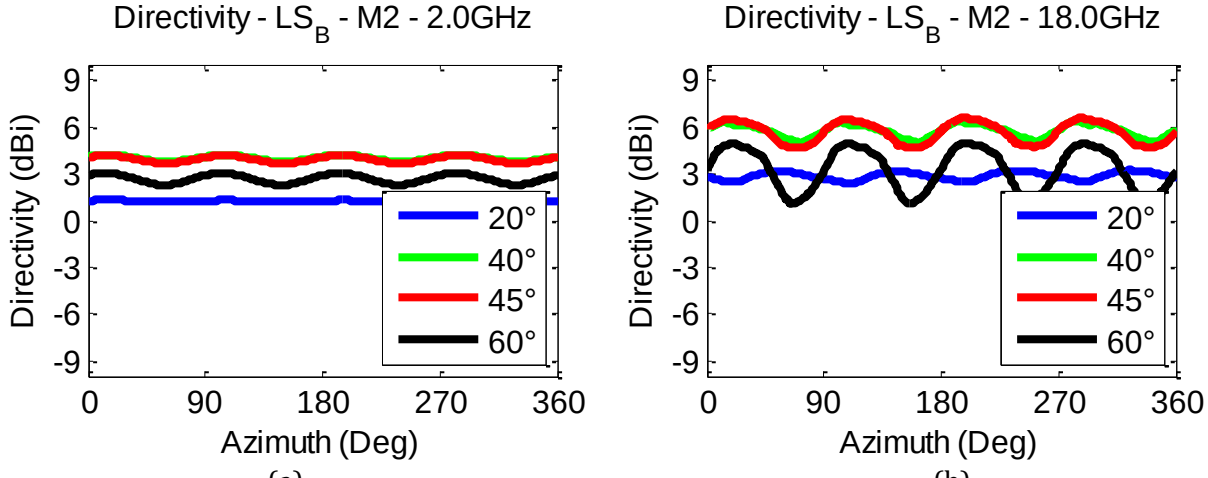

FIGURE 3-189: RADIATION PATTERNS – LS – GND – AZ – M2 – MAG [2 (A) & 18 (B) GHZ]

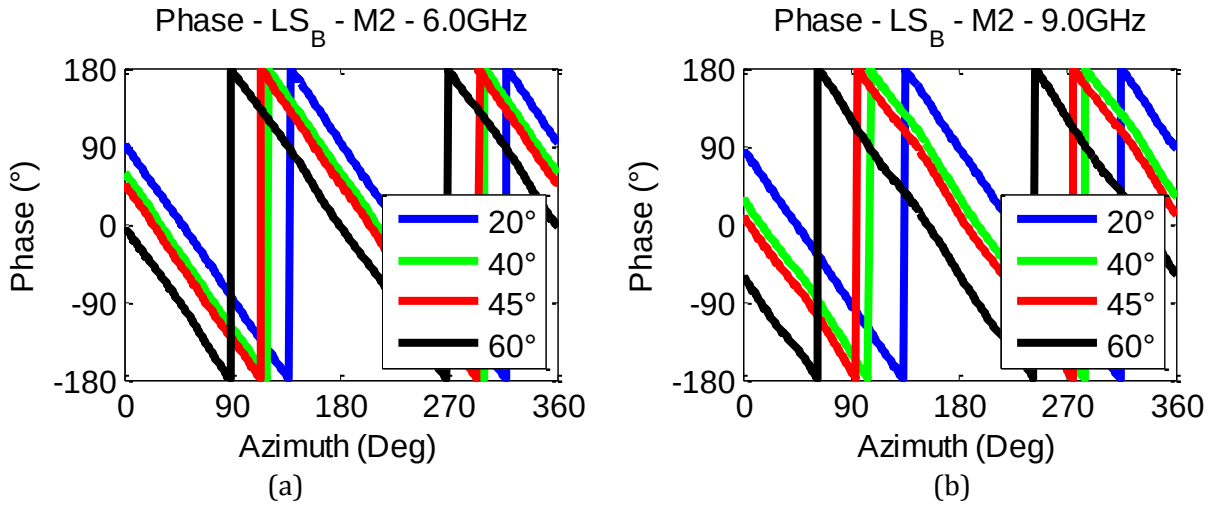

FIGURE 3-190: RADIATION PATTERNS – LS – GND – AZ – M2 – PHA [6 (A) & 9 (B) GHZ]

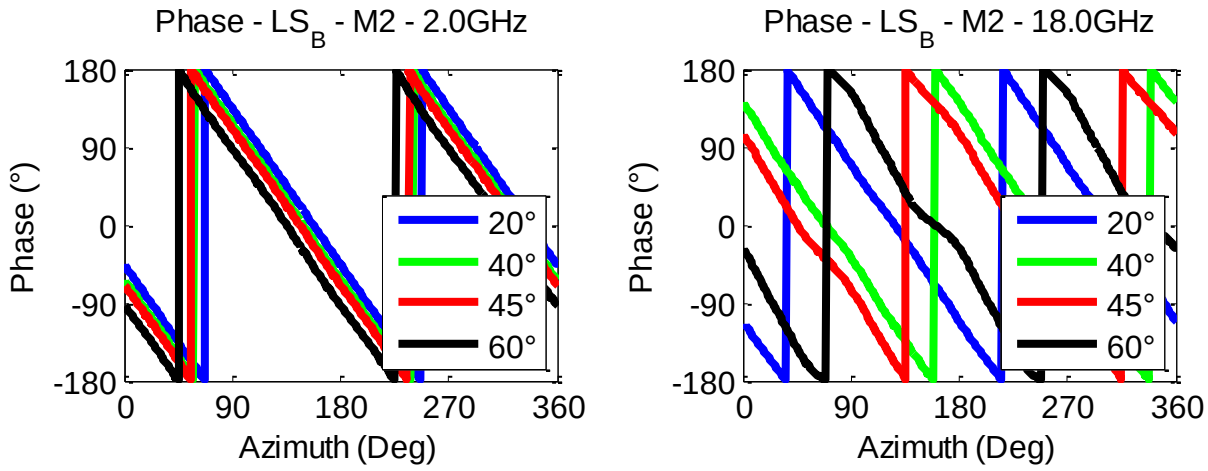

(a) (b)

FIGURE 3-191: RADIATION PATTERNS – LS – GND – AZ – M2 – PHA [2 (A) & 18 (B) GHZ]

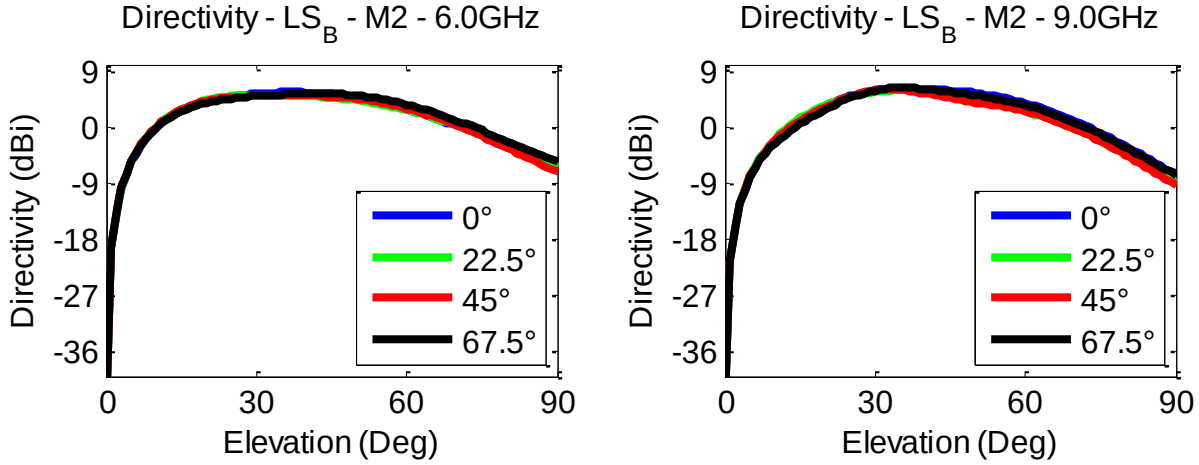

(a) (b)

FIGURE 3-192: RADIATION PATTERNS – LS – GND – EL – M2 – MAG [6 (A) & 9 (B) GHZ]

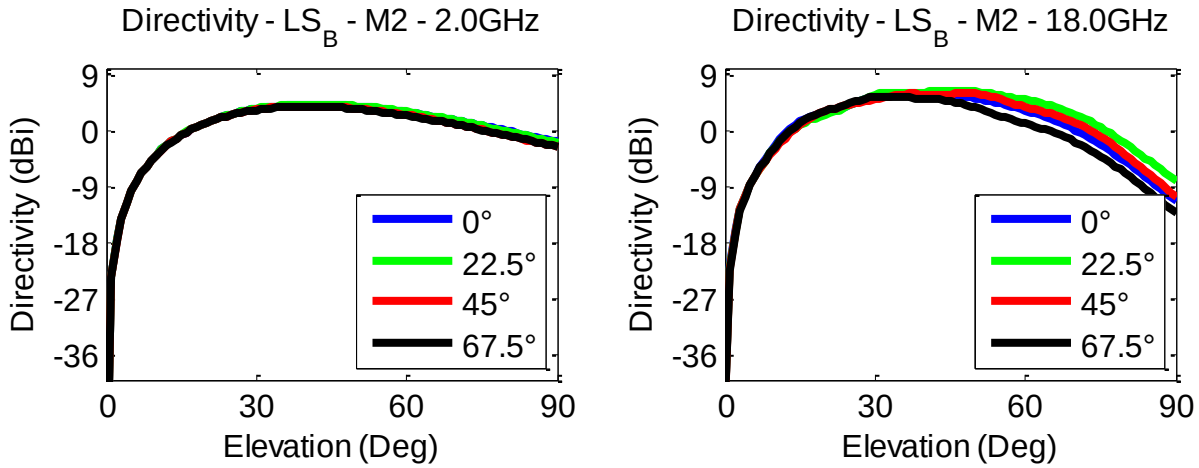

(a) (b)

FIGURE 3-193: RADIATION PATTERNS – LS – GND – EL – M2 – MAG [2 (A) & 18 (B) GHZ]

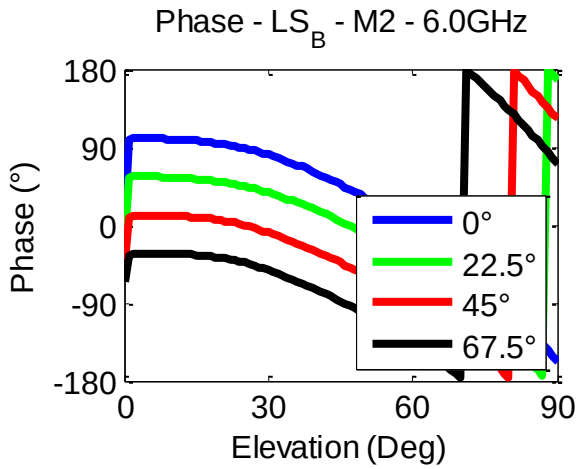

(a)

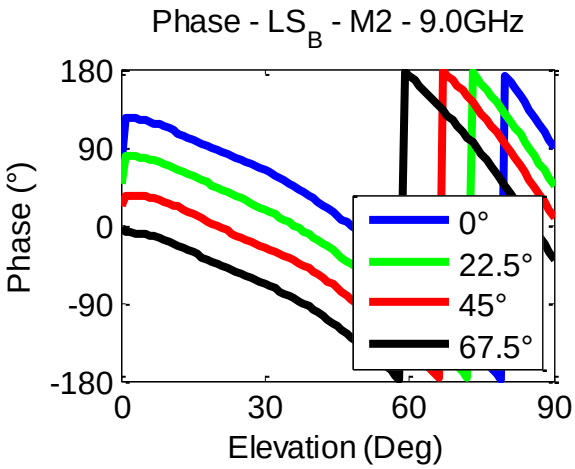

(b)

FIGURE 3-194: RADIATION PATTERNS – LS – GND – EL – M2 – PHA [6 (A) & 9 (B) GHZ]

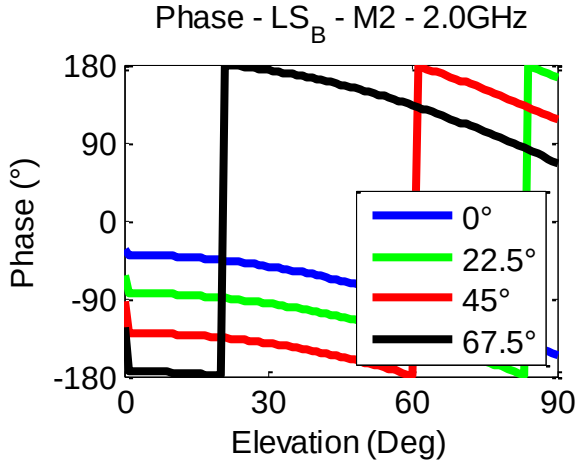

(a)

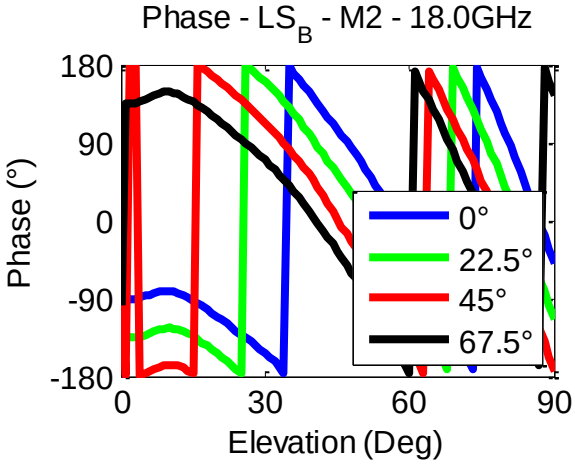

(b)

FIGURE 3-195: RADIATION PATTERNS – LS – GND – EL – M2 – PHA [2 (A) & 18 (B) GHZ]

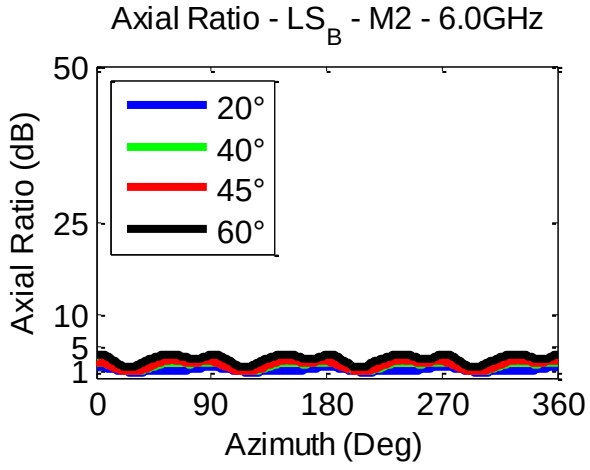

(a)

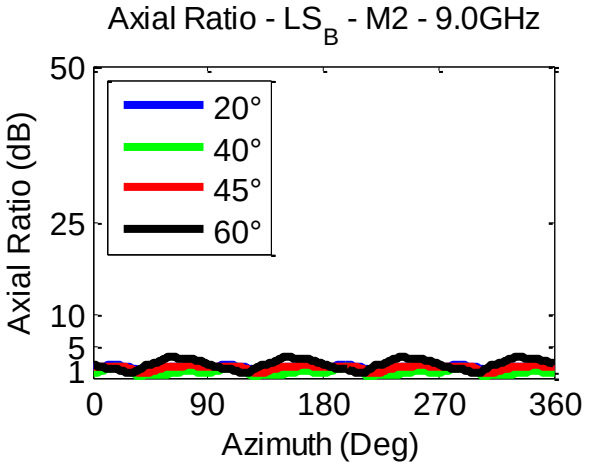

(b)

FIGURE 3-196: AXIAL RATIOS – LS – GND – AZ – M2 [6 (A) & 9 (B) GHZ]

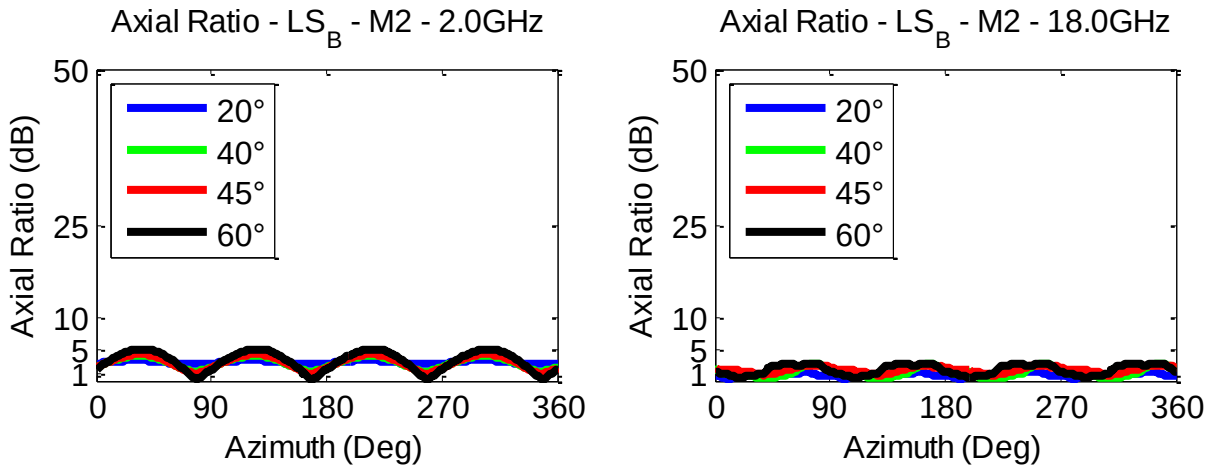

(a) (b)

FIGURE 3-197: AXIAL RATIOS – LS – GND – AZ – M2 [2 (A) & 18 (B) GHZ]

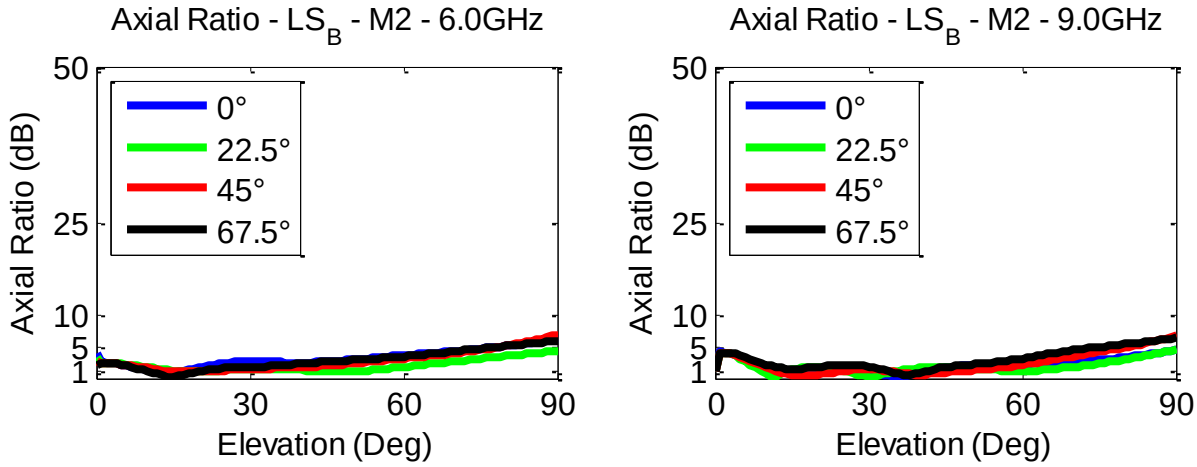

(a) (b)

FIGURE 3-198: AXIAL RATIOS – LS – GND – EL – M2 [6 (A) & 9 (B) GHZ]

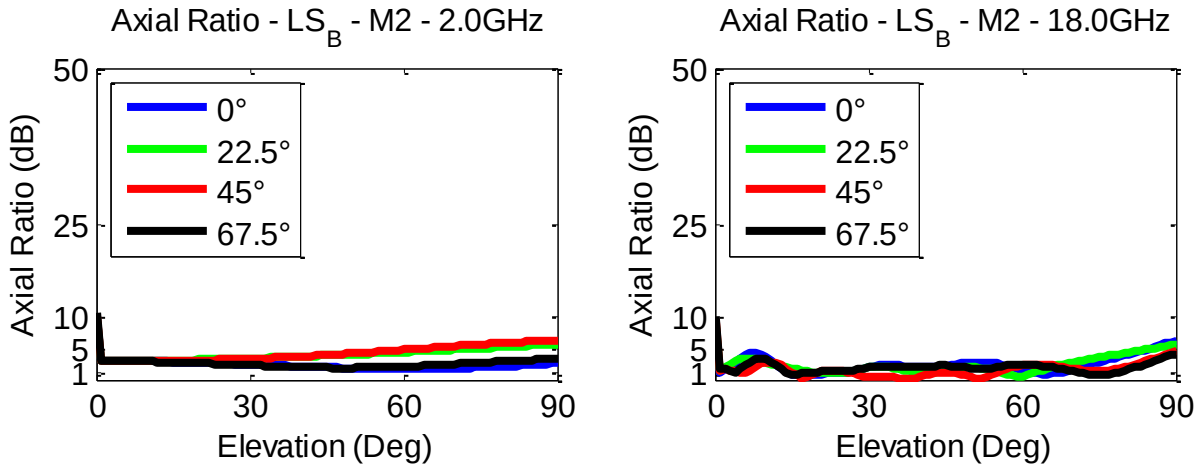

(a) (b)

FIGURE 3-199: AXIAL RATIOS – LS – GND – EL – M2 [2 (A) & 18 (B) GHZ]

CHAPTER 4: CONCLUSION

The ability of six frequency independent antenna designs to radiate in the first and second modes of operation within a defined frequency band while being confined to an inner and outer circumference has been presented. The spiral antenna results correlate closely with those in literature and the circular log-periodic and circular sinuous results. The tradeoffs associated with each design type are compared. The presented results are a step toward understanding the various types of frequency independent antennas and their limitations. Future work is suggested to continue the process of finding and documenting ideal designs.

4.1 OBSERVATIONS

The four-arm spiral antennas have the ability to radiate in the three distinct modes of operation in the same circular polarization component with each mode operating at an increasing circumference. The four-element circular log-periodic and the circular sinuous have the ability to radiate in the first mode of operation in either circular polarization component as well as in the second mode of operation in linear polarization with each mode operating from the same circumference. Increasing the tooth length, for the log-periodic, or the interleave, for the sinuous, will allow for the design to radiate at lower frequencies.

4.2 COMPARISON

The various results coalesce into a summary of the ability of each antenna type to radiate in the separate modes of operation. The experimental results confirm the accuracy

of the simulations. The return loss results show the stability of the impedance for the spiral antennas and the effect truncation has when the spiral is excited with low frequencies. They also show the instability of the impedance of the circular log-periodic and circular sinuous antennas. The impedance of the sinuous is the first indication that it is characteristically a blend between the spiral and the circular log-periodic designs. The farfield radiation pattern results continue to show the stability and low axial ratios of the spiral antennas compared to the instability and high axial ratios of the circular log-periodic. Although the second design, or long-tooth version of the circular log-periodic is shown to have relatively low ripple and axial ratio in the first mode, proving the design can be optimized for preferred characteristics. The circular sinuous is shown to have ripple and axial ratios that rival the spiral in the first mode of operation, but the four-element version is incapable of a true circularly polarized second mode.

Comparing the first mode of operation for the same circular polarization component has shown that the spiral will radiate in the first mode at a circumference equal to one wavelength, the circular log-periodic will radiate at a circumference related to the tooth length and that the circular sinuous will radiate at a circumference around one wavelength with a small variation related to the amount of interleave between the elements. The two circular log-periodic designs operate around 1.25-1.75λ and are less efficient than the other designs presented.

4.3 FUTURE WORK

A final step in this effort will be to take experimental data to verify the simulation data that has been presented. All six antennas have been built and are to be tested but the results are pending at the time of publication. The antennas will be tested in a compact

farfield chamber that is capable of characterizing their radiation patterns in the simulated spectrum of 2.0-18.0GHz mounted inside a test-body (29). The experimental data will show the inherent variation that occurs when attempting to realize a design. Small deviations from the design, related to coaxial cable, non-flat elements and other non-ideal characteristics will likely have an impact on the ability to form the radiation modes.

To make a full comparison, it would be advantageous to simulate the impedance of the first mode across the spectrum. Due to the requirement of needing phase shifts with an imaginary component, this is not possible using the time domain solver. This could be accomplished by creating frequency domain models but many frequencies would have to be run in order to achieve accurate impedance results.

The elements of the circular log-periodic and circular sinuous were shown in their most basic form. The elements could be optimized for the properties compared. The circular log-periodic teeth can be confined to a fixed width and the circular sinuous elements can be modulated with a variable growth rate that creates a fixed width arm. To further the current study, using fixed-width versions of the circular log-periodic and circular sinuous to compare directly with the Archimedean spiral may show results that have lower axial ratios and ripple. Beyond optimizing the individual elements, the number of elements could be increased. As the number of elements is increased, the space about azimuth is being more finely discretized. Increasing the number of elements will lead to an increasing number of ripples with lower variation, or ripple, in the farfield. It will also result in having increased input complexity (30). In order to operate in the first mode of operation, using an eight element antenna will require 45° phase-shifts broadband. Increasing the number of elements for the spiral will lead to its active region remaining at

the same circumference for the most presented, with higher order modes occurring at greater circumferences. The circular sinuous is expected to have an active region that remains at the same circumference for each mode of operation, but increasing the number elements for the circular log-periodic will lead to shorter teeth and potentially to a larger active region circumference. A study could be made of the tradeoff between the number of modes, overall circumference and polarization requirements. In the future, phase-shifters with the ability to control phase to individual degrees at wide bandwidths will allow a larger number of elements to be used in real-time without the need for post-processing.

Finally, equations have previously been developed to describe the currents that exist on spiral arms and the way the phases align at a circumference to form the radiation mode. Developing current equations for the other two designs could create a quick design method that leads to desired attributes. The challenge in this would be to accurately track the phase along the elements of the circular log-periodic which is a standing-wave antenna versus the spiral and circular sinuous which are traveling-wave antennas.

APPENDIX

APPENDIX A: SIMULATION RESULTS

Shown in Figure A-1 is the broadband modal return loss plot for the circular log-periodic, with π/16-overlap or longer tooth version, which was fabricated for experimental testing. The first dip in the return loss occurs at 2.3GHz and is directly linked with a tooth of the antenna as the higher frequency dips occur at the logarithmic growth rate a property that holds for both designs. The broadband modal return loss is viewed as normal behavior for a quasi-frequency-independent structure. As the teeth become longer, the characteristic dips shift lower in frequency. Finally, only and eight dips are shown in the frequency band selected, which suggests that if the simulations were run at higher frequencies more dips should occur, up to the total number of teeth.

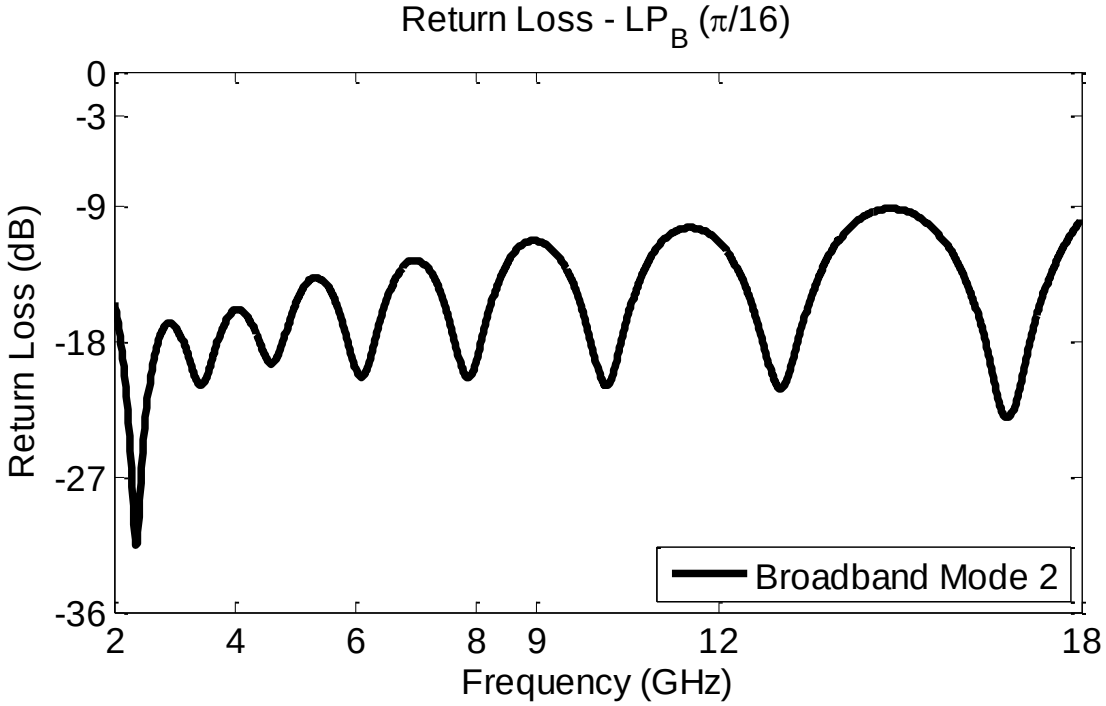

FIGURE A-1: CIRCULAR LOG-PERIODIC [Π/16] BROADBAND MODE 2 RETURN LOSS

RETURN LOSS [MODE 3 / -1]

Shown in Figures A-2 through A-7 are the modal return loss plots comparing the first mode of operation with the third mode. The impedance of the third mode of operation is shown to be equal with the third mode of operation in every case with the exception of the spiral antennas lower frequencies and the circular sinuous with π/3-interleave at 18.0GHz. The spiral antennas have different impedance at the lower frequencies because they are not designed to be large enough to radiate in the third mode of operation below 4.0GHz. The Archimedean spiral differs all the way up to 8.0GHz, which is attributable to truncation effects. Finally, the circular sinuous with π/3-interleave is radiating off of the first partial length that leads into the first wrap at 18.0GHz and for this reason, it is not equivalently matched when radiating in the negative first mode of operation. The remainder of the frequencies for this antenna and the remainder of the results for the other three antennas operate in the negative first mode equally well as they do the first mode albeit with opposite-sense circular polarization.

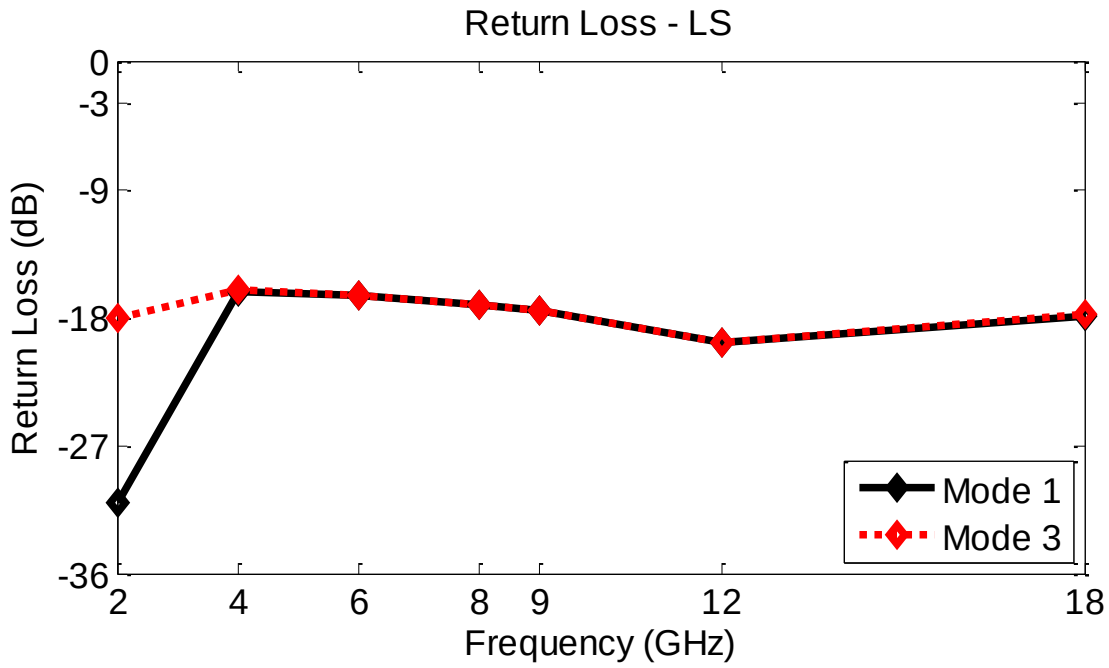

FIGURE A-2: LOGARITHMIC SPIRAL MODAL RETURN LOSS

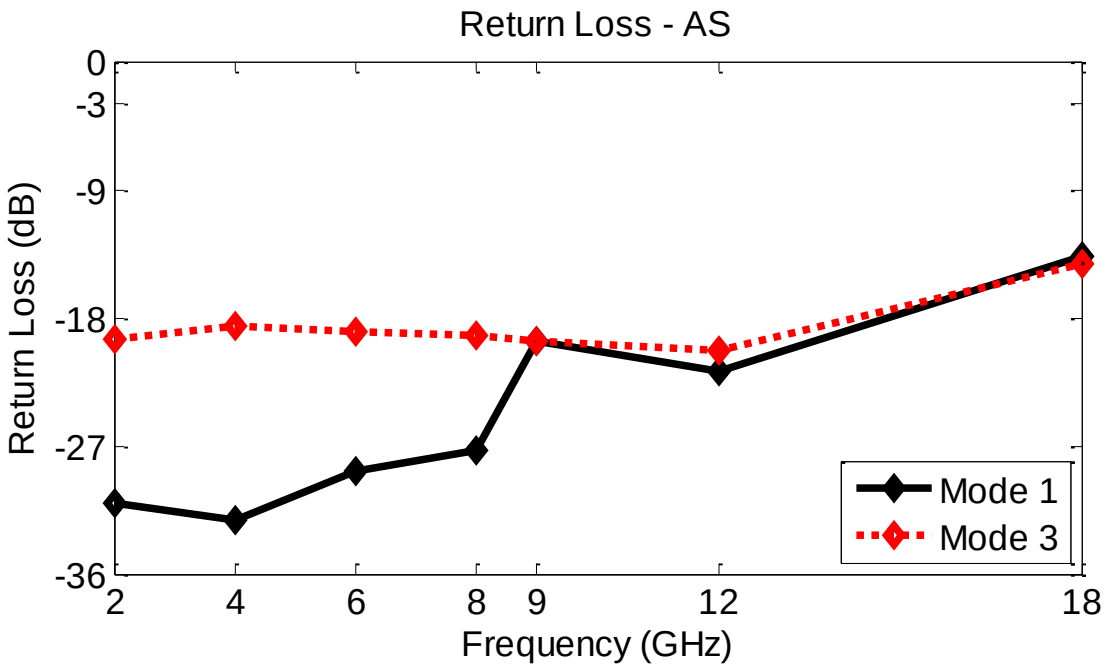

FIGURE A-3: ARCHIMEDEAN SPIRAL MODAL RETURN LOSS

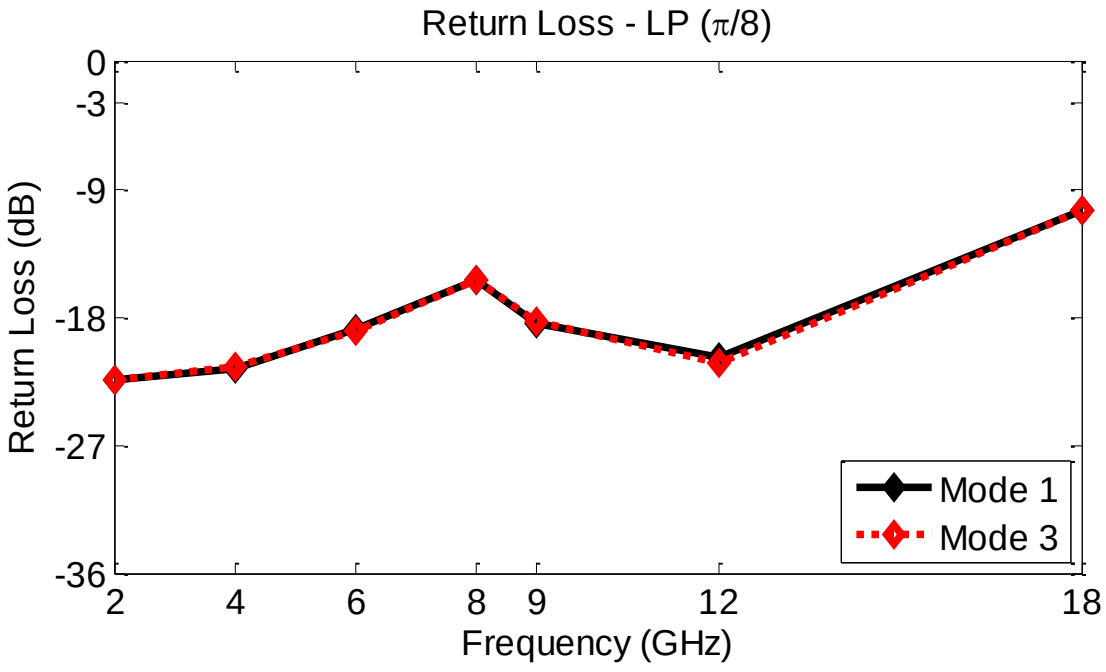

FIGURE A-4: CIRCULAR LOG-PERIODIC [Π/8] MODAL RETURN LOSS

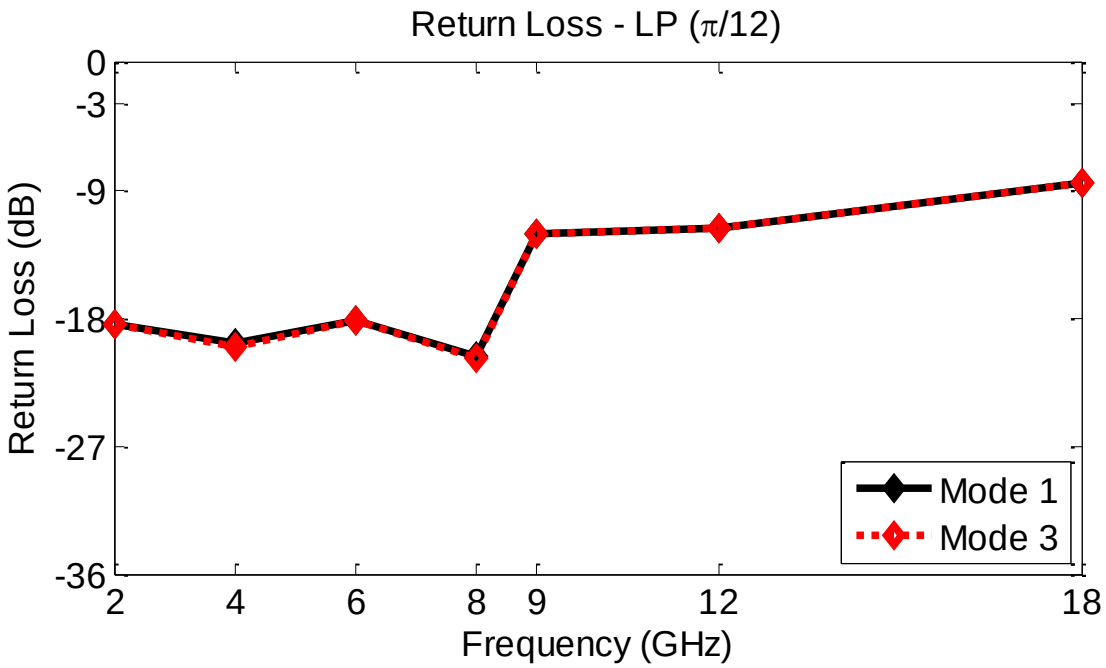

FIGURE A-5: CIRCULAR LOG-PERIODIC [Π/12] MODAL RETURN LOSS

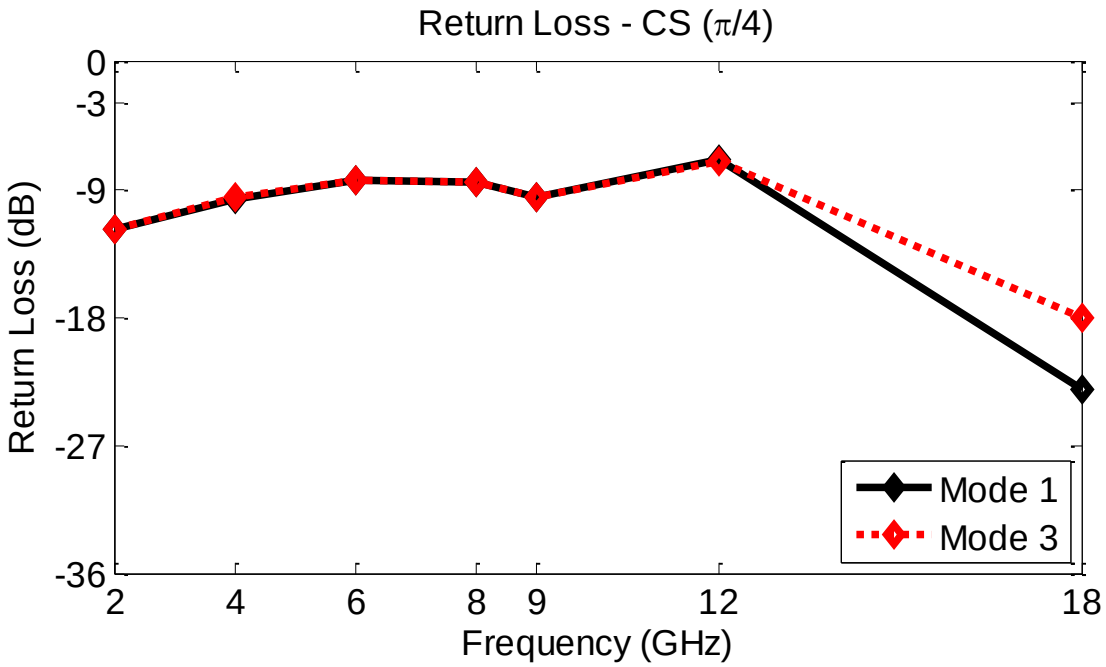

FIGURE A-6: CIRCULAR SINUOUS [Π/4] MODAL RETURN LOSS

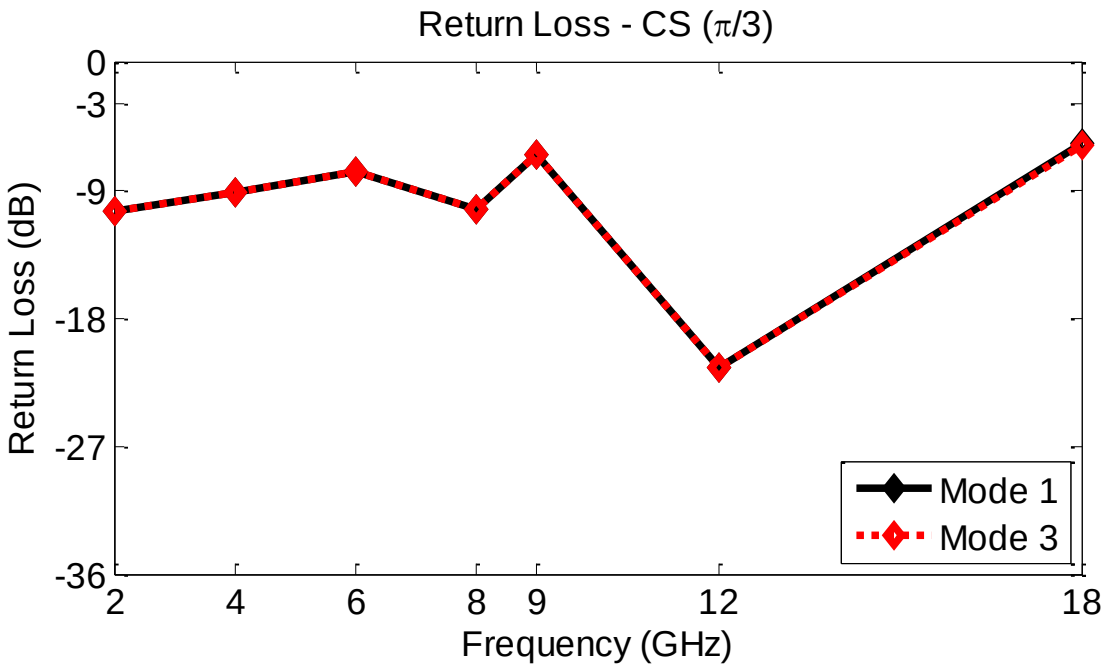

FIGURE A-7: CIRCULAR SINUOUS [Π/3] MODAL RETURN LOSS

MAGNETIC FIELD SURFACE PLOTS [COLOR]

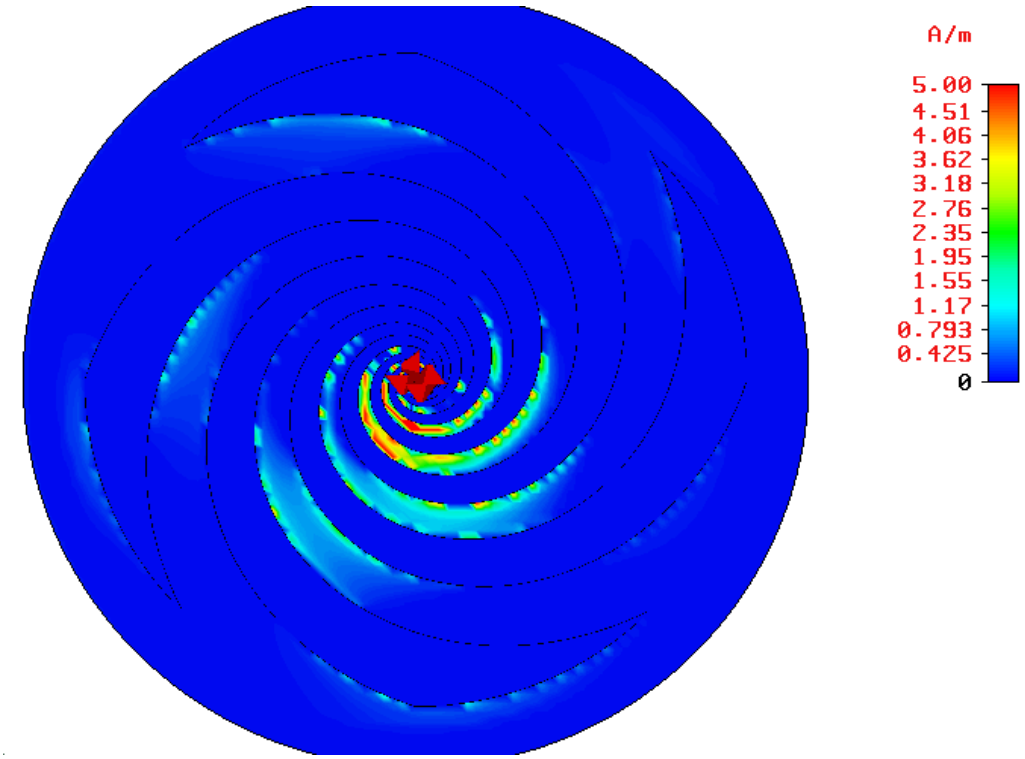

FIGURE A-8: LOGARITHMIC SPIRAL NORMAL H-FIELD [4.0GHZ - MODE 1]

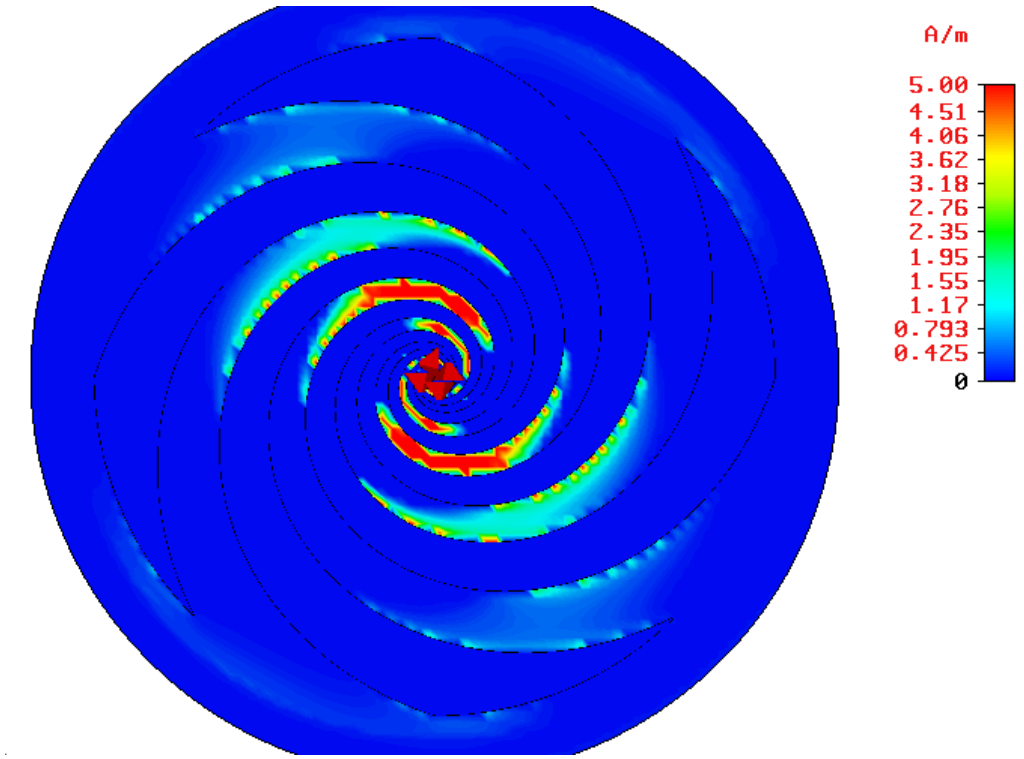

FIGURE A-9: LOGARITHMIC SPIRAL NORMAL H-FIELD [4.0GHZ - MODE 2]

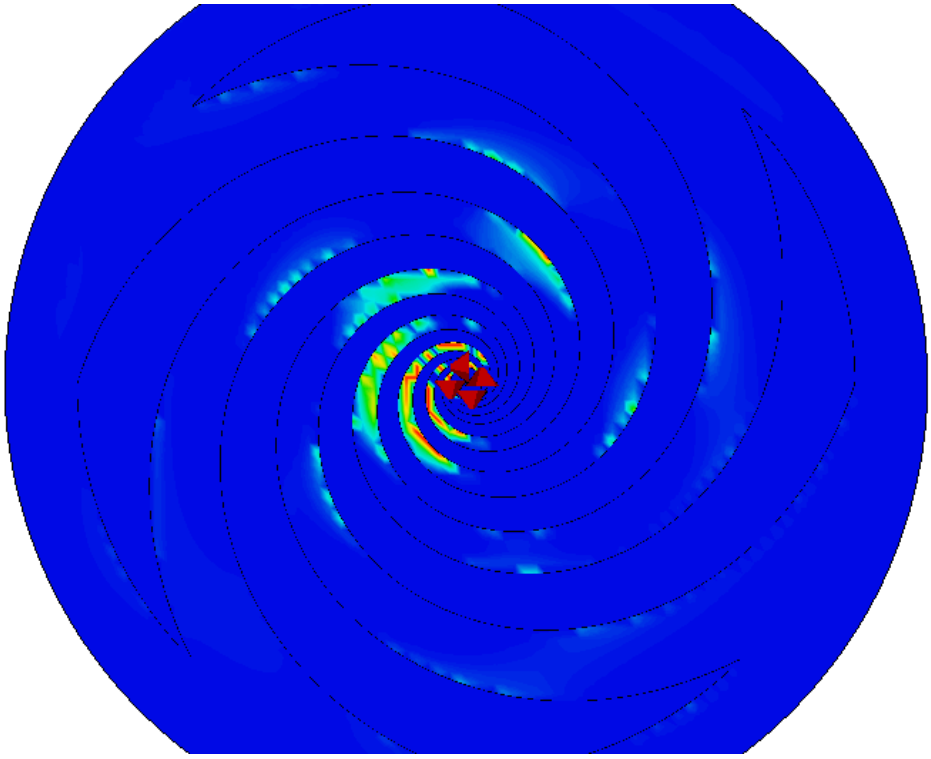

FIGURE A-10: LOGARITHMIC SPIRAL NORMAL H-FIELD [8.0GHZ - MODE 1]

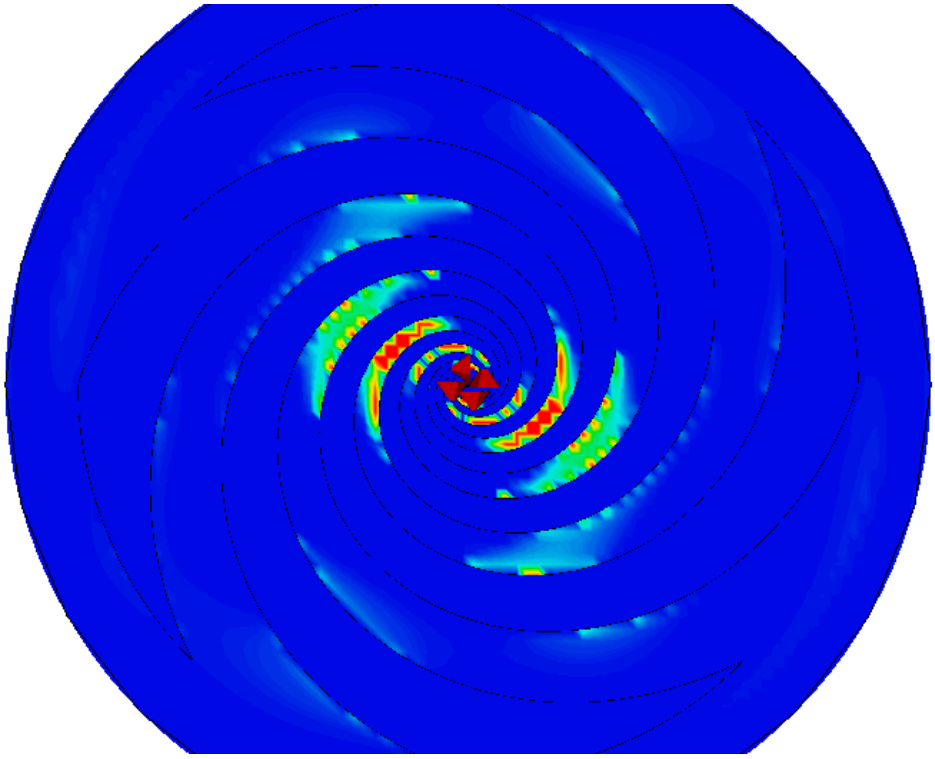

FIGURE A-11: LOGARITHMIC SPIRAL NORMAL H-FIELD [8.0GHZ - MODE 2]

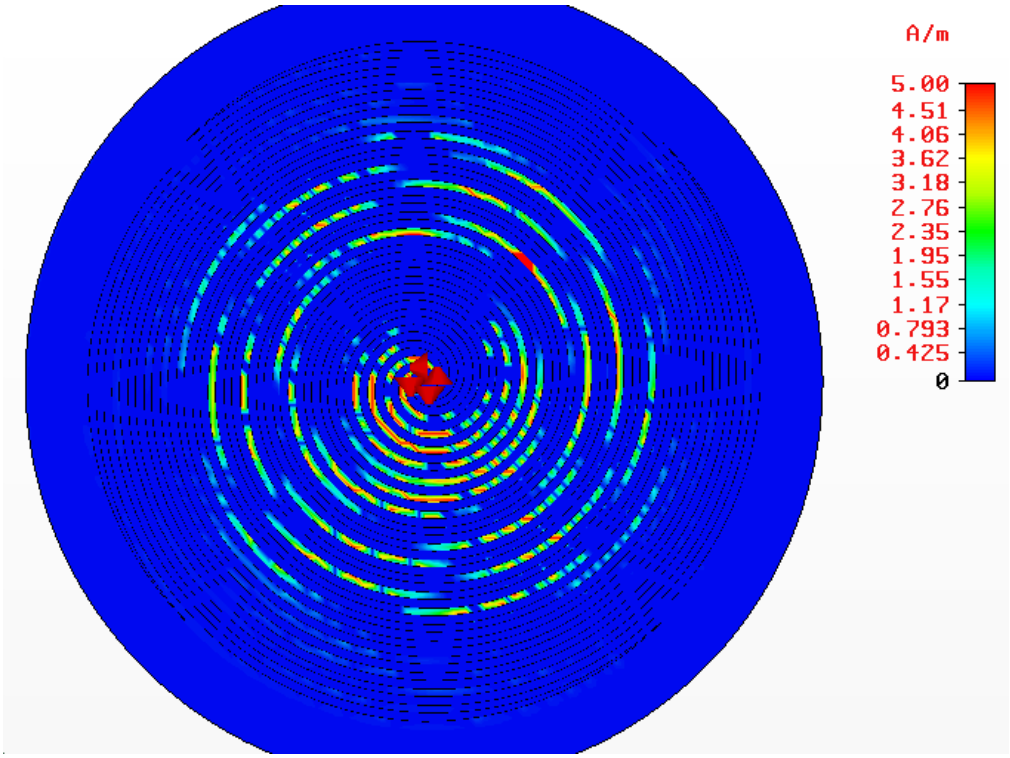

FIGURE A-12: ARCHIMEDEAN SPIRAL NORMAL H-FIELD [4.0GHZ - MODE 1]

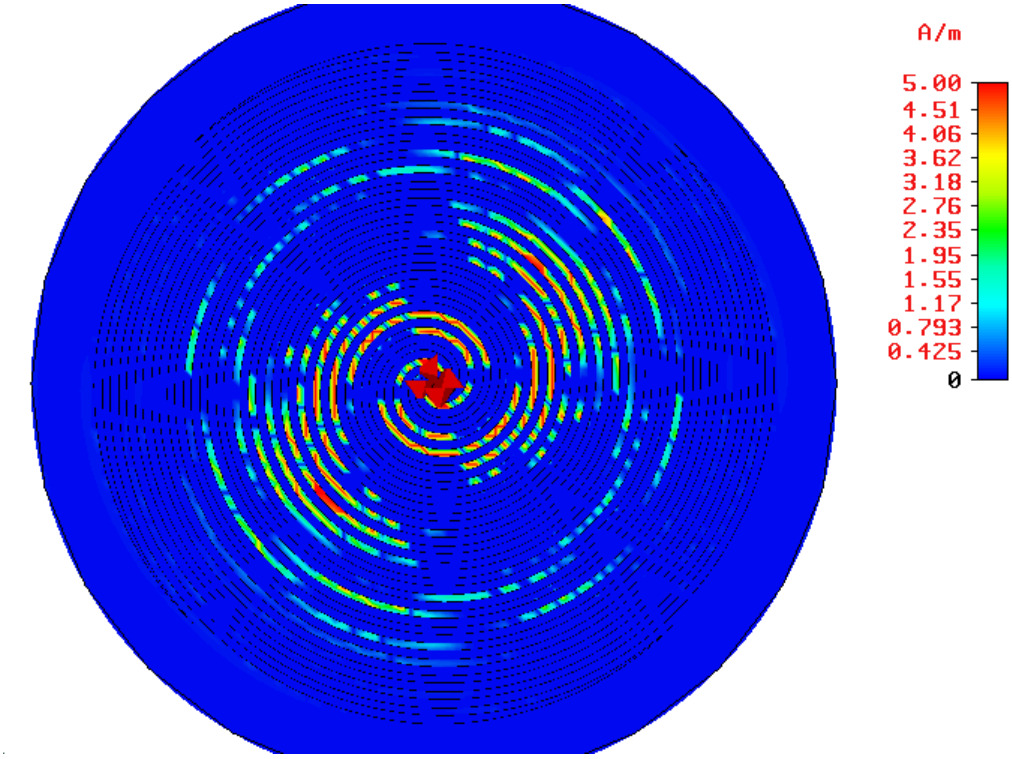

FIGURE A-13: ARCHIMEDEAN SPIRAL NORMAL H-FIELD [4.0GHZ - MODE 2]

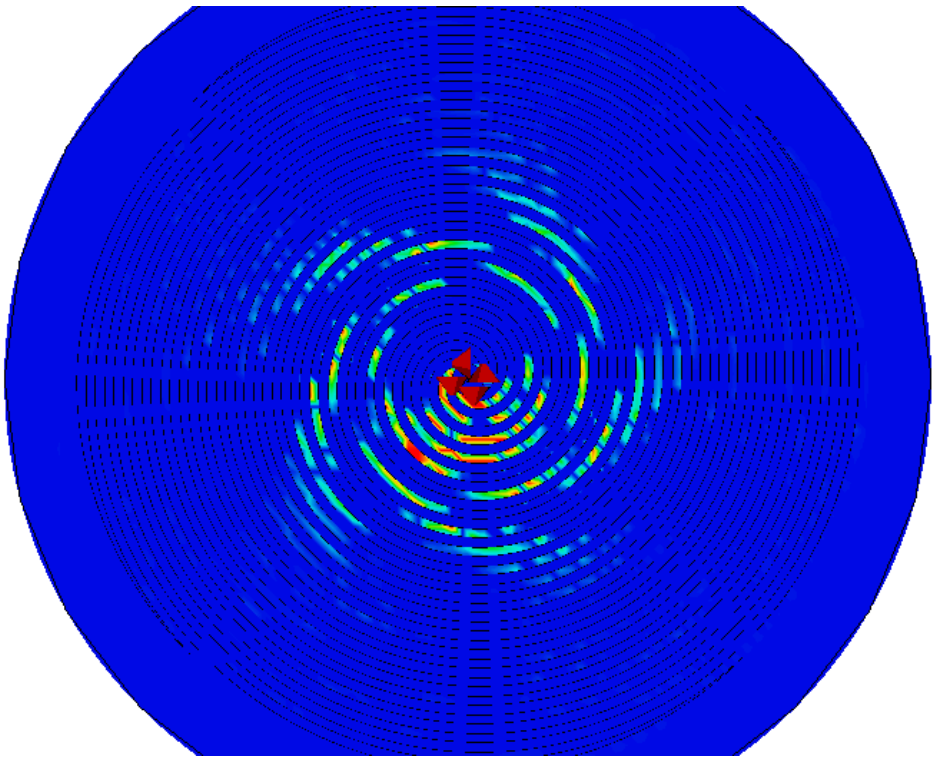

FIGURE A-14: ARCHIMEDEAN SPIRAL NORMAL H-FIELD [8.0GHZ - MODE 1]

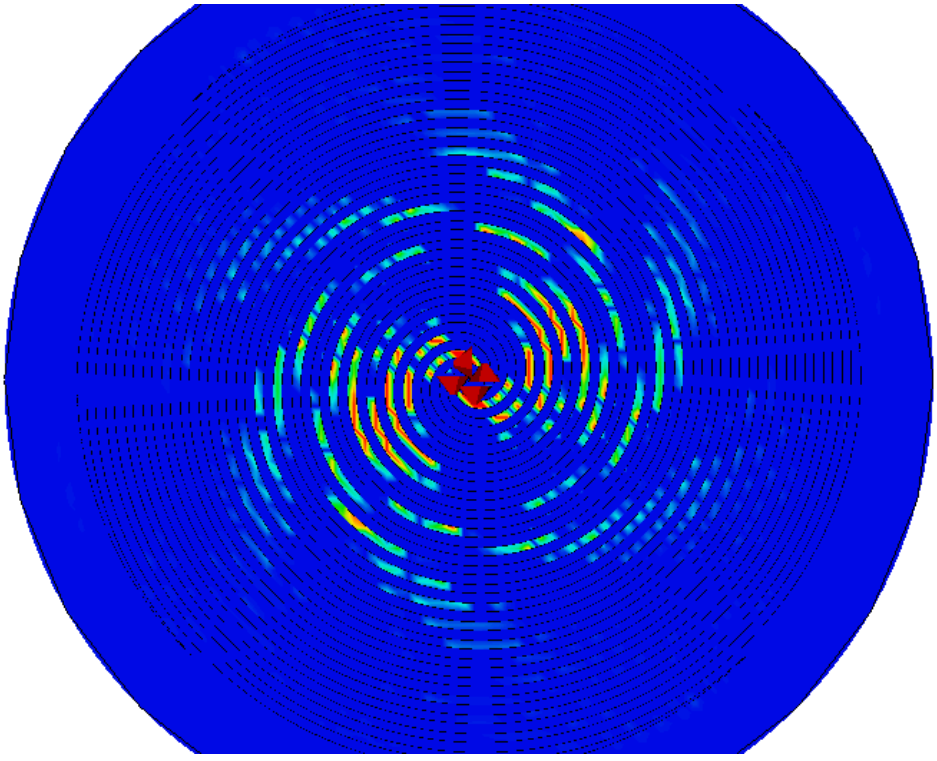

FIGURE A-15: ARCHIMEDEAN SPIRAL NORMAL H-FIELD [8.0GHZ - MODE 2]

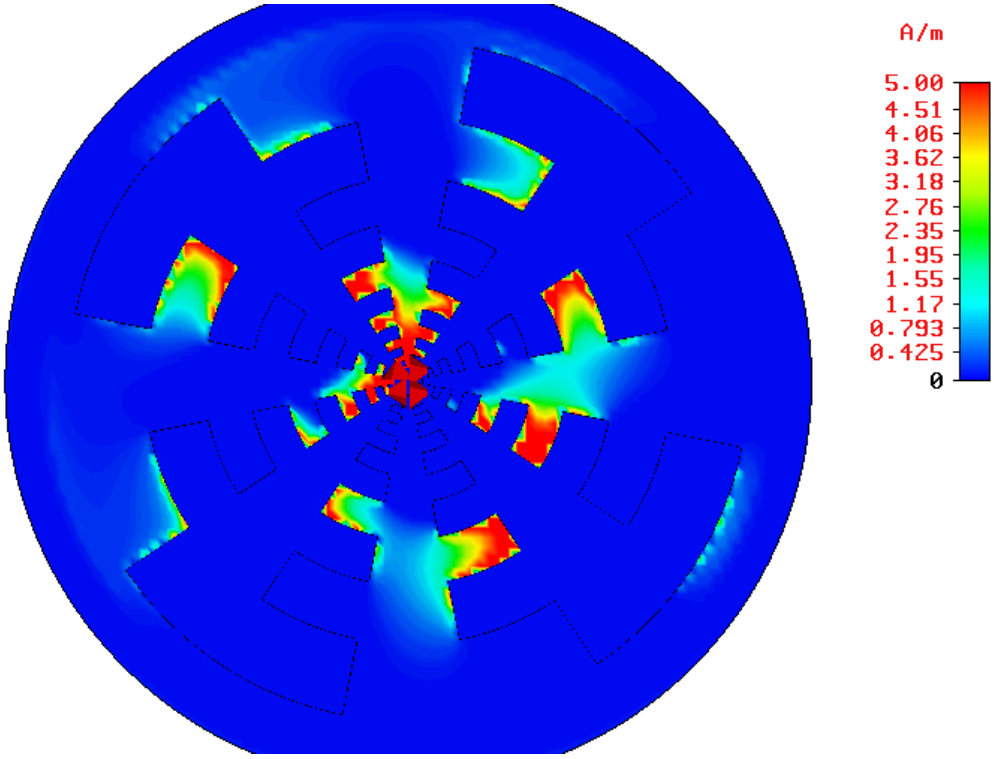

FIGURE A-16: CIRCULAR LOG-PERIODIC [Π/8] NORMAL H-FIELD [4.0GHZ - MODE 1]

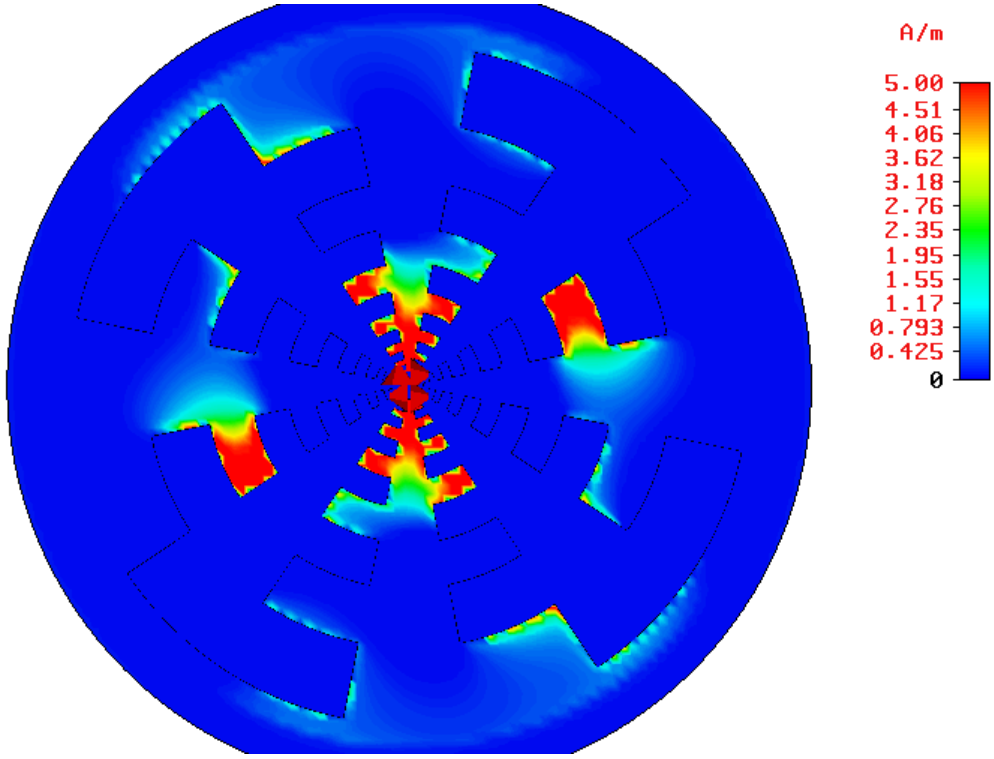

FIGURE A-17: CIRCULAR LOG-PERIODIC [Π/8] NORMAL H-FIELD [4.0GHZ - MODE 2]

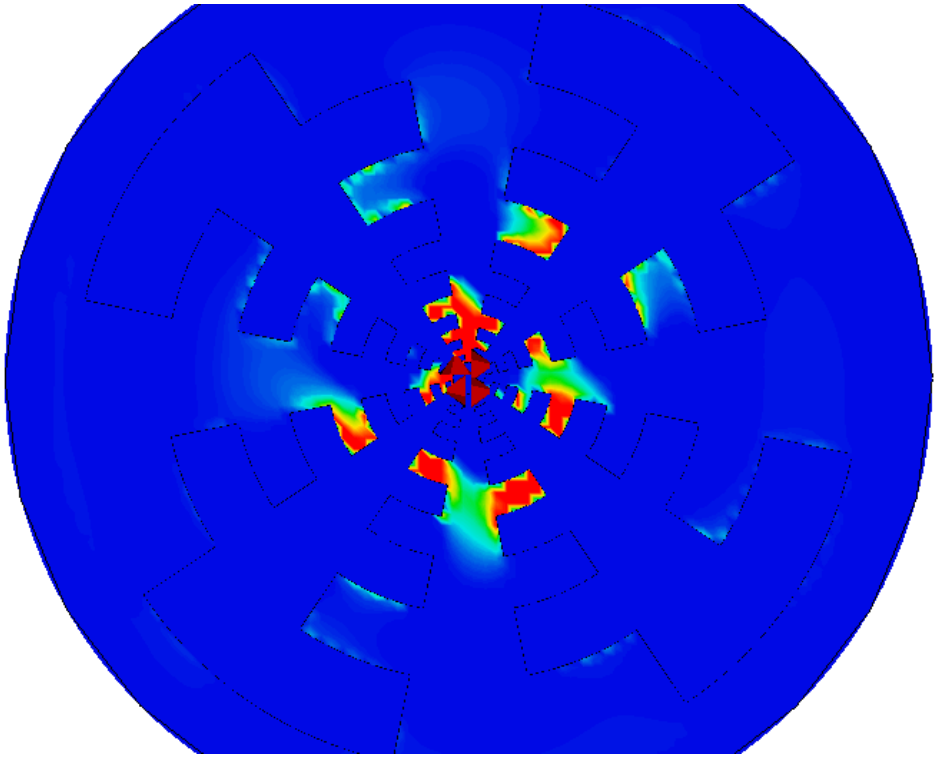

FIGURE A-18: CIRCULAR LOG-PERIODIC [Π/8] NORMAL H-FIELD [8.0GHZ - MODE 1]

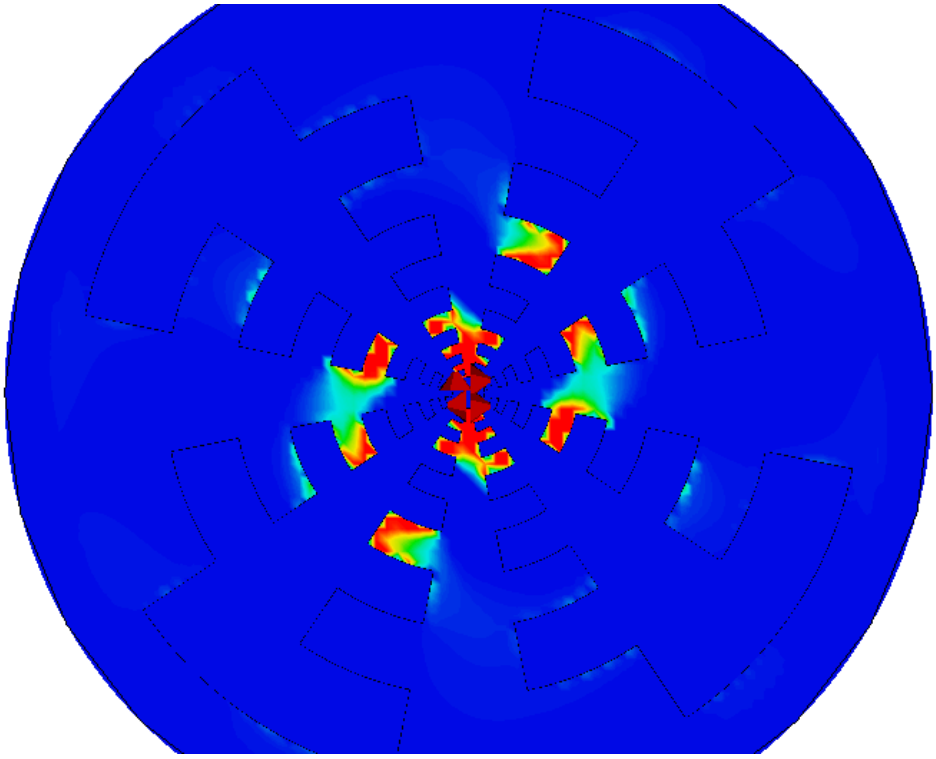

FIGURE A-19: CIRCULAR LOG-PERIODIC [Π/8] NORMAL H-FIELD [8.0GHZ - MODE 2]

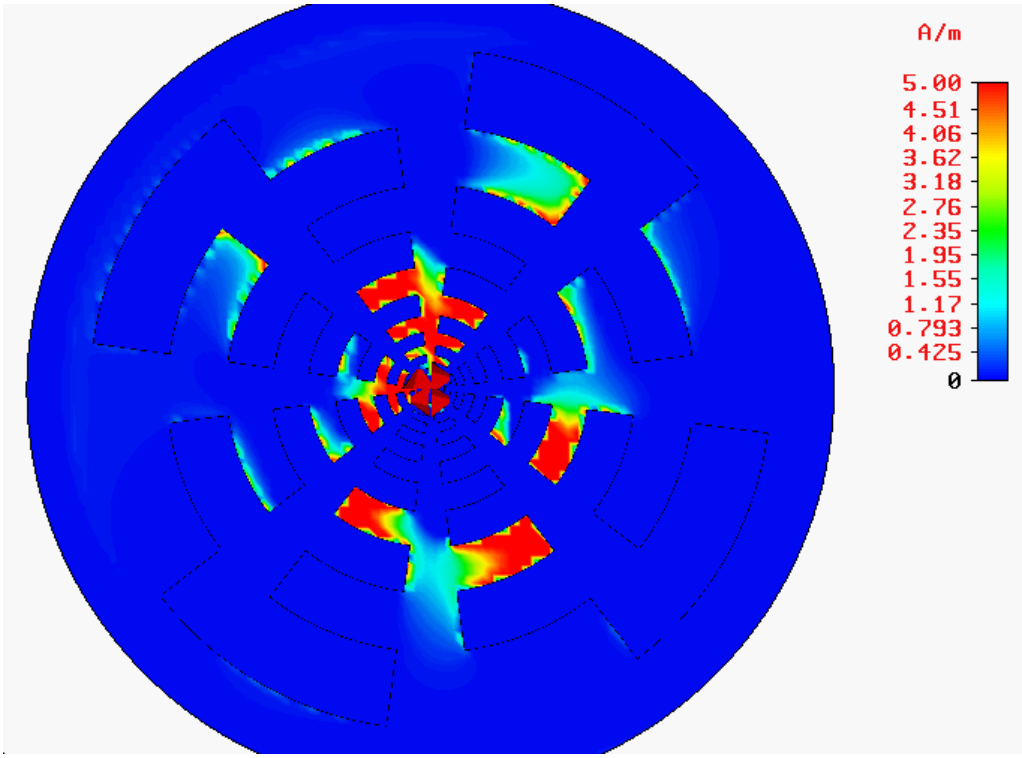

FIGURE A-20: CIRCULAR LOG-PERIODIC [Π/12] NORMAL H-FIELD [4.0GHZ - MODE 1]

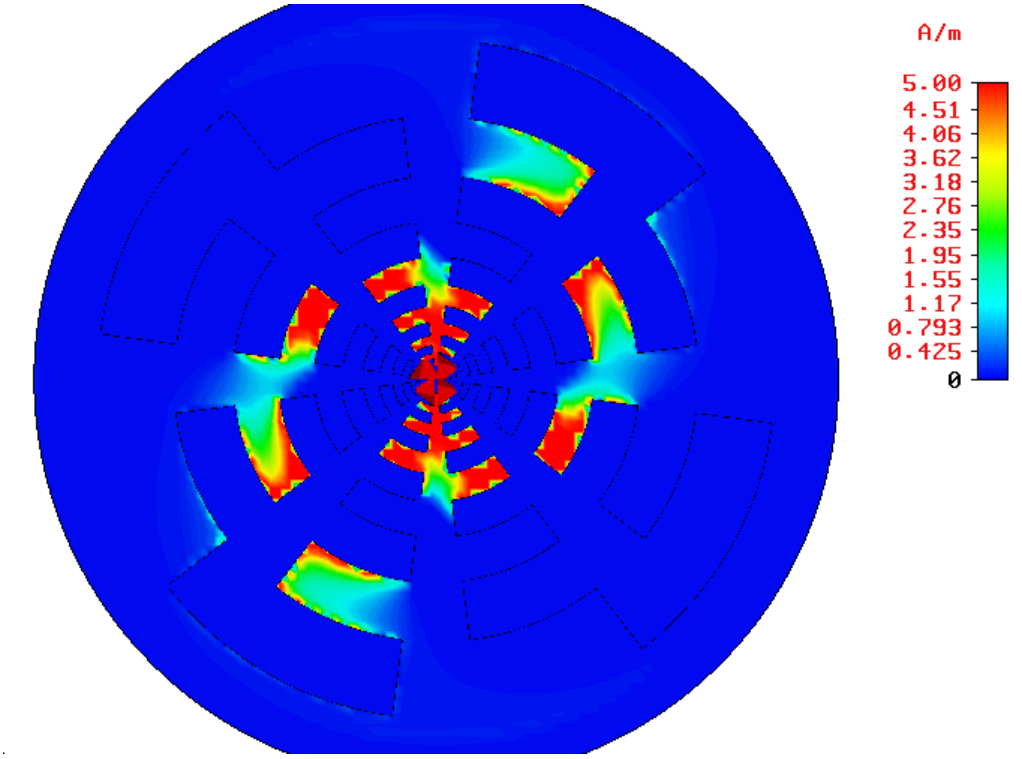

FIGURE A-21: CIRCULAR LOG-PERIODIC [Π/12] NORMAL H-FIELD [4.0GHZ - MODE 2]

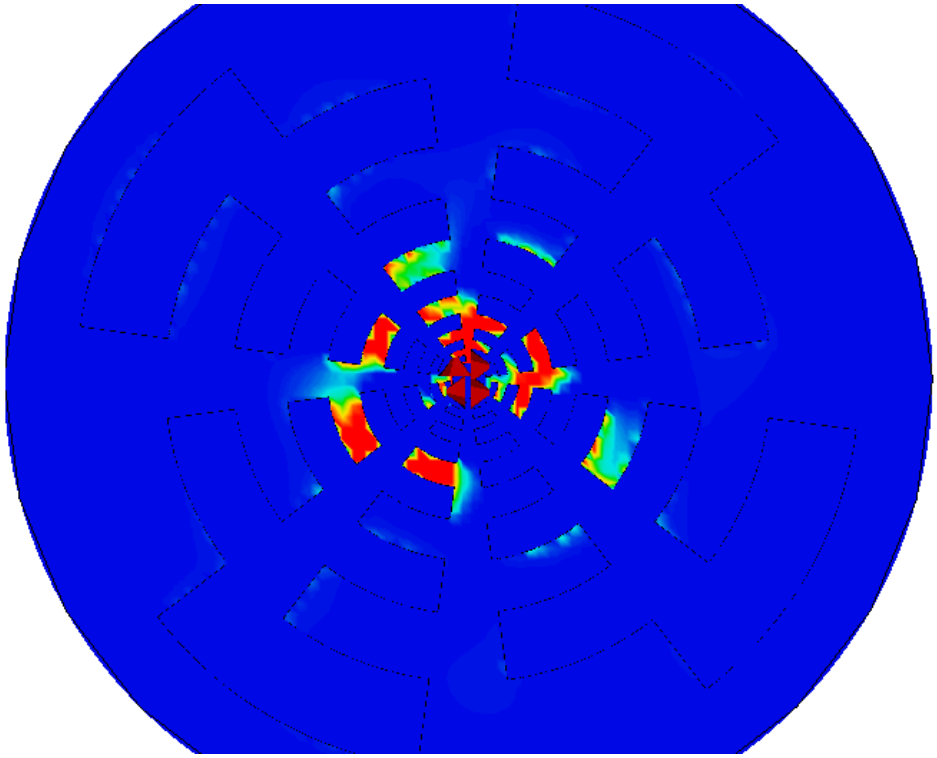

FIGURE A-22: CIRCULAR LOG-PERIODIC [Π/12] NORMAL H-FIELD [8.0GHZ - MODE 1]

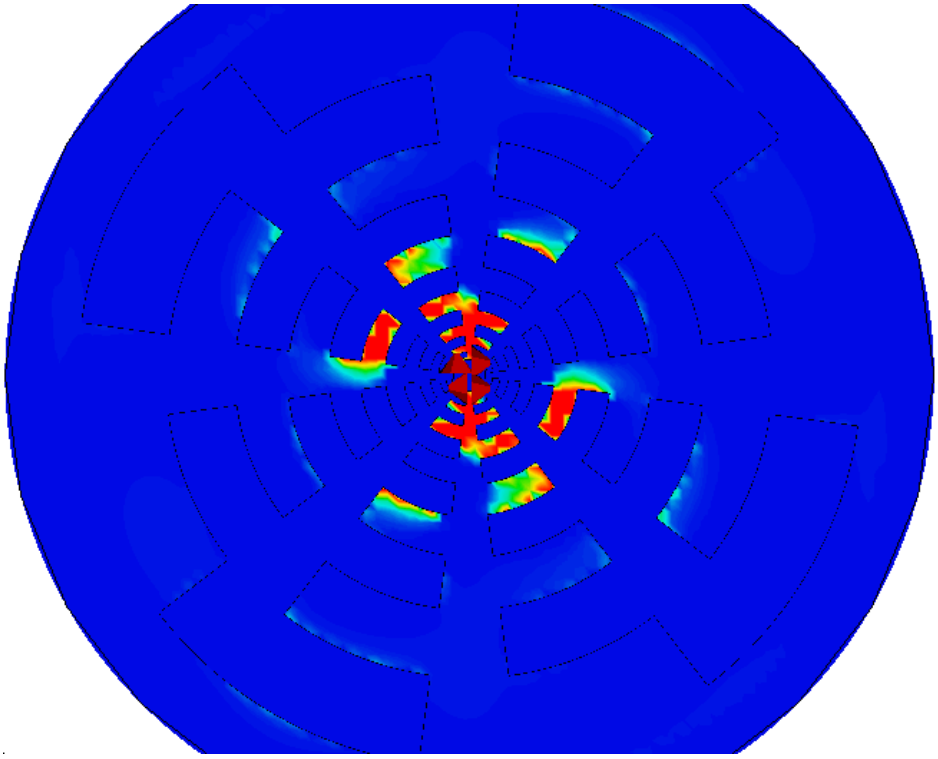

FIGURE A-23: CIRCULAR LOG-PERIODIC [Π/12] NORMAL H-FIELD [8.0GHZ - MODE 2]

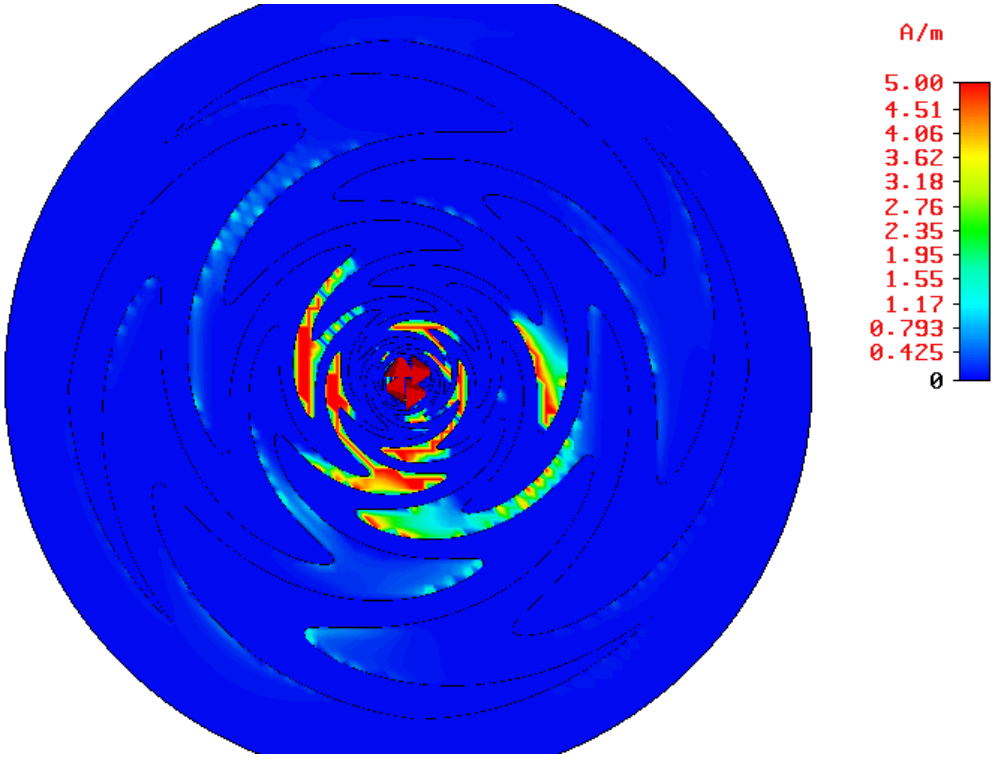

FIGURE A-24: CIRCULAR SINUOUS [Π/4] NORMAL H-FIELD [4.0GHZ - MODE 1]

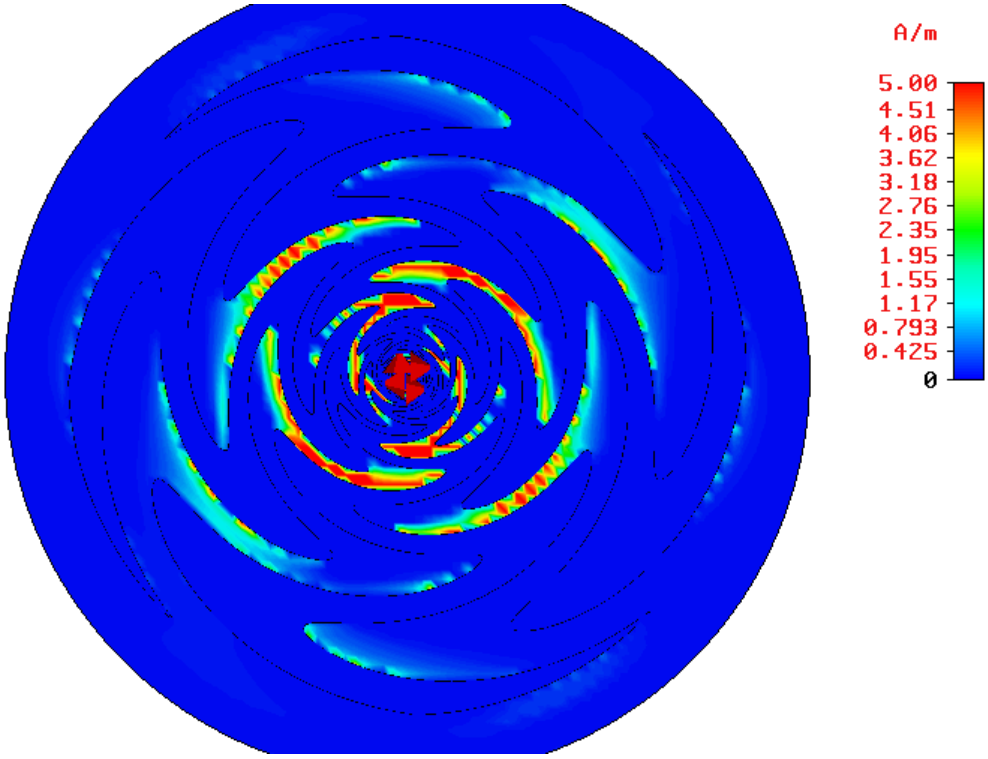

FIGURE A-25: CIRCULAR SINUOUS [Π/4] NORMAL H-FIELD [4.0GHZ - MODE 2]

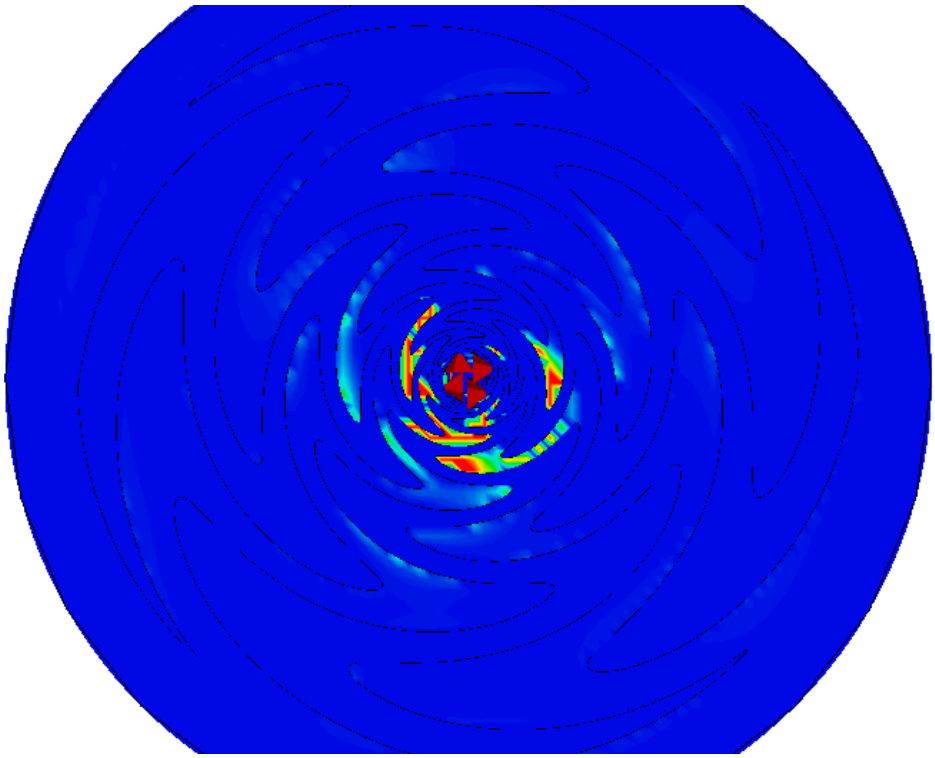

FIGURE A-26: CIRCULAR SINUOUS [Π/4] NORMAL H-FIELD [8.0GHZ - MODE 1]

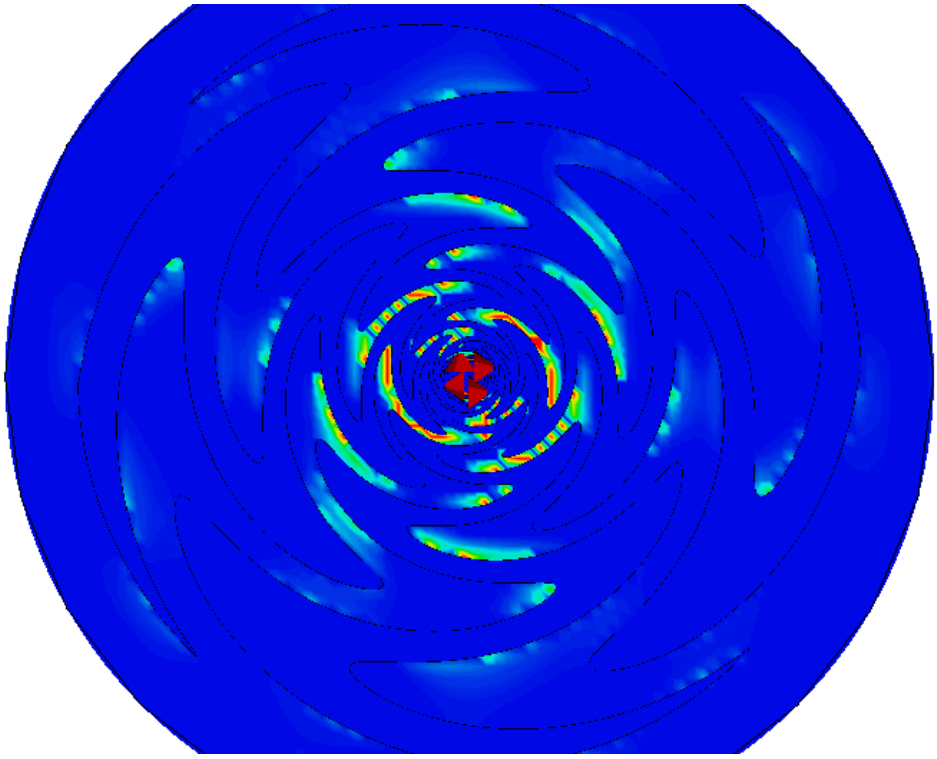

FIGURE A-27: CIRCULAR SINUOUS [Π/4] NORMAL H-FIELD [8.0GHZ - MODE 2]

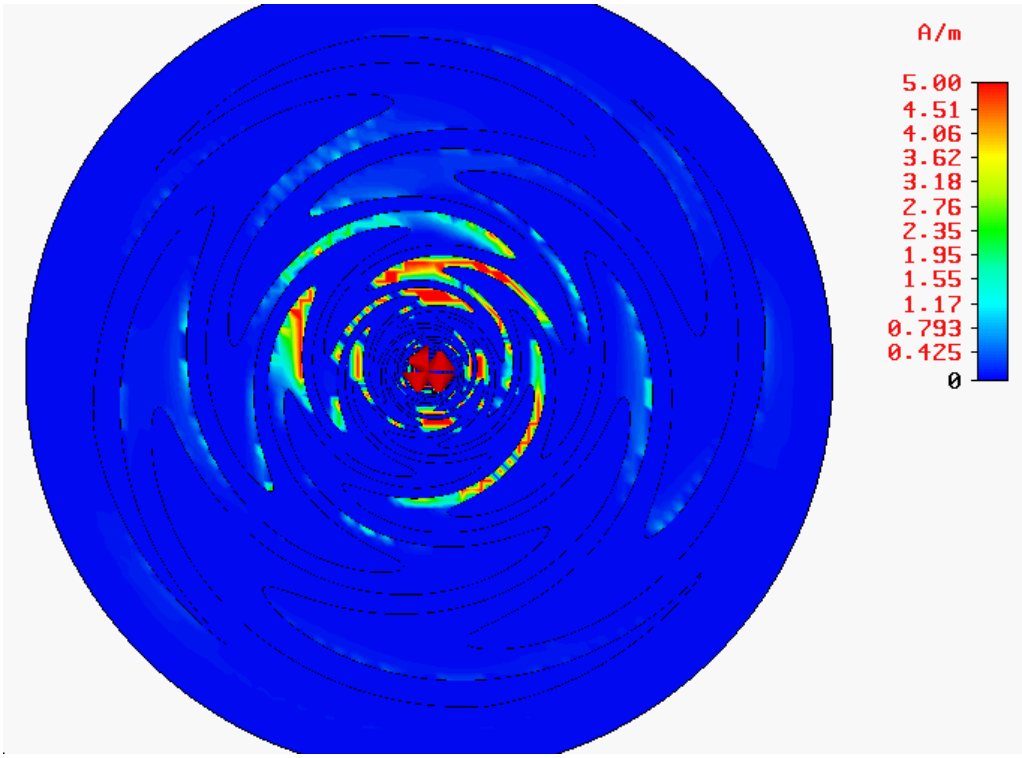

FIGURE A-28: CIRCULAR SINUOUS [Π/3] NORMAL H-FIELD [4.0GHZ - MODE 1]

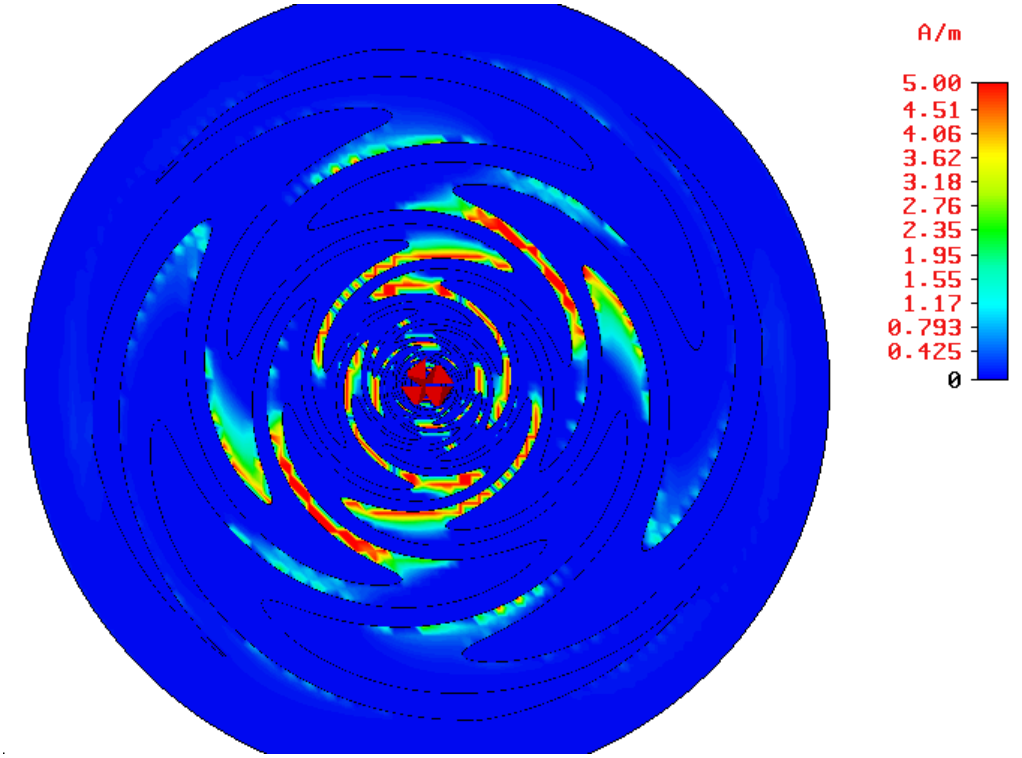

FIGURE A-29: CIRCULAR SINUOUS [Π/3] NORMAL H-FIELD [4.0GHZ - MODE 2]

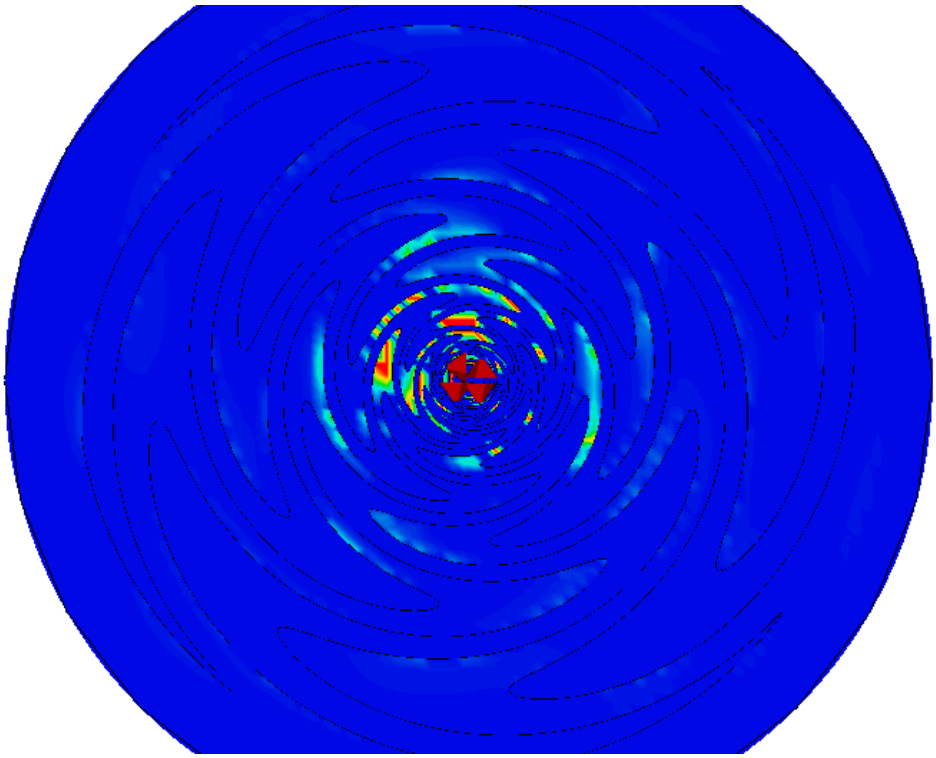

FIGURE A-30: CIRCULAR SINUOUS [Π/3] NORMAL H-FIELD [8.0GHZ - MODE 1]

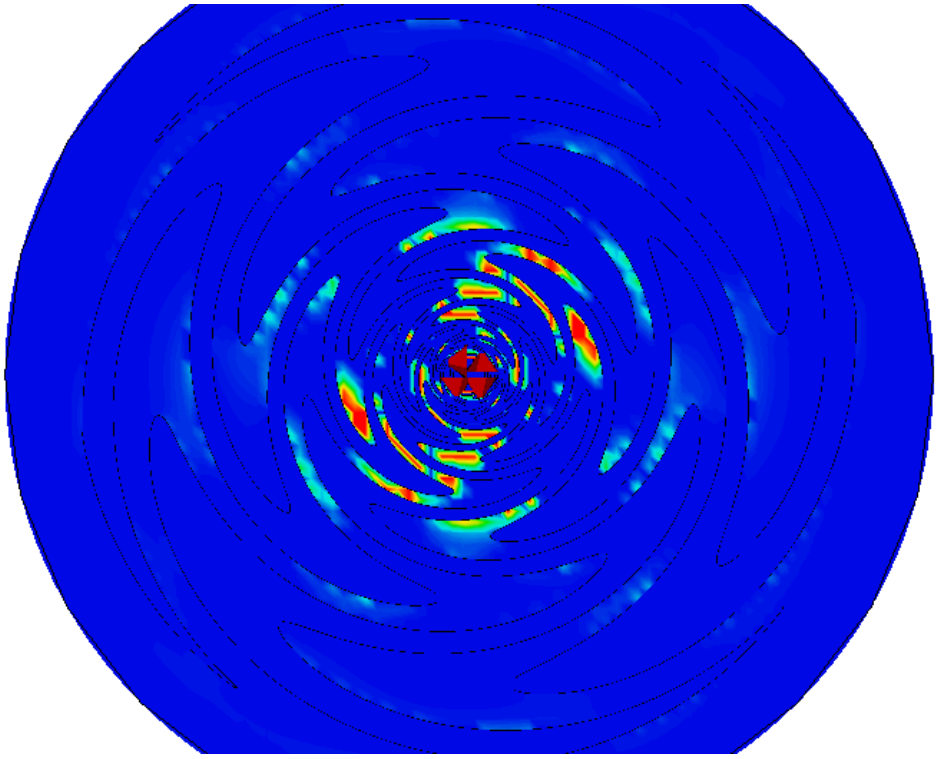

FIGURE A-31: CIRCULAR SINUOUS [Π/3] NORMAL H-FIELD [8.0GHZ - MODE 2]

BIBLIOGRAPHY

BIBLIOGRAPHY

1. **Volakis, John L.** *Antenna Engineering Handbook.* Fourth Edition. New York : McGraw-Hill, 2007. 978-0071475747.

2. **Balanis, C. A.** *Frequency Independent Antennas.* Third Edition. New York : Wiley-Interscience, 2005. 978-0471667827.

3. **Stutzman, Warren L. and Thiele, Gary A.** *Antenna Theory and Design.* Second Edition. New York : John Wiley & Sons, Inc., 1998. 0-471-02590-9.

4. *The Spiral Antenna.* **Bawer, R. and Wolfe, J.** March 1960. IRE Int. Conv. Rec. Vols. AP-8, pp. 84-95.

5. *Broadband Logarithmically Periodic Antenna Structures.* **DuHamel, R. H. and Isbell, D. E.** March 1957. IRE Int. Conv. Rec. Vols. AP-5, pp. 119-128.

6. *The Equiangular Spiral Antenna.* **Dyson, J. D.** April 1959. IRE Trans. Ant. Prop. Vols. AP-7, pp. 181-187.

7. **DuHamel, R. H.** *Dual Polarized Sinuous Antenna. 4,658,262* United States of America, April 14, 1987.

8. *Angle Estimation with a Multi-Arm Spiral Antenna.* **Pasala, K. M. and Penno, R. P.** March 1999. IEEE Aerospace Conf. . Vol. 3, pp. 195-207.

9. **Schneider, S. W., et al., et al.** New Ways to Locate a Threat. *Aircraft Survivability.* 2003, Fall 2003, pp. 31-35.

10. *Various Modes of the Equiangular Spiral Antenna.* **Sivan-Sussman, R.** September 1963. IEEE Trans. Ant. Prop. Vols. AP-11, pp. 533-539. 0018-926X.

11. **Corzine, R. G. and Mosko, J. A.** *Four-arm Spiral Antennas.* Norwood : Artech House, Inc., 1990. 0-89006-348-6.

12. *The Logarithmic Spiral in a Single-Aperture Multimode Antenna System.* **Deschamps, G. A. and Dyson, J. D.** January 1971. IEEE Trans. Ant. Prop. Vols. AP-19, pp. 90-96.

13. **Radcliffe, J. S.** Experimental Validation of the Angle-of-Arrival Estimation Capabilities of a Four-arm Spiral Antenna. [Thesis]. s.l. : University of Dayton, December 2005.

14. **Turner, E. M.** *Slot Spiral Antenna. 2,863,145* United States of America, December 2, 1958.

15. *The Archimedean Two-Wire Spiral Antenna.* **Kaiser, J.** May 1960. IRE Trans. Ants. Prop. Vols. AP-8, pp. 312-323.

16. *Frequency Independent Antennas.* **Rumsey, V. H.** March 1957. IRE Int. Conv. Rec. Vols. AP-5, pp. 113-118.

17. **Rumsey, V. H.** *Frequency Independent Antennas.* New York : Academic Press, Inc., 1966.

18. **Kraus, J. D.** Broadband and Frequency-Independent Antennas. *Antennas.* Second Edition. New York : McGraw-Hill, 1988, 11.

19. **Filipovic, D. S. and Cencich, T.** Frequency Independent Antennas. [book auth.] J. Volakis. *Antenna Engineering Handbook.* Fourth Edition. New York : McGraw-Hill Professional, 2007, 13.

20. *Impedance Properties of Complementary Multiterminal Planar Structures.* **Deschamps, G. A.** December 1959. IRE Trans. Ant. Prop. Vols. AP-7, pp. 371-378.

21. **Mushiake, Y.** Self-Complementary Antennas. *IEEE Ant. Prop. Mag.* December 1992, Vol. 34, pp. 23-29.

22. *Invesitation of a Broad-Band Cavity-Backed Array Antenna.* **Karr, B. A., et al., et al.** July 2004. IEEE. Trans. Ant. Prop. Vol. 52, pp. 1913-1916.

23. **DuHamel, R. H. and Scherer, J. P.** Frequency Independent Antennas. [book auth.] R. Johnson. *Antenna Engineering Handbook.* Third Edition. New York : McGraw-Hill, 1993, 14.

24. *Two-Arm Sinuous Antennas.* **Buck, M. C. and Filipovic, D. S.** May 2008. IEEE Trans. Ant. Prop. Vol. 56, pp. 1229-1235.

25. **Huffman, J. A. and Cencich, T.** Modal Impedances of Planar, Non-complementary, N-fold, Symmetric Antenna Structures. [ed.] T. Milligan. *IEEE Antennas and Propagation Magazine.* February 2005, Vol. 47, 1, pp. 110-116.

26. **Ramo, S., Whinnery, J. R. and Van Duzer, T.** Waveguides with Cylindrical Conducting Boundaries. *Fields and Waves in Communication Electronics.* Third Edition. Hoboken, NJ : John Wiley & Sons, Inc., 1994, 8, pp. 395-461.

27. *Plot of Modal Field Distribution in Rectangular and Circular Waveguides.* **Lee, C. S., Lee, S. W. and Chuang, S. L.** March 1985. IEEE Trans. on Microwave Theory and Techniques. pp. 271-274.

28. *The electromagnetic simulation software package MAFIA 4.* **Clemens, M., et al., et al.** s.l. : IEEE, 1999. ICCEA. pp. 565-568.

29. *A Phase-Stationary High Performance Antenna Test Body.* **Shamansky, H., et al., et al.** s.l. : AMTA, November 1995. Antenna Measurement Techniques Association Symposium.

30. *Multiple Beams From Linear Arrays.* **Shelton, J. P. and Kelleher, K. S.** November 1961. IRE Trans. Ant. Prop. Vols. AP-9, pp. 154-161.